Experimental Characterization and Quasi-Dimensional Modeling of Cyclic Combustion Variations in Spark Ignition Engines

Zur Erlangung des akademischen Grades Doktor-Ingenieur (Dr.-Ing.)
genehmigte Dissertation von Philipp Krost, M.Sc. aus München
Tag der Einreichung: 07.03.2018, Tag der Prüfung: 13.06.2018

Darmstadt 2018 — D 17

1. Gutachten: Prof. Dr.-Ing. Christian Hasse
2. Gutachten: Prof. Dr. techn. Christian Beidl

TECHNISCHE UNIVERSITÄT DARMSTADT

Fachbereich Maschinenbau
Simulation reaktiver Thermo-Fluid Systeme

Experimental Characterization and Quasi-Dimensional Modeling of Cyclic Combustion Variations in Spark Ignition Engines

Genehmigte Dissertation von Philipp Krost, M.Sc. aus München

1. Gutachten: Prof. Dr.-Ing. Christian Hasse
2. Gutachten: Prof. Dr. techn. Christian Beidl

Tag der Einreichung: 07.03.2018
Tag der Prüfung: 13.06.2018

Darmstadt 2018 — D 17

Bitte zitieren Sie dieses Dokument als:
URN: urn:nbn:de:tuda-tuprints-76022
URL: http://tuprints.ulb.tu-darmstadt.de/7602

Dieses Dokument wird bereitgestellt von tuprints,
E-Publishing-Service der TU Darmstadt
http://tuprints.ulb.tu-darmstadt.de
tuprints@ulb.tu-darmstadt.de

Veröffentlicht unter CC BY-NC-ND 4.0 International
https://creativecommons.org/licenses/

Danksagung

Die vorliegende Arbeit entstand während meiner Tätigkeit als Doktorand in der Antriebsforschung bei der BMW Group in München.

Zuallerst möchte ich mich sehr herzlich bei Herrn Prof. Dr.-Ing. Christian Hasse für die wissenschaftliche Betreuung dieser Arbeit und die Übernahme des Hauptreferats bedanken. Insbesondere möchte ich ihm danken für die von ihm entgegengebrachte Zeit für Rücksprachen, seine kritischen Anmerkungen, Ideen und seinen Enthusiasmus für die motorische Verbrennung, die für mich sehr motivierend war.

Weiterhin möchte ich mich bei Herrn Prof. Dr. techn. Christian Beidl für das Interesse an meiner Arbeit und der Übernahme des Korreferats sehr bedanken.

Herrn Dr.-Ing. Christian Schmidt und Herrn Matthias Klietz möchte ich danken für die Ermöglichung der Promotion und dem mir damit entgegengebrachten Vertrauen.

Meinem Betreuer Walter Hübner möchte ich sehr danken für die vielen fachlichen Diskussionen, seine kontinuierliche Unterstützung, dem stets offenen Ohr, auch für nicht-fachliche Themen und die tiefen Einblicke in die unkonventionelle Motorenwelt. Des Weiteren möchte ich ihm danken für die großzügige Bereitstellung von Hardware, sei es immer genügend Prüfstandszeit mit den Versuchsmotoren zur Verfügung zu haben oder um leistungsstarke Workstations für die umfangreichen Simulationen zu bekommen.

Herrn Dr.-Ing. Jens Neumann danke ich für die zahlreichen fachlichen Gespräche für die Entwicklung des Zyklenschwankungsmodells. Seine Ideen brachten mir viele neue Sichtweisen auf die Implementierung und Umsetzung des Modells. Darüberhinaus möchte ich ihm sehr für die Korrektur der schriftlichen Ausarbeitung meiner Dissertation danken, durch die diese einen qualtitativ hochwertigen Feinschliff erhalten hat.

Bei meinen BMW-Kollegen Alois Abel, Manuel Dorsch, Bastian Esefeld, Stefan Frommater, Daniel Haas, Manfred Holzmann, Ulrich Knoll, Daniel Langmandel, Hannes Orlick, Lukas Schäfer und Frithjof Schwerdt möchte ich mich für die vielen Gespräche, Diskussionen und die Unterstützung zu Ausarbeitungs-, Fach-, Prüfstands- und auch Simulationsthemen bedanken. Lukas Schäfer möchte ich noch zusätzlich danken für die Erzeugung und Auswertung von 3D CFD Daten mehrerer Versuchsmotoren. Insbesondere möchte ich hier meinen Mit-Doktoranden Martin Henke hervorheben. Ihm danke ich für die vielen Stunden an fachlichen und nicht-fachlichen Gesprächen, für die Erzeugung von Simulationsdaten aus der chemischen Reaktionskinetik für die Simulationsmodelle und das Korrekturlesen von Papern. Meinen Doktoranden-Kollegen an der TU Bergakademie Freiberg, Stefan Buhl und Frank Hartmann, möchte ich danken für die Erzeugung und Auswertung von 3D CFD Simulationsdaten der Versuchsmotoren.

Meinen Studenten Pawel Nicinski und Jan Witzel danke ich für ihre guten Beiträge zu meiner Arbeit. Ich hoffe sie konnten so viel Wissen und Erfahrung für sich gewinnen, wie ich durch ihre Arbeit.

Des Weiteren möchte ich den hier nicht weiter namentlich genannten Mitarbeitern der Abteilungen EA-3x, LT-5x und LT-23 für ihre Unterstützung bei meiner Promotion danken.

Bei meiner Familie und meinen Freunden möchte ich mich sehr bedanken für ihre stetige Motivation und Unterstützung sowie auch für ihr Verständnis der knappen Zeit.

Mein größter Dank gilt jedoch meiner Frau Moni, die trotz ihrer intensiven beruflichen Einspannung durch ihre unermüdliche Liebe, Geduld und Ermutigung sowie ihr stetiges Verständnis sehr zum Erfolg dieser Arbeit beigetragen hat.

Abstract

Variances in spark ignition (SI) engine parameter settings are still expanding, thus the need for engine calibration is further increasing and virtual engine calibration to optimize engine parameters is being more frequently considered. In particular, the focus of engine calibration is to maximize fuel efficiency and power output while also reducing exhaust emissions up to the engine smoothness limit. This limit is determined by high cycle-to-cycle variations (CCV) and can be detected from indicated mean effective pressure (*IMEP*) fluctuations from one engine cycle to the other. These CCV dictate the stability of the combustion process and engine vibration; thus, the aim is to limit these variations to a certain comfort level.

The objective of this thesis is to set up a zero-dimensional (0D) physical cyclic combustion variations model which can predictively describe CCV. In this work, first, extensive measurement data are produced by investigating five SI engines with different underlying combustion processes. These include both conventional engines and unconventional engines with a long expansion stroke via the crank and valve trains. Engine parameters are varied, in order to experimentally characterize CCV regarding the influence from the fluid mechanics, the chemical gas composition and the thermodynamical state.

The CCV model itself is set up based on recently developed 0D models for turbulence, ignition and combustion; these are initially calibrated by means of 3D CFD data and measurement data. In the model development process, first, a stochastic model is developed to offer the possibility to impose fluctuations. From research into the literature, the physical causes of CCV are extracted. In particular, the new CCV model considers results from 3D CFD Large Eddy Simulations regarding the influence of global and local in-cylinder flow fluctuations, the most significant causes of CCV. For the first time within the 0D/1D simulation environment, flow fluctuations can be taken into account thanks to their availability in the 0D turbulence model used. In the first instance, it is shown that the new CCV model is able to reproduce experimentally observed CCV qualitatively. In order to also describe cyclic combustion variations quantitatively, beside the fluctuations due to these physical causes, factors influencing CCV, i.e. several engine parameters are introduced in the new CCV model.

After the development process, the new CCV model is first verified with the design engine by means of experimental data and another commercial CCV model, considered state of the art. It is shown that the new CCV model is able to reproduce not only the fluctuations in the *IMEP*, but also the underlying fluctuations in the combustion process. Then, with no further calibration, the newly designed CCV model is successfully validated by means of the other engines and engine parameter variations investigated. Furthermore, it is explicitly shown that the new model, in contrast to the state-of-the-art model, is able to accurately describe CCV at two engine operating points with the same engine speed and load, but different internal residual gas rates and in-cylinder turbulence levels. Summing up, the new CCV model offers more encouraging results, enabling it to be used for virtual engine calibration even for cases in which no actual test engine is available.

Kurzfassung

Die Vielfalt der Parametereinstellungen von Ottomotoren steigt kontinuierlich an, so dass der Aufwand für die Motorapplikation stetig zunimmt. Aufgrund dessen gewinnt die virtuelle Motorapplikation an Bedeutung und kommt immer häufiger zum Einsatz. Primäres Ziel ist es, die Effizienz und die Leistung des Motors bei gleichzeitiger Emissionsreduktion bis zur Motorlaufgrenze zu erhöhen. Die Laufgrenze wird durch hohe zyklische Verbrennungsschwankungen definiert und kann mithilfe von Schwankungen des indizierten Mitteldrucks von Motorzyklus zu Motorzyklus detektiert werden. Diese Zyklenschwankungen definieren die Stabilität des Brennverfahrens und ein Ziel der Motorapplikation ist es deshalb, diese Schwankungen auf ein bestimmtes Niveau zu begrenzen.

Das Ziel dieser Arbeit ist die Neuentwicklung eines nulldimensionalen, physikalisch basierten Zyklenschwankungsmodells. Dieses soll zyklische Verbrennungsschwankungen prädiktiv beschreiben können. Zunächst wird eine umfassende Messdatenbank erzeugt, die aus Messungen an fünf verschiedenen Ottomotoren mit unterschiedlichen Brennverfahren besteht. Hierbei handelt es sich sowohl um konventionelle als auch um unkonventionelle Ottomotoren; letztere zeichnen sich durch eine verlängerte Expansion über den Kurbeltrieb oder den Ventiltrieb aus. Für die Untersuchung der Zyklenschwankungen werden bestimmte Motorparameter variiert, um diese Schwankungen hinsichtlich des Einflusses der Strömungsmechanik, der chemischen Gaszusammensetzung und der Thermodynamik experimentell zu charakterisieren.

Das Zyklenschwankungsmodell basiert auf drei bereits entwickelten, nulldimensionalen Turbulenz-, Zünd- und Verbrennungsmodellen, die zunächst sowohl mit 3D CFD Daten als auch mit Messdaten kalibriert werden. Diese drei Modelle können bisher nur das gemittelte Arbeitsspiel darstellen. Als erstes wird ein Stochastikmodell entwickelt, um Schwankungen auf bestimmte Parameter aufprägen zu können. Aus einer umfangreichen Literaturrecherche werden die bedeutendsten Ursachen für Zyklenschwankungen ermittelt. Im neuentwickelten Zyklenschwankungsmodell werden vor allem die Ergebnisse aus 3D CFD Large Eddy Simulationen herangezogen, die sowohl die lokalen als auch die globalen Strömungsschwankungen als die physikalischen Hauptursachen für zyklische Verbrennungsschwankungen identifiziert haben. Diese Größen werden im nulldimensionalen Turbulenzmodell berechnet, womit es zum ersten Mal möglich ist, auf diese Größen Schwankungen innerhalb der null-/eindimensionalen Simulationsumgebung aufzuprägen. Bei der ersten Validierung wird gezeigt, dass das neuentwickelte Zyklenschwankungsmodell qualitativ die in den Experimenten identifizierten zyklischen Verbrennungsschwankungen reproduzieren kann. Um diese auch quantitativ zu beschreiben, werden neben der Aufprägung von Schwankungen auf die Parameter der physikalischen Ursachen Rechenterme eingeführt, die die Einflüsse durch die Variation bestimmter Motorparameter auf die Zyklenschwankungen beschreiben.

Das finale Zyklenschwankungsmodell wird zunächst anhand der Messdaten des Auslegungsmotors und mittels eines kommerziellen Zyklenschwankungsmodells, das dem Stand der Technik entspricht, verifiziert. Es wird gezeigt, dass das neuentwickelte Zyklenschwankungsmodell nicht nur die Schwankungen des indizierten Mitteldrucks, sondern auch die zugrundeliegenden Schwankungen in der Verbrennung reproduzieren kann. Im nächsten Schritt wird das neue Zyklenschwankungsmodell, ohne einer weiteren Kalibrierung, erfolgreich anhand der anderen untersuchten Ottomotoren und Variationen verschiedener Motorparametern validiert. Des Weiteren wird explizit gezeigt, dass das neue Modell im Gegensatz zum kommerziellen Zyklenschwankungsmodell zyklische Verbrennungsschwankungen bei zwei verschiedenen Motorbetriebspunkten mit gleicher Drehzahl und Last, aber unterschiedlichem internen Restgasgehalt und Turbulenzniveaus, akkurat reproduzieren kann.

Zusammenfassend bleibt festzuhalten, dass das neu entwickelte Zyklenschwankungsmodell viel versprechende Ergebnisse zeigt. Somit kann dieses auch für eine virtuelle Motorapplikation verwendet werden, selbst in Fällen ohne real vorhandenen Prüfstandsmotor.

Contents

List of Figures

List of Tables

ABBREVIATIONS

Symbol	*Meaning*
$aFTDC$	After firing top dead center
$bFTDC$	Before firing top dead center
$BMEP$	Break mean effective pressure
CA	Crank angle
CAD	Crank angle degree
CCD	Charge-coupled device
CCV	Cycle-to-cycle variations or cyclic combustion variations
CFD	Computational fluid dynamics
CO	Carbon monoxide
CO_2	Carbon dioxide
COV	Coefficient of variation
DI	Direct injection
DNS	Direct numerical simulation
DOE	Design of experiment
ECU	Electronic control unit
EGR	Exhaust gas recirculation
EOP	Engine operation point
EV	Exhaust valve
EVC	Exhaust valve closing
EVO	Exhaust valve opening
EVT	Exhaust valve timing
FE	Finite element
FID	Flame ionization detector
FRM	Fast running model
$FTDC$	Firing top dead center
GT	Gamma Technologies
H_2	Hydrogen
$HCCI$	Homogeneous-charge compression ignition
ICE	Internal combustion engine
$IMEP$	Indicated mean effective pressure

$ITDC$	Ignition top dead center
IV	Intake valve
IVC	Intake valve closing
IVL	Intake valve lift
IVO	Intake valve opening
IVT	Intake valve timing
LES	Large eddy simulation
LIF	Laser-induced fluorescence
$MFB0\%$	Crank angle of the 0% mass fraction burnt point
$MFB5\%$	Crank angle of the 5% mass fraction burnt point
$MFB10\%$	Crank angle of the 10% mass fraction burnt point
$MFB50\%$	Crank angle of the 50% mass fraction burnt point
$MFB75\%$	Crank angle of the 75% mass fraction burnt point
$MFB90\%$	Crank angle of the 90% mass fraction burnt point
NO_x	Nitrogen oxide
O_2	Oxygen
PDF	Probability density function
PFI	Port fuel injection
PID	Proportional-integral-derivative
PIV	Particle image velocimetry
PTA	Pressure trace analysis
$RANS$	Reynolds-averaged Navier-Stokes
SI	Spark ignition
SRM	Stochastic reactor model
ST	Spark timing
TDC	Top dead center
THC	Total hydrocarbons
TKE	Turbulent kinetic energy
TPA	Three pressure analysis
$WLTC$	Worldwide Harmonized Light-Duty Vehicles Test Cycle
WOT	Wide-open throttle

GREEK SYMBOLS

Symbol	*Meaning*	*Unit*
α	Heat transfer coefficient	$W/(m^2K)$

α	Temperature exponent within s_L	-
β	Pressure exponent within s_L	-
Δ	Differential	$\%$
ϵ	Compression ratio	-
ϵ	Turbulent dissipation rate	m^2/s^3
κ	Heat capacity ratio	-
λ	Heat conduction	W/mK
λ	Air-fuel equivalence ratio	-
λ_w	Wall friction number	-
μ	Mean value (statistics)	-
μ	Discharge coefficient	-
μ	Dynamic viscosity	kg/ms
Π	Pressure ratio	-
ρ	Density	kg/m^3
σ	Standard deviation	-
τ	Characteristic burning time	s
ϕ	Equivalence ratio	-
φ_{CS}	Combustion start	CAD
φ_{CD}	Combustion duration	CAD
ω	Angular velocity	1/s

LATIN SYMBOLS

Symbol	*Meaning*	*Unit*
A	Area	m^2
B_m	Maximum laminar flame speed	m/s
B_Φ	Laminar flame speed roll-off value	m/s
C_f	Coefficient of wall friction	-
c_m	Mean piston velocity	m/s
c_u	Circumferential velocity	m/s
D_0	Flame-related diffusion coefficient evaluated at $T = T_0$	m^2/s
D	Diameter	m
D_{bore}	Diameter of cylinder bore	m
D_t	Turbulent diffusion coefficient	m^2/s
Da	Damköhler number	-
E	Energy	J

h	Specific enthalpy	J/kg
HV	Heating value	kJ/kg
j	Specific angular inertia	J/kg
k	Turbulent kinetic energy	m^2/s^2
l	Valve lift	mm
L	Angular momentum	-
l_F	Laminar flame thickness	m
$l_{F,t}$	Turbulent flame brush thickness	m
l_t	Turbulent length scale	m
m	Mass	kg
p	Pressure	bar
Pr	Prandtl number	-
r	Radius	m
r_k	Spark kernel radius	m
R	Specific gas constant	J/kgK
Re	Reynolds number	-
rpm	Revolutions per minute	min^{-1}
q	Heat flux	W
s_{piston}	Piston stroke	m
s_L	Laminar burning velocity	m/s
s_T	Turbulent burning velocity	m/s
$s_{T,k}$	Turbulent burning velocity of the spark kernel	m/s
Sc	Schmidt number	-
t	Time	s
T_0	Inner layer temperature	K
T_0	Reference temperature $T_0 = 293.15$ K	K
T	Temperature	K
T_u	Tumble number	-
u	Specific internal energy	J/kg
u'	Turbulent fluctuation velocity	m/s
V	Volume	m^3
V_c	Compression volume	m^3
V_h	Volume of cylinder stroke	m^3
v	Flow velocity	m/s

w	Flow velocity	m/s
x	x direction	m
$x_{physical\ limit}$	Physical limit (normalized)	-
Y	Mass concentration	-

SUBSCRIPTS

Symbol	*Meaning*
b	Burnt
$dens$	Density
$diss$	Dissipation
e	Entrained
f	Flame
k	Kernel
l	Lower
L	Laminar
p	Pressure
$prod$	Production
ref	Reference
s	Eccentricity
$shear$	Shearing
t	Integral
T	Turbulent
u	Unburnt
x	x-directional
y	y-directional
z	z-directional

1 Introduction

Politics and customers worldwide are continuously increasing pressure on the automobile industry to reduce fuel consumption and thus the carbon dioxide (CO_2) emissions, in order to conserve crude oil resources, to counteract global warming and to limit fuel prices as oil prices rise. In the last few years, it has been possible to reduce fuel consumption of spark-ignition (SI) engines, in particular, by implementing advanced technologies such as turbo charging, direct fuel injection and fully variable valve trains. Nevertheless, even greater technological progress is necessary to meet future CO_2 emission targets. Approaches for significantly increasing efficiency include SI engines with a variable compression ratio and/or a long expansion stroke by means of a valve train or crank train, among others.

Independently of the technology implemented to increase fuel efficiency, all SI engines show characteristic cyclic combustion variations, also known as cycle-to-cycle variations (CCV). Cyclic combustion variations can been seen from fluctuations of the indicated mean effective pressure (IMEP) or the combustion rate from one engine cycle to the other. It is commonly known among development engineers specialized in internal combustion engines (ICE) that high cycle-to-cycle variations primarily occur in very low load ranges (high residual gas rate, in order to reduce gas exchange losses) or in very high load ranges (late combustion centers due to knock limitation) in engine maps. Since these variations represent the stability of the combustion process and thus engine smoothness, the aim is to limit them to a certain comfort level. Consequently, optimal engine parameters cannot always be chosen for maximum fuel efficiency. Even with optimal engine parameters for a given operating point, not all cycles burn optimally; thus they reduce fuel economy and power [64, 82, 93].

The phenomenon of cyclic combustion variations has been the focus of engine research for several decades [96, 133], yet their physical causes are not fully understood or quantified even today. Besides the possibility of experimental analysis through indicated cylinder pressure measurements or optical measurements, a very detailed understanding of the physical causes can come from three-dimensional Computational Fluid Dynamics (3D CFD), solving space in all three directions or Large Eddy Simulations (LES) with their high-resolution images of the turbulent flow field in the combustion chamber [36–38, 106, 125]. However, these LES investigations are only rarely used due to the high demand of computing resources and long computing times required since several consecutive cycles need to be calculated. The focus of the industrial development of engine combustion processes is usually on the whole engine map, rather than only on a few operating points; thus, several engine parameters are varied in large design of experiments (DOE). In this respect, zero-dimensional/one-dimensional (0D/1D) simulation tools (e.g. GT-Power [67]) are commonly used in the automobile industry for engine map-wide working-process calculations or analysis of measurements, in order to investigate the gas exchange and combustion process. In contrast to the 3D CFD simulation environment, 1D solves space only in one direction, commonly in the flow direction, whereas 0D simulation environments do not solve space at all, but are only time-dependent.

In recent decades, several approaches have been used to simulate CCV with 0D/1D simulation tools; both semi-empirical [103, 124, 127] and physical [33, 106] approaches. As has been shown, these approaches can predict cyclic combustion variations in terms of quality, for example correctly predicting CCV trends for a combustion center variation, but not reliable in terms of quantity, that is the absolute value for CCV, for engine map-wide simulation or operating point focus. The reason is that these models are either limited to an empirical approach or to the sole inclusion of only a few physical causes of CCV, in order to simulate cycle-to-cycle variations. The existing models usually only investigate CCV in one specific SI engine and only in a few engine operating conditions. The CCV model presented in this study aims to cover several of the physical causes of cyclic combustion variations. The aim is to investigate different conventional and unconventional engine combustion processes and integrate the knowledge gained into the model developed. Furthermore, this model aims to predict CCV based on changing engine parameters such as speed, load, spark timing, valve lift and timing, as well as the air-fuel equivalence ratio λ. To build the new CCV model on a physical basis, it is set up based on existing physically based predictive models for turbulence, ignition delay and combustion [49–51, 91, 92], in order to calculate the mean engine cycle.

The objectives of this thesis are outlined as follows.

- The CCV model approach shall be developed with, applied to and investigated with different combustion/engine concepts. One objective of this thesis is to validate the new CCV model not only by means of conventional engines but also with unconventional combustion processes, in order to ensure that the new CCV model functions in various contexts. For the purpose of validation, a large pool of measurement data of five different SI engines is to be build up.
- For the mean cycle simulation, the newly developed CCV model shall use existing turbulence, ignition and combustion models as a sophisticated modeling basis which previous CCV model developers did not have access to. These models allow the most significant physical causes of cycle-to-cycle variations to be implemented within the 0D/1D simulation environment, since these causes are described as parameters. Previous CCV model development processes were therefore limited, since not all physical CCV causes could be implemented.
- A new stochastic model as part of the CCV model is to be designed and then coupled with the above models. Thus, for the first time, the new CCV model shall enable a physical description of cyclic combustion variations, not only one gained by empirical tuning.
- Furthermore, the aim of the new model is not only to integrate the most significant physical causes of cyclic combustion variations, but also more factors influencing them in terms of engine parameter variations than in previous approaches. Thus, more universal statements can be made regarding the precise functioning of the newly developed CCV model.
- A further objective is to thoroughly investigate the sensitivity of modeling CCV regarding the mean cycle combustion simulation.

The proposed CCV model can then be used in the context of virtual engine application of SI engines with different combustion processes (degree of different turbulence generation, different residual gas rates, different air-fuel mixtures), in order to reduce the number of experiments on engine test benches. Furthermore, it can be included in the virtual evaluation of a new engine design where no existing test engine is available, and the maximum running smoothness is thus estimated. Implementing this model in engine process calculations, especially regarding engine smoothness limits leads to more reliable simulation results and makes 0D/1D simulation even more attractive in comparison to the more time-consuming and expensive engine test bench operation.

Chapter 2 gives a theoretical overview of cyclic combustion variations. Research into the literature provides the definition as well as the physical causes and effects of CCV. First, the definition describes how to recognize CCV. Then, the complexity of the physical causes is summed up and illustrated according to its influencing factors: the in-cylinder-flow-field, mixture homogeneity, ignition and combustion processes. This is followed by a presentation of different existing approaches for modeling CCV in the 0D/1D simulation environment.

Chapter 3 presents the experimental setup and specifications of five investigated test bench engines. Three of these are research engines, equipped with a long expansion stroke via the valve train or crank train. These are used for a first experimental analysis of CCV with regard to fluid mechanics, the thermodynamic in-cylinder state and the chemical mixture composition. The other two, four-cylinder production engines, are analyzed for a further investigation of cyclic combustion variations and to validate the CCV model developed in this study. Furthermore, the method used to evaluate the experimental data regarding CCV is exhibited.

The numerical setup of the 1D gas dynamic and 0D combustion process simulation is introduced in Chapter 4. In particular, the engine model setup with implemented burn rates gathered from measurement data is compared to engine models with predictive turbulence, ignition delay and combustion calculation. Furthermore, the calibration of the engine models with measurement data and 3D CFD data is presented.

In Chapter 5, the new CCV model is introduced. First, the aims and ideas of the model approach are described. Then, the basic model is presented as is the stochastic model and its setup and features. This is followed by connecting the stochastic model to the physical causes and parameters, identified as influencing CCV in the predictive turbulence, ignition delay and combustion models, in order to complement the CCV

model. Finally, the model calibration process is shown in detail.

Chapter 6 presents the application of the new CCV model for all five engines. The simulation results are subsequently compared to measurement data and a CCV model defined as the state of the art. Furthermore, the potential and limitation of the developed 0D/1D CCV model are investigated and discussed.

The last chapter gives a summary of the study and an outlook for future research work to be done.

2 Fundamentals of cycle-to-cycle variations

The appearance of combustion variations in internal combustion engines from one cycle to the other has been known for over 100 years [24, 88, 99]. During that time, many studies have been conducted to investigate cycle-to-cycle variations with regard to their physical causes, impacts on engine behavior and countermeasures to reduce CCV [64, 69, 93, 96, 133]. The complexity of the number and nature of their physical causes has been broken down into numerous boundary conditions of the underlying SI combustion processes such as direct fuel injection, high turbulence development, residual gas recirculation and lean combustion [23, 58, 94, 125, 134]. Investigations have also been undertaken regarding changes to the hardware, such as different combustion chamber configurations (piston and head) or intake valve surface properties [6, 133]. In the following, first the definition of CCV will be specified along with the impacts. Then, an overview of the physical causes and the different factors influencing them will be given. This includes listing various influences inside and outside the combustion chamber and extracting the most important causes of CCV to be used for simulating cyclic combustion fluctuations. Last, the most promising previous approaches will be introduced, along with the state of the art in CCV modeling.

2.1 Definition and impact of cycle-to-cycle variations

In the following subsection, the definition of CCV as well as different ways to detect and visualize them are shown and compared. The occurrence of cyclic combustion fluctuations evoke several major disadvantages on engine operation - reduced engine smoothness, lower power output, lower engine efficiency and higher pollutant emissions - which are explained in the subsequent subsection on their impact along with a description of countermeasures to prevent CCV.

2.1.1 Definition and detectability

Cycle-to-cycle variations can be defined as fluctuations in physical engine parameters inside and outside of the combustion chamber from one cycle to the other. There are different ways to display these cyclic variations, e.g. their occurrence can easily be detected on engine test benches with indicated pressure measurements of individual cylinders. Variations in the course of the cylinder pressure are implicated by the randomly varying development of the combustion process from one engine cycle to the other and between different cylinders. Examples of pressure curves for 10 consecutive cycles for a four-cylinder SI production engine operated at low engine speed and load are illustrated in Figure 2.1. The mean engine cycle is also displayed, for comparison.

Another way to detect CCV is by measuring total hydrocarbon (THC) emissions with a fast-response flame ionization detector (FID) in the exhaust manifold within each engine cycle. This data gives information about cycles in which the combustion has not yet ended when the exhaust valves open. Hydrocarbons could also be left in the squish crevice, leading to unburned fuel in the form of THC emissions exiting the combustion chamber. Unburned fuel in the exhaust may lead to the destruction of monoliths in the three-way-catalyst due to very high temperatures over a certain operation time [74]. These examples show that the appearance of CCV can be detected using a number of measurement technologies. It is therefore necessary to categorize them according to their physical background. For an overview, Ozdor et al. [95] categorized the detectable in-cylinder parameters into

- cylinder-pressure-related parameters: indicated mean effective pressure, maximum pressure peak, crank angle at maximum pressure peak.
- combustion-related parameters: ignition delay, burn duration and maximum burn rate obtained from a pressure trace analysis.
- flame-front-related parameters: initial flame front radius obtained from optical measurements.
- exhaust-gas-related parameters: gaseous and solid exhaust components.

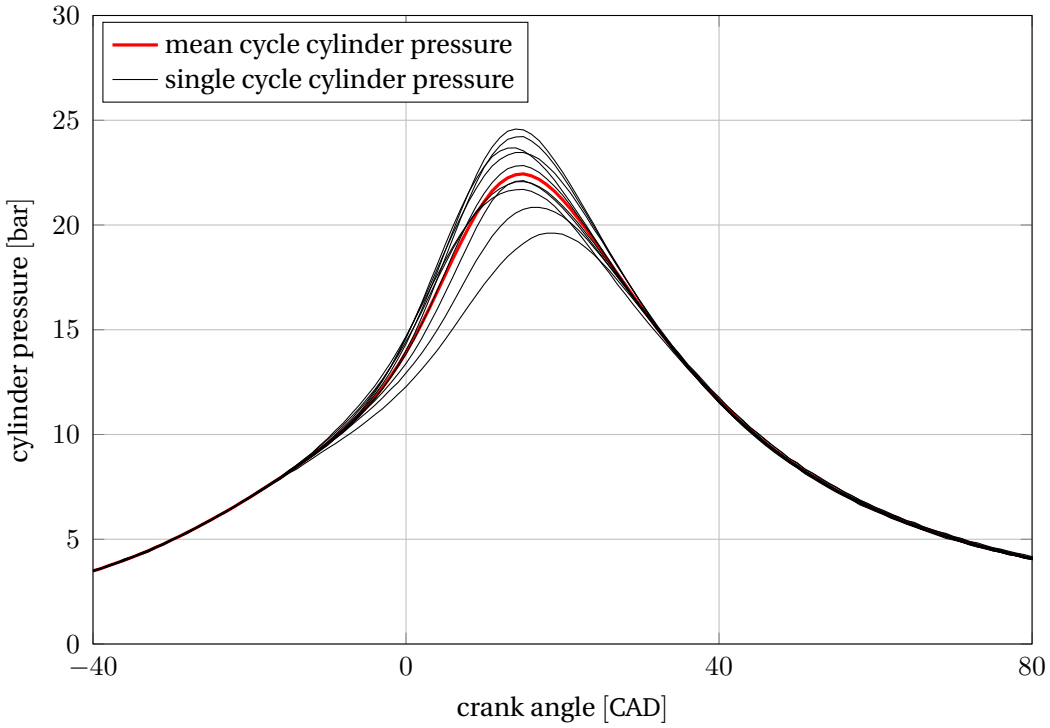

Figure 2.1.: Pressure curves of 10 consecutive cycles including the mean cycle.

Further details of this overview can be found in the literature [64, 80, 84, 95, 112]. With the increasing usage of 3D CFD Large Eddy Simulations (LES) when evaluating CCV, the cyclic resolution of the in-cylinder charge motion can extend this overview, thus including flow-related parameters of global and local flow structures. All these fluctuations in CCV-related parameters can differ from one other in height or behavior, depending on the engine operation points and the engine geometry and technology used, and act as a basis for comparison. Historically, and from a user-oriented point of view, the cylinder-pressure-related fluctuations, in particular the indicated mean effective pressure (*IMEP*) fluctuations, are the most common ones to describe CCV in matters of engine development. The fluctuations in the maximum cylinder pressure and crank angle at maximum cylinder pressure are not the first choice to specify cycle-to-cycle variations due to the non-linearity of slow burning cycles as explained in [84], see Figure 2.2. The cylinder pressure evaluation of a stable operating point (COV_{pmax} < 5 % and COV_{IMEP} < 2 %, for definition see below) and an unstable operating point are illustrated in Figure 2.3. At the stable operating point, the maximum cylinder pressure is linear faced with the crank angle at which it occurs. In contrast, the unstable engine operation exhibits a typical behavior that is defined as *hook-back* and *return* by Matekunas [84]. Thus, it is no longer possible to correlate the maximum cylinder pressure proportionally to the crank angle where it occurs.

In addition, for the engine-map-wide analysis of cycle-to-cycle variations, *IMEP* fluctuations, as a direct measure of deviations in the engine's thermal work, are easier to compare than the actual complex and interwoven physical causes of CCV concerning the combustion process, e.g., the maximum cylinder pressure in repsect of its position [64, 66].

In statistics, one means of quantifying the amount of symmetric variation in a data-set of n observed values x_i *(i=1,...,n)* and an arithmetic mean value $\bar{x}$ is the standard deviation σ [75]. The standard deviation is calculated from the positive square root of the variance σ^2, see the following equations.

$$\sigma^2 = \frac{1}{n}\sum_{i=1}^{n}(x_i - \bar{x})^2 \tag{2.1}$$

with

$$\bar{x} = \frac{1}{n}\sum_{i=1}^{n} x_i = \frac{x_1 + x_2 + ... + x_n}{n} \tag{2.2}$$

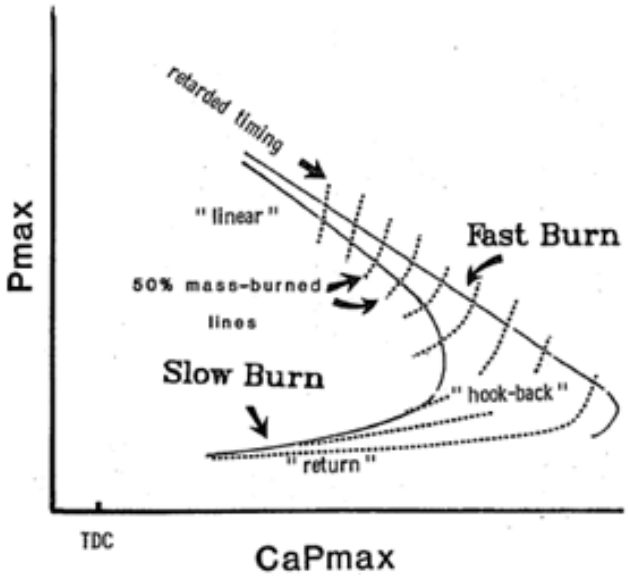

Figure 2.2.: Maximum pressure p_{max} against $CA_{p_{max}}$. Reprinted with permission Copyright 1983 SAE International. Further distribution of this material is not permitted without prior permission from SAE. [84]

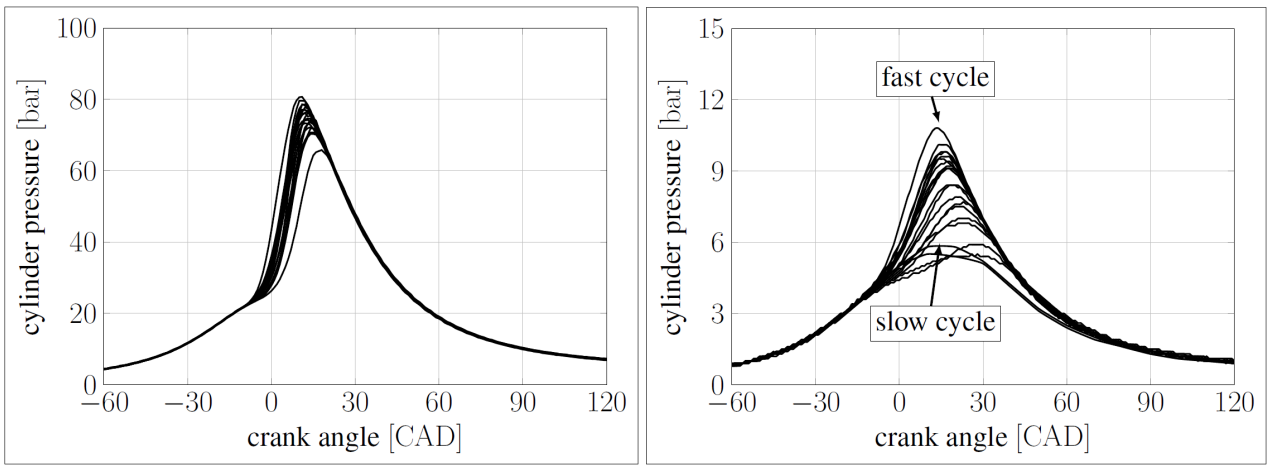

Figure 2.3.: Cylinder pressure evaluation of a stable operating point (left) and an unstable operating point (right).

and

$$\sigma = +\sqrt{\sigma^2} \tag{2.3}$$

For a better comparison with respect to engine smoothness, the standard deviation σ is scaled to the mean value $\bar{x}$ with the result of the coefficient of variation (*COV*) [75].

$$COV = \frac{\sigma}{\bar{x}} \times 100\,[\%] \tag{2.4}$$

Thus, the variation in the indicated mean effective pressure is better comparable at a glance engine-map-wide [64]. The following equation illustrates the calculation of COV_{IMEP} with n equaling the number of cycles investigated.

$$COV_{IMEP} = \frac{\sqrt{\frac{1}{n}\sum_{i=1}^{n}(IMEP_i - \overline{IMEP})^2}}{\overline{IMEP}} \times 100\,[\%] \tag{2.5}$$

Similarly to the calculation of COV_{IMEP} in Equation 2.5 COV_{pmax}, $COV_{CA,pmax}$, etc. can be described. Engine operating points with a very high COV_{IMEP} are usually implied by cycles with combustion that is not ended when

the exhaust valve(s) open(s) or even when misfire occurs. This can be the case when the engine is operated at high exhaust gas rates, very lean air-fuel mixtures or very late ignition timings. These high COV_{IMEP} may lead to an asymmetric probability distribution of the *IMEP* that cannot be reproduced with the standard deviation alone. In order to represent this asymmetric distribution, so-called skewness is needed. However, skewness causes the statistical analysis to be more complex and the additional benefit is negligible. Also, these extreme engine operating points may disregard the comfort level and lead to high pollutant emissions; thus, they are commonly not applied to production engines.

With the definition and statistical description of CCV in mind, several ways of visualizing the results of the statistical analysis of certain engine parameters are presented. Generally, CCV of cylinder pressures can be illustrated as in Figure 2.1. However, for other engine output parameters investigated, different forms of illustrations provide more information about CCV. These are 1D plots for illustrating one or several specific operating point(s) or engine map-wide 2D contour plots which are shown by way of example for the *IMEP* in Figure 2.4.

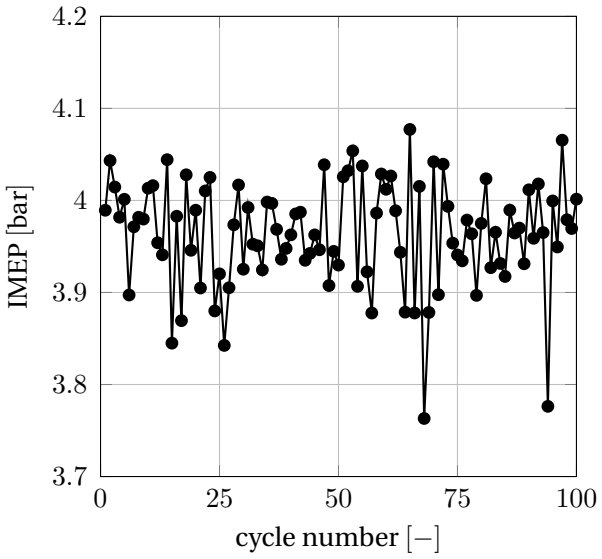

(a) 100 consecutive cycles at a mean *IMEP* of 4 bar.

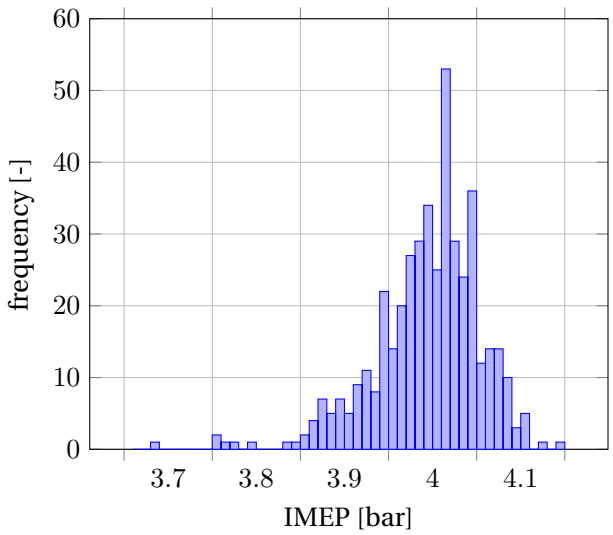

(b) Frequency distribution of 440 cycles at a mean *IMEP* of 4 bar.

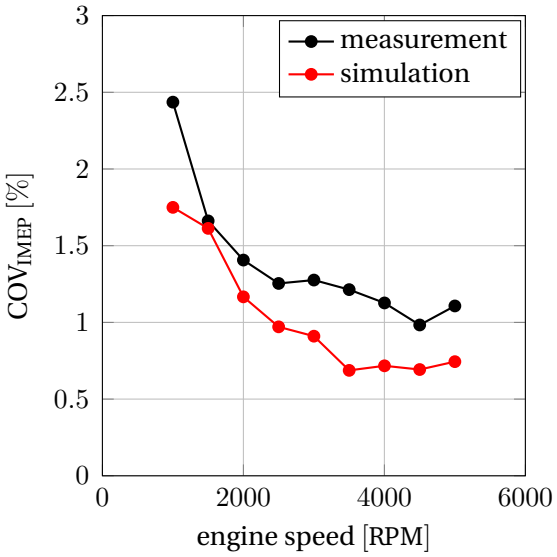

(c) COV_{IMEP} for an engine speed variation at constant load of 4 bar.

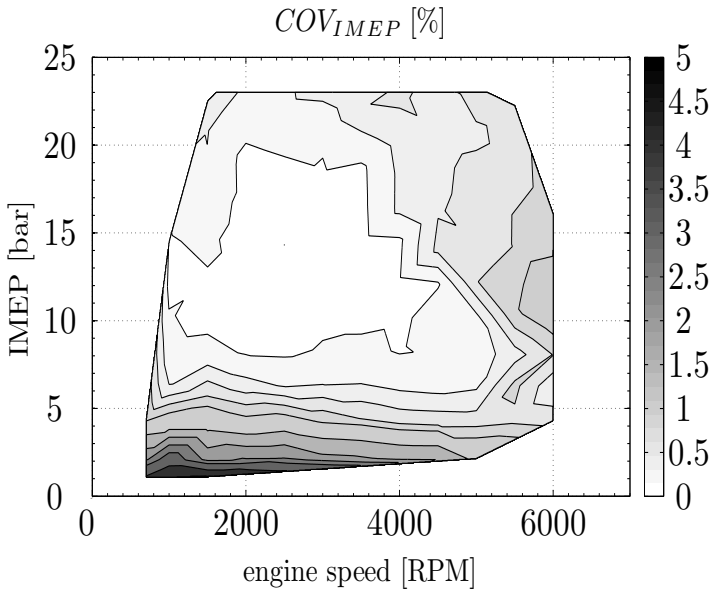

(d) 2D contour plot illustrating COV_{IMEP} engine map-wide.

Figure 2.4.: Different ways of illustrating cycle-to-cycle variations.

Subfigure 2.4 (a) shows consecutive engine cycles of an example engine operating point with a mean *IMEP* of 4 bar. It gives a good overview of the *IMEP* output of individual cycles and can directly be correlated to the combustion rate when explicitly compared to mass fraction burn (*MFB*) points such as *MFB5%*, *MFB50%* and *MFB90%* (for illustration see Appendix A). Also, with *IMEP* being around 0 bar for an individual cycle, misfire can easily be detected at first sight. Subfigure (b) shows a frequency distribution. This distribution can be obtained from the statistical analysis of a certain number of consecutive engine cycles. It shows the *IMEP* output with defined increments. The wider the margin of deviation is from the statistical mean value, the higher the cycle-to-cycle variations are. This can be transferred to a higher standard deviation of the parameter that is investigated. For a simulation-to-measurement comparison of CCV in specific engine parameter variations, as will be used in Chapters 5 and 6, subfigure (c) provides a practical presentation format. In this example, a variation in the engine speed and the fixed engine parameters of the air-fuel ratio, valve timings and ignition timing is illustrated for COV_{IMEP}. At a glance, the differences between the simulation and measurement data can be seen qualitatively and quantitatively. The 2D contour plot in subfigure (d) shows COV_{IMEP} across the engine map. With this illustration format, different causes of CCV can be investigated, e.g., high cycle-to-cycle variations at full load have different causes than at a low engine speed and load. With the help of further 2D contour plots considering *MFB50%*, valve timings and the resulting exhaust gas rates (*EGR*), along with other engine parameters, these causes can be detected.

2.1.2 Impact

Engine operation conditions with high cyclic combustion variations - apart from other appearances such as drivetrain vibrations or engine mounting - can result in an irregular power output. This might be both audible and perceptible to the customer, especially when the engine is idling (less important in future due to comprehensive series production engine start/stop systems) or at a low engine load. Thus, the engine manufacturers' ambition is to reduce CCV, improving drivability and comfort [25, 31, 58, 65, 95].

Furthermore, cycle-to-cycle variations can cause up to 10 percent of engine power reduction, while the fuel economy does not change. In the literature, a rise in efficiency of 6 percent is reported when CCV is eliminated arithmetically [82]. Engine design is usually based on the average engine cycle; however, CCV cause faster and slower burning cycles. For example, since spark timing is optimized for the mean cycle, deviations will inevitably result in a higher fuel economy and lower power output. This can also be seen at low engine loads, where de-throttling strategies which involve raising exhaust gas rates may increase not only fuel efficiency but also cyclic variations, see Figure 2.5.

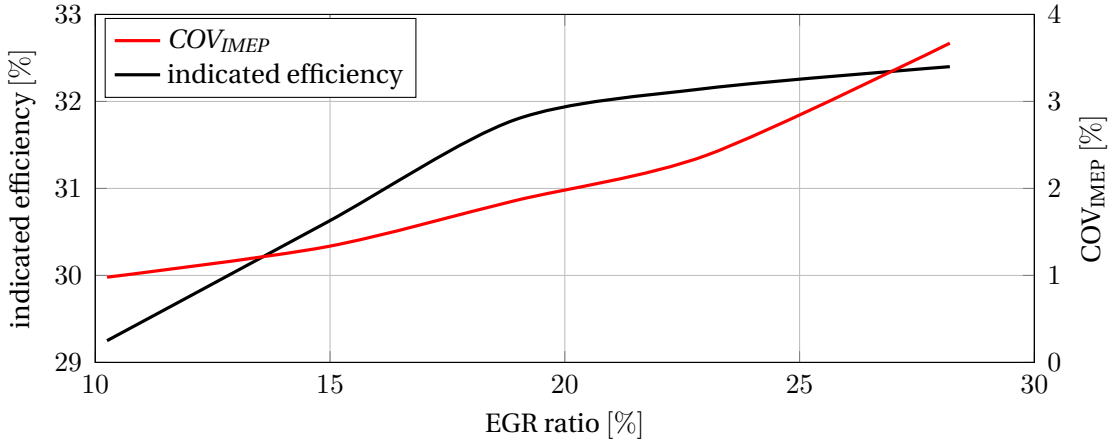

Figure 2.5.: Indicated efficiency and COV_{IMEP} vs. *EGR* ratio of a SI engine (engine speed = 2000 rpm, *IMEP* = 2 bar, $\lambda = 1$, MFB50% = 8 CAD).

In addition, at high engine loads, the phenomena of knock has to be kept in mind. Due to combustion variations, an adequate distance to the knock limit has to be kept which in return again reduces the fuel efficiency. Some engine operation conditions may not even be operational. For instance, if knock occurs, the spark timing is retarded, causing higher CCV and in return possibly resulting in undrivability due to extreme engine rough-

ness. Therefore, one elementary way to alter cyclic combustion variations regarding ignition is by changing its timing [6–8, 127]. Figure 2.6 by Wenig [127] illustrates this schematically.

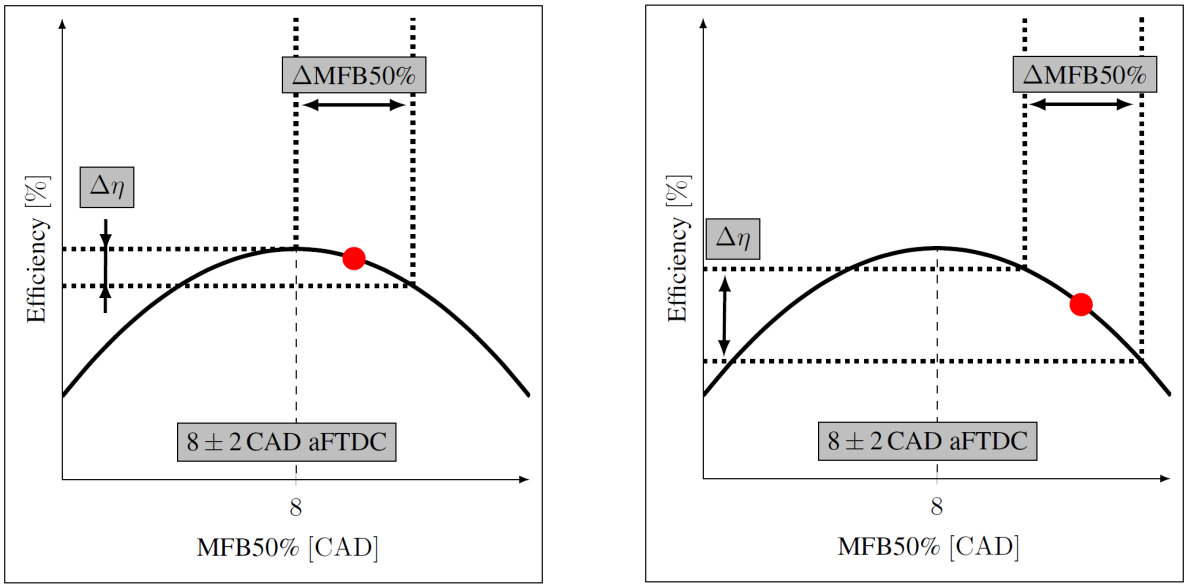

Figure 2.6.: Influence of ignition timing and center of combustion on engine efficiency adapted from Wenig [127].

The change in the ignition timing and therefore the center of combustion influences engine efficiency, which directly correlates with the indicated power output. At the efficiency optimum of around 8 crank angle degrees (CAD) after firing top dead center (aFTDC), small variations in the ignition timing with ± 2 CAD have only small effects on changes in efficiency, see Figure 2.6 on the left. However, at a higher deviation from the efficiency optimum, compare Figure 2.6 on the right, the same fluctuations in ignition timing significantly increase the impact on changes in efficiency, on the indicated power output and thereby also on the cyclic combustion variability.

Other effects are detectable at operation points with extremely slow burning cycles, resulting in incomplete combustion or even misfire and in return causing unburned fuel in the exhaust system in the form of high carbon monoxide (CO) emissions and, in particular, THC emissions [65, 73, 82, 95, 117]. These events have to be avoided due to the strict emission regulations.

With these impacts in mind, reducing CCV unlocks an unused potential of increasing fuel efficiency and engine power while simultaneously reducing pollutant emissions. Some examples are given in Section 2.3.

2.2 Physical causes of cycle-to-cycle variations

Previous researchers on cyclic combustion variations separated the occurrence of CCV into physical causes and influencing factors [95, 112]. Physical causes are the origins of cycle-to-cycle variations, whereas influencing factors can be interpreted as the sensitivity of SI engines towards CCV. The latter, in contrast to the causes, can be affected by different measures such as spark plug electrode orientation. A second way to classify the occurrence of CCV is linking them to linear, non-linear, so-called chaotic, and stochastic correlations [25, 31, 52, 53, 81, 126]. Stochastic correlations can be associated with the physical causes, whilst linear and non-linear correlations can be assigned to the influencing factors.

The complexity of the nature of physical causes and influencing factors has been investigated with measurements and simulations in numerous studies. From a historical point of view, and thus due to the few available technical capabilites, indicated cylinder pressure measurement [72, 97, 116] and 0D simulations [7, 118] in the first instance have provided information about the existence of and phenomena around physical causes. The development of sophisticated optical methods and fast-increasing computing power provide an explicit insight

into the separated sources and the relevance of the physical causes. Detailed information on the in-cylinder volume is essentially obtained from various types of optical measurements [13, 42, 57] and 3D CFD Reynolds-averaged Navier-Stokes (RANS) [108] and Large Eddy Simulations [37, 61, 106], as well as a combination of the two [18, 48, 110].

In this section, the physical causes of CCV will be highlighted in different categories. Cycle-to-cycle variations can be correlated with external factors (outside of the cylinder) and in-cylinder factors. External factors mainly depend on gas exchange processes such as fluctuations in the inducted air, injected fuel and amount of *EGR* from cycle to cycle. In contrast, the fluid flow, the formation of the fuel spray, the charge mixture and the initial flame kernel as well as the flame-wall quenching, among other things, are in-cylinder processes. However, the individual contributors to these complex processes throughout the combustion process are difficult to classify and may even be different for specific SI engines. Certain causes can interact with each other, e.g., turbulent intensity can influence the mixture homogeneity. Furthermore, the relative importance of each cause is not fully understood today and still is an area of active research. Therefore, the interactions of individual processes in a cause-and-effect chain are far better established [59]; they are illustrated in Figure 2.7.

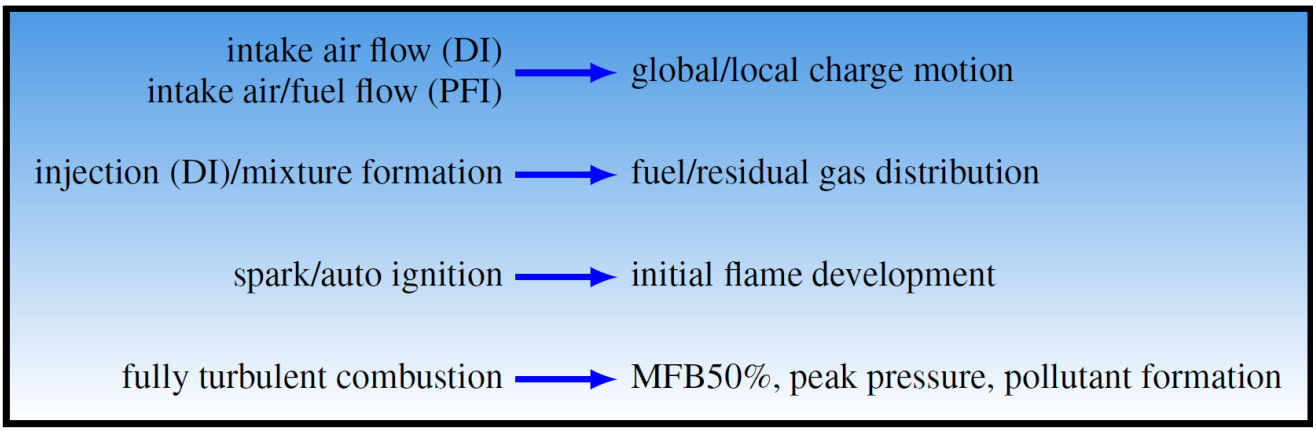

Figure 2.7.: Cause-and-effect chain of engine combustion (left) leading to different cyclic combustion variations (right); adapted from Hasse [59].

As engine combustion is influenced by a large number of successive and parallel processes, the cause-and-effect chain clearly describes the general level of consecutive processes (on the left), opposed to the resulting CCV observations (on the right). Starting with the gas exchange process, the intake flow mainly determines both the cyclic cylinder charge and its global and local in-cylinder motions. In the second step, the fuel injection, in particular, if injected directly into the combustion chamber, determines the mixture formation and fuel distribution by interaction with the in-cylinder flow field. Conversely, the injection pulse also affects the global and local flow fields. In the subsequent step, under normal combustion conditions, the ignition is induced by the spark plug. In the initial ignition phase, the early flame kernel is primarily determined by the local flow field, *EGR* and air-fuel ratio. In the main combustion phase, fluctuations in the flame propagation, flame quenching and pollutant formation are triggered as the subsequent causes of the effects described above. In the following, these individual steps are described in detail.

2.2.1 Global and local charge motion

The global and local in-cylinder flow structure is mainly established by the design of the intake port, as well as by the configuration of the intake valve and the combustion chamber. During the intake process, the separation of the flow at the machined edges in the intake port and at the inlet valve face as well as the change in flow direction on the piston surface are of significant relevance for determining the flow structure [60, 61]. Several studies [14, 19, 62] report the formation of a large-scale rotating vortex through the intake jet and piston deflection, referred to as tumble, to be substantially subject to cycle-to-cycle variations.

A publication by Vermorel et al. [123] based on Large Eddy Simulations shows a high level of cyclic tumble intensity variations at the time when the inlet valve closes (IVC), which have been generated during the intake

phase. These have a direct effect on large-scale velocity fluctuations, which can affect the flame expansion velocity and the direction of the initial flame. Furthermore, they observed variations in the tumble breakdown from cycle to cycle which in turn indirectly influence the fluctuations in the small-scale velocity field. These small-scale fluctuations will be described in detail in the next paragraph. Hasse et al. [61] performed LES for a motored engine operation. The authors' results also show considerable deviations in the global flow velocity field in individual engine cycles compared to the mean cycle. When single cycles are examined, more vortex structures are seen to be present, and also on a smaller level than in the average cycle. In addition, the center and the magnitude of the large structures fluctuate cyclically. This outcome corresponds the results gained by Qin et al. [105] using LES and particle image velocimetry (PIV) measurements.

Another publication [21] also investigated the effect of macroscopic motion fluctuations and compared these to kinetic energy variations of the flow field. With the help of PIV measurements, they found out that during fired stoichiometric engine operation the kinetic energy variations are more significant, regarding cyclic combustion variations, than the macroscopic flow fluctuations, whereas this behavior is inverted during lean engine operation. Enaux et al. [38] examined a stable fired engine operating point ($COV_{pmax} < 5\,\%$ and $COV_{IMEP} < 2\,\%$) in a specific port fuel injection (PFI) research engine with the help of LES and compared their results to PIV measurements. The in-cylinder flow dynamics of LES are in good agreement with experimental outcomes. They conclude that although during the intake stroke the absolute fluctuations are maximized, the highest relative variations are found during the compression stroke. Using PIV measurements of a motored engine the authors of [13] indicate that cyclic variability of the global flow is due to the non-linear nature of the largest coherent structures, rather than being due to the weaker random turbulent components.

Richard et al. [106] analyzed global flow versus local flow characteristics by means of LES results. The authors identified the local flow in the vicinity of the spark plug as almost independent of the global flow field. Local flow structures are affected by the spark plug existence as a source of disrutpion, rather than by the large-scale tumble structure. This behavior is only visible when investigating individual cycle results, not in the average engine cycle. As [36, 61, 123] have outlined, local flow fluctuations are a significant cause of CCV. Small-scale turbulence fluctuations generated by the tumble breakdown in the vicinity of the spark plug induce important cyclic combustion variations early in the combustion and can even have a greater impact than large-scale fluctuations [123]. Thereby, high levels of small-scale fluctuations caused by a strong tumble drop can be correlated to the fastest burning cycles. LES results gathered by Enaux et al. [36] using the same research engine mentioned above [38] also confirm that the local velocity field is a main factor triggering CCV. The LES results indicate that the local flow structure has an impact on the formation of the initial flame kernel. Unfavorable cyclic flows deflecting the flame kernel to the spark plug along with the nearby cylinder head environment, can increase heat losses of the flame and lead to partial flame quenching. Furthermore, local below-average turbulence intensity in a single engine cycle can also be a reason for slow initial flame development in the same cycle. Both phenomena increase cyclic combustion variability. Granet et al. [48] first confirm their LES results using chemiluminescence and LIF (laser-induced fluorescence) experiments. Then, the work group verifies Enaux's findings of the considerable influence of the local flow on CCV. In cycles where the local flow interferes heavily with the initial flame kernel, the flame can split into two flames. It might be possible to quench the second kernel early at the cylinder walls, whereas the main flame kernel at the spark plug might burn out slower than in the average cycle. Granet et. al. [48] also show that positioning the initial flame kernel 1 mm further into the combustion chamber can prevent the aforementioned split, thus confirming the severe affect of the local velocity field at the spark plug.

The literature sources mentioned above have clearly shown the flow field fluctuations in the vicinity of the spark plug at ignition timing to be a main triggering factor of CCV. Enaux et al. [36] observed a second, less significant CCV effect, the free turbulent flame propagation, between mass fuel burning times *MFB10%* and *MFB50%*. This can reverse the initial trend of burning velocity. Although the effect is not absolutely clear, it is assumed that this cause may depend on the initial flame development history and on the occurring flame wall interactions due to the global flow fluctuations.

2.2.2 Mixture homogeneity

Several studies investigated the physical causes of fuel and residual gas mixture inhomogeneity on cycle-to cycle variations, though with contradicting conclusions. Early studies by Pundir [104], correlating cyclic pressure variations to cyclic exhaust emission fluctuations, and by Johansson [69, 70], investigating early combustion, indicate that charge non-homogeneity has a notable effect on CCV. Ball [7] outlined that the level of influence depends on the underlying combustion process and engine operating point. Engines with optimal combustion chambers regarding a minimum number of edges and keeping high turbulence levels at ignition timing are considered to have lower CCV influences from mixture fluctuations. On the other hand, the engine operating point can also influence mixture homogeneity. Lee et al. [80] show with the help of an optical spark plug and Rayleigh scattering measurements that an inhomogeneous lean in-cylinder charge can be correlated to cyclic combustion variations due to lower laminar flame velocities. In contrast, an inhomogeneous stoichiometric charge is not confirmed to be a major contributor to CCV. This finding is also confirmed for high *EGR* [122], which increases the risk of mixture non-homogeneity. For this engine operating point, the laminar flame velocity can also be regarded as lower, thus increasing CCV.

With a continuing increase in efficiency and decrease in pollutant emissions in the engine development process in recent years, strong focus has been laid on homogenizing the in-cylinder charge. Thus, recent studies consider CCV arising from mixture non-homogeneity to be of minor importance [1]. Goryntsev et al. [47] investigated the influence of the direct fuel injection pulse on mixture homogenization by means of Large Eddy Simulations. Their findings show that the fuel pulse has a relevant influence on the turbulent intensity and its resulting fluctuations. However, no clear enhancement regarding mixture homogenization is found. PIV measurements were undertaken in the publication by Bode et al. [12] to investigate the fuel spray interaction with the in-cylinder flow field. Here, the specific spark-ignition engine, characterized by a spray-guided direct-injection (DI) system, is operated at a low engine load and with a stratified fuel-air mixture. It is shown that the spray is nearly unaffected by the large-scale flow structures in the intake stroke. This fact is reversed when fuel is injected during the compression stroke, in which case the upward flow opposes the spray propagation. However, in this study, no direct conclusion is drawn regarding the quality of the mixture homogenization. This conclusion is confirmed by Adomeit et al.[2], who furthermore investigated a stratified injection strategy by means of LES. They found strongly differing mixtures at ignition timing with notable asymmetries, which in combination with high-turbulence fluctuations can result in misfires. Vermorel et al.[123] verified these findings by means of LES and using a premixed gaseous fuel-air mixture. In this study, variations in the local or global charge mixture were not found to be of sufficient relevance to induce significant fluctuations in the combustion process.

2.2.3 Ignition and initial flame kernel development

It is well established that the ignition phase plays a significant role in CCV [101]. As described in the previous subsections, the spark and the subsequent initial flame kernel are severely affected by local flow fluctuations. Bates [9] extensively investigated spark discharge and early flame kernel growth in a SI engine under slightly lean combustion operation by means of two image-intensified charge-coupled-device (CCD) video cameras. First, he concluded that, if in every cycle the spark energy release exceeds a certain threshold and the spark release is of a duration of at least one millisecond, the spark plug's energy release itself does not act as a source of CCV. His findings reveal that the initial flame kernel shows great variation in size, shape and location related to the particular local flow structure from cycle to cycle. Larger initial flame kernels correlate with a higher burn rate raise and shortened ignition delay. The flame kernel shape is self-similar throughout individual cycles, i.e. the subsequent fully propagated turbulent flame is of a similar shape, though affected by wall interferences. Stretched initial flame kernels and circular flame fronts coincide with a faster combustion, whereas flat, i.e. not-elongated, flames exhibit lower burn rates. The cycle-dependent location or eccentricity of the spark particularly determines the heat loss to and distortion by the spark plug electrodes, cf. the study by Herden [63] in Subsection 2.3.1. However, the subsequent flame kernel formation and its dispersion in the location is reported to have a major effect on CCV. Aleiferis et al. [3] confirm these results with a lean-burn SI engine. The study indicates that the initial flame kernel size is a major factor regarding CCV. This is shown by correlation coefficients of the flame kernel size in comparison to the *MFB5%* and the *IMEP*, which are -0.96 and 0.85, respectively, for a given engine operating point. A further study by Pischinger et al. [102] also shows not only the contact area

of the initial flame and the electrode but also its corresponding heat loss to be of importance for cyclic combustion variability. In particular, at the charge-diluted engine operation limit, the heat loss fluctuations can be the main CCV triggering factor. Ayala et al. [5] outline the extension of the charge dilution limit by means of an admixture of fuel types with high laminar flame velocities, such as hydrogen. At stoichiometric equivalent ratios and with a low residual gas rate, Bates [9] and Etheridge [39] report the cyclic flame kernel development to be stabilized and, thus, the CCV to be reduced.

2.2.4 Flame burn-off and subsequent cycle effects

Cyclic fluctuations in the flame-wall quenching are known to have an effect on CCV. Suckart et al. [119] investigated the flame-wall quenching distance by means of wall heat flux measurements at different engine operating points. The existence of cyclic flame-wall quenching is qualitatively measurable. However, the level of CCV cannot be quantified due to the complex determination of the flame-wall interactions. Firstly, this is due to the limitation of the number of measuring points inside the combustion chamber. Secondly, the flame orientation when hitting chamber walls can not be captured. A head-on flame quenching releases a higher heat flux than side-wall flame quenching. Suckart et al. [119] conclude that the cyclic variation in the flame-wall quenching distance depends on the prior mixture homogenization and on the turbulent flame propagation near the combustion chamber walls.

Among other things, Fischer [42] investigated the effects of cyclic flame-wall quenching on exhaust emissions. Flame-wall quenching exists independently of the present turbulence intensity and flow field in the combustion chamber. At high turbulence intensity levels, the fuel spray contact with the combustion chamber walls and thus any resulting THC emissions can be neglected. Nevertheless, the high THC emissions which still occur can be correlated to flame quenching at the border area of the flame on the combustion chamber walls. These THC emissions can be found in the subsequent engine cycle after the gas exchange.

However, despite the existence of unburned hydrocarbon and residual gas in the subsequent cycle, Abdi Aghdam et al. [1] found that these effects are only of marginal relevance to cyclic combustion variations. This confirms the conclusion drawn by Ball [7]. Cyclic cylinder charging fluctuations regarding variations in the amount of fuel, air and residual gas left from the previous cycle can be neglected when the engine is operated stiochiometrically. Nonetheless, at the charge dilution limit, under the occurrence of partial burning or complete misfire, CCV can be detected from the loss of power output from this single misfired engine cycle. Also, Hinze [65] indicates that cyclic variations are seen to influence residual gas when the engine is idling, although his research shows that the in-cylinder turbulence and the charge motion have the most significant effect on CCV. Today, with very strict exhaust emission regulations, one single misfiring engine cycle can disrupt the entire exhaust emission certification [10].

2.3 Influencing factors and countermeasures

It is commonly known that cyclic combustion variations cannot be eliminated completely, but only reduced. Dai et al. [26] report efforts to minimize combustion variations by controlling the engine application system in real time. However, monitoring the timings of fuel injection and ignition as well as the fuel metering of individual cylinders may not be satisfactory, since it only includes the observation of previous cycles. Cycle-to-cycle variations are linked not only to deterministic processes but also to purely stochastic ones. While deterministic processes can be controlled, a publication by Larimore et al. [78] gives an example of controlling the *EGR* ratio for a gasoline HCCI engine; engine operation conditions evoking high stochastic processes have to be minimized. The authors of [26] and [28] point out that the most desired countermeasure to reduce CCV is to accelerate the combustion process. This can be done by various measures, some of which will be described in the following.

2.3.1 In-cylinder flow

Stochastic fluctuations in the turbulent in-cylinder flow cannot be prevented. However, increasing the global flow velocities of swirl and tumble motions leads to an improvement in the turbulent intensity near the firing

top dead center (FTDC). Furthermore, squish flows are also reported to have a positive effect, increasing turbulence at the start of combustion [122].

These measures can be induced by different adaptations of several influencing factors. One factor is the engine speed. A rising engine speed directly increases the turbulent kinetic energy level in the combustion chamber, which correlates with lower CCV [6]. Herden [63] reports an increased flow velocity at the spark plug as the engine speed rises, as illustrated in Figure 2.8.

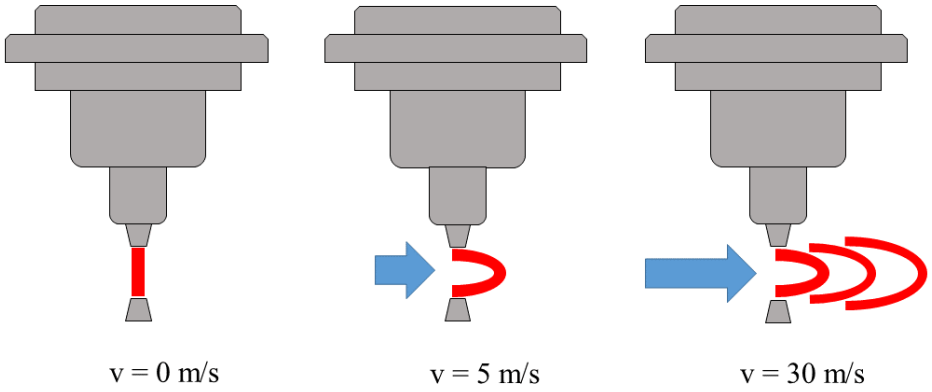

Figure 2.8.: Deflection of the initial spark plasma at different local flow velocities according to Herden [63].

At first, this increase in speed has a positive effect, since initial flame quenching at the spark plug electrodes can be reduced. The initial flame is deflected and still established in one flame kernel (v = 5 m/s). At this point, the ignitability is maximized and stabilized. With further increasing local flow velocities, the initial spark plasma is torn away from the spark plug and reignition occurs, i.e. several flame kernels are developed [63]. Combustion variability can be worsened with more than one flame kernel.

Another factor is the intake manifold, which influences the in-cylinder flow field structure. For instance, the authors of [93] and [94] outline that raising the turbulent intensity via an enhanced tumble motion, stabilizes the ignition delay times. Fischer et al. [42, 43] investigated different systems to induce a large-scale tumble structure. The authors report an improvement in CCV if the main intake flow is centered between the two intake valves. This stabilizes the intake flow and intensifies the large-scale tumble motions, resulting in an improved combustion development and reduced THC emissions. Another study [6] compares a standard intake valve to a shrouded valve that introduces a higher swirl component to the global charge motion, thus increasing the turbulent kinetic energy (TKE). This additional charge motion accelerates flame propagation velocities and therefore, decreases cyclic combustion variations [122].

Enaux et al. [37] are able to prove the strong influence of the local velocity field at the spark plug on combustion variations with the help of Large Eddy Simulations. Their calculations demonstrate that the global tumble structure has a major impact on the local flow at the spark plug in consecutive engine cycles. With a stabilized tumble motion, the local flow structure is built up similarly in successive cycles. Thus, the authors are able to confirm the variability of the local flow as one of the main triggers of CCV.

Operating gasoline engines with a high charge dilution, either by means of exhaust gas recirculation or by lean fuel-air ratios, requires high in-cylinder charge motions. Both [79] and [122] indicate that high swirl motions are more convenient to decrease ignition delay times than tumble motions. Also, the burn duration is enhanced with a distinct swirl in contrast to tumble motions, thus efficiently decreasing COV_{IMEP}.

2.3.2 Fuel type, fuel injection and mixture formation

It has long been known that fuel characteristics have a measurable effect on cycle-to-cycle variations [95, 116, 133]. These characteristics include, among other things, the heating value, the fraction of oxygen and the carbon to hydrogen ratio, which determine the laminar flame speed and burn rates. The authors report a more

stable cyclic cylinder pressure development with increased burn rates due to higher laminar flame speeds and therefore, lower cyclic combustion variations. Vice versa, with leaner air-fuel ratios, the laminar flame speed decreases with the consequence of higher CCV [6].

In order to reach high combustion stability, a perfect homogeneous mixture formation is to be aspired to [35, 101, 104, 120]; this also reduces the risk of knock at high engine loads [122]. There are several ways to achieve a homogeneous fuel-air mixture. One is to strongly increase the global and local flow velocities for a high degree of turbulent cylinder charge mixing. In particular, it should be taken into account that the fuel-air mixture has to be transported to the spark plug consistently during every engine cycle. This measure is essential when direct fuel injection is applied to the combustion engine. Here, the air- and spray-guided combustion processes are advantageous in comparison to the wall-guided direct-injection ones.

Although port fuel injection is commonly known to achieve homogeneous air-fuel mixtures, attention must be paid to the injection timing and angle at a low engine speed and load, as well as at load steps. The authors of [58] report an optimal port fuel injection timing to be shortly before the intake valves open for idle engine operation. Schueck et al. [111] investigate the formation of particles at locally rich fuel-air mixtures. The authors indicate that the optimal port fuel injection timing for engine load steps is synchronous with the intake valve opening in combination with a charge motion flap in the intake manifold. Furthermore, they outline that the angle of each injector nozzle should be wide but the spray angle itself should be narrow, in order to minimize fuel-intake-wall interactions.

In SI engines, the in-cylinder charge can be diluted with excessive charge either through a leaner air-fuel ratio or through an increasing amount of internal or external residual gas. Both changes regarding the internal chemical state cause a decrease in laminar flame speeds. This in turn raises the cyclic combustion variability [64].

2.3.3 Ignition process

The location, quantity and property of the ignition source are one of the dominant factors in cycle combustion variations [7, 122, 133]. High spark discharge energies, double ignition systems, surface ignition (glow ignition from abnormal combustion is not meant) and alternative ignition processes, such as plasma or laser ignition, enable the air-fuel cylinder charge to burn faster. Furthermore, it should be mentioned that laser ignition has the additional advantage of being independent of the local flow, consequently further reducing CCV [35, 55].

Fluctuations in the ignition timing have a direct effect on cyclic combustion and thus need to be minimized. Cyclic variable discharge characteristics also have an important effect. The spark discharge duration is of particular relevance. Above all, taking optimal ignition timing as a basis, fully variable valve trains with inconsistent cyclic cylinder charges also have an effect on CCV [35].

The orientation of the spark plug in relation to the local flow has a measurable effect on CCV [109]. If the spark plug and, especially, the ground electrode protect the spark channel from the local flow, the initial spark kernel can be formed more consistently with every engine cycle and the risk of blow-outs is limited. The investigation carried out by [96] shows that the *COV* of pressure-related parameters doubles from the worst to the best spark plug orientation using a conventional J-type spark plug.

Furthermore, the spark plug design can influence combustion variability. The authors of [96] and [63] analyzed several spark plugs with one or more electrodes, as well as outstanding or diminished electrodes. They outline how the local flow at the spark plug depends on CCV. Ozdor et al. [96] report a significant reduction in COV_{IMEP} with four diminished electrodes at an idle engine speed and load. At other engine operating points, there is no evidence for this spark plug type being advantageous. However, they still conclude that the different electrode properties have a considerable influence. Ball [7] indicates that thin electrodes reduce the heat transfer from the initial flame to the electrode. This results in a faster initial flame kernel growth and thus improved cycle-to-cycle variations.

As already mentioned in Subsection 2.1.2, the ignition timing significantly influences the level of cyclic combustion variations. CCV is increased, if the engine is not operated at an optimum center of combustion. In

addition, Bates et al. [9] point out that with late ignition timings near FTDC a higher energy release is needed to overcome the increased pressures, thus the cyclic combustion variability is worsened.

2.3.4 Combustion chamber and gas exchange components configuration

Van Basshysen [122] reports an improvement in cyclic combustion variations with a higher engine compression ratio or variable compression ratios. In particular, in the case of low engine loads, the cylinder pressure at ignition timing is raised without the risk of knocking. Enhancing the thermodynamical state by means of higher cylinder pressures and temperatures at the end of the compression stroke shortens the ignition delay and increases the flame propagation speed. Furthermore, a compact combustion chamber configuration reduces flame paths.

The publications by [6] and [132] also declare the compression ratio as an influencing factor. Furthermore, the authors investigated the influence of different piston and intake valve surface types, as well as the combustion chamber configuration. A bowl-in piston increases TKE in comparison with a flat piston; however, the TKE center is further away from the spark plug, which can reduce the burn rates. TKE is increased with a shrouded intake valve in comparison with a conventional valve; this leads to improved combustion burn rates. However, Matekunas [84] indicates that there is a loss of volumetric efficiency because the inlet flow area is partially masked. The examination of the combustion chamber leads to the conclusion that an open chamber should be preferred, in order to minimize CCV. With an open chamber, the flame propagation is spherical, inducing higher flame speeds and reducing flame-wall quenching. In contrast, squish combustion chambers increase CCV, since the variation in the turbulence generation by the squish flow was found to be dominant, thus increasing cyclic combustion variability.

Ozdor et al. [96] identify an improvement in cyclic cylinder pressure variations if the valve and piston leakage and thus the cylinder charge fluctuations are minimized. The authors gained this insight from a motored engine operation, in which the $COV_{p,\,max}$ is consistent at 0.5 % to 2 %. Thus, they hypothesize that at fired engine operation, this pressure leakage persists, producing a background noise. As already mentioned in Subsection 2.3.3, in-cylinder charge variations are due to the fluctuations from fully variable valve trains (unsteady cyclic valve cam phasing and valve lift setting). Furthermore, Ball [7] outlines that *IMEP* fluctuations can be induced in the gas exchange by the fuel, the residual gas composition and the temperature as well as variations in the compressible fresh charge from one engine cycle to another.

With the influencing factors made obvious, different measures can be taken to have the in-cylinder fuel/air volume penetrated more rapidly and the chamber walls reached earlier, thus minimizing the flame-wall quenching distance. The faster the combustion, the better the combustion-to-volume correlation, since more energy is released near FTDC.

2.4 0D/1D modeling of cycle-to-cycle variations

Three decades ago, the first quasi-dimensional CCV model approaches were developed, with the focus on virtually reproducing cycle-to-cycle variations from experiments [83] or by modeling non-linear combustion kinetics, in order to better understand cyclic combustion variations [27]. Since then, several more CCV models have been established. These model approaches are based on empirical backgrounds [89, 103, 129], reaction kinetics [39, 40, 121] and a reduction from 3D CFD Large Eddy Simulations [33, 106]. First, 3D LES characteristics concerning CCV modeling are depicted, then previous 0D/1D models will be listed briefly as well as 0D/1D model approaches, which are considered state of the art and described in detail.

2.4.1 3D Large Eddy Simulations

For the detailed investigation and modeling of the causes of cyclic combustion variations, insights into the in-cylinder and gas exchange processes and phenomena are essential. One possibility is optical measurements of SI engines such as the particle image velocimetry (PIV). However, finding direct correlations, for example to the fluctuating in-cylinder local and global flow structure in the post-processing of the measurement data is very

challenging and not straight forward. In contrast, 3D CFD Large Eddy Simulations permit at least the same level of insight as these optical measurements. Moreover, flow fluctuations, globally and locally, can immediately be extracted as demonstrated by Richard et al. [106]. Furthermore, cyclic flow separations at the machined edges of the intake port are hard to measure optically, whereas LES also renders these results. Therefore, one more advantage of LES is the possibility to use the findings directly in lower-dimensional simulation environments [106]. However, the long (wall-clock) LES calculation times have to be kept in mind. The more common RANS approaches cannot identify the phenomena of cyclic combustion variations, since most of the fluctuations have to be modelled [59]. The physical causes extracted from Large Eddy Simulation results from the literature are used in this study, in order to develop the new cyclic combustion variations model.

2.4.2 Previous 0D/1D modeling

Martin et al. [83] investigated CCV by means of a deterministic model, describing the fluctuations in the *IMEP*. This model was used to analyze correlations between the *IMEP* from the current and prior engine cycles. The authors found out that there is only a feedback effect from the prior engine cycle with very lean air-fuel mixtures, not when the engine is operated stoichiometrically.

Shen et al. [112] used an existing turbulent entrainment model and extended it by adding the calculation of the initial flame kernel size and temperature, which varied cyclically. The convection velocity at the spark plug was taken into account by modeling the flame kernel not as a sphere but as an ellipsoid. Furthermore, the cyclic variation in the flame kernel location was varied according to empirical findings from previous experimental studies, not just arbitrarily. In addition, the turbulence intensity fluctuated from one cycle to another. The authors first analyzed the statistics on combustion duration times from their simulation results and from measurements. Then, they compared the simulation and experiments and concluded that the fluctuations in turbulence intensity in the vicinity of the spark plug have the most significant impact on CCV. The variations in the flame kernel location are less important, and the fluctuating EGR can be neglected.

Stone et al.[118] also used a turbulent entrainment combustion model to simulate CCV. In contrast with Shen's model, only constant fluctuations in the flame kernel displacement were implemented. The authors then compared the simulation results to measurements regarding the variation of fuel, air fuel mixture, ignition timing and throttle setting. For the validation statistics of the *IMEP*, the maximum cylinder pressure, the maximum pressure rise, the burn rate and the flame speed are used. This CCV model is able to describe cyclic combustion variations from experiments qualitatively, but not quantitatively. Stone et al. state that flame kernel displacements do have a notable effect on CCV, but turbulence intensity also has to be taken into account for a better description of CCV.

Daw et al. [30] state that cycle-to-cycle variations in engines cannot be described by a combination of a non-chaotic deterministic component and a stochastic component. Rather, CCV can be specified by the superimposition of a nonlinear low-deterministic component and a stochastic component. In the specific CCV model, fluctuations in the EGR, air-fuel ratio and combustion efficiency are implemented. The residual gas rate and air-fuel ratio are perturbed randomly. As the combustion efficiency is determined with the air-fuel ratio, its fluctuations directly results from the perturbation of the air-fuel ratio. With these perturbations the authors expected to account for prior engine cycle effects, but, no clear correlation could be established. Nevertheless, statistics on the heat release rate gathered from simulation results, compared to those from experiments, showed good agreement.

The model developed by Dai et al. [26] uses a nonlinear regression method to describe *IMEP* fluctuations. A regression term was determined using 6000 engine operating points from 13 different engines. The resulting mathematical term of the 3rd order included the influences of the ignition delay (*MFB0%-MFB10%*), burn duration (*MFB10%-MFB90%*), center of combustion (*MFB50%*), engine speed, load, EGR and air-fuel ratio. The CCV model is able to describe the COV_{IMEP} qualitatively for variations in engine speed, load, spark timing, air-fuel ratio and residual gas rate. The COV_{IMEP} is also met quantitatively for experimental values below 5 %.

Another CCV model devised by Ball [7] only perturbed the combustion burn rate in the first version of the model. However, since the COV_{IMEP} was underestimated in most cases compared to experimental data, Ball

extended the CCV model by implementing one further perturbation of the completeness of combustion, with considerably better results. Furthermore, the author investigated cyclic variations in nitrogen oxide (NO_x) emissions. The CCV model underestimated NO_x standard deviations in comparison to the measurement. Ball states that NO_x formation is very sensitive to the EGR and to the in-cylinder temperature. Thus, he concludes that the underestimation is due to the lack of perturbations in the residual gas rate and in-cylinder temperature in his CCV model.

2.4.3 State-of-the-art 0D/1D modeling

State-of-the-art CCV models are characterized by significantly improved underlying combustion models in comparison to the CCV models from the section above. Furthermore, up-to-date highly-resolved optical measurements and 3D CFD simulations have now been performed with a more detailed and deeper insight into the physics of cyclic combustion variations. This information has been used to develop new quasi-dimensional CCV models, as described below. First, models with an empirical background will be outlined. Then, physical model approaches will be described.

Empirical Approach

Poetsch et al. [103] developed a new CCV model and applied it to transient driving cycle simulations. It was also intended to provide the foundation for an additional engine knock model. The new CCV model includes random perturbation on the three Vibe parameters, i.e. the form parameter m, the combustion start φ_{CS} and the combustion duration φ_{CD}. The mean values and standard deviations of all three Vibe parameters are determined for every operating point in the engine map, and thus depend on the engine speed and load. Since the Vibe parameters are adjusted individually, good agreement is found between the simulation and experimental data. However, this model can only be used for the specific naturally aspirated SI engine investigated. Millo et al. [89] repeated the same procedure, obtaining new mean values and standard deviations for the Vibe parameters, for a turbocharged SI engine.

Another CCV model, developed by Vitek et al. [124], perturbs the turbulent length scale, as a parameter for calculating the turbulence intensity, a parameter influencing the ignition delay and a flame-wall interaction parameter. Furthermore, Vitek implemented cross-correlations between the three parameters to describe the CCV at different engine operating points. Both, the PDFs and cross-correlations of the perturbation parameters are optimized, in order to match the burn rate from the experiment as closely as possible. The start of combustion and the shape of the burn rate are determined by the ignition delay parameter and turbulent length scale, respectively, while the wall-combustion parameter is seen as a fine-tuning parameter. The investigation reveals that the PDFs are simple to implement, while finding a cross-correlation for several engine operating points was very time-consuming and even not completely possible. Therefore, Vitek et al. [124] conclude that 3D CFD LES should be a good measure to find cross-correlations directly for the perturbed parameters. This has now been done by the same authors [125], but not implemented yet in a quasi-dimensional CCV model.

The CCV model developed by Sjeric et al. [113] implements perturbations on the calculation of the turbulence production during the intake stroke. The standard deviation for this perturbation is determined by matching COV_{IMEP} from the simulation to the measurement. The turbulence production term is used to evaluate further turbulence parameters. These turbulence parameters are used in the ignition and combustion model, thus also implying that there are fluctuations in the early flame kernel development and the full turbulent combustion propagation. Cycle-to-cycle variations were investigated on a research engine with a compression ratio of 8, at 900 rpm, with a wide-open throttle (WOT), a stoichiometric air-fuel ratio and regarding an ignition timing variation. Spark timing (ST) variation between 5 CAD and 20 CAD before the firing top dead center (bFTDC) is shown in Table 2.1. The simulation results (*Simulation V1*) are in good agreement with experimental data. Thus, the authors conclude that the turbulence fluctuations are the main CCV triggering factor. Note that this CCV model was only applied to ignition timing variation. Next to the perturbation of the turbulence production term, Sjeric et al. [114] extended the existing CCV model to include a cyclic variation in the flow angle at the spark plug and the stratification of the air-fuel equivalence ratio. For this second investigation, Sjeric used the same research engine from above again, however, additionally with compression ratios of 9 and 10 and also at an engine speed of 1200 rpm. The standard deviations in the three factors which are perturbed are fixed for all

IMEP [bar]	ST5	ST10	ST15	ST20
experiment: mean cycle	6.52	7.31	7.87	8.15
simulation: mean cycle	6.79	7.31	7.71	8.00
experiment: standard deviation	0.35	0.30	0.25	0.20
simulation V1: standard deviation	0.31	0.25	0.22	0.18
simulation V2: standard deviation	0.39	0.30	0.21	0.14

Table 2.1.: Comparison of the mean cycle and the standard deviation in the *IMEP* of the experimental data and the simulation results for ignition timing variation. [113, 114]

engine operating points, in order to globally match the experimental data as well as possible. Furthermore, the random distributions of the three perturbation factors are independent of each other. For a good comparison with the first version of the CCV model, the same engine operating points are shown in Table 2.1, labeled *Simulation V2*. No significant improvement could be realized. In addition, Sjeric et al. [114] performed a sensitivity analysis regarding the three perturbation factors. The most significant effect on cyclic combustion variations comes from the turbulence production term, which is responsible for up to 93 % of the overall CCV. Secondly, varying the air-fuel equivalence ratio can cause up to 47 % of CCV, whereas the fluctuation in the flow angle at the spark plug has the lowest impact and can cause up to 11 % of CCV.

Another quasi-dimensional CCV model approach is a stochastic reactor model (SRM), as described by Etheridge et al. [39, 40] and Tuner [121]. In a SRM, in-cylinder homogeneity is replaced by statistical homogeneity, which is described by imposing PDF distributions on certain physical quantities such as the in-cylinder temperature, residual gas mass fraction, turbulent mixing time, entrainment rate constant and heat transfer rate. Thus, the cylinder mass is divided into a random number of virtual packages, known as particles. Each particle is uniquely defined by its chemical composition, temperature and mass. Furthermore, the particle can exchange mass with other particles and transfer heat to the cylinder walls. In each particle, detailed reaction kinetics are solved for the calculation of combustion. Since a SRM exists within the quasi-dimensional environment, no spatial resolution of the particles is provided. A certain number of particles is needed, in order to accurately provide cyclic combustion variations from a physical point of view and not only by an excessively coarse discretization. Tuner [121] reports a minimum resolution of 500 particles to describe CCV. Although the CCV agree well regarding variations in the maximum cylinder pressure, the PDFs have to be calibrated for individual engine types [39].

The CCV model developed by Wenig [127, 128] has recently been implemented in the commercial 0D/1D gas exchange and combustion process simulation tool GT-Power [46]. Cyclic combustion variations are modeled by inducing fluctuations in two constants within the formulation of the laminar burning speed s_l: the maximum laminar speed and the laminar speed roll-off value. Furthermore, fluctuations in the flame kernel growth are induced. The perturbation of s_l includes the CCV effects of charge dilution and is normalized regarding different engine types (lean-operated gas engine and SI engine with different residual gas rates), whereas the inflammation phase fluctuations take into account the influences of the variation of the ignition delay. The model was designed based on four different engine types and engine parameter variations regarding speed, load, air-fuel ratio, EGR, valve lift and timing. Furthermore, the focus of this approach was to minimize the simulation time, thus a total of 15 parameter variation calculations, i.e. 15 consecutive engine cycles, were needed, in order to simulate CCV (five variation calculations on s_l and three on the inflammation phase). In addition, for a more precise quantitative description of CCV, influencing factors are considered for the determination of the fluctuation level of s_{l0}. The influencing factors are the ignition delay *MFB0%-MFB10%*, the burn duration *MFB10%-MFB90%*, the unburned gas temperature and the engine speed. The inflammation phase fluctuations are solely weighted with the engine speed.

As an example, the simulation results of the MAHLE downsizing engine investigated are compared to measurement data. The CCV model was calibrated once for the engine map regarding the perturbation factors s_l and the inflammation phase. Although this CCV model shows qualitatively and partially quantitatively good results, no direct physical CCV causes such as turbulence quantities were implemented. Furthermore, the cross-correlations regarding the influencing factors were found by fitting measurement data. This may lead to a worse description of CCV in engine types, which were not taken into account when developing the model.

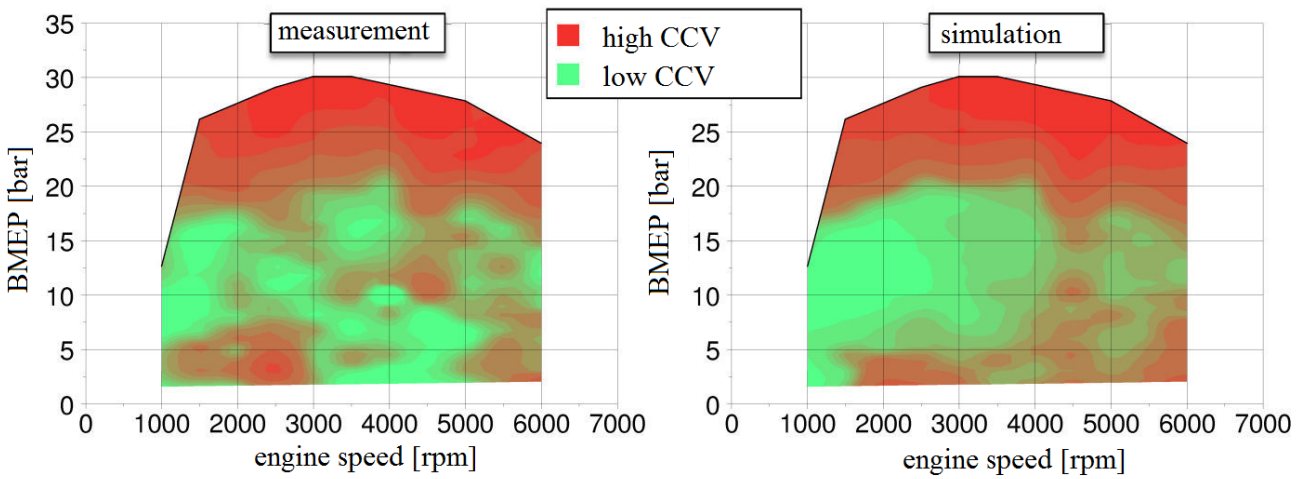

Figure 2.9.: Comparison of simulated and measured CCV of the MAHLE downsizing engine. Reprinted with permission [127].

Physical Approach

Dulbecco et al. [33] developed a CCV model implementing the physical causes obtained from 3D CFD Large Eddy Simulations. Two major CCV causes have been identified using LES: the fluctuations in the tumble ratio and the integral length scale. First, a sensitivity analysis was undertaken regarding the effect of both perturbations on the cyclic cylinder pressure. Based on the information gathered from the sensitivity analysis, the standard deviations of both perturbed parameters are determined by means of five engine operating points (EOPs). These include four EOPs with low and high engine speeds and loads at low EGR. One EOP contained a high EGR. The standard deviations are calibrated comparing the *COV* of the *IMEP*, the maximum cylinder pressure and the angle of the maximum cylinder pressure gathered from simulation data with that found in the experimental data. The resulting standard deviation functions include a dependence on *IMEP* and charge dilution for the tumble ratio and only a constant for the integral length scale. Next, the developed CCV model is applied to an engine map-wide simulation with engine speeds and loads outside of the calibrated EOPs. The simulation results are in good agreement with the measurements. Furthermore, an additional variation in EGR is reproduced well by the simulation. However, the CCV model reaches its limit when applied to a set of EOPs with increased internal aerodynamics. For the increased tumble ratio, the CCV model strongly overestimates the COV_{IMEP} from experimental data. The authors propose that with further LES computations, more detailed information on CCV causes can be extracted, thus further improving the CCV model.

This was done by Richard et al. [106]. Again, LES was used to investigate CCV causes in a SI engine. Perturbation functions were directly extracted, i.e. the mean values and the standard deviations, of the tumble ratio, the integral length scale and, additionally, to the CCV model described above, the flow convection at the spark plug. First, the CCV model was validated on the engine which was used to develop the model. Simulation results regarding variation in the spark ignition timing, the air-fuel ratio and the EGR at a constant engine speed and load (i.e. in similar flow conditions) showed coherent trends in comparison to the measurement. The CCV model was next applied to a different engine speed and load, respectively. The standard deviations in the three factors perturbed were adjusted to match the relative perturbations of the mean values (which were different due to the changed flow conditions). Again, cyclic combustion variations found by measurement were matched qualitatively. However, quantitatively, the COV_{IMEP} differed between simulation and experiment. Furthermore, the developed CCV model was applied engine map-wide to a similar SI engine. Again, the standard deviations of the tumble ratio and the integral length scale were calibrated once for this engine, in order to match the COV_{IMEP} from experiment as good as possible. Figure 2.10 illustrates the COV_{IMEP} found by simulation and its absolute error compared with the experimental data.

The CCV model is able to qualitatively describe experimental data with a maximum absolute error in COV_{IMEP} of 2 % in the main part of the engine map. The authors conclude that the potential to describe CCV predictively

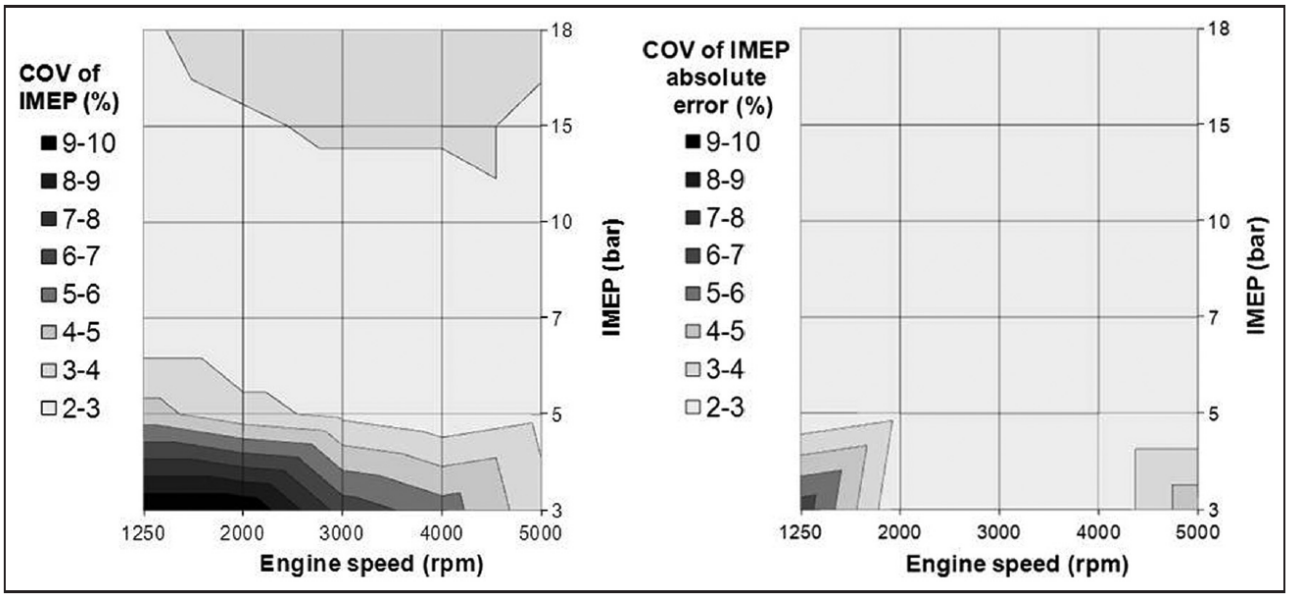

Figure 2.10.: Left: COV_{IMEP} found by simulation; Right: absolute error of COV_{IMEP} between simulation and experiment. Reprinted with permission [106].

is high, if CCV mechanisms from physical LES are integrated into a quasi-dimensional model approach. Furthermore, as proposed in [4], less calibration is required for physical CCV models.

Summary and outline

As seen in the sections above, some current CCV model approaches are partially able to describe cyclic combustion variations both qualitatively and quantitatively. However, all models show weaknesses when the model is applied to specific SI engines that were not used for the model development. Furthermore, individual calibration of the individual model approach perturbation factors led only to a partial improvement. In addition for empirical model approaches in particular, calibration procedures take up a lot of time and computational resource capacities [89, 103]. There are several possible reasons for this. The first possibility is that the underlying turbulence, ignition and combustion models used to calculate the mean cycle were not sophisticated enough. Secondly, some models were based on statistical distributions of perturbed parameters that did not reproduce the physical CCV causes and factors influencing them well. Rather, these approaches are the result of a fitting procedure of experimental cyclic cylinder pressure variations. This was due to the lack of detailed knowledge on the CCV cause-and-effect chain. On the other hand, the model approaches that were built on a physical basis did not include all the significant CCV causes. Furthermore, only one or a few different engine types were used to develop the model. Most of the model approaches described took into account only some ways in which engine parameter variations such as engine speed, load, ignition timing and air-fuel ratio, among other things, influenced CCV. For an overview, the state-of-the-art CCV models are listed in a table in Appendix D.

To conclude, the quasi-dimensional model approaches described are able to reproduce some features of experimentally and virtually observed cyclic combustion variations. However, their shortcoming is the incapability to determine CCV mechanisms predictably for interpolated/extrapolated engine operating conditions, without re-calibrating the parameters perturbed. Thus, there is still a definite need for CCV prediction which was not realized until now.

The CCV model developed in this study will differ in terms of the points mentioned above. First of all, the new CCV model will be based on a sophisticated base model that includes the predictive description of turbulence, ignition and combustion for the 0D simulation of the mean engine cycle. Each model part is to be calibrated individually, e.g. the turbulence model is calibrated by means of detailed 3D CFD data. When designing the new CCV model, the corresponding physical background of CCV has to be considered, including all the relevant causes and factors influencing the cyclic combustion variability. This is the second starting point, since

the model approaches described above have only considered a few causes of CCV. Furthermore, for different combustion processes and various possible engine operating parameters, the particular dependence of cyclic combustion variability has to be included. That means that the model needs to reflect the impact of the highly varying level of the fluid dynamics, the chemical gas composition and the thermodynamic state for different types of SI engines. Therefore, the new CCV model closes the gap between very detailed and time-consuming 3D CFD LES and the low-detail empirically-based quasi-dimensional CCV models, hence allowing CCV to be described predictively.

3 Experimental analysis of cycle-to-cycle variations

This chapter first describes the different SI engines investigated. Then, the experimental setup regarding the measurement systems and the experimental design for the analysis of cycle-to-cycle variations are outlined. Afterwards, a detailed evaluation of the measurement data including its limitations is provided.

3.1 Investigated engines

In this study, two different SI combustion processes are investigated. The first combustion process represents a four-cylinder production engine, labeled B48A20O0, with two different compression ratios achieved by means of changing the engine's piston. However, although this engine is from production, the engine application is not ready for series production. The second combustion process is characterized by its very long expansion stroke by means of the valve or the crank train.

3.1.1 Four-cylinder production engine

The configuration of the four-cylinder production engine is described in detail in the following. Two different compression ratios, set up by changing the piston, are investigated. One piston is a serial production piston with an $\epsilon = 10.2$, whereas the second piston was designed, in order to increase the compression ratio to $\epsilon = 14.0$. Figure 3.1 illustrates the different piston surfaces. It is obvious that the high compression ratio is achieved by filling

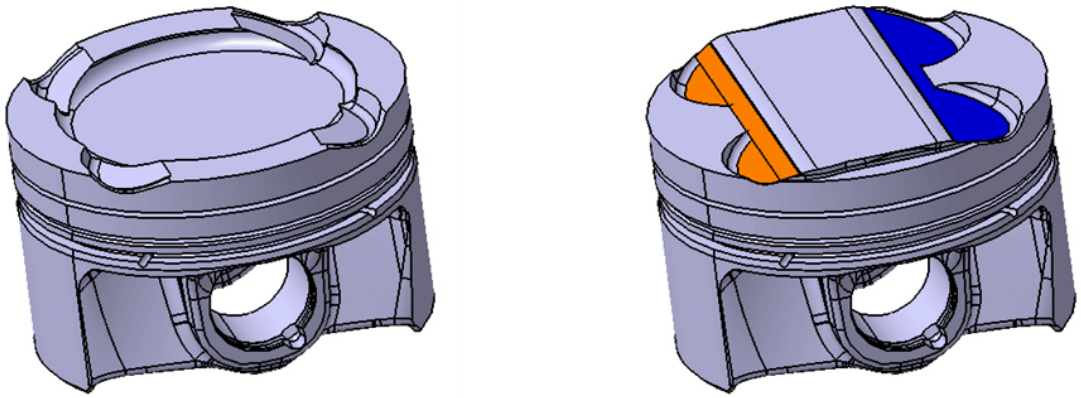

Figure 3.1.: Piston crowns of the serial production piston (left, $\epsilon = 10.2$) and the piston with a high compression ratio (right, $\epsilon = 14.0$). Source: BMW Group.

the piston bowl. Thus, the piston crown is domed. Regarding the in-cylinder flow structure, these different piston surfaces are expected to significantly differ, especially in the compression stroke. The B48A20O0 combines state-of-the-art technologies such as exhaust gas turbocharging, a fully variable valve train and gasoline direct injection. Table 3.1 gives and overview of the engine's configuration.

3.1.2 Research engines with a long expansion stroke

Two types of SI research engines, characterized by a long expansion stroke, are investigated in this study. Both engines are derived from the naturally aspirated BMW F800 two-cylinder motorcycle engine. One research engine, labelled TT1.2 in the following, realizes the long expansion stroke by means of the crank train. The complex crank train is illustrated in Figure 3.2.

engine name	B48A20O0
power output (nominal)	170 kW @ 4750-6000 rpm
maximum torque	350 Nm @ 1250-4500 rpm
cylinder bore	82.0 mm
piston stroke	94.6 mm
compression ratio	10.2 and 14.0
engine displacement	1998 cm^3
intake port type	Tumble port
exhaust turbocharging	Twin scroll concept
valves per cylinder	2 intake / 2 exhaust
intake valves strategy	Valvetronic: variable valve timing δ = 70 CAD, continuous variable valve lift 0.2-9.7 mm and valve phasing (valve lift difference) for low valve lifts
exhaust valves strategy	Variable valve timing δ = 60 CAD and maximum valve lift 9.3 mm
load control	Intake valve lift and timing, throttle and turbocharger wastegate strategy
injection system	Homogeneous, stoichiometric high-precision direct-injection system with an injection strategy synchronous to induction

Table 3.1.: Details of the four-cylinder SI production engine investigated.

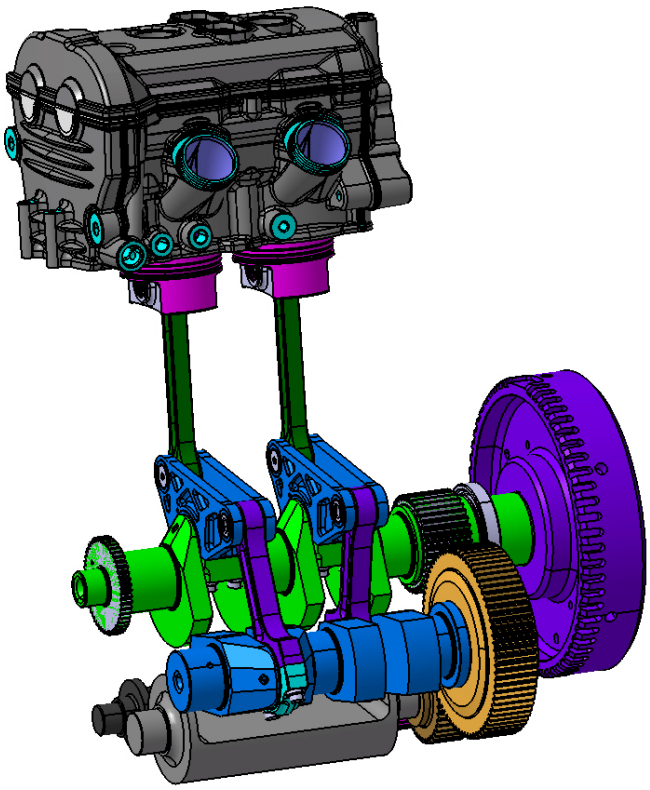

Figure 3.2.: CAD model of the research engine with a long expansion stroke via the crank train. Source: BMW Group.

This engine is characterized by a smaller geometric compression stroke volume in comparison to the expansion stroke volume. In contrast, the second research engine, labelled TT1.3 in this study, realizes the long expansion stroke via the valve train. The latter is also known as the Miller combustion process. The compression stroke volume and the expansion stroke volume are the same geometrically for the TT1.3. The decreased compression stroke volume is achieved by an early intake valve closure. For the investigation of the TT1.3, two different intake cam shafts are used, one labelled 320, the other 400. These numbers define the effective compression stroke volume, which directly characterizes the effective compression ratio. In Table 3.2, details of the TT1.2 and the TT1.3 are displayed. For a better visualization, not only the cylinder volume profiles but also the

engine name	TT1.2	TT1.3
cylinder bore	82.0 mm	82.0 mm
compression stroke	75.6 mm	125.6 mm
expansion stroke	122.5 mm	125.6 mm
compression ratio (geo.)	11.7	320: 19.1 400: 19.1
compression ratio (eff.)	11.7	320: 9.5 400: 11.7
expansion ratio	18.3	19.1
intake port type	Power port	Power port
intake valves strategy	Fixed valve lift and timing, in order to achieve a high cylinder charge	Fixed early valve closing and fixed Miller valve lift
exhaust valves strategy	Fixed valve timing and lift	Fixed valve timing and lift
load control	Pure throttle strategy (naturally aspirated)	Pure throttle strategy (naturally aspirated)
injection system	Homogeneous, stoichiometric port fuel injection	Homogeneous, stoichiometric port fuel injection

Table 3.2.: Details of the research engines investigated with a long expansion stroke.

exhaust and intake valve lift profiles are illustrated in Figures 3.3 and 3.4 for the TT1.2 and TT1.3, respectively.

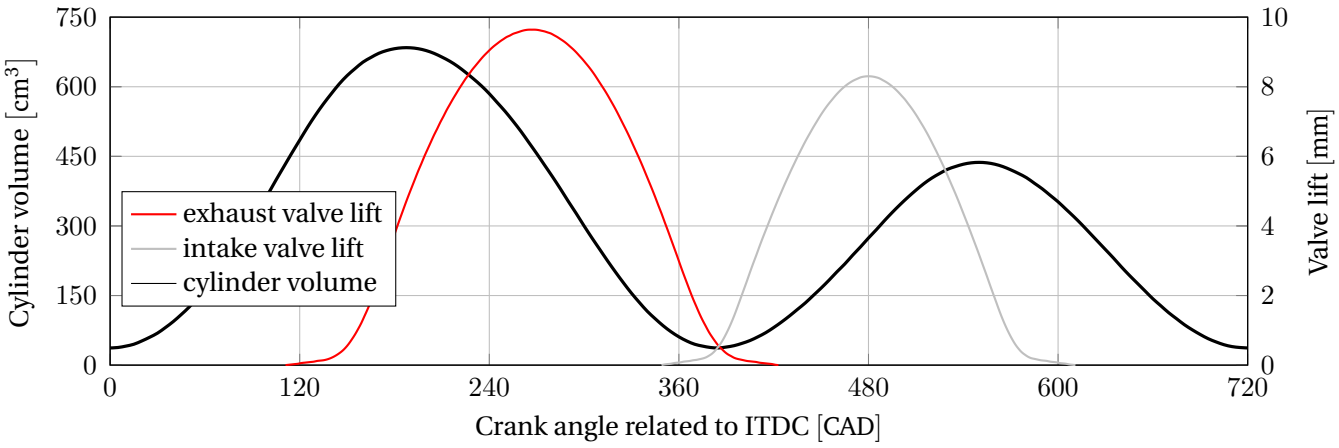

Figure 3.3.: Cylinder volume and exhaust and intake valve lift profiles of the TT1.2.

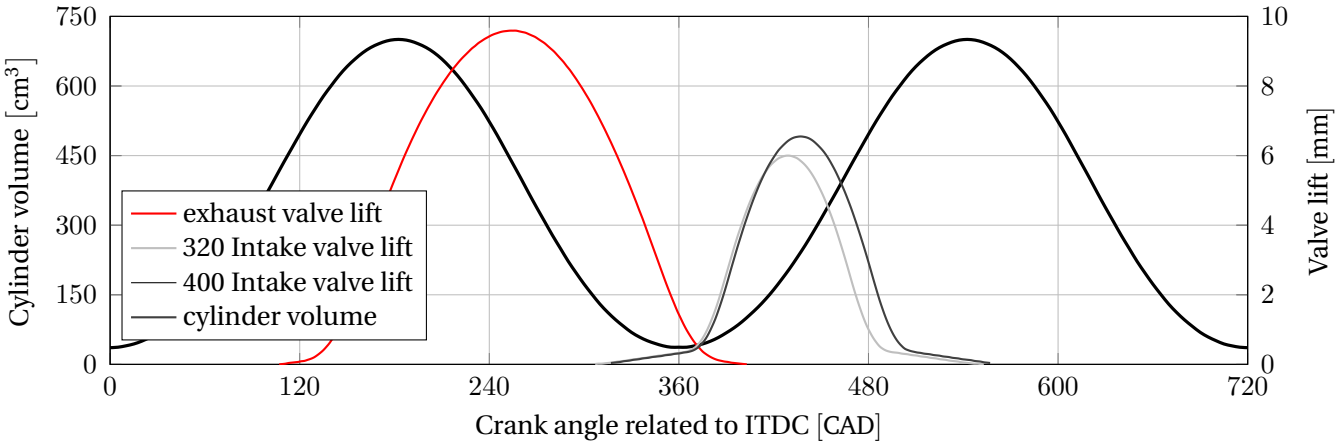

Figure 3.4.: Cylinder volume and exhaust and intake valve lift profiles of the TT1.3 with the 320 and 400 intake cam shafts.

FTDC is at 0 CAD. In the first figure the difference between the cylinder compression and expansion volume is obvious at first sight. The intake valve of this engine is open throughout the intake stroke. For the TT1.3, by contrast, the equal cylinder volumes can be seen alongside the different intake valve lifts of both cams.

3.2 Experimental setup

In this section, the experimental setup regarding the automation and indication measurement system is described in detail. Possible limitations of the indication measurement system are outlined. Furthermore, the experimental characterization of cyclic combustion variations is described by classifying CCV into the influences of the fluid mechanics, the chemical gas composition and the thermodynamical state. For this purpose, the measurement plan is displayed for the SI engines investigated, including the respective engine parameter variations.

3.2.1 Measurement system

Two measurement systems can be identified. The automation system includes the activation of the test bench brake and communicates with the engines' electronic control unit (ECU). This communication allows different engine parameters to be actuated, such as valve timing, lift or ignition timing. Furthermore, it includes the measurement of so-called slow measurement values such as temperatures and pressures in the gas exchange components and the fuel mass measurement. These values are an average over a specific measurement time. In contrast, the indication system receives its values crank angle resolved. These values include the measurement of the cylinder pressure as well as the pressure in the intake and exhaust ports of the engine. In addition, the indication measurement system is able to receive values from measurement techniques which feature cycle-resolved values. E.g., the cyclic ignition timing is measured via a clip-on ammeter on the ignition cables.

Automation measurement system

All sub-measurement systems are integrated into the automation measurement system, in this case the D2T Morphee system. This includes all the values averaged for one measuring point, needed for experimental analysis in Section 3.3 and to calibrate the full cylinder simulation models in Chapter 4. Since no dynamic tests are performed in this work, a unique measuring point correlates to one single stationary engine operating point.

Temperatures are measured by thermocouples, and absolute pressures by resistance strain gauges at the following engine locations:

- temperature/pressure at the engine inlet (air filter)
- temperature/pressure at compressor inlet (only B48 engine)
- temperature/pressure at compressor outlet (only B48 engine)
- temperature/pressure at air intercooler inlet (only B48 engine)
- temperature/pressure at air intercooler outlet (only B48 engine)
- temperature/pressure in the intake manifold downstream of the throttle
- temperature/pressure in the intake port
- temperature/pressure in the exhaust port
- temperature/pressure at turbine inlet (only B48 engine)
- temperature/pressure at turbine outlet (only B48 engine)
- temperature/pressure at catalyst inlet
- temperature/pressure at catalyst outlet

The fuel mass for each measuring point is determined by a fuel flow meter including fuel density measurement (AVL PLU KMA4000) and the engine speed and load are controlled by an asynchronous electric machine. The latter includes a measurement adapter to determine the effective power output. Furthermore, data on exhaust emissions concerning CO_2, CO, THC and NO_x as well as the air-fuel equivalence ratio λ are received from an engine exhaust gas analyzer (Pierburg AMA 4000), extracted upstream of the catalyst. By means of the measured fuel mass flow and the λ the air mass flow can be determined. Fuel properties regarding the lower heating value, research octane number and the C-/H- ratio are analyzed once for each fuel tank charge.

Indication measurement system

The crank-angle-resolved pressure measurement is realized by means of piezoresistive (intake and exhaust pressure measurement) and piezoelectric (cylinder pressure measurement) crystals. Since this measurement technique only allows relative pressure changes, referencing is applied to obtain absolute pressures. For the intake and exhaust port indication pressure measurements, this is done by referencing on the respective pressures from the resistance strain gauges. In contrast, the cylinder pressure is adapted during the compression stroke with closed intake valves. At two explicit crank angles, usually 100 CAD and 40 CAD bFTDC, the indicated pressure curve is adapted to the polytropic pressure calculation for both crank angle degrees (y-axis shift). Furthermore, the pressure curve has to be fitted alongside the crank angle (x-axis shift). This is due to a shift in the maximum pressure related to the actual TDC of the piston. Because of heat losses from the cylinder charge near the TDC, the actual pressure at TDC is lower. The x-axis shift is determined by a capacitive measurement of the actual piston TDC in correlation to the maximum pressure. The difference is called the thermodynamical loss angle, and is usually about 0.7 CAD. A sensitivity analysis involving virtually varying the loss angle on the indication system has shown that an incorrect determination of only 0.1 CAD can lead to absolute uncertainties of up to 0.4 % regarding the *IMEP*. Therefore, this TDC determination is done before and after each measurement campaign, in order to guarantee the measurement quality.

The measurement-respective assignment to a definite crank angle degree is done by an incremental encoder. For the engines investigated, the measurement principle is an optical system which includes a gear wheel, light-emitting diode and a receiver in the form of a photo diode, enabling a resolution of ≤ 0.1 CAD.

Limitations for the measurement of cycle-to-cycle variations

As described in Chapter 2, cycle-to-cycle variations can easily be detected by the coefficient of variation of the *IMEP*. The *IMEP* is determined by the work induced from the in-cylinder pressure on the cylinder volume change. Therefore, the cylinder pressure measurement is of most significance. Uncertainties regarding the indication measurement system directly lead to an inaccurate investigation of CCV. In the following, the possible measurement errors are outlined.

One possible error can be engine vibrations, which influence the determination of the crank angle degree by the incremental encoder or the cylinder pressure signal from the piezoelectric crystals. Therefore, it has to be ensured that the encoder is mounted in a decoupled form. For the piezoelectric crystals, decoupled mounting is not possible, though engine vibration influences can be reduced by low pass filters, which can be applied to the pressure signal.

The water-cooled piezoelectric crystals used to measure the cylinder pressure are the Kistler 6041B. Kistler [56] emphasis the product's low thermal shock error and high accuracy. For a given reference operating point of 1500 rpm and an *IMEP* of 9 bar, the short-term drift is identified as ≤ 0.25 bar, the $\Delta IMEP$ and the Δp_{max} as ≤ 1 %. Downstream of the crystal, first a signal intensifier and then an analog-to-digital converter are located. Both are subject to noise, leading to further uncertainty. This error can be minimized by using a short cable to link the crystal to the intensifier and converter, as well as by isolating the cable [17, 56].

Summing up, the development of the new CCV model in this work can only be as accurate as the measurements of the cylinder pressure.

3.2.2 Experimental design

In this section, the measuring plan is outlined for the TT1.2, TT1.3 (320 and 400 intake cam shafts) and the B48 (serial and $\epsilon = 14$ pistons). Depending on the possible engine parameter settings, these variations are classified into the CCV influence from fluid mechanics, the chemical in-cylinder gas composition and the thermodynamical state. Not all variations are possible for each engine because of limited test bench times or restrictions due to the specific engine characteristics. In particular, the TT1.2 and TT1.3 only permit a small number of variations in the engine speed or load due to high engine vibrations at other speeds or loads. The results from the experimental analysis regarding CCV are shown in Chapter 6 alongside the simulation results.

3.2.3 Influence of fluid mechanics

The influence of fluid mechanics is observed by the variation of engine speed, boost pressure and intake valve closure. In the latter case, the exhaust valve timing is adjusted accordingly, in order to keep the internal EGR constant across the variation. Below Table 3.3 illustrates the variations of the individual engines.

variation	engine speed	boost pressure	intake valve closure
TT1.2	x	-	-
TT1.3 320	x	-	-
TT1.3 400	x	-	-
B48 serial pistons	x	x	x
B48 $\epsilon = 14$ pistons	x	-	-

Table 3.3.: Engine parameter variations to investigate the influence of fluid mechanics on CCV in different SI engines.

3.2.4 Influence of the chemical in-cylinder gas composition

The influences of the chemical gas composition on CCV are analyzed by examining changes in the air-fuel equivalence ratio and the internal residual gas. Table 3.4 displays the variations found in the engines investigated.

variation	air-fuel equivalence ratio	internal residual gas
TT1.2	x	-
TT1.3 320	x	-
TT1.3 400	-	-
B48 serial piston	x	x
B48 $\epsilon = 14$ piston	-	x

Table 3.4.: Engine parameter variations to investigate the influence of the chemical gas composition on CCV in different SI engines.

3.2.5 Influence of the thermodynamical state

Finally, the influences of the thermodynamical state on CCV are investigated regarding the variations of engine load and ignition timing. The engine load determines the amount of in-cylinder charge, which directly effects the pressure and temperature properties at a constant ignition timing. The same can be said for the ignition timing, though in the reverse direction. Hereby, the cylinder charge is constant, but different pressures and temperatures are accounted for by changing the timing of the in-cylinder charge ignition. The variations investigated are shown in Table 3.5

variation	engine load	ignition timing
TT1.2	x	x
TT1.3 320	x	x
TT1.3 400	x	x
B48 serial piston	x	x
B48 $\epsilon = 14$ piston	x	-

Table 3.5.: Engine parameter variations to investigate the influence of the thermodynamical state on CCV in different SI engines.

3.3 Experimental Analysis

In this section, the experimental analysis is described. As already mentioned above in Section 3.2.1, the most important measured variable to analyze cyclic combustion variations is the indicated cylinder pressure. This evaluation is performed with a so-called pressure trace analysis (PTA), using the indicated cylinder pressure, as well as the indicated intake and exhaust port pressures. Results from the PTA are shown in Chapter 6 together with the output from the simulation.

3.3.1 Pressure Trace Analysis

The pressure trace analysis (PTA) is performed in the commercial 0D/1D gas exchange and combustion tool GT-Power [45]. In this tool, the PTA is named "three pressure analysis". Only one single cylinder is considered in the simulation model, as illustrated in Figure 3.5 for better visualization. The engine gas exchange periphery

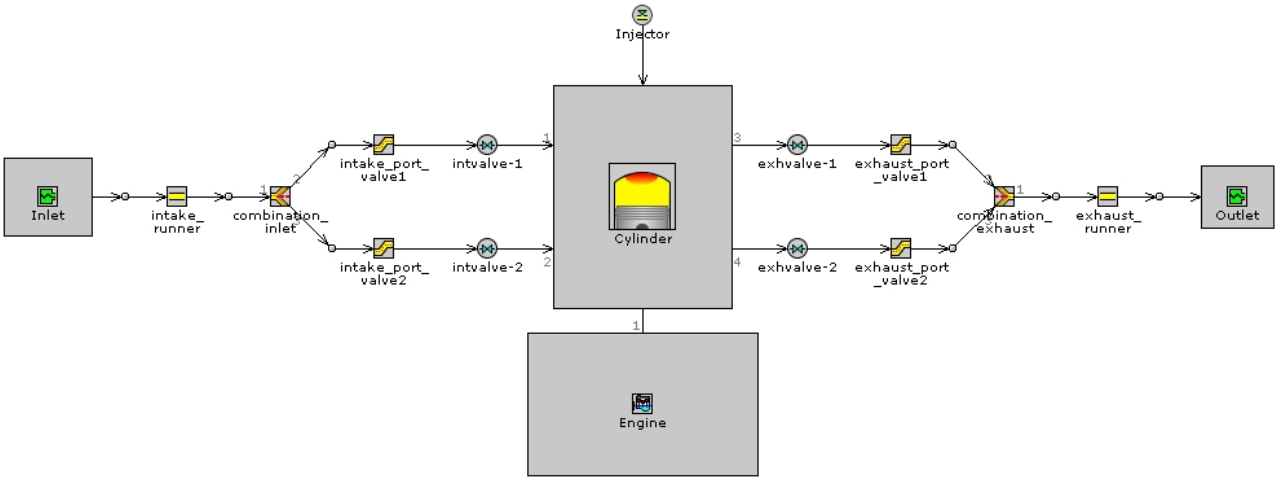

Figure 3.5.: Single cylinder PTA simulation model.

is truncated at those positions, where the intake and exhaust pressure transducers are located in the actual test engine. The end environment is placed at those points and the measured indicated intake and exhaust port pressures imposed (Inlet and Outlet in the illustration). Depending on the fuel injection system, the fuel is directly injected into the combustion chamber (as shown in this figure) or into the intake port. The measured indicated cylinder pressure is imposed in the cylinder. To run a PTA, further input is needed; this is listed in the following.

- The average intake and exhaust pressure are needed, when the adjustment has not worked correctly during the measurement on the engine test bench. If the adjustment is already correct in the measurement data, then, this will lead to no changes in the input.
- To precisely analyze the gas exchange by means of the measured indicated intake port pressure, the average intake temperature is needed. As a result, the intake charge density can be calculated.

- The gas exchange analysis also requires the intake and exhaust valve lift and timings.
- To analyze the combustion, either the injected fuel mass per cycle or λ is needed.
- Furthermore, fuel properties regarding the lower heating value, evaporation heat, density and C-/H ratio are needed.
- The friction mean effective pressure (the difference between *IMEP* and *BMEP)* is needed.
- In the case of an unconventional crank train, the cylinder volume characteristics and motion over crank angle have to be explicitly implemented in the model. Otherwise, the cylinder volume curve can be calculated from the combination of compression ratio, cylinder stroke and bore.
- Finally, the measured exhaust emissions are needed. Since only CO and THC are measured directly, H_2 is calculated according to the formula proposed by Witt [130].

Next, the actual PTA can be started. From the low pressure parts, the gas exchange regarding the determination of the intake mass flow and internal EGR is calculated. The PTA provides a dummy burn rate which is used to analyze the combustion for the first cycle. Starting with the second cycle, the conditions at IVC are taken and the burn rate is calculated from the imposed measured cylinder pressure. At every cycle, the measured and simulated cylinder pressure are compared and the burn rate is adjusted until steady state convergence is reached. However, if differences are found in comparison to the measurement data, further adaptations can be made. First, this includes the comparison of the measured and simulated air mass flow. Adaptations to the valve discharge coefficients can lead to improvements. Furthermore, deviations in the cylinder high pressure part can be due to an over- or underestimation of the heat transfer rate to the cylinder walls when using the heat transfer model developed by Woschni [64]. Here, adjustments regarding the wall heat transfer can also lead to a better description of the simulated cylinder pressure. Since the focus of this section is on the CCV analysis, the calibration of a 0D/1D simulation model is described in detail in Chapter 4.3.1.

This evaluation procedure is first carried out for the average measured engine operating point, in order to obtain the mean cycle results regarding the combustion burn rate, the cylinder charge, the residual gas rate and the cylinder heat transfer. To analyze cyclic combustion variations, the individually measured intake, exhaust and cylinder pressures are imposed in another PTA model. In this model, all other settings are kept the same as for the mean cycle PTA model. Measurement data are available on 440 recorded individual engine cycles. The multicycle PTA for each engine operating point then provides results on the 440 *IMEP*, p_{max} and combustion burn rates. Possible illustrations of the multicycle PTA results are then as exemplified in Figure 2.4. Furthermore, statistics regarding the standard deviation and the coefficient of variation for the multicycle PTA results can be calculated according to the Equations 2.1 - 2.4. These results are used for the comparison and validation of the new CCV model in Chapter 6.

Although the PTA uses measured values for the evaluations, it is still subject to limitations, which are outlined in the Section 3.3.2.

3.3.2 Limitations of the experimental analysis

First, the limitations of the indicated measurement from Section 3.2.1 have to be kept in mind for the pressure trace analysis. The analysis cannot be more precise than the provided measured input data. Furthermore, the PTA itself is subject to additional limitations, which are outlined in the following.

- From the direct measurement data, incorrect cyclic adjustments of the cylinder pressure during the compression stroke can lead to small deviations in the calculation of the *IMEP*. Brunt and Emtage [15, 16] note that wrong pressure referencing causes the highest error when determining the combustion burn rate from a PTA.
- Furthermore, if engine vibrations influence the cylinder pressure signal, deviations are observed in the calculation of p_{max}. This uncertainty can be reduced by imposing a low pass filter on the cylinder pressure signal.

- Influences of engine vibrations on the indication encoder can lead to correlation uncertainties of the cylinder pressure to the definite crank angle. However, these quantities cannot be taken into account directly, but can only be observed if a cylinder pressure phasing error is reported.

- Inaccuracies regarding the simulated intake mass flow and heat transfer rate directly influence the calculation of the multicycle *IMEP*. The discharge coefficients and the heat transfer model are optimized for the mean cycle; therefore, deviations can result from the multicycle intake port and cylinder pressure. For example, for the highest and lowest cylinder pressure curves, the heat transfer model might underestimate or overestimate the heat transfer to the cylinder walls for the individual cycles, respectively. This can then lead to uncertainties in the calculation of the *IMEP* and burn rate statistics.

Summing up, the limitations of the experimental analysis have to be kept in mind when comparing measurement data to simulation data. In particular, the influence of the analysis uncertainties affect the calibration of the predictive ignition and combustion models in Chapter 4 as well as the development of the new CCV model in Chapter 5.

4 Simulation methodology

SI engines are becoming more complex due to an increasing number of variable engine parameters. This is leading to a need for more test bench experiments for engine investigation and application. These experiments are cost-intensive and time-consuming, pushing the focus towards the use of different simulation methodologies. In this chapter, Subsection 4.1 first outlines the difference between simulation methodologies in terms of how they simulate the engine gas exchange and combustion. Since the 0D/1D simulation environment is used to model CCV in this study, the physics implemented in this environment are described in detail in Subsection 4.2. The different ways to model engine combustion non-predictively and predictively are outlined in Sections 4.3 and 4.4, respectively. Additionally, both these sections describe the calibration procedure regarding the gas exchange and wall heat transfer. In the latter section, the physics of the highly sophisticated, previously developed turbulence, ignition and combustion models are explicitly specified along with the particular calibration procedures. Finally, Section 4.5 lists the requirements for the simulation of cycle-to-cycle variations.

4.1 Different levels of simulation

The different simulation levels are generally defined by the modeling depth, complexity and detail of the physics, on the one hand, and by the computing time on the other hand, as illustrated in Figure 4.1. The

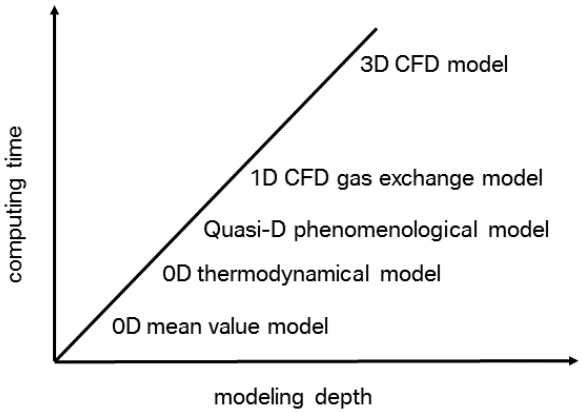

Figure 4.1.: Comparison of the computing time vs. the modeling depths of different simulation methodologies, according to [85, 122].

higher level of modeling details goes along with an increased computing time. Furthermore, a greater modeling depth, including the physical description of the engine phenomena, needs less empirical input, e.g. from experiments, thus allowing an advanced level of accuracy. The usage of a certain simulation methodology depends on the particular application objective and intended purpose for the combustion engine investigated, such as analyzing the flow dynamics in the gas exchange system or the in-cylinder mixture formation and combustion process.

The 3D CFD methodology includes the most detailed description of the flow field. Here, direct numerical simuluation (DNS) provides the highest level of detail, but is significantly restricted by computing times. LES is used more frequently, but RANS simulations are still the most widespread. RANS simulations solve equations regarding mass, momentum and energy conservation in both time and three-dimensional space. Since this space is discretized in very small volumes, it can result in extremely high computing times, e.g. when modeling the entire gas exchange system. Thus, 3D CFD is usually applied to specific investigations of individual engine parts with the inclusion of boundary conditions from lower-level simulation methodologies. Within the 3D CFD RANS methodology, the combustion is usually modeled by means of physical and chemical submodels [85, 86, 122].

Computing times can be reduced with 1D CFD methodologies. These can be regarded as the simplification of 3D CFD with only one spatial dimension, thus all physical quantities are equal crosswise to the flow direction and local flow effects are not resolved. This methodology is usually applied to the simulation of the entire gas exchange system. Each component, i.e. the intake and exhaust pipes, flowsplits, valves and the environment, is specified by one or more volumes and the volume boundaries are connected by orifices. This approach is built upon the filling-and-emptying method, which is considered zero-dimensional and, thus only time-dependent. As a result, only conservation equations of mass and energy are solved. However, in order to establish the one-dimensional methodology, the gas dynamics also need to be described, i.e. the compression waves. Therefore, additionally, the conservation of momentum in the intake and exhaust system has to be evaluated. Within the 1D CFD environment, a so-called fast running model (FRM) can further speed up computing times by combining components of the intake and exhaust system to only a few large volumes [44, 85, 86, 122].

Within the 1D CFD gas exchange environment, this methodology is usually connected to either quasi-dimensional phenomenological models or 0D thermodynamical models describing the in-cylinder physics. Due to the lower detail of their modeling depths, the thermodynamical models consume less computing time than phenomenological models. 0D thermodynamical models are either semi-predictive or non-predictive combustion models. So-called Vibe substituted burn rates are an example of a semi-predictive combustion model. Here, the shape and length of the burn rate is characterized by three parameters and dependent on several engine parameters such as the fuel injection and timing. In contrast, the non-predicitve combustion model only consists of fixed burn rates, obtained from an experimental analysis or specified by the user and independent of any engine parameters. 0D thermodynamical combustion models are usually used to simulate stationary and transient engines or, when these engine simulations are implemented in simulations of an entire vehicle [45, 85, 122].

Phenomenological combustion models are characterized by modeling the heat release rate of the combustion process using physical and chemical models. Due to these submodels and their quasi-dimensional resolution, phenomenological combustion models are able to predict the burn rate. Thus, the combustion process is determined similarly to 3D CFD models, though the three-dimensional resolution of the turbulent flow structures within the combustion chamber cannot be described. The combustion process can be split into its individual sequences, which are then described by the submodels. Among others, the most important ones are the description of the development of in-cylinder turbulence, the ignition process and the subsequent main and burn-off combustion phases. Phenomenological models are applied to simulations in which in-cylinder processes such as the mixture formation, ignition, combustion and the formation of exhaust emissions are investigated in more detail. Furthermore, these models do not need much calibration and can be used for extrapolated engine parameters with little risk. [49, 85, 122].

If the highest priority is placed on computing times, mean value models are used. The gas exchange and combustion process is no longer predicted, so mean value models are characterized by the lowest level of detail. As in a FRM, components of the intake and exhaust system are merged to create larger volumes. However, the conservation of momentum is not solved and no pressure waves in the gas exchange system are evaluated. The time step increment of the solver is increased and fluctuating parameters are no longer solved in terms of crank angle degree, thus for example, the intake pressure is cycle-averaged. The air mass flow is constant within an engine cycle; however, it still can be used to describe the turbo lag in transient simulations, for example. Since the engine work process is no longer calculated, the process parameters of volumetric efficiency, indicated mean effective pressure and exhaust energy fraction have to be obtained from external maps. These three parameters are then determined from the maps using input parameters such as the fuel injection timing, ignition timing and others. The three maps can be determined with large design of experiments (DOE) of the input parameters obtained by means of higher-level simulations or experimental data. Then, these maps are either generated by means of trained neural nets or determined with polynomial functions [45].

With the different simulation methodologies in mind, the best trade-off between computing times and modeling details is the 1D CFD gas exchange combined with phenomenological in-cylinder models to model cycle-to-cycle variations in this study. First, this simulation methodology is sufficient to investigate the gas exchange with good results for the gas dynamics concerning the pressure, temperature and mass flows. Secondly, the in-cylinder processes, especially significant for the analysis of cycle-to-cycle variations, can still be modeled in

detail. Thirdly, as described in the previous chapter, a large number of engine operating points for the different SI engines investigated are used to develop and then validate the CCV model. This calls for short computing times, which are achieved with this method. However, for this combined 0D/1D approach, some measurement data and 3D CFD data will still be essential to calibrate the gas exchange and combustion models. These procedures are described in more detail in the next sections. Once the model has been set up fully, this approach aims to be able to predict the gas exchange and combustion for different engines and operating points which are not used to set up the model.

In the next section, the simulation environment applied in this study is described in detail. Since cyclic combustion variations are mainly an in-cylinder phenomenon, the different types of combustion modeling possibilities and aspects are specified in the following sections.

4.2 0D/1D simulation environment fundamentals

This section provides a detailed description of the fluid mechanics and thermodynamics of spark ignition engines within the 0D/1D simulation environment which is used in this study.

4.2.1 Spark ignition engine model setup

Both the 1D CFD gas exchange as well as the 0D and quasi-dimensional combustion process calculations are performed with the commercial software GT-Power [44, 45]. Figure 4.2 presents an overview of the BMW B48 four-cylinder engine simulation model including all main engine parts. Based on the individual B48 engine parts, separated into the gas exchange system and the combustion chamber system, the simulation environment fundamentals are explained in the following. The B48 engine is used, since advanced technologies such as turbocharging and fully variable valve trains are implemented. The simulation of the other engines investigated follows the same procedure, though neglecting the non-present parts, e.g. the turbocharger.

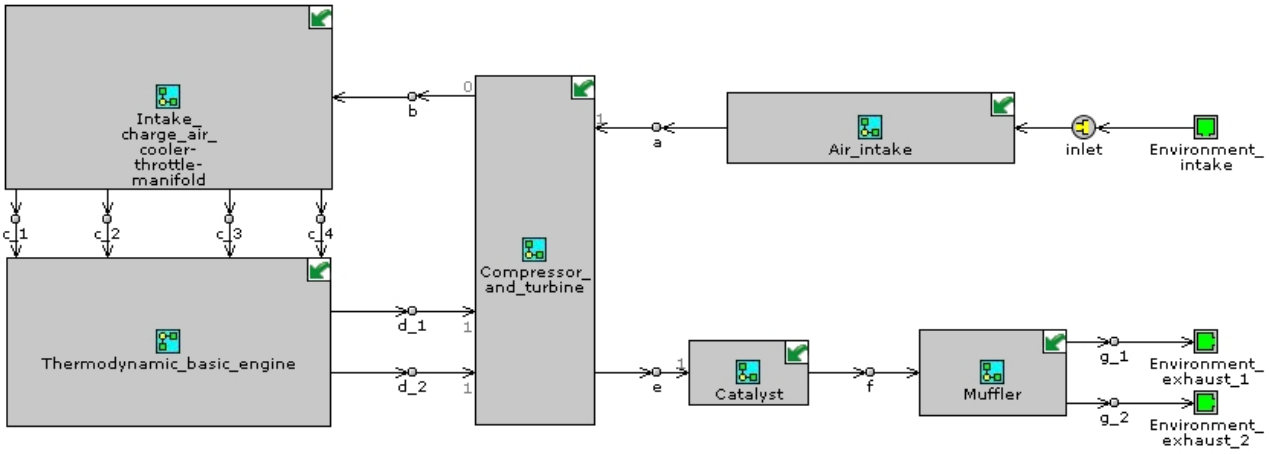

Figure 4.2.: GT Power engine model for the BMW B48 illustrating the main engine parts.

4.2.2 Gas exchange system

In this section, the individual gas exchange components and their evaluations are described. The engine periphery consists of pipes, flowsplits, throttles, a turbocharger and orifices, among other things. First, the pressure and temperature from the environment are imposed on the engine air intake with an oxygen mass concentration $Y_{O_2}^{air} = 0.233$ and nitrogen mass concentration $Y_{N_2}^{air} = 0.767$. The air is induced with ambient conditions by the air filter and followed by the intake muffler. The air filter is modeled as a pipe, whereas the intake muffler

is modeled as a system of pipes and flowsplits.

The pipes and flowsplits are characterized by volumes with a variable cross-sectional area A. The gas dynamics are determined by means of transient Navier-Stokes equations for compressible fluids, see Figure 4.3 for an illustration of the determination parameters of gas dynamics devised by Merker et al. [85, 86].

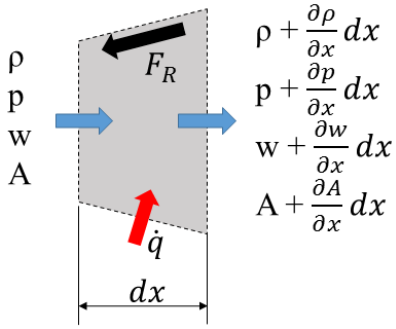

Figure 4.3.: Pipe section with a variable cross-sectional area to determine 1D gas dynamics according to [85].

The 1D flow direction x is described by the following conservation equations for mass (4.1), energy (4.2) and momentum (4.5), respectively. With these equations, the physical parameters of pressure, temperature and mass can be evaluated. The discretization length is denoted as dx. Note, that gravity, friction and thermal conduction in the fluid are neglected [44, 85, 86]. The conservation of mass is written as in the following:

$$\frac{\partial \rho}{\partial t} + w\frac{\partial \rho}{\partial x} + \rho\frac{\partial w}{\partial x} + \rho w\frac{d(ln(A))}{dx} = 0 \tag{4.1}$$

with the density ρ, flow velocity w and cross-sectional area A. The conservation of energy is written as in the following equation.

$$\frac{\partial}{\partial t}\left[\rho\left(u + \frac{w^2}{2}\right)\right] = -\frac{\partial[w\rho(h + \frac{w^2}{2})]}{\partial x} - w\rho\left(h + \frac{w^2}{2}\right)\frac{\partial(ln(A))}{\partial x} + \dot{q} \tag{4.2}$$

Here, u accounts for the internal energy and h for the enthalpy. The energy E can also be described by

$$E = m\left(u + \frac{w^2}{2}\right) \tag{4.3}$$

where m is the volume mass. The heat flux to the volume walls $\dot{q}$ can be determined according to Newton's approach, shown in the following equation.

$$\dot{q} = \alpha A_{wall}(T_{wall} - T_{environment}) \tag{4.4}$$

α is the heat transfer coefficient to the wall and A_{wall} the surrounding surface area. The conservation of momentum is formulated as follows.

$$\frac{\partial(\rho w)}{\partial t} = -\frac{\partial(\rho w^2 + p)}{\partial x} - \rho w^2\frac{\partial(ln(A))}{\partial x} - \rho C_f \tag{4.5}$$

p describes the pressure and C_f defines the coefficient of wall friction. C_f can be determined by the following equation for a fully-developed pipe flow.

$$C_f = \frac{\lambda_w}{D}\rho\frac{w^2}{2}\frac{w}{|w|} \tag{4.6}$$

The λ_w is the dimensionless wall friction number and D the diameter of the volume. The ideal gas law can be used to link the pressure, temperature and density and volume.

The compressor is located downstream of the intake system. The compressor is mechanically connected to the turbine by means of a shaft. Within the 1D CFD simulation environment, the compressor is modeled by maps consisting of the shaft speed, pressure ratio, reduced mass flow and compressor efficiency. These maps are obtained from experimental data, gained from turbocharger flow test benches. An air intercooler is then connected downstream of the compressor, in order to reduce the air temperature when boost pressure is generated. The intercooler, modeled as a pipe heat exchanger, consists of many small tubes. The heat transfer coefficient is determined to be high, in order to prescribe the air flow temperatures from the experimental data across the entire engine map. Since the intercooler is modeled as a pipe, the evaluation of gas dynamics, is applied as described above. Due to the number and diameter of the small tubes and the resulting friction at the tube walls, a pressure drop can be observed. The intercooler is followed by the throttle, which controls the intake manifold pressure. In this simulation environment, the throttle is modeled by an orifice. This orifice is described by two discharge coefficients, one for the forward and one for the reverse flow direction. The discharge coefficients define the flow restrictions as the opening angle of the throttle varies, i.e. the diameter of the orifice varies, and the flow is disturbed at the throttle with resulting pressure losses (of the flow). Thus, the discharge coefficients $\mu_{Throttle}$ are dependent on the throttle angle and are determined on flow test benches according to the following equation [45, 85, 86].

$$\mu_{Throttle} = \frac{\dot{m}_{air,effective}}{\dot{m}_{air,theoretical}} \tag{4.7}$$

The effective air mass flow $\dot{m}_{air,eff}$ is obtained by measuring the throttle on the flow test bench, while the theoretical air mass flow is determined according to Equation 4.8.

$$\dot{m}_{theoretical} = A\sqrt{p_0\rho_0}\sqrt{\frac{2\kappa}{\kappa-1}\left(\pi^{\frac{2}{\kappa}} - \pi^{\frac{\kappa+1}{\kappa}}\right)} \tag{4.8}$$

A describes the throttle cross-section, p_0 the pressure, ρ_0 the density in front of the throttle and π the pressure ratio between the inlet and outlet of the throttle. The throttle is followed by the pipe system of the intake manifold, the intake valves, the actual combustion chamber and the exhaust valves. The flow through the valves depending on the valve lift is again described by discharge coefficients, which are again determined on a flow test bench. The cylinder head and the exhaust valves are connected to the exhaust manifold pipe system. The turbine and wastegate, connected to the turbocharger shaft, then follow. The wastegate is modeled in the same way as the throttle and is also described by discharge coefficients. Depending on the requested boost pressure, the wastegate is actuated. The turbine is determined by maps similarly to the compressor. First the catalyst and then the exhaust mufflers (double flow) are located downstream of the turbine. The pressure drop and temperature change are specified for the catalyst by means of measurements. Finally, the exhaust mufflers are connected to the environment with the same ambient conditions as for the intake [44, 85, 86].

4.2.3 Combustion chamber system

In this CCV study, the combustion chamber is the most important sub-system within the 0D/1D simulation environment. By means of the gas exchange system, the cylinder air charge is determined by the actuation of the intake valve lift and timing, as well as the exhaust valve timing. As reported in [49, 107], there is a definite need to calibrate the valves discharge coefficients, especially for engines with fully variable valve trains, in order to best match the cylinder charge found in measurement data. The calibration procedure is described in the next section. After IVC, the cylinder air charge and residual gas fraction are determined. Corresponding to the targeted air-fuel equivalence ratio, the fuel mass to inject is evaluated. The combustion chamber system can be described by mass and energy conservation equations. For the direct-injected B48 engine, the mass equation is determined as follows.

$$\frac{\partial m_{cylinder}}{\partial t} = \frac{\partial m_{air}}{\partial t} + \frac{\partial m_{fuel}}{\partial t} + \frac{\partial m_{exhaust}}{\partial t} + \frac{\partial m_{blow-by}}{\partial t} \tag{4.9}$$

The mass conservation equation for the engines with port fuel injection investigated is defined similarly; however, the intake mass flow already consists of air and fuel. This difference comes into play for the energy conservation equation, the first law of thermodynamics, see Equation 4.10.

$$\begin{aligned}\frac{\partial U_{cylinder}}{\partial t} = \frac{\partial Q_{wall}}{\partial t} + \frac{\partial Q_{fuel}}{\partial t} - p_{cylinder}\frac{\partial V_{cylinder}}{\partial t} + \frac{\partial m_{intake}}{\partial t}h_{intake} + \frac{\partial m_{exhaust}}{\partial t}h_{exhaust} \\ + \frac{\partial m_{blow-by}}{\partial t}h_{blow-by} + \frac{\partial m_{fuel}}{\partial t}h_{fuel}\end{aligned} \tag{4.10}$$

$U_{cylinder}$ defines the in-cylinder internal energy and is determined by the heat losses to the cylinder walls Q_{wall}, the heat release from the fuel Q_{fuel}, the work from the volume change $p_{cylinder}\,\partial V_{cylinder}$ and the input from the fuel enthalpy flow $\partial m_{fuel} h_{fuel}$, if the fuel is directly injected. The other terms are obtained either by blow-by or by the gas exchange and determine the enthalpy flows. To solve the mass and energy equations, again, the ideal gas law is needed.

The heat losses to the cylinder walls Q_{wall} are determined with Newton's approach.

$$\frac{\partial Q_{wall,i}}{\partial t} = \alpha A_{wall,i}(T_{wall,i} - T_{gas}) \tag{4.11}$$

Here the index *wall,i* correlates to the piston, head and liner. Thus, there are three heat flux equations to be solved. $T_{wall,i}$ can be modeled as fixed temperatures or obtained from the finite-element temperature solver for the three surface areas. The latter needs water and oil temperatures from stationary measurements as well as detailed geometrical information about the cylinder head and liner and piston as input parameters. Then, it calculates the thermal conduction between the oil, cooling water and cylinder walls. T_{gas} is calculated using the two-zone model, described below.

The heat transfer coefficient α can be determined with empirical models. In this study, the heat transfer model following the modified Woschni approach (1990) is used [45, 85], in order to obtain estimated heat transfer results for full and part engine loads. Thus, α can be determined to be as shown in the following equation.

$$\alpha = 127.93 D^{-0.2} p^{0.8} T^{-0.53} w^{0.8} \tag{4.12}$$

In this equation D is defined as the cylinder bore diameter, p as the cylinder pressure and T as the average cylinder temperature. The characteristic velocity w is set to be

$$w = C_1 c_m + C_2 \frac{V_h T_1}{p_1 V_1}(p - p_0) \tag{4.13}$$

for the original version of the Woschni approach. C_1 is a constant, depending on the combustion and gas exchange and c_m is equal to the mean piston velocity. C_2 is the second constant and equal to 0.00324 for direct-injected engines and to 0.00622 for port-fuel-injected engines. V_h is defined as the cylinder stroke volume, T_1, p_1, V_1 as the temperature, pressure and volume at IVC and p_0 as the pressure for the motored (non-fired) engine operation. C_1 is defined as follows.

$$C_1 = 6.18 + 0.417 \frac{c_u}{c_m} \text{ for the gas exchange} \tag{4.14}$$

$$C_1 = 6.18 + 0.417 \frac{c_u}{c_m} \text{ for the combustion} \tag{4.15}$$

The circumferential speed c_u is determined on a blower test bench. A modified term w is used, if the following equation is met.

$$2 C_1 c_m \left[1 + \left(\frac{V_c}{V}\right)^2 IMEP^{-0.2}\right] \geq C_2 \frac{V_h T_1}{p_1 V_1}(p - p_0) \tag{4.16}$$

Then, w is determined to be:

$$w = C_1 c_m \left[1 + \left(\frac{V_c}{V}\right)^2 IMEP^{-0.2}\right] \tag{4.17}$$

Here, the compression volume V_c, the actual cylinder Volume V and the indicated mean effective pressure *IMEP* are included. *IMEP* is set to 1, if *IMEP* $\leq$ 1 bar.

The heat release from fuel $\frac{\partial Q_{fuel}}{\partial t}$ is shown in the following equation.

$$\frac{\partial Q_{fuel}}{\partial t} = \frac{\partial m_{fuel}}{\partial t} H V_l \tag{4.18}$$

HV_l accounts for the lower heating value of the gasoline used. The mass fuel flow $\frac{\partial m_{fuel}}{\partial t}$ is a result of the air mass flow and the air-fuel equivalence ratio λ. The conversion of this air-fuel mixture, i.e. the combustion process, is one of the key issues in this study. As already mentioned in Section 4.1, the 1D CFD gas exchange simulation methodology can be combined with quasi-dimensional phenomenological and 0D thermodynamical models, i.e. predictive and non-predictive combustion models, respectively. In this study, for both combustion model types the two-zone approach is chosen, which separates the combustion chamber into two (main) zones: the burned and the unburned zone. Each zone can be seen as an ideally stirred zero-dimensional reactor and the ideal gas law is used to determine the parameters of the pressure, temperature, density and volume. The unburned zone includes the homogeneous air-fuel mixture and residual gas. The burned zone contains all of the reaction products. The transition of the individual species from the unburned to the burned zone is determined by the burn rate. The mass-averaged temperature of both zones defines the in-cylinder temperature T_{gas} for the heat transfer model from above.

In the following two sections, the non-predictive and predictive combustion model approaches are described in detail. Additionally, in both sections, the respective calibration procedures are explained.

4.3 Model setup with non-predictive combustion

For the investigation of cycle-to-cycle variations in this study, in the simulation setup, each computed simulation case correlates to one stationary engine operating point to be analyzed, since no dynamic engine operations such as driving cycles are examined. Therefore, non-predictive combustion models can be used to adequately match the full-cylinder SI engine model with data from the PTA (singe-cylinder simulation model) and experiments. The non-predictive combustion model evaluates neither the in-cylinder turbulence nor the combustion, but provides a burn rate profile as a function of the crank angle degree. This burn rate profile is directly taken from the PTA, as described in Chapter 3.3.1. This makes the burn rate unaffected by any in-cylinder factor changes such as the charge, residual gas fraction or air-fuel equivalence ratio. Each engine operating point investigated, i.e. each simulation case, is therefore configured with its own burn rate profile [45, 85].

The following section describes the procedure for calibrating the full-cylinder simulation model using measurement data and the PTA. The calibrated full-cylinder model with non-predictive combustion is then used to compare and calibrate the engine model with predictive combustion in Section 4.4.

4.3.1 Model calibration with non-predictive combustion models

Within the 0D/1D simulation environment, three significant engine parameters and outputs need to be in closer focus, i.e. the fresh cylinder charge, the cylinder pressure and the *IMEP*. The fresh cylinder charge correlates almost directly with the engine load and is a significant input parameter for the predictive combustion model. It is strongly influenced by the modeled gas dynamics in the intake system and, here, especially affected by the correct modeling of the valve discharge coefficients. The *IMEP*, on the other hand, is mainly determined by the high-pressure phase of the working cycle. Regarding the first law of thermodynamics, one term is mainly based on empirical approaches, i.e. the heat transfer model. As this model is still subject to weaknesses and empiric, small adjustments can be made to better match the simulated cylinder pressure to that measured, if there are deviations. However, this can only be done if other important engine parameters such as the air charge, EGR, air-fuel equivalence ratio, among other things, match the experimental data very well. The target of the calibration procedure with non-predictive combustion models is to find a single set of discharge coefficients and heat transfer adjustment parameters for the individual SI engines investigated.

Previous studies [44, 49, 107] point out that the adjustment of the valve discharge coefficients is an adequate instrument to reproduce the measured air mass flow. As described in Section 4.2.2, the discharge coefficient specifies the friction losses and the flow constriction through an orifice. Especially when an engine is operated with small intake valve lifts and overlapping valves, the discharge coefficients need to be adapted. One reason is that valve overlapping is not included in the discharge coefficient determination on the flow test bench. Secondly, only one pressure difference between the two sides of the valve is usually used on the flow test bench, which can lead to uncertainties in the discharge coefficients. Moreover, since no actual piston is used opposite

the valve on the flow test bench, possible restricting flow circulations around the valve are not taken into account [44, 85].

The calibrated discharge coefficients were determined according to the procedure described in [49]. Discharge coefficient characteristic curves for forward and backward flows were determined with respect to different valve lift and timings for the B48 engine, for both the intake and exhaust valves. Figure 4.4 illustrates the forward discharge coefficient for the intake valves.

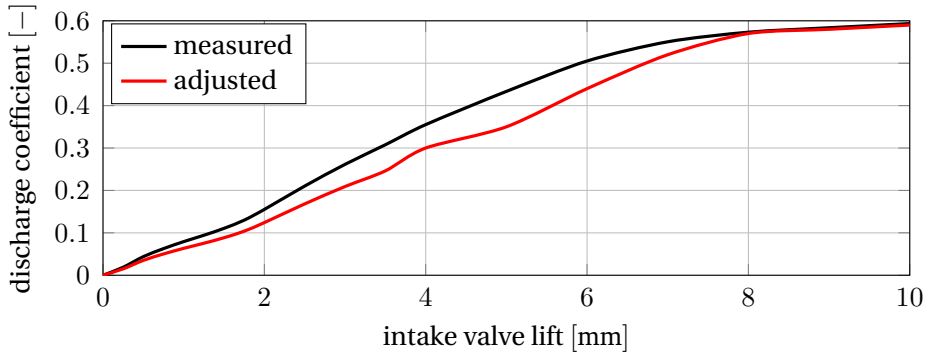

Figure 4.4.: Measured and adjusted forward discharge coefficients of the B48 intake valve.

The other two engines investigated, the TT1.2 and TT1.3, only needed minor coefficient adjustments due to their fixed maximum intake valve lift and minor valve overlapping. Before the adjustment of the discharge coefficient, the maximum error when determining the cylinder air charge relative to the measured values was as high as 7 % for very small intake valve lifts and large valve overlaps. This error was reduced to below 4 % by adjusting the discharge coefficient.

In particular, for naturally aspirated engines, it can be necessary to apply a correction factor for the intake port diameter and length [44]. The intake flow from a large volume, e.g. the intake muffler, into a small pipe with a sharp flow contraction can lead to flow restrictions and thus flow separation from the pipe walls. This is due to flow circulations on the pipe walls right after the contraction. Due to velocity changes, the pressure waves reflect at this contraction. In order to match the measured pressure waves, the pipe port diameter and length can be adjusted.

Due to the empirical design of the Woschni heat transfer model and the lack of knowledge about the in-cylinder wall temperatures, an adjustment is performed regarding the heat transfer coefficient α. For the SI engines investigated, no measured wall heat fluxes and thus no temperatures were available. Similarly to the procedure used by Dumboeck [34] and specified by GT-Power [45], α was multiplied with a calibration factor. After checking that engine parameters relevant to the gas exchange, such as the cylinder charge, are within a narrow error margin to the measurement data, the *IMEP* and the cylinder pressure found by measurement and simulation are compared. Deviations in the cylinder pressures in the expansion phase may be caused by an inaccurate wall heat transfer rate. Increasing the calibration factor from unity in the case of an overestimated cylinder pressure provides a better match. This procedure is carried out individually for each engine operating point, i.e. each simulation case, using an optimizer. The calibration factor ranges between 0.8 and 1.2. A global calibration factor map regarding the engine speed, load and ignition timing was not generated, since it would still lead to deviations regarding changes in the EGR, air-fuel equivalence ratio and IVC.

Other possible calibration procedures which were not implemented in the simulation models in this study, are the correction of the environment pressure, i.e. the average intake pressure, or the correction of the actual intake valve lift for variable-lift engines. However, neither procedure can be treated as or explained by a physical approach. The determined discharge coefficient, port diameter and length, along with heat transfer corrections from above, are directly adopted into the full-cylinder model, including the predictive combustion models described in the next section.

4.4 Model setup with predictive combustion

The predictive turbulence, ignition and combustion models described in this section constitute the essential issue in this study, since these are the basis for the development of the new cyclic combustion variations model. Individual CCV factors are directly disturbed in these models, as described in Chapter 5. The objective and accordingly the output of the three models is the burn rate.

The models are included in the entrainment approach, which has been thoroughly investigated by Grill [54], Nefischer [90, 91] and Grasreiner [49]. In this approach three zones are defined during combustion, as illustrated in Figure 4.5 [49].

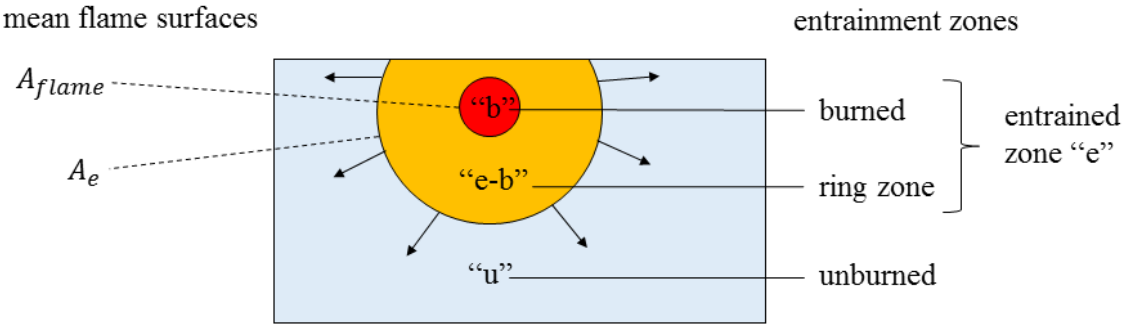

Figure 4.5.: Illustration of the three zones in the entrainment approach according to Grasreiner [49].

The unburned zone "u" consists of a homogenous air-fuel mixture and residual gas, while the burned zone "b" contains the final reaction products. In between, there is a third zone "e-b", which includes the entrained fresh gas and the burned products. A_{flame} denotes the flame surface area, while A_e is the surface area of the entrained zone. The actual burn rate is then determined by the difference of the mass in the burned and entrained zones per time step and a characteristic burning time, as shown in the description of the combustion model, see Subsection 4.4.3. For a better overview of the turbulence, ignition and combustion models in the entrainment approach, an illustration is taken from Dorsch [32], see Figure 4.6. The determination of the flame surface, laminar and turbulent flame speed are implemented in the combustion model. In the next subsections, first the structure and the function of the individual models are described in detail, then this is followed by a depiction of the individual calibration procedures.

4.4.1 In-cylinder turbulence modeling

Turbulence can be specified by a fluctuating flow velocity regarding the average flow value. The turbulent energy of turbulent flows continuously dissipates into heat. This can also be depicted as an energy cascade, which determines the breakdown of the large-scale flow motion into smaller scales. As the flow motion interacts with the laminar flame, thus describing the actual turbulent combustion process, the need for an accurate determination of turbulence is evident [71, 85]. Therefore, a physical quasi-dimensional in-cylinder turbulence model, newly developed by Grasreiner [49, 50] by means of 3D CFD simulations, is used in this study. This model describes the formation and decay of the global charge motions, tumble and swirl, and the generation and dissipation of the TKE. The following equations are directly adopted from [49, 50].

Within the 0D simulation environment, the TKE k, as illustrated in the differential Equation 4.19, can be described by the balance of

- TKE production dk_{prod} by external energy supply via the intake charge motion and shearing effects
- TKE dissipation dk_{diss} and
- TKE density dk_{dens} change through cylinder volume alteration.

$$dk = dk_{diss} + dk_{dens} + dk_{prod} \tag{4.19}$$

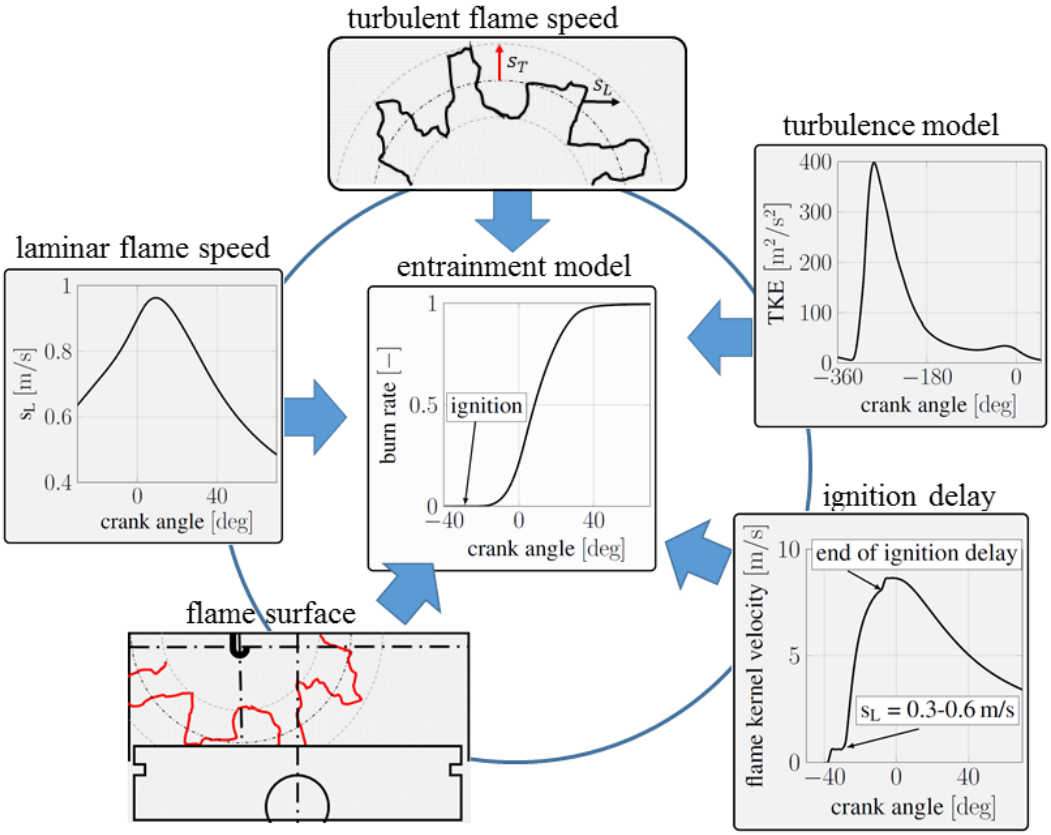

Figure 4.6.: Illustration of the turbulence, ignition and combustion models within the entrainment approach according to Dorsch [32] and Grasreiner [49].

The dissipation term is determined by the following equation.

$$dk_{diss} = -\frac{k^{\frac{3}{2}}}{l_t} \tag{4.20}$$

The integral length scale l_t can be described by:

$$l_t = C_{lt,CFD}\ (l_{valve,intake})^{lt_{exp}} \left(\frac{V_{cylinder}}{V_{cylinder,mean}}\right)^{\frac{1}{3}} \tag{4.21}$$

In this equation $C_{lt,CFD}$ is obtained as a calibration factor from 3D CFD, $l_{valve,intake}$ is the maximum intake valve lift and lt_{exp} a calibration factor, cf. Appendix C, $V_{cylinder}$ the actual cylinder volume as a function of the crank angle and $V_{cylinder,mean}$ the mean cylinder volume in a single engine cycle. Here, the influence of the intake valve lift on the largest flow motion, the integral length scale, is taken into account. The cylinder density influence can be written as in Equation 4.22.

$$dk_{dens} = -\frac{2}{3}\frac{k}{\rho}d\rho \tag{4.22}$$

Grasreiner's [49] updated turbulence model particularly improves the description of the TKE production term dk_{prod}. This term can be classified into two time-dependent terms. One term defines the intake stroke with open intake valves, the other term determines the compression and expansion stroke, in which the intake valves are closed. It should be noted that turbulence generation from exhaust gas flows during the gas exchange is neglected, as well as the interaction with combustion.

Turbulence production with closed intake valves

For the latter, with closed intake valves, the TKE production is calculated for a fixed cylinder charge mass. Here, turbulent kinetic energy can only be gained by shearing effects as follows.

$$dk_{prod} = dk_{prod,shear} \tag{4.23}$$

$dk_{prod,shear}$ explains the TKE production from shearing effects and is influenced by the rate of change in the rotational energy $dE_{direction,rotational,shear}$. The index *direction* defines the direction of rotation around the x, y, and z axes, as illustrated in Figure 4.7.

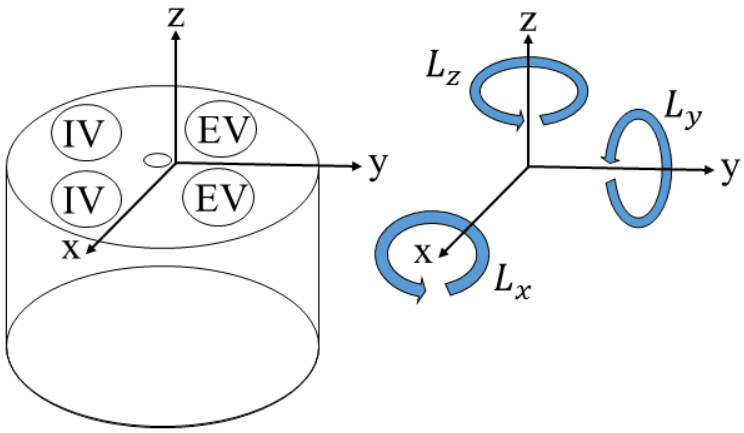

Figure 4.7.: Illustration of the global charge motions around the x, y, z axes, according to Grasreiner [49], with EV the exhaust valve, IV the intake valve.

$$dk_{prod,shear} = -\frac{1}{m_{cylinder}} \sum_{direction} dE_{direction,rotational,shear} \tag{4.24}$$

The rate of change in the rotation energy can be calculated from the angular momentum $L_{direction}$ and its derivative as follows.

$$dE_{direction,rotational,shear} = 2\frac{E_{direction,rotational}}{L_{direction}} dL_{direction,shear} \tag{4.25}$$

The angular momentum L is a result of simplifying the description of the 3D charge motion. L can be described by a vector, accounting for the three directions in space.

$$\vec{L} = \begin{pmatrix} L_x \\ L_y \\ L_z \end{pmatrix} = m_{cylinder} \begin{pmatrix} j_x\omega_x \\ j_y\omega_y \\ j_z\omega_z \end{pmatrix} \tag{4.26}$$

In the above equation, the main tumble component is described by L_x, the minor tumble component by L_y and the swirl component by L_z. L_y can be neglected and will be accounted for in the main tumble component. Furthermore, the angular momentum can be described by multiplying the mass specific angular inertia $j_{x,y,z}$ and the angular velocity $\omega_{x,y,z}$. The angular inertia can also be written as in Equations 4.27 and 4.28.

$$j_{xy} = \frac{1}{4}\left(\left(\frac{D_{bore}}{2}\right)^2 + \frac{s_{piston}^2}{3}\right) \tag{4.27}$$

$$j_z = \frac{1}{2}\left(\frac{D_{bore}}{2}^2\right) \tag{4.28}$$

Including a decaying function for charge motion, the shearing effects described above therefore directly influence the tumble decay and swirl decline and enables the generation of turbulent kinetic energy.

When the intake valves are opened, the turbulence production is put together by the following equation.

$$dk_{prod} = dk_{prod,shear} + dk_{prod,intake} \tag{4.29}$$

$dk_{prod,shear}$ again explains the TKE production from shearing effects. This time, the mass balance, i.e. the incoming mass flow, has to be solved simultaneously with the shearing effects. The last term $dk_{prod,intake}$ is directly responsible for the turbulent kinetic energy generated during the intake stroke. This term is also divided into two main flow directions: tumble and swirl. The incoming fresh charge for the tumble component $L_{x,intake}$ can be determined with Equation 4.30.

$$\frac{d}{dt}L_{x,intake} = j_{xy}\ \dot{m}_{intake}\ Tu_x\ \omega_{engine} \tag{4.30}$$

In this equation, Tu_x is a prefactor for tumble generation, determined either by flow bench experiments or 3D CFD calculations. ω_{engine} is equal to the angular velocity of the engine. The swirl production comes into play when the mass flow through one intake valve is higher than for the other. This can occur for the B48 engine at small intake valve lifts. So-called valve phasing is implemented, which means that the lift from one intake valve is higher than for the other, thus inducing a higher intake mass flow and angular momentum. The change in the angular momentum $L_{z,intake}$ can be written as follows.

$$\frac{d}{dt}L_{z,IVi,intake} = r_{z,intake}\ \dot{m}_{IVi,intake}\ v_{IVi,intake} \tag{4.31}$$

$r_{z,intake}$ can be seen as the distance from one intake valve center to the center of both intake valves. The intake mass flow $m_{IVi,intake}$ may be split, due to the valve phasing. Index i can be substituted by 1 or 2, depending on the numbered intake valve. For reverse intake mass flows, the angular momentum loss can be written as the following equation.

$$\frac{d}{dt}L_{direction,IVi,intake} = L_{direction}\frac{\dot{m}_{IVi,intake}}{m_{cylinder}} \tag{4.32}$$

Thus, the angular momentum adds up to:

$$dL_{direction,intake} = \sum_{IVi} dL_{direction,IVi,intake} \tag{4.33}$$

Therefore, the overall tumble change can be written as:

$$dL_{xy} = dL_{xy,shear} - dL_{x,intake} \tag{4.34}$$

and the overall swirl change as:

$$dL_z = dL_{z,shear} + dL_{z,intake} \tag{4.35}$$

with both equations applying to the change in the rotational energy $E_{rotational,intake}$, i.e. the change in the global charge motion, in the following equation.

$$dE_{rotational,intake} = 2\sum_{direction}\left(\frac{E_{rotational,direction}}{L_{direction}}dL_{direction,intake}\right) \tag{4.36}$$

The change in the kinetic energy dKE_{intake} from the mean mass gas flow over both intake valves can be determined with the following equation.

$$\frac{dKE_{intake}}{dt} = \frac{1}{2}\sum_{IVi}(\dot{m}_{IVi}\ v_{IVi}^2) \tag{4.37}$$

v_{IVi} accounts for the intake flow velocity. Summing up, the measure for instant shearing turbulence $dk_{prod,intake}$ can be written as in Equation 4.38.

$$dk_{prod,intake} = C_{prod,intake}\frac{dKE_{intake} - dE_{rotational,intake}}{m_{cylinder}} \tag{4.38}$$

The constant $C_{prod,intake}$ integrates the turbulent efficiency at high dissipation rates.

Bearing in mind the detailed description of the zero-dimensional turbulence, some parameters are needed to determine the ignition delay and the combustion in the next two sections. Also, to develop the CCV model in Chapter 5, in particular, the calculation of the integral length scale l_t and the TKE production term dk_{prod} have to be kept in mind.

4.4.2 Ignition modeling

The ignition delay is defined as the time between the ignition and the combustion up to the CAD at which 5 % of the fuel mass (*MFB5%*) is burned. As discussed in Grasreiner et al. [51], the ignition delay has to be predicted ± 3 CAD in comparison to experiments, in order to achieve an *IMEP* accuracy of ≤ 6 %. Furthermore, concerning the research into the literature on CCV described in Chapter 2, the importance of the accurate description is obvious. An inaccurate determination of the *MFB5%* would lead to subsequent weaknesses in the development and application of the newly designed CCV model.

Following Grasreiner's quasi-dimensional approach [51], the flame kernel mass burn rate, i.e. the difference between the burned and entrained zones for the ignition delay modeling, can be calculated as follows.

$$\frac{d}{dt}m_k = \rho_u \; s_{T,k} \; 4\pi r_k^2 \tag{4.39}$$

The initial flame kernel radius r_k, i.e. at ignition timing, is set to half of the distance between the two electrodes of the spark plug. Further into the combustion, r_k can be determined by the following equation.

$$r_k = \sqrt[3]{\frac{3}{4\pi}V_b} \tag{4.40}$$

with V_b equal to the burned volume. The turbulent flame kernel velocity $s_{T,k}$ up to *MFB5%* can be described as follows.

$$s_{T,k} = max\left(s_L, s_T - \frac{2}{r_k}(D_0 + D_t^{'})\right) \tag{4.41}$$

Depending on the level of the first or second term, the one calculating the higher burning velocity is used. The laminar burning speed s_L can be written following Metghalchi's approach [64] as:

$$s_L = (B_m + B_\phi(\phi - \phi_m)^2)\left(\frac{T_u}{T_{ref}}\right)^\alpha \left(\frac{p}{p_{ref}}\right)^\beta (1 - 2.06(EGR)^{0.77}) \tag{4.42}$$

B_m, B_ϕ, ϕ_m, α and β are constants which are dependent on the specific fuel, and can be extracted from the literature [64]. The turbulent flame speed can be determined according to Peters [100].

$$s_T = 0.195 \; u^{'} \; Da\left(\sqrt{1 + \frac{20.52}{Da}} - 1\right) + s_L \tag{4.43}$$

D_0 - the flame diffusivity at the inner flame layer with temperature T_0 - can be described according to Smooke [115]:

$$D_0 = \frac{1}{\rho_u} 2.5810^{-5} \; \left(\frac{298}{T_0}\right)^{0.7} \tag{4.44}$$

According to Peters, the turbulent diffusivity $D_t^{'}$ can be written as:

$$D_t^{'} = \sqrt{\frac{c_\mu \; c_s}{2Sc_t}} \; l_{f,t} \; \sqrt{k_k} \tag{4.45}$$

In this equation c_μ and c_s are constants, Sc_t the turbulent Schmidt number, k_k the kinetic energy and $l_{f,t}$ the turbulent flame brush thickness. The latter can be expressed as

$$l_{f,t} = l_f + c_{f,t} \; l_t \; \sqrt[4]{1 + \frac{1}{Da^2}} \tag{4.46}$$

This equation consists of the laminar flame thickness l_f, calibration constant $c_{f,t}$, integral length scale l_t, variable flow velocity $u^{'}$ and Damköhler number *Da*, which can be expressed as:

$$Da = \frac{l_t}{l_f}\frac{s_L}{u^{'}} \tag{4.47}$$

Since flame-wall quenching occurs even before *MFB5%*, the flame restrictions have to be taken into account following this equation:

$$A_k(r_k) = 4\pi r_k^2 - (A_{head} + A_{liner} + A_{piston}) \tag{4.48}$$

Here, A_{head} corresponds to the cylinder head area, A_{liner} to the crank-angle-dependent cylinder liner area and A_{piston} to the surface area of the piston. Furthermore, an expansion factor *Ex* is introduced. Its detailed derivation can be found in [49]. It describes the density change caused by combustion. Here, the unburned cylinder charge is compressed. Therefore, the expansion factor decreases as combustion progresses. *Ex* is determined with the following equation.

$$Ex = c_{Ex} \frac{\frac{\rho_u}{\rho_e}}{(\frac{\rho_u}{\rho_e} - 1)x_e + 1} \tag{4.49}$$

c_{Ex} is a calibration factor and x_e the ratio of the entrained mass to the total cylinder mass. Then, the entrained kernel mass flow can be written as:

$$\frac{d}{dt} m_{e,k} = Ex \ \rho_u \ s_{T,k} \ A_k(r_k) \tag{4.50}$$

The final flame kernel burn rate can then be expressed as:

$$\frac{d}{dt} m_{b,k} = \frac{m_{e,k} - m_{b,k}}{\tau} \tag{4.51}$$

with τ as a characteristic time scale, which will be described in the Subsection 4.4.3. As presented, the ignition model determines the transition from laminar to turbulent flame propagation and integrates the expansion influence from combustion. Furthermore, the ignition model significantly depends on the correct thermodynamical and turbulent input parameters for the calculation of s_L, s_T, and $s_{T,k}$. Section 4.4.4 describes the investigation of the laminar burning velocity concerning its correct functioning, including the case of lean air-fuel mixtures, as well as the calibration procedure for the *MFB5%*. Regarding the CCV modeling, the radius of the initial flame kernel r_k will become important.

4.4.3 Combustion modeling

The combustion model describes the release of fuel from *MFB5%* to the end of combustion. Again, the entrainment approach, as shown in Figure 4.5, is used. The calculation of the main combustion phase follows the quasi-dimensional approach, published in [11, 49, 90]. As in the ignition model, the instant burn rate can be determined as follows.

$$\frac{dm_b}{dt} = \frac{m_e - m_b}{\tau} \tag{4.52}$$

The entrained mass can be expressed over time with Equation 4.53.

$$\frac{dm_e}{dt} = \rho_u \ A_e \ u_e \tag{4.53}$$

As illustrated in Figure 4.5 the entrained area is larger then the actual flame area. The determination of A_e is described below. The entrained velocity u_e can be seen as the velocity at which the unburned eddies enter the reaction zone. u_e can be described with Equation 4.54.

$$u_e = Ex \ s_{T,eff} \tag{4.54}$$

Here, the expansion factor *Ex* from Equation 4.49 is used again. Furthermore, the effective turbulent flame velocity $s_{T,eff}$ is divided into two crank-angle-dependent sections. First, up to *MFB5%* the $s_{T,eff}$ is set as $s_{T,k}$ from Equation 4.41. Then, after *MFB5%*, $s_{T,eff}$ is determined with the turbulent flame velocity s_T according to Peters from Equation 4.43. Finally, the characteristic burning time τ can be described taking the approach that

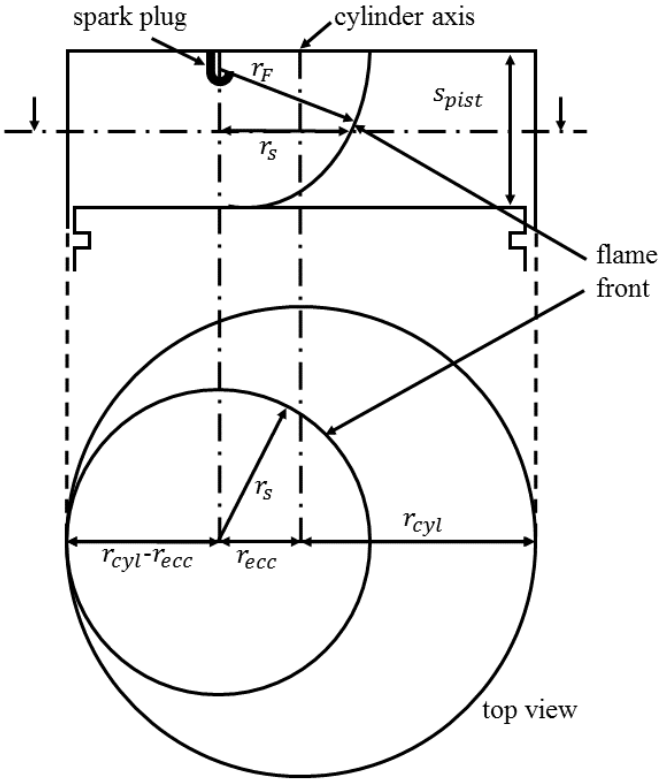

Figure 4.8.: Illustration of the three zones within the entrainment approach according to Grasreiner [49] and Blizard and Keck [11].

the actual flame burning is still laminar, see the following equation. Here, the square root term can also be seen as the Taylor length.

$$\tau = \sqrt{\frac{15\ l_t\ \nu}{u'}} \frac{1}{s_L} \tag{4.55}$$

The correct calculation of the entrained surface area A_e is of great importance for an accurate determination of the burn rate. Figure 4.8 shows the parameters implemented for the calculation, including parameters to account for the flame-wall interaction according to [11, 49, 54]. Some assumptions are made beforehand: that the flame propagation is completely spherical, the combustion chamber is pancake-shaped and the head and the piston are flat. When A_e touches the wall, this leads to that area being neglected for further entrainment. r_F defines the actual flame radius, r_{ecc} the flame eccentricity, r_s the planar projected flame radius and s_{pist} the piston position. Other parameters are used as auxiliary parameters for the complex calculation of the wall interactions. At ignition timing, A_e still can be seen as spherical. Further into the combustion phase, the first contact area is the cylinder head. This area and the other areas on the cylinder liner and piston are then subtracted from the spherical area [11, 49, 54, 90].

The introduction of the flame eccentricity, even for engines with centered spark plugs, can be explained as follows [54]. Positioning the start of combustion in the exact middle of the combustion chamber leads to unrealistically sharp burn rates, since wall touching occurs almost simultaneously. However, even for engines with a centered spark plug, the flame propagation is never completely spherical. Therefore, this eccentricity parameter can be used to smooth, i.e. calibrate, the burn rate, although this parameter might not reflect the exact position of the spark plug.

Finally, the flame-wall quenching distance is described, as shown in the following equation according to [90].

$$s_{quench} = C \frac{\lambda_b}{\rho_u\ s_L\ c_{p,b}} \tag{4.56}$$

The constant C is set to 5. λ determines the heat conduction and $c_{p,u}$ the heat capacity. In particular, flame quenching is relevant with respect to the burn-off phase in which most of the flame-wall interactions take place. As Grasreiner [49] clearly showed, deviations in the *MFB90%* have only a negligible effect on the *IMEP*, while the amount of unburned fuel left has a significant influence on the engines' power output.

From this combustion model, the flame eccentricity and the flame-wall quenching distance are considered for the CCV model development. The procedure used to calibrate the combustion model is described in the next section. Furthermore, an examination of the laminar burning velocity s_L for very lean air-fuel mixtures and alternative formulations is also undertaken in the next section. As illustrated, the entrainment model is based on an empirical approach of some kind, such as the expansion factor. However, model adjustments are usually required for quasi-dimensional approaches. Nevertheless, the entrainment approach can still be seen as basically physical.

To summarize, with all three models presented in Section 4.4, it is possible to predictively and accurately describe the combustion process within the quasi-dimensional simulation environment. A proof of concept for these models has already been undertaken by Grasreiner [49]. Therefore, there is a sophisticated simulation basis on which to design the CCV model in Chapter 5, which is of essence for accurate cyclic combustion variations modeling.

4.4.4 Model calibration with predictive combustion models

Model calibration regarding the gas exchange and the cylinder heat transfer model has already been described above. The calibration results are directly implemented in the simulation models with predictive combustion. Since the predictive turbulence, ignition and combustion models are still only a simplification of the physical backgrounds, including assumptions, there is a definite need for the calibration of physical constants, in order to best match the respective SI engine. By means of the calibration procedure, a single set of constants is to be found for each SI engine investigated, in order to accurately predict the combustion for a large variety of engine operating points. In the following, first the procedure used to calibrate the turbulence model by means of 3D CFD data is described. Then, the determination of the laminar burning speed for the ignition and combustion model is compared to detailed reaction kinetics with the software Cantera [22]. A further calibration of the two latter models with measurements is also depicted.

3D CFD data

Due to its physical basis, the turbulence model only has a minimal need for calibration. Grasreiner [49, 50] defined a calibration procedure by means of 3D CFD data. 3D CFD RANS data in the present study was provided by TU Freiberg, as well as internally by BMW, see Appendix B for information on 3D CFD simulation properties. The objective of calibration is to precisely match the turbulent kinetic energy k near ignition top dead center (ITDC). Therefore, errors in k at IVC, at the second k peak near TDC and at the combustion peak have to be minimized. k is selected, since this value is directly used to calculate $s_{T,k}$ and s_T. For the B48 engine with its tumble ports, a comparison of the angular momentum around the x, y and z axes can also be carried out. Five calibration factors are determined: $C_{prod,intake}$ from Equation 4.38, $C_{prod,z}$ and $C_{prod,xy}$ as calibration factors for $dk_{prod,shear}$ as well as C_{diss} and C_{dens} for the dissipation and density change terms, respectively.

The calibration procedure is depicted for the B48 engine with serial pistons. Since the turbulence model was already calibrated for the B48 predecessor engine N20 [50], only minor adjustments had to be undertaken. Results are shown for the turbulent kinetic energy of the B48 in Figure 4.9. First, the four engine operating points are set out as in Table 4.1. Special focus is concentrated on the calibration of the turbulent kinetic energy for lower engine speeds, since these are very relevant for simulations of frequent engine operating points in common driving cycles such as the WLTC or in real driving emission tests on the road.

In this figure, the dotted line in black shows the turbulent kinetic energy for the uncalibrated 0D turbulence model, i.e. the original calibration parameter for the N20 engine is used. The dashed, red line illustrates the TKE from the turbulence model after the calibration procedure. The uncalibrated turbulence model already meets Grasreiner's defined requirement of $\pm 15\,\%$ to achieve an accurateness of $\pm 5\,\%$ for the calculation of s_T, except

engine parameter	unit	EOP1	EOP2	EOP3	EOP4
engine speed	[rpm]	1500	1500	1500	3000
IMEP	[bar]	4	10	20	10
intake valve lift	[mm]	3.2	8.4	8.8	8.0
intake valve timing	[CAD]	55	78	90	69
exhaust valve timing	[CAD]	77	101	102	109

Table 4.1.: Engine operating points for the comparison of kinetic energy from 3D CFD and 0D.

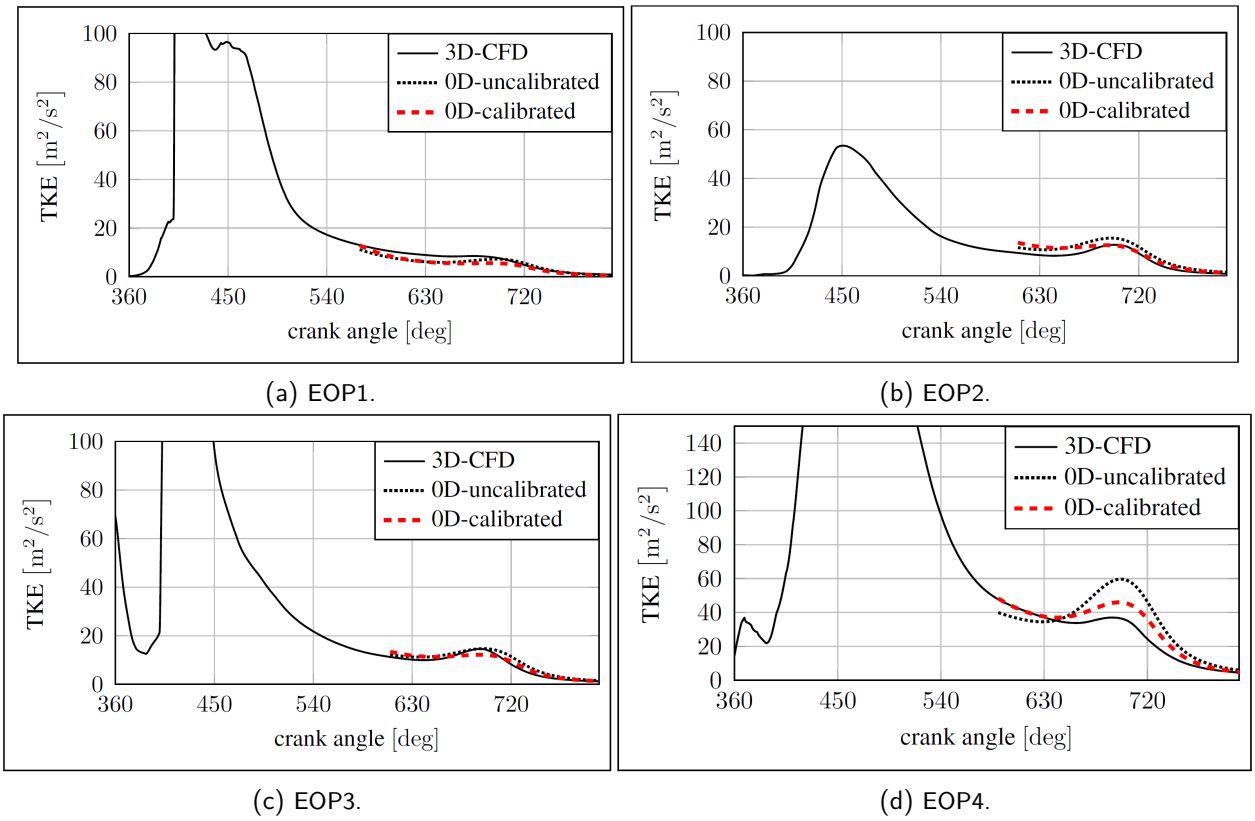

(a) EOP1. (b) EOP2.

(c) EOP3. (d) EOP4.

Figure 4.9.: Comparison of the TKE between 3D CFD data and the uncalibrated and calibrated 0D turbulence model for the B48 engine with serial pistons.

for the engine operating point at 3000 rpm. As can be seen, all calibrated TKE curves show an improved match to the results from 3D CFD. Hence, the difference between the two 0D trends shows the highly sophisticated underlying turbulence model with its fundamental physics. Since the chosen turbulence model calibration parameter set is fixed for each unique engine, the calibration parameters are determined so as to best match the TKE for the four engine operating points investigated.

The calibration of the B48 engine with the high compression ratio delivers the same calibration factors; only the dissipation calibration factor is increased. In contrast, the calibration procedure took more effort for the TT1.2 and TT1.3, due to its different crank and valve train as well as their intake ports, which are optimized for natural aspiration. The final individually calibrated parameters are then fixed for all simulations of the distinct SI engines. The calibration factors for the individual engines are shown in Appendix C.

Chemical reaction kinetics data

In order to achieve an accurateness of ± 3 CAD for the *MFB5%* and *MFB50%*, the quantitative error in the calculation of the laminar burning velocity s_L has to be within the margins of ± 5 %. First, the errors in the thermodynamic parameters pressure, unburned temperature and residual gas fraction have to fall below the values set out in Table 4.2. These values were gained by a sensitivity analysis carried out by Grasreiner [49].

parameter	unit	error limit
pressure	[bar]	± 5 %
unburned temperature	[K]	± 4 %
residual gas fraction	[%]	± 10 %

Table 4.2.: Error limits for thermodynamic parameters according to Grasreiner [49].

The thermodynamic values are obtained either by the gas exchange simulation or the evaluation of the ideal gas law within the combustion chamber when the valves are closed. The formulation of s_L according to Metghalchi [87], see Equation 4.42, has been extensively calibrated. Furthermore, several authors [54, 90] have positively verified its functioning, including variations on the engine speed, load, ignition timing and EGR. However, Grill [54] adjusted the last term, determining the influence of EGR within the formulation of s_L.

This work explicitly compares s_L in Metghalchi's formulation and detailed reaction kinetics from Cantera [22] regarding iso-octane as the fuel investigated. Cantera's data is obtained internally from BMW. In this study, within Cantera a perfectly stirred reactor is used with the Jerzembeck reaction mechanism [68] to calculate s_L. The comparison includes different engine speeds, engine loads and EGR, confirming that s_L functions within the defined margins. However, for the variation in the air-fuel equivalence ratio λ, the error limits are exceeded. Here, for $\lambda \geq 1.4$, the laminar burning speed is underestimated. This can also be recognized when comparing the *MFB50%* in terms of the simulation and measurement data. The simulation *MFB50%* exceeds the defined error tolerance of ± 3 CAD.

An alternative formulation for s_L from Ewald [41] is then investigated. He adjusted the EGR term within s_L. Ewald's confidential matrix for the calculation of s_L is illustrated in Table 4.3. The analysis and adjustment were carried out for iso-octane. Moreover, Ewald also adjusted the formulation of the laminar flame thickness. However, no improvements regarding very lean air-fuel mixtures can be found.

parameter	unit	error limit
pressure	[bar]	1 - 50
unburned temperature	[K]	300 - 800
air-fuel equaivalence ratio	[-]	0.5 - 2.0
residual gas fraction	[%]	0 - 30

Table 4.3.: Valid parameters for the application of s_L according to Ewald [41].

One explanation is that the implemented pressure and unburned temperature used to calculate s_L are obtained from measurements with gasoline E10 (90 % gasoline, 10 % ethanol) as the fuel. This might lead to these deviations for very lean mixtures. Therefore, the CCV model development in the next chapter is undertaken only up to a λ of 1.4. Engine operating points exceeding this air-fuel ratio are supposed to be present only very rarely for existing lean engine concepts such as the BMW N53 engine. Moreover, new lean engine concepts are not to be expected in the future due to the very strict emission regulations, leading to more expensive exhaust gas treatment, thus decreasing the need to describe a high λ accurately.

Measurement data

The ignition and combustion models are calibrated with measurement data according to the procedure defined in [49, 51]. Several engine operating points, spread across the engine map and accounting for the variation in different engine parameters, are used for the calibration procedure. The objective is to minimize the sum of errors when determining *MFB5%* and *MFB50%*, since both values are of great importance for the determination of the *IMEP*. Two calibration constants are available in each of the models. The ignition model is calibrated with

- $c_{f,t}$, scaling the transition from laminar to turbulent burning velocity within the formulation of the turbulent flame brush thickness and
- c_{Ex}, weighting the expansion factor *Ex*.

The combustion model is calibrated with

- C_{burn}, scaling the characteristic burning time τ and
- C_{EGR}, changing the EGR-related term within the formulation of the laminar burning velocity.

The experimental burn rates used for calibration are obtained from the PTA as described in Chapter 3. After the calibration, the final calibration factors are fixed for the individual SI engines for all simulations.

Results are shown for the TT1.2 and TT1.3 (320) in Figures 4.10a - 4.11b. Engine parameters and engine operating points (EOP) for both engines are set according to Table 4.4. Note that for the TT1.2 only EOP1 is shown. The deviations of *MFB5%* and *MFB50%* are below $\pm$ 1 CAD for both engines. However, recognizable deviations

engine parameter	unit	EOP1	EOP2	EOP3
engine speed	[rpm]	3000	3000	3000
engine load	[bar]	WOT	WOT	0.1WOT
MFB50%	[CAD]	8	24	8
λ	[-]	1	1	1
EGR	[%]	3	3	9

Table 4.4.: Engine operating points used to compare the simulated and measured burn rates for the TT1.2 and TT1.3.

occur in the later part of the combustion. Nonetheless, the deviations for the *MFB90%* are within 3 CAD. After the *MFB90%* the deviations are higher. One reason may be the temperature shock effect of the indication cylinder pressure crystal, determining the end of combustion too slow in the case of experiments (see Chapter 3 for more details). Furthermore, as indicated, this discrepancy has little effect on the determination of the *IMEP*.

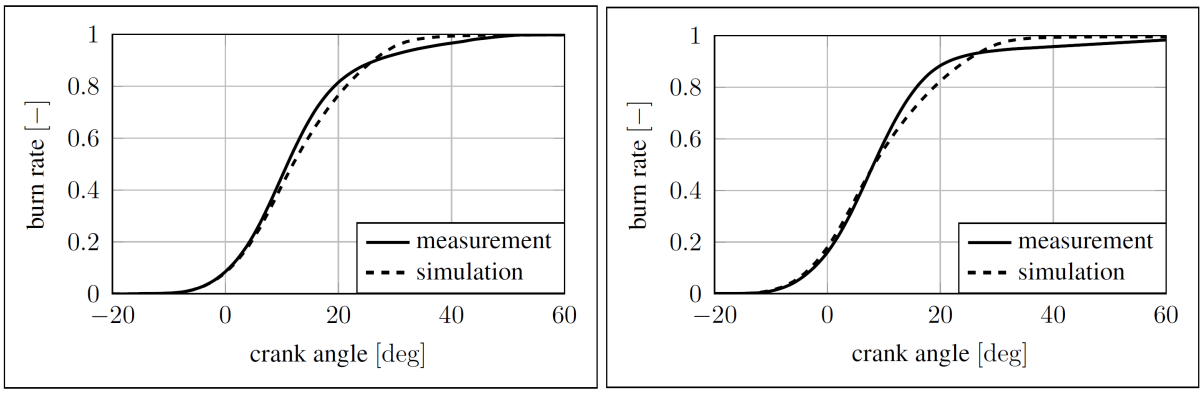

(a) EOP1 of the TT1.2.

(b) EOP1 of the TT1.3 (320).

Figure 4.10.: Comparison of the measured and simulated burn rates for EOP1.

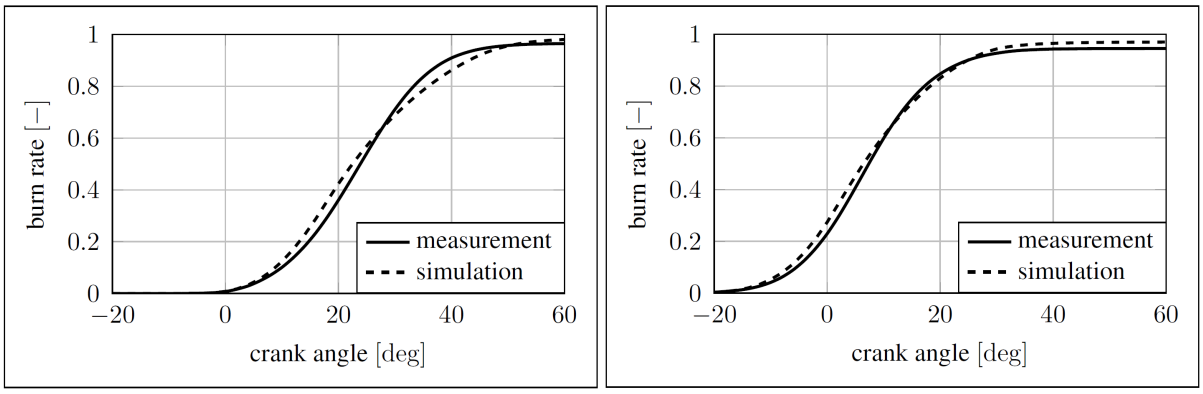

(a) EOP2 of the TT1.3 (320).

(b) EOP3 of the TT1.3 (320).

Figure 4.11.: Comparison of the measured and simulated burn rates for EOP2 and EOP3.

Results for B48 engine with serial pistons and final calibrated turbulence, ignition and combustion models are shown in Figures 4.12 and 4.13.

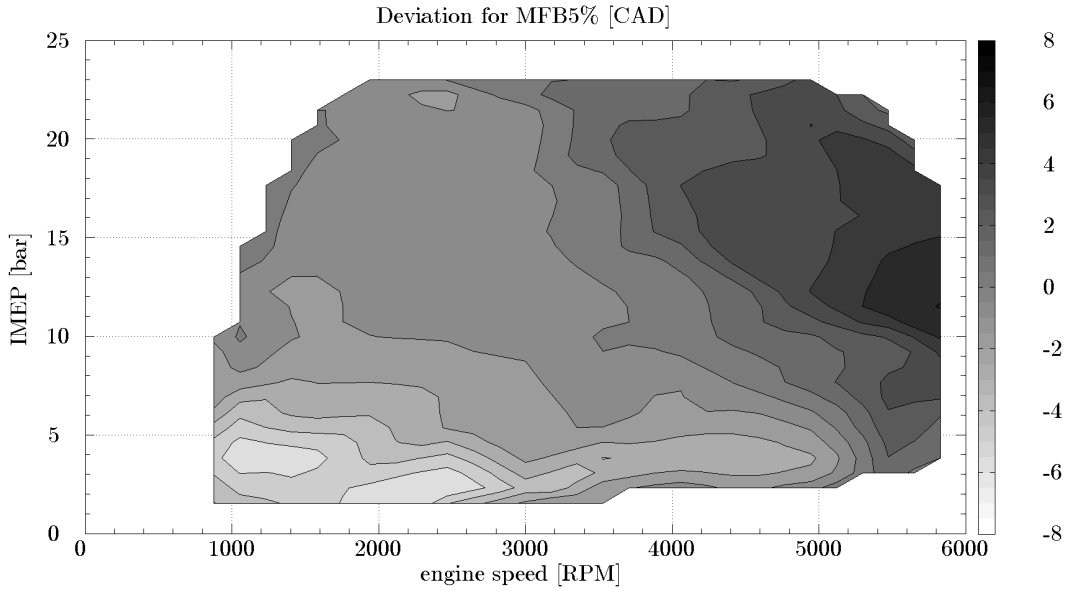

Figure 4.12.: Differential engine map of *MFB5%*: differences between simulation and measurement.

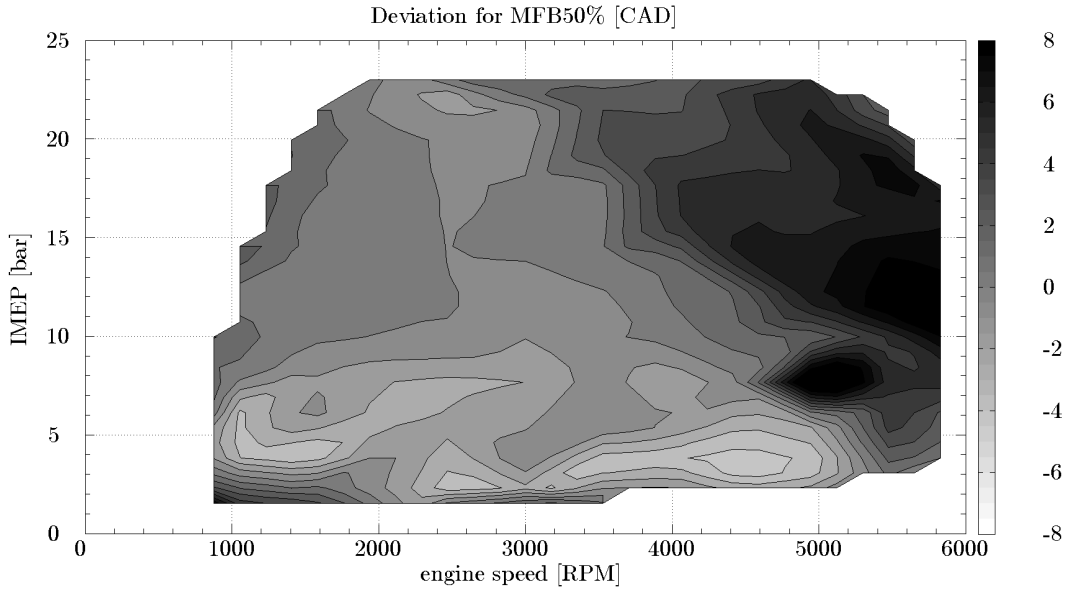

Figure 4.13.: Differential engine map of *MFB50%*: differences between simulation and measurement.

The two illustrations show the engine-map-wide difference between the simulation and the measurement results for the *MFB5%* and *MFB50%*, respectively. In the main part of both maps the accurateness is within the defined margins of ± 3 CAD. However, deviations occur for very low engine loads. In this area the combustion is overestimated. One reason is the limits on the gas exchange process, with small intake valve lifts and a high valve overlap. Because of this, the air charge determination is overestimated and the EGR underestimated, resulting in an accelerated combustion. In the area of very high engine speeds and in the mid-range engine load area, both the *MFB5%* and *MFB50%* are underestimated. In this map range an advanced ignition timing is conducted, due to the decreased time available for combustion. The difference between the simulation and measurement data might be due to an underestimation of the turbulent kinetic energy, resulting in an excessively slow transition

from laminar to turbulent combustion. Nevertheless, the overall results show sufficient quality and can serve as a superior basis for simulating cyclic combustion variations.

4.5 Requirements for the simulation of cycle-to-cycle variations

As can be seen from the illustrations above, some differences between the simulation and the measurement can be found for *MFB5%* and *MFB50%*, in particular for the B48 engine. This will become important when modeling CCV; the limits are described in Section 6.6.1.

In order to simulate cyclic combustion variations, the simulation first has to reach a steady state. This is determined by the cyclic differential, e.g. for the speed of the turbocharger shaft or cylinder charge from cycle to cycle. Furthermore, when a finite-element (FE) solver is used to determine the combustion chamber temperatures, a steady state also has to be reached. Otherwise, the increasing or decreasing heat transfer has a direct influence on the *IMEP*. This in turn affects the calculation of COV_{IMEP} without the CCV model being active. Thirdly, all proportional-integral-derivative (PID) controllers need to be switched off before simulating CCV. If not, the controller might counteract on its variable, thus again influencing COV_{IMEP}.

5 Cycle-to-cycle variations model development

Parts of this chapter have previously been published in [76, 77].

This chapter presents a newly designed CCV model. The need for a new model is explained in the summary of Chapter 2.4.3. The objectives for the new CCV model are itemized in the following:

- The new model aims to not simply reflect CCV on an empirical basis, which means that the model always requires time-consuming calibration, each time when engine properties are changed. Instead, by providing a physical description of CCV, the new model is intended to more accurately and more robustly predict cyclic combustion variations.
- A further objective is to accurately describe the SI cyclic combustion variations throughout the engine operating range.
- The new CCV model is designed to be applied to different combustion processes, comprising conventional and unconventional engine types.
- All significant physical causes of cyclic combustion variations are to be integrated into the new CCV model. These relevant causes are extracted from the research into the literature as described in Chapter 2.2.
- Furthermore, the factors influencing cycle-to-cycle variations from Chapter 2.3 are to be applied in the CCV model.

Since the cyclic combustion variations are to be modeled predictively, the underlying models have to accurately describe the physical background of engine combustion. Therefore, as the second foundation, the previously developed highly sophisticated, quasi-dimensional turbulence, ignition and combustion models are used, cf. Chapter 4.4. These models can ensure the high validity of simulation results. In particular, the turbulence model can be seen as an essential improvement in comparison with earlier developed CCV models. Therefore, for the first time, the significant CCV causes related to in-cylinder flow can be modeled precisely.

In the following sections, first the CCV model approach, i.e. the physical basis regarding the CCV causes, is explained. Then, the structure and functioning of the stochastic model are described in detail. This is followed by a description of how to calibrate the CCV model implementing the factors influencing CCV. As an excursion, further modeling investigations and implementations concerning other possible CCV causes are presented.

5.1 CCV model approach - the physical basis

The CCV model approach taken in this study is on a physical basis. However, some assumptions are made for modeling cyclic combustion variations.

- No spatial resolution of the combustion chamber is available within the 1D/0D simulation environment. Therefore, the identified physical causes of CCV are applied to the global quasi-dimensional description of the individual causes, depicted in the turbulence, ignition and combustion models.
- For all SI engines investigated, it is assumed that the inhomogeneity regarding the air-fuel ratio and exhaust gas rate (EGR) can be neglected. This assumption applies well the TT1.2 and TT1.3, due to their PFI. The argumentation for the B48 engine with its DI system is more difficult. Note that in this study, the B48 engine is only operated with a single injection during the intake stroke. First, measurements are taken at the same operating points in a research engine which is similar to the B48 and provides both a PFI and a DI system. The possible inhomogeneity is then investigated by comparing the O_2 and CO exhaust emissions of the two systems. No significant differences can be found between the exhaust gas contents of the two injection systems. Thus, it can be expected that the B48 DI system induces only low inhomogeneity regarding air-fuel mixtures. The inhomogeneity concerning EGR is also expected to be low, due to its high turbulence-generating in-cylinder flow. Secondly, the research into the literature described in Chapter 2 concluded that the flow-related CCV causes are more important than possible mixture inhomogeneities.

The TT1.3 (with the 320 intake cam shaft) is used to design the new CCV model, since this research engine was first to become available for extensive measurements regarding different engine parameter variations.

5.1.1 Physical fluctuation parameters

The phenomenological turbulence, ignition and combustion models from Chapter 4 describe in detail the underlying physics of the in-cylinder flow and combustion for the mean engine cycle. The physical causes of CCV identified through the research into the literature in Chapter 2 can only be applied in the 0D/1D simulation environment when these correlations are described. The main causes of cyclic combustion variations that are integrated into the new CCV model are listed in Table 5.1. Here, the left column contains the specific physical cause and the second column shows the implementation and impact on the particular physical value in the underlying turbulence, ignition and combustion models. The right-hand column holds the formal symbol from Chapter 4 for each physical cause.

physical cause	impact on physical value	formula symbol
intake flow, shear effects	TKE production	dk_{prod}
global flow structure	integral length scale	l_t
convection at spark plug	initial flame kernel size	$r_{k,init}$
local flow velocity	flame kernel eccentricity	r_{ecc}
flame-wall interactions	flame quenching distance	s_{quench}

Table 5.1.: Integration of physical causes in the new CCV model.

In order to simulate CCV in the subsequent stages of the CCV model development, fluctuations are enforced on these specific physical values, as will be described in Section 5.1.2. At this point, the cause-and-effect chain from Figure 2.7 is drawn upon as an explanation for the individual physical causes; this is described in detail in the following paragraphs.

In-cylinder flow parameters

A fluctuating global flow is represented by the TKE production dk_{prod}, which captures the intake flow and shearing effects. As Grasreiner [49] has shown, the intake flow plays a more important role in TKE production than the shearing effects. Thus, the global flow during the intake stroke mainly influences the fluctuation of dk_{prod}. The second physical value, the integral length scale l_t, directly affects the dissipation term dk_{diss}. The dissipation of the in-cylinder flow takes effect in the intake and compression strokes. A further sensitivity analysis from Grasreiner [49] shows, that the dissipation is responsible for the destruction of most of the TKE built up during the intake stroke. The dissipation is expected to have a great effect on the simulation of CCV.

Details about the fluctuation of the dk_{prod} and on l_t are extracted from the LES investigation published by Richard et al. [106]. The LES were conducted for a PFI engine operated at 1200 rpm and at throttled load. First, the authors directly correlate the tumble fluctuations to variations in TKE. This is not surprising, since the TKE is mainly built up from the breakdown of the large-scale flow motion such as the tumble. Then, the authors extract a normal distribution of the tumble fluctuations at IVC. The standard deviation is evaluated as 6.5 %. However, as Enaux et al. [38] found out by means of LES, the relative fluctuations in the flow are higher in the compression stroke than in the intake stroke. Furthermore, additional investigations by Richard et al. [106] showed that the fluctuations in the in-cylinder flow are significantly influenced by the engine speed and load. In another study of [20, 21] 2D PIV measurements were conducted and the cyclic variation of the kinetic energy, the TKE and the tumble number were analyzed in the last half of the compression stroke in a similar SI engine to the one investigated by Richard. Significant fluctuations of the kinetic energy, the TKE as well as the tumble are reported and visualized by the authors. These findings and conclusions are taken into account when developing the CCV model.

The fluctuations in l_t are determined at spark timing by Richard et al. [106]. At this time, the standard deviation for l_t was evaluated as 10 %. As this value is extracted at the end of the compression stroke, it is assumed

that the standard deviation is higher earlier in the stroke.

Pera et al. [98] investigated CCV by means of 2D direct numerical simulations (DNS). Their findings from the DNS also indicate that the turbulence structure fluctuations, i.e. the varying relocations of individual vortices, are the dominant CCV factor. Thus, the fluctuations in the turbulence intensity and the integral length scale are of great importance for CCV.

Combustion parameters

Further into the cause-and-effect chain, the third physical cause from Table 5.1 is determined to be convection fluctuations at the spark plug. At ignition timing and a short period after, these cyclic variations in heat transfer directly influence the cyclically variable build-up of the initial flame kernel size $r_{k,init}$ [9, 63, 109].

Furthermore, the flow convection fluctuations also drive the flame kernel eccentricity r_{ecc} variations of $r_{k,init}$. Hence, the local flow fluctuations can be reproduced. Richard et al. [106] evaluated the standard deviation for the fluctuating spark plug flow velocity to be around 25 %. Furthermore, the LES investigations revealed that the local flow fluctuations in the vicinity of the spark plug are independent of the global flow variations. These findings are taken into account when developing and calibrating the CCV model. The authors conclude that the fluctuations in the local flow are of most significance for cyclic combustion variations. Pera et al. [98] again confirm this conclusion.

The last physical cause considered in the new CCV model is the flame-wall interaction. By means of heat flux measurements, Suckart et al. [119] found that the flame-wall quenching distance s_{quench} can vary from one engine cycle to another. However, due to the low number of measuring points within the combustion chamber and the very complex post-processing, no exact level of fluctuations is given. Therefore, a lower range of fluctuations in the quenching distance is proposed in the CCV model developed here.

5.1.2 Setup of the stochastic model

Until now, the previously developed predictive turbulence, ignition and combustion models have only been able to simulate the mean engine cycle. Thus, a stochastic model has to be developed. The objective of this stochastic model is to generate fluctuations. These fluctuations are imposed on the physical causes within physical limits in every engine cycle. In the general framework of 0D/1D modeling, this approach is feasible and has been used in several studies [106, 124, 127]. It should be noted that the previously developed models and the presented CCV model are programmed in FORTRAN.

First, the stochastic model determines a probability density function (PDF). The assumptions for the PDF are as follows:

- In order to limit the complexity of the CCV model development, no skewness of the normal distribution is taken into account. This is a valid assumption, since the significant physical causes respond to a normal distribution, cf. [106].
- The PDF is fixed to a standard deviation of 2σ, thus accounting for 95.45 % under the PDF. Nevertheless, enough emphasis is still placed on the boundary area of the PDF. Furthermore, from visual analysis, the normal distribution from [106] is of the same order.

The mean value of each of the five causes is shown in the following matrix with example values, typical of SI engines, in order to explain the following procedure.

$$\text{mean value}_{\text{physical cause}} = \begin{bmatrix} dk_{prod} \\ l_t \\ r_{k,init} \\ r_{ecc} \\ s_{quench} \end{bmatrix} = \begin{bmatrix} 10\,\frac{m^2}{s^2} \\ 2\,mm \\ 1\,mm \\ 2\,mm \\ 100\,\mu m \end{bmatrix}$$

As can be seen, the individual physical causes have a wide range of dimensions. This would complicate the process of determining individual PDFs in terms of their mean value and the standard deviation and, in particular, also complicate the calibration process in Section 5.2. Therefore, in the following, a substitute is introduced which will be multiplied with the mean value for each of the five physical causes in every engine cycle (if the CCV model is active). This substitute is the support value x_i from the PDF.

Now, the stochastic model determines the PDF according to the following equations. Since a unique PDF is generated for every individual physical cause, the particular physical values are substituted in the following by the index *i*, with index *i* being one of the five physical causes.

$$PDF(x_\mathrm{i}) = \frac{1}{\sigma\sqrt{2\pi}} e^{\frac{-(x_\mathrm{i}-\mu)^2}{2\sigma^2}} \tag{5.1}$$

In the PDF, μ is set to 1. The standard deviation σ can be written as in the following:

$$\sigma = \frac{2x_{physical\ limit}}{2\sigma_{number}} \tag{5.2}$$

in which σ_{number} is fixed to 2 (standard deviation of 2σ). Therefore, the standard deviation σ can also be expressed as in the following equation.

$$\sigma = \frac{2x_{physical\ limit}}{4} \tag{5.3}$$

Then, $x_{physical\ limit}$ can be defined as follows.

$$x_{physical\ limit} = 2\sigma. \tag{5.4}$$

The physical limits of the five implemented causes are extracted from the literature as shown in Section 5.1 or specified according to the calibration procedure described below. For the next steps, in order to explicitly demonstrate the functioning of the stochastic model, an example is given using the initial flame kernel size $r_{k,init}$. The standard deviation is exemplified with $\sigma_{r_{k,init}} = 0.15$. Thus, applied to Equation 5.4, it yields:

$$x_{physical\ limit,r_{k,init}} = 2\sigma_{r_{k,init}} = 0.3 \tag{5.5}$$

The resulting probability density function for this example is presented in Figure 5.1. After the evaluation of the

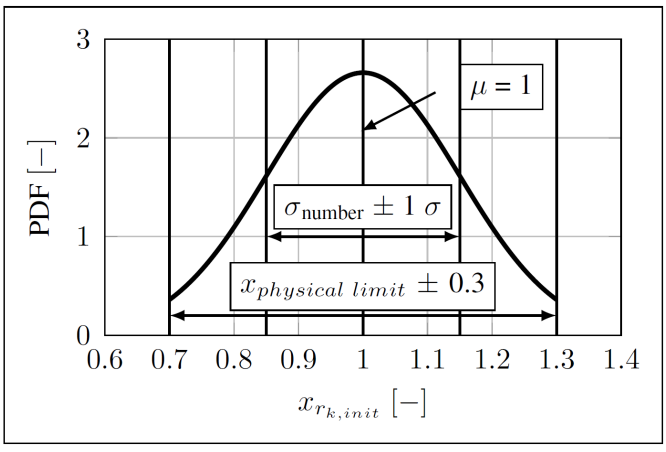

Figure 5.1.: Probability density function and its characteristics, shown for $x_i = x_{r_{k,init}}$.

PDF, the stochastic model calls upon an inherent FORTRAN function to extract a random number between 0 and 1. Then, this random number is multiplied with the PDF in each engine cycle. However, since the probability density function is characterized by two minima and one maximum, no distinct allocation is possible. Therefore, the PDF is discretized with an intermediate step into $n = 121$ points. First, the increment is determined as $x_{\Delta,r_{k,init}}$ between $\pm\, x_{physical\ limit,r_{k,init}}$ as in the following equation.

$$x_{\Delta,r_{k,init}} = \frac{2x_{r_{k,init}}}{121} = 0.00496 \tag{5.6}$$

Regarding the $PDF(x_{r_{k,init}})$, this then yields:

$$x_{r_{k,init}} = \{-x_{physical\ limit} + \mu, -x_{physical\ limit} + x_\Delta + \mu, ..., x_{physical\ limit} + \mu\} = \{0.7, 0.705, ..., 1.3\} \tag{5.7}$$

Thereafter, every discretized $PDF(x_{r_{k,init}})$ is summed up as $sumPDF(x_{r_{k,init}})$. The sum of all PDFs at every flame kernel size $x_{r_{k,init}}$ increment considered is formulated as follows:

$$sumPDF(x_{r_{k,init}}) = \sum_{x_{r_{k,init}}=-x_{physical\ limit,r_{k,init}}+\mu}^{x_{physical\ limit,r_{k,init}}+\mu} PDF(x_{r_{k,init}}) \tag{5.8}$$

and illustrated in Figure 5.2. After the intermediate step of calculating $sumPDF(x_{r_{k,init}})$, the stochastic model

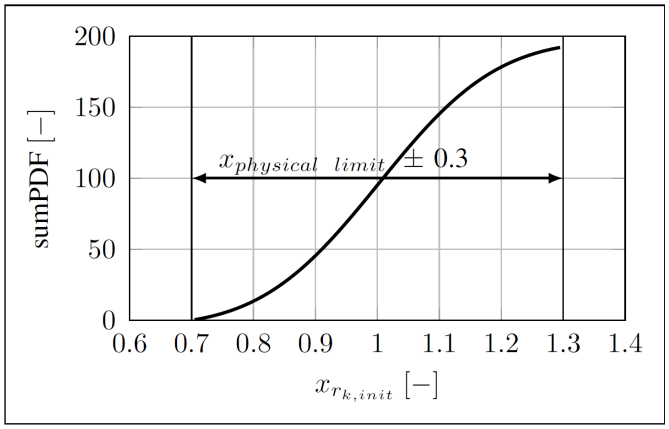

Figure 5.2.: Summation of the particular PDF and its characteristics, shown for $x_i = x_{r_{k,init}}$.

is able to call up the random number procedure and multiplies it with sumPDF. In this example, sumPDF is summed up to a value of 192, see Figure 5.2 at $x_{r_{k,init},maximum} = 1.3$. Hence, a random number of 0 equals a sumPDF of 0 which is referenced to the PDF and here, $x_{r_{k,init},minimum}$ is 0.7. A random number of 1 determines a sumPDF of 192, thus defines the $x_{r_{k,init},maximum}$ as 1.3 within the PDF. Then, the support value $x_{r_{k,init}}$ can be multiplied with the mean value of $r_{k,init}$.

This procedure is performed periodically for each of the five selected physical causes in every engine cycle, when the CCV model is active. The stochastic model is switched to active after the simulation has reached a steady state according to Chapter 4.5. Prior to that, only the mean value of each physical cause is evaluated, as calculated in the turbulence, ignition and combustion model.

As an example, the working principle of the stochastic model is illustrated for the initial flame kernel size in Figure 5.3. Here, the mean value of $r_{k,init}$ is already multiplied with the support value $x_{r_{k,init}}$. $r_{k,init}$ in the mean cycle is determined to be half the distance between the two spark plug electrodes, in this case 1 mm. Since the physical limit is set to 0.3, the minimum and maximum values of $r_{k,init}$ are 0.7 mm and 1.3 mm, respectively. In the first five cycles, the CCV model is not active; therefore, the mean cycle is simulated. Note that the five mean cycles are examples, usually the transient response is longer. Starting from cycle number six, the stochastic model is active, leading to a fluctuation in the initial flame kernel size from one engine cycle to another.

Additionally, further randomness is integrated in the stochastic model through the implementation of a seed, which is dependent on the time and date. The seed is implicitly used in the FORTRAN function *RANDOM NUMBER*. Therefore, after each simulation the cycle-to-cycle variations can differ slightly, as also seen in experiments from one measurement to the other with the exact same engine parameters.

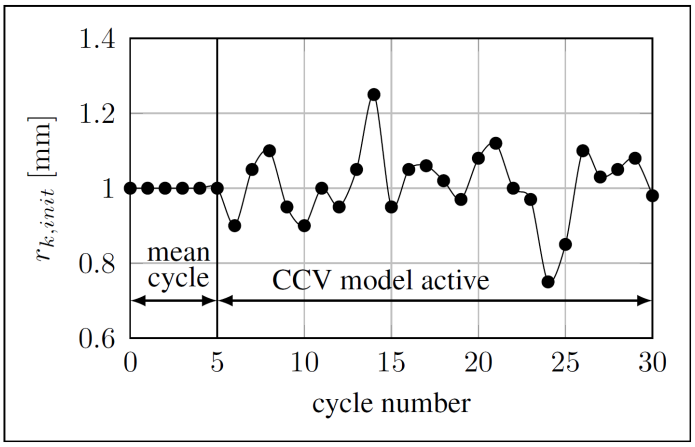

Figure 5.3.: Working principle of the new CCV model.

With the CCV model active, the combustion and thus the *IMEP* fluctuate from one engine cycle to the other. Starting with cycle six in the example from above, the COV_{IMEP} is calculated with respect to Equation 2.5 in Chapter 2.1.1. Other cyclic fluctuation engine parameters can be evaluated accordingly; for the general equation on *COV*, see Equation 2.4.

5.1.3 Sensitivity study on the five physical causes

As already mentioned, the standard deviations are individually determined for each physical cause. Moreover, every physical cause is weighted according to Section 5.2, in order to account for the influence of different engine parameters. For a better understanding and as a pre-step for the CCV model calibration, a sensitivity analysis is performed for the TT1.3 (320 intake cam shaft) and the B48 with serial pistons. In the following, the μ is always set to 1. The physical limit $x_{physical\ cause}$ is varied between 0.2 and 0.7. Then, the PDF is calculated for the individual five causes. Figures 5.4 and 5.5 illustrate the sensitivity analysis for the TT1.3 and B48, respectively, at a similar operating point listed in Table 5.2.

engine speed	3000	[rpm]
engine load	WOT	[-]
MFB50%	8	[CAD]
λ	1	[-]
EGR	3.0	[%]

Table 5.2.: Reference engine operating point for the sensitivity analysis.

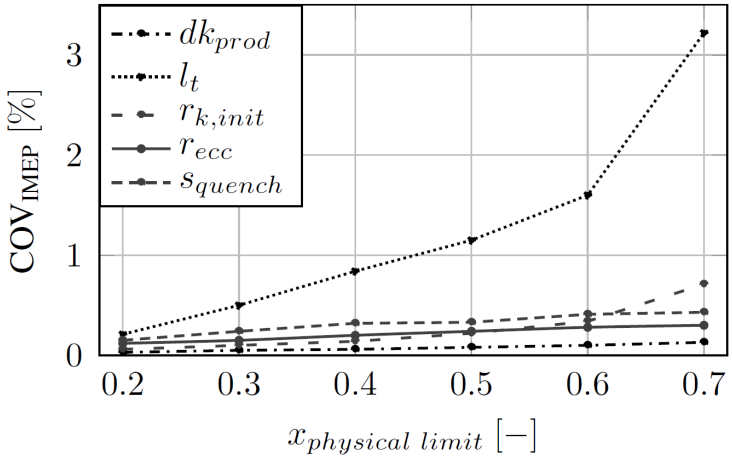

Figure 5.4.: Sensitivity analysis of the five implemented physical causes for the TT1.3.

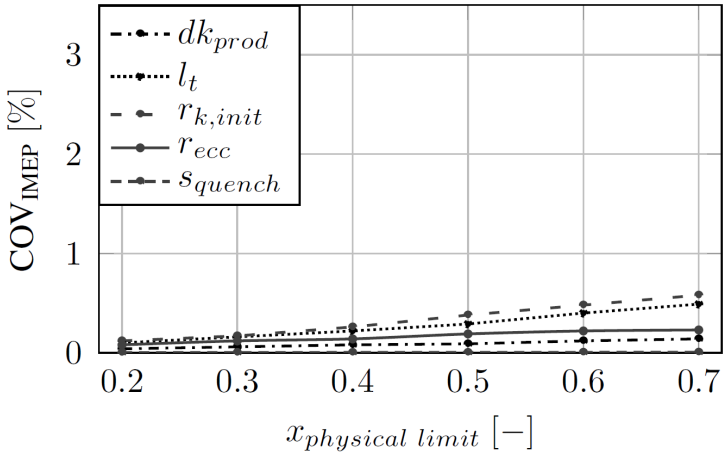

Figure 5.5.: Sensitivity analysis of the five implemented physical causes for the B48.

At first sight, the TT1.3 shows significant sensitivity to the integral length scale, whereas the other four physical causes are at a similar, lower level. The TT1.3 combustion process is characterized by low turbulence intensity, which is reflected in the high impact of turbulence dissipation. This result corresponds with the findings from Omura et al. [93] in the literature. On the other hand, the sensitivity of the B48 combustion process to the individual causes is on a much lower level. Here, the initial flame kernel size and the integral length scale appear to be most significantly affected. The TKE production term and the flame kernel eccentricity are on only a slightly lower level. These findings correspond with the theory from Section 5.1.1. Finally, the flame quenching distance seems to be nearly negligible for the B48 operating point. The latter result can be clarified with the burn rate and, in particular, the burn-off phase in the mean cycle. Both are considerably advanced in comparison to the TT1.3, as illustrated in Figure 5.6 for this specific engine operating point.

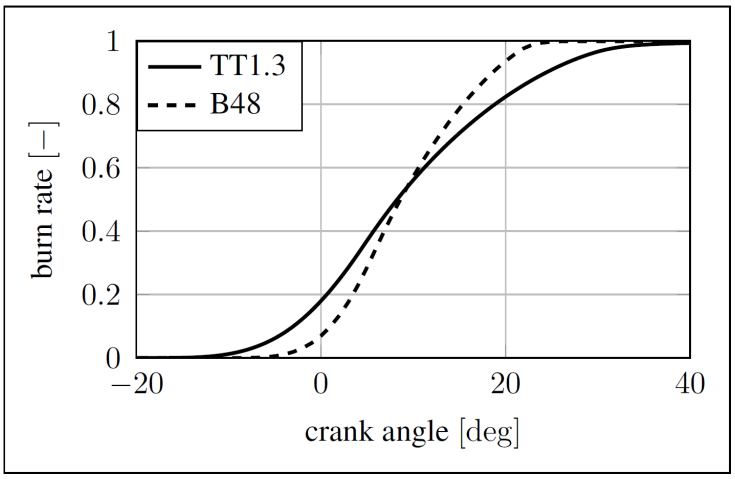

Figure 5.6.: Comparison of burn rates of the B48 and TT1.3 combustion processes.

This sensitivity analysis demonstrates the great dependence of cyclic combustion variations on the underlying combustion process. It is evident that the individual steps and their variations in the cause-and-effect chain can have different effects on CCV.

5.2 CCV model calibration strategy

In the next step of the new CCV model development, the physical limits of the five CCV causes are initially fixed for a given reference engine point. This reference point is defined for the TT1.3 (320), which is used as the design engine, see Table 5.2 from above. From the literature [106, 109, 119], physical limits, i.e. fluctuation ranges, for the five integrated physical causes are extracted and imposed on each individual cause. Table 5.3 presents these fixed values. Since the mean value μ of the probability density function is set to 1, these physical limits have still

to be seen as in relation to μ. As an example, this means that the mean value of $r_{k,init}$ is 1 mm and $r_{k,init}$ can range between 0.8 mm and 1.2 mm. The cycle-to-cycle variations from the simulation match the CCV from measurements for this reference engine operating point. With the fixed physical limits implemented, the new CCV

physical cause	physical limit
dk_{prod}	0.38
l_t	0.38
$r_{k,init}$	0.2
r_{ecc}	0.3
s_{quench}	0.3

Table 5.3.: Fixed physical limits of the five implemented physical causes for the reference engine operating point.

model is already able to qualitatively describe cycle-to-cycle variations. For example, when the ignition timing is retarded or the engine load reduced, the model reflects the right trend for CCV. Both engine parameter variations mentioned are displayed in Figure 5.7. This figure illustrates the COV_{IMEP} found by simulation, including fluctuations with the fixed physical limits from above, and that found by measurement. The left figure shows

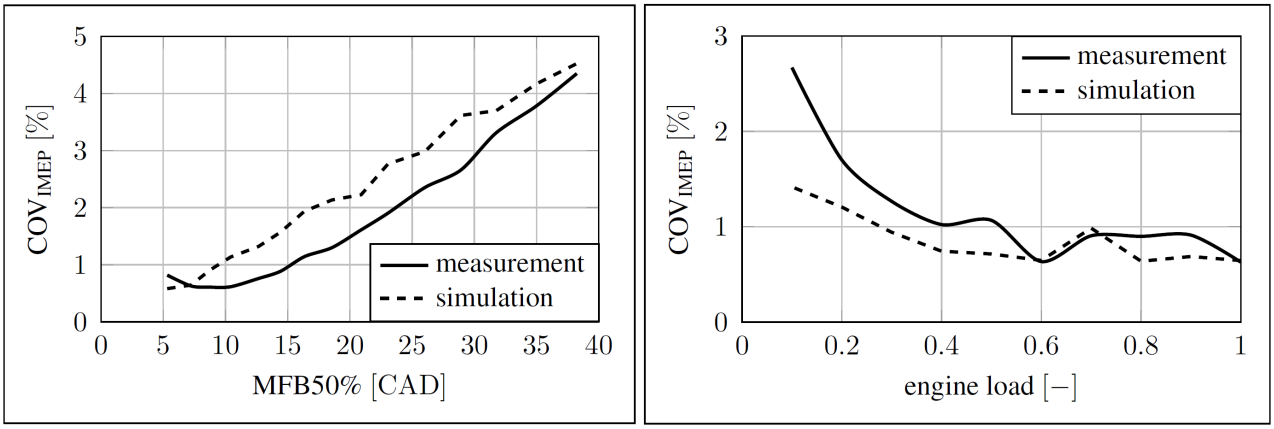

(a) MFB50% variation of the TT1.3 (320).

(b) engine load variation of the TT1.3 (320).

Figure 5.7.: Qualitative reproduction of CCV by physical causes fluctuations.

the ignition timing variation by means of the *MFB50%*. For low *MFB50%*, the simulation matches the COV_{IMEP} found by measurement well, since this center of combustion is in the region of the reference engine operating point. However, for later *MFB50%*, the simulation overestimates the CCV found by measurement, though it still describes the correct trend. In Figure 5.7 (b), the variation in engine load from partial load to full load (WOT) is depicted. For very low engine loads, the simulation underestimates the COV_{IMEP}, though the right tendency is reproduced towards higher engine loads.

Before the calibration procedure is described, a further sensitivity analysis is carried out regarding the $COV_{MFB0\%\text{-}MFB5\%}$, $COV_{MFB5\%\text{-}MFB90\%}$, $COV_{MFB75\%\text{-}MFB90\%}$ and $COV_{MFB50\%}$, used for additional comparison, not for calibration, in the following two Figures 5.8 and 5.9. The engine operation point is the reference point from the TT1.3 (320) from Table 5.2. Additionally, the four specific *COV* characteristics found by measurement for this operating point are displayed in the illustrations as a red beam. This is intended to indicate about the adequacy of the chosen fixed limits of the physical causes in Table 5.3.

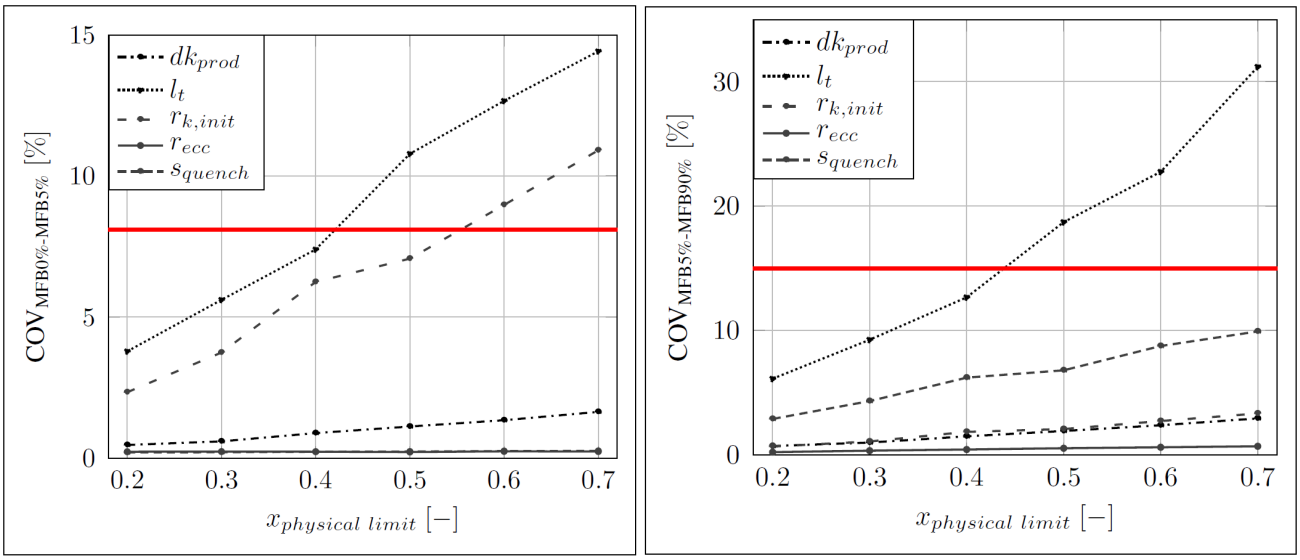

(a) $COV_{MFB0\%\text{-}MFB5\%}$. (b) $COV_{MFB5\%\text{-}MFB90\%}$.

Figure 5.8.: Sensitivity analysis of $COV_{MFB0\%\text{-}MFB5\%}$ and $COV_{MFB5\%\text{-}MFB90\%}$ regarding the five physical causes by means of the TT1.3 (320) reference engine operation point.

In Figure 5.8 (a) it can be seen that the integral length scale has the highest influence on the fluctuation in the ignition delay. The physical cause showing the second highest sensitivity is the initial flame kernel size, which is reasonable, since it directly determines the early combustion phase. The other parameters are only of minor importance. Figure 5.8 (b) shows similar behavior of the integral length scale, determining the fluctuations in the main combustion phase. Here, the flame-wall quenching distance is also shown to be of significance. The other physical causes can be considered as of low importance.

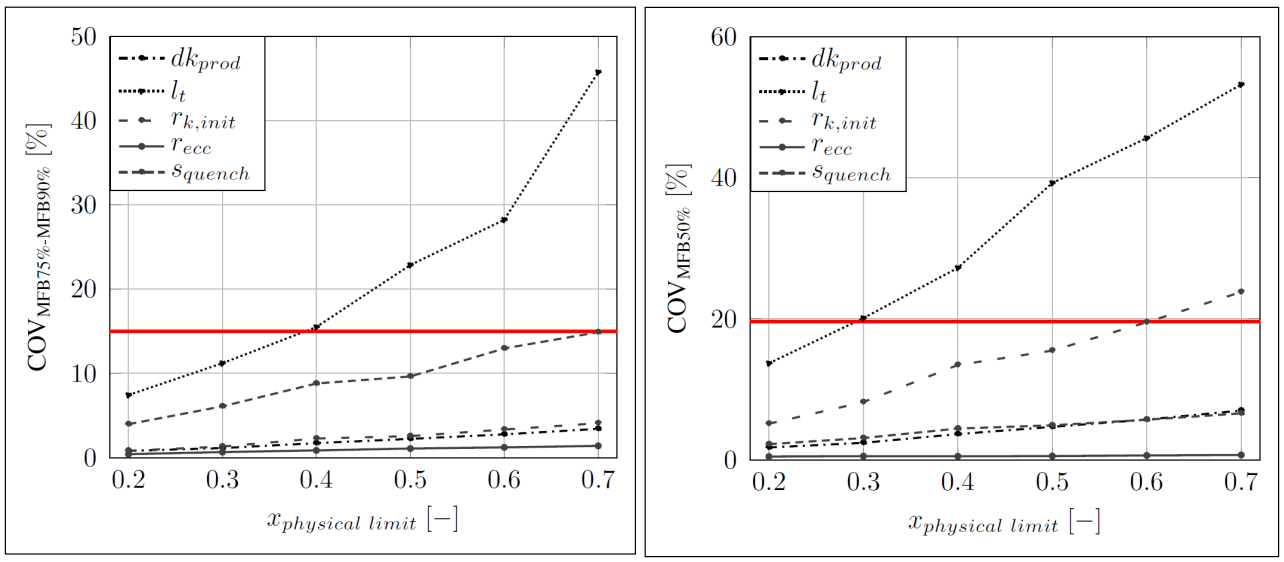

(a) $COV_{MFB75\%\text{-}MFB90\%}$. (b) $COV_{MFB50\%}$.

Figure 5.9.: Sensitivity analysis of $COV_{MFB75\%\text{-}MFB90\%}$ and $COV_{MFB50\%}$ regarding the five physical causes by means of the TT1.3 (320) reference engine operation point.

The investigation of the burn-off combustion phase fluctuations in Figure 5.9 (a) illustrates that the integral length scale is still of significance at the end of combustion. The second important parameter is the flame-quenching distance, as expected, especially for the relatively slow combustion of the TT1.3 (320), described above. Other physical causes can be seen as negligible. The fourth fluctuation investigated concerns the center of combustion in Figure 5.9 (b). Here, both the integral length scale and the initial flame kernel size are impor-

tant; the other physical causes are insignificant. Since the flame-wall quenching distance already shows high sensitivity for the $COV_{MFB5\%\text{-}MFB90\%}$, its effect can be expected to come into play after the *MFB50%*. In the sensitivity study it was demonstrated that the new CCV model approach behaves physically. With this sensitivity analysis in mind, the calibration procedure is performed.

It can be stated that the CCV model does not yet exactly, i.e. quantitatively, correspond with the measurement results. Therefore, there is a definite need to calibrate the model. The model is calibrated by means of a parameterization regarding the engine speed, load, *MFB50%* and air-fuel equivalence ratio λ, in order to directly assess the physical limits. The new CCV model should react predictively to other engine parameters, such as boost pressure, valve lift and timing, due to the underlying physical turbulence, ignition and combustion models. The valve lift and timings determine the EGR, among other values, thus directly affecting the evaluation of the laminar flame speed, calculated in the ignition and combustion model. In summary, this parameterization accounts for the factors influencing cyclic combustion variations.

For the calibration procedure, an extensive number of measurements are available regarding the four engine parameters of the TT1.3 (320), as defined in Table 5.4. This table specifies the limit values and the increments of each parameter.

engine parameter	unit	min value	max value	increment value
engine speed	[rpm]	2000	3500	500
engine load	[-]	0.1*WOT	WOT	0.1*WOT
MFB50%	[CAD]	5	38	1.5
λ	[-]	1.0	1.6	0.1

Table 5.4.: Measurement data basis for the CCV model parameterization.

Starting from the reference engine operating point from Table 5.2, each engine parameter is varied individually. The COV_{IMEP} from the experiment is compared to the COV_{IMEP} from the simulation. Mathematical equations are then identified for the five physical causes, as described in the following. The influencing factor equation of the initial flame kernel size is determined by comparing the measured coefficient of variation of the ignition delay $COV_{MFB0\%\text{-}MFB5\%}$ to the value from the simulation. This procedure is also conducted for the flame kernel eccentricity concerning the burn duration $COV_{MFB5\%\text{-}MFB90\%}$ and for the flame-wall quenching distance regarding the burn-out phase $COV_{MFB75\%\text{-}MFB90\%}$. The TKE production term and integral length scale are directly calibrated by comparing COV_{IMEP} found by measurement to that found by simulation.

Table 5.5 displays the resulting matrix of the calibration procedure. Detailed terms for the factors influencing CCV for each physical cause can be found in Appendix E. Additionally, in the engine load equations regarding

physical cause	engine speed	engine load	λ	*MFB50%*
dk_{prod}	logarithmic	exponential	constant	polynomial
l_t	logarithmic	exponential	constant	polynomial
$r_{k,init}$	constant	constant	polynomial	polynomial
r_{ecc}	constant	constant	polynomial	polynomial
s_{quench}	constant	constant	polynomial	polynomial

Table 5.5.: Parameterization matrix of the four engine parameters and five physical causes.

dk_{prod} and l_t, a λ correction factor is applied. When the air-fuel equivalence ratio is varied, applying a leaner mixture, the fuel mass and thus also the engine load decreases. However, the air cylinder charge remains almost the same, which results in similar flow structures within the combustion chamber. As already described above, the global flow structure fluctuations are independent of the local flow variations. Therefore, dk_{prod} and l_t are determined by other equations than are $r_{k,init}$ and r_{ecc}. The output of these influencing factor equations still determine the physical limits, though with the dependence of the specific engine operation point in mind. Therefore, this matrix is integrated into the calculation of the probability density functions and their individual standard deviations within the stochastic model. The equations are connected multiplicatively, since the

engine parameters influence the physical causes independently of one another. Finally, the influencing factor term for each physical cause is multiplied with the fixed physical limits from Table 5.3.

To demonstrate this more clearly, two engine maps regarding the mean cycle *MFB50%* and the physical fluctuation limit of the initial flame kernel size are illustrated in Figures 5.10 and 5.11. The engine used is the B48 with serial pistons. First of all, it can be seen that in the mid-region engine speed and load the physical fluctuation limit is in the range of 0.2. In this map range, the center of combustion is approximately 7 [CAD] $\pm$ 3 [CAD]. The ignition timing and thus the center of combustion are retarded for very low engine loads and in the low-end torque range; here, the fluctuation limit is increased. A third area can be found at high engine speeds and loads. In this engine map range, an enrichment strategy is implemented, in order to counteract the high exhaust gas temperatures. A richer air-fuel mixture reduces the fluctuation in the initial flame kernel size, as described in the literature in Chapter 2.2.3.

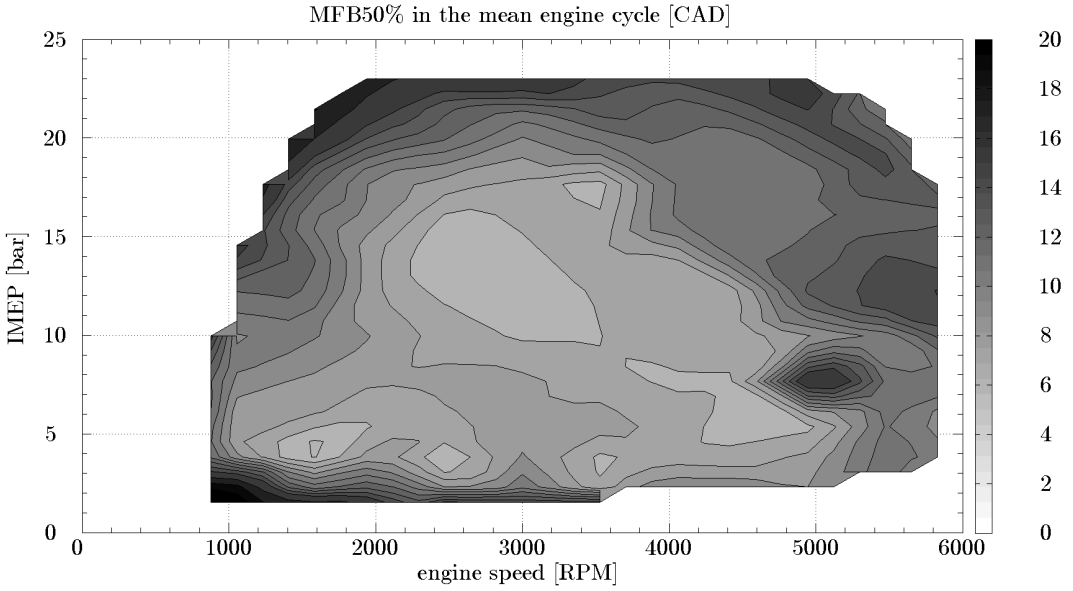

Figure 5.10.: MFB50% engine map from the B48 (serial pistons) mean cycle simulation.

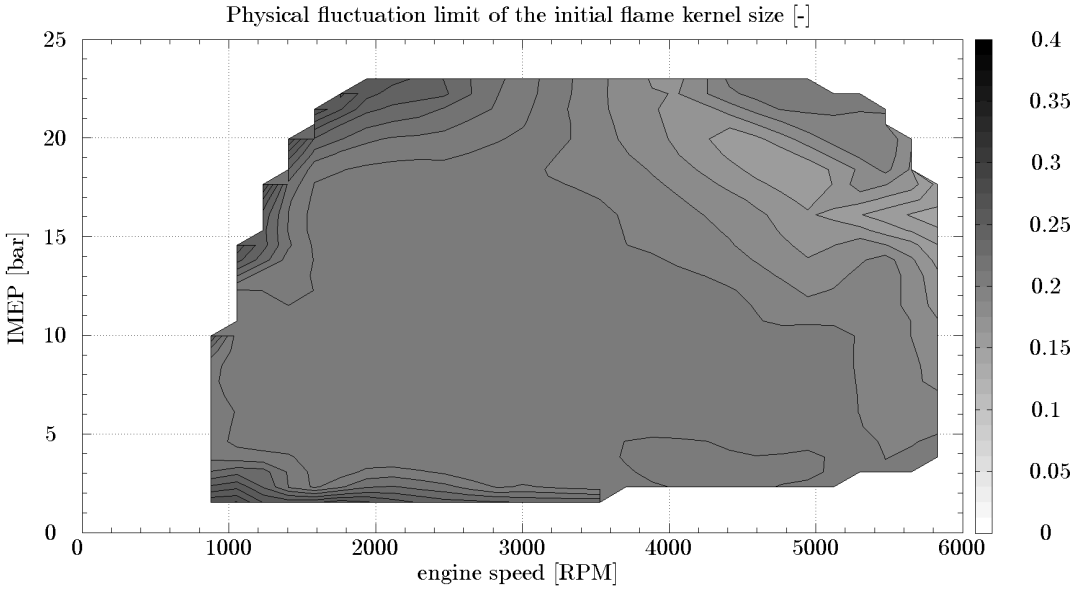

Figure 5.11.: Engine map including the physical fluctuation limits of the initial flame kernel size.

Finally, as an example and for a better visualization of the CCV model application, the cylinder pressure curves gathered by measurement and the simulation with the new CCV model are illustrated in Figure 5.12. 20 consecutive cycles found by measurement and using the new CCV model of the B48 are displayed, respectively. The operating point was 3000 rpm, 0.25*WOT, *MFB50%* at 8 CAD and with a stoichiometric air-fuel ratio.

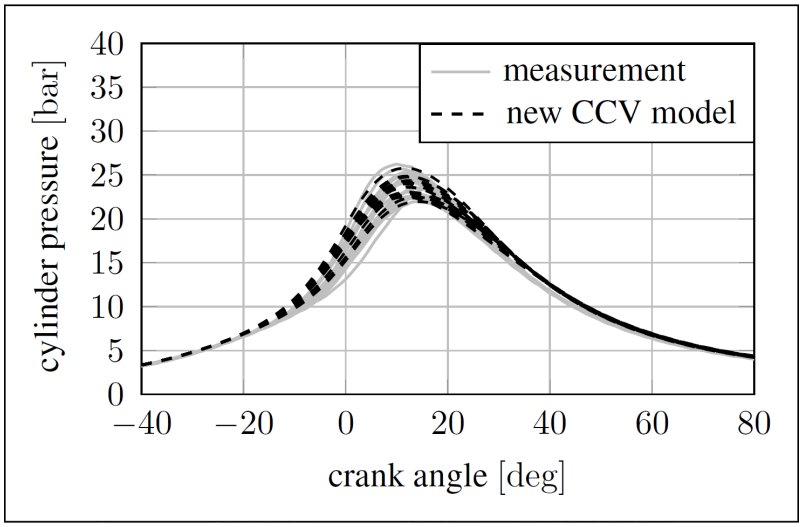

Figure 5.12.: Example comparison of cylinder pressure curves found by measurement and simulation with the new CCV model.

As can be seen in the illustration, the cylinder pressure curves found by simulation are a good match for the ones found by measurement. Comparing COV_{IMEP} found by measurement and the simulation also indicates a correspondence. In Chapter 6 the underlying cyclic combustion is investigated in more detail, in order to verify the physical functioning of the CCV model.

Summing up, the new CCV model is only parameterized once by means of the TT1.3 (320). The CCV model is used exactly as designed for the other SI engines investigated. Chapter 6 will examine whether this approach is feasible.

5.3 Further modeling investigation and implementation

Another physical cause of CCV, found in the literature is the influence arising from sources outside of the cylinders. This topic is assessed in the following. Furthermore, the CCV model is made flexible to suit different users.

5.3.1 Investigation of the external factors

As described in the literature section [131], external CCV factors are considered only as minor causes. Examples of external factors include variations in the cylinder air charge, air-fuel equivalence ratio and EGR from one engine cycle to the other. All three factors can be correlated to fluctuations in the gas exchange process, except for DI systems, where a varying λ may originate from injection fluctuations such as changes in the injection pressure. As an example, Figure 5.13 displays the fluctuating pressure from the intake and exhaust port in the crank angle degree range, when the specific valve is open. The B48 engine was operated at 1500 rpm and an *IMEP* of 14 bar. Exhaust valve open (EVO) occurs at 120 CAD and EVC at 390 CAD, while IVO is at 310 CAD and IVC at 570 CAD.

Fluctuations in the exhaust pressure have an greater effect on variations in EGR, while fluctuations in the intake pressure have a greater influence on variations in the cylinder charge. It can be seen that, in particular, the pressure fluctuations appear in the first part of the specific open valve. Note that although the relative fluctuations in the intake pressure are small, this can still have a noticable effect. Dorsch [32] reports that deviations

of 7-10 mbar in the average intake pressure can change the fuel consumption results by ± 0.1 % in simulated driving cycles.

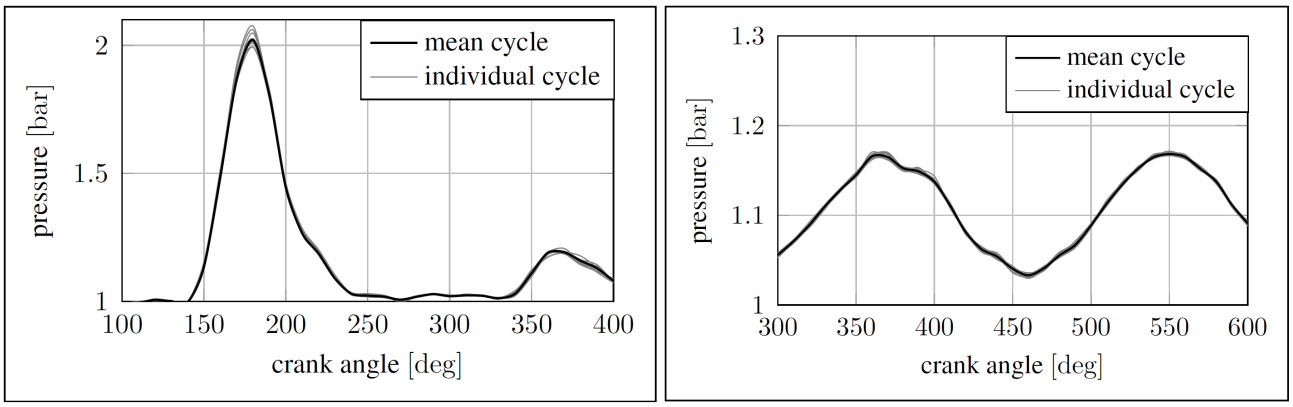

(a) Exhaust pressure). (b) Intake pressure.

Figure 5.13.: Fluctuating pressure in the intake and exhaust port.

Since the cylinder EGR and charge determination are calculated from these pressure curves, a coefficient of variation can be derived for the EGR and for the cylinder charge. Statistics are obtained from the evaluation of 440 consecutive measured engine cycles and eleven B48 engine operating points from low to high loads and at 1500 rpm. For a better visualization, the engine load variation is investigated and displayed in Figure 5.14. Engine parameters are included as well as combustion and gas exchange analysis results. Obviously, the cylinder air charge (not shown here) increases proportionally with the engine load. Furthermore, COV_{IMEP} from the experimental analysis of CCV is shown. The $COV_{IMEP,\,LP}$ accounts for a coefficient of variation for the *IMEP* from a simulation in which only the cycle-specific intake and exhaust pressures are imposed on the gas exchange components. The burn rate used is derived from the mean engine cycle for each engine load. Thus, it is able to determine the individual influence that the cylinder air charge has on CCV, and how other external factors influence the *IMEP*.

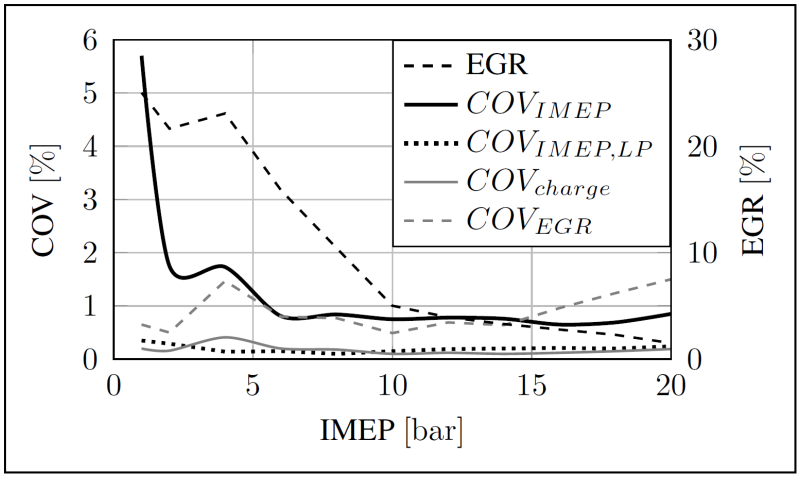

Figure 5.14.: Fluctuating pressure in the intake and exhaust ports.

The EGR is high for low engine loads and low for high engine loads. With respect to the cylinder air charge and EGR, statistics are calculated according to Equation 2.4. The COV_{EGR} ranges around 1 % and the COV_{charge} around 0.2 %. Comparing the COV_{IMEP} to the $COV_{IMEP,\,LP}$ it is obvious that the latter is at least three times smaller.

In conclusion, purely external factors can be seen as of minor importance for cyclic combustion variations. However, simulations with a mean cycle intake and exhaust pressure and together with the CCV model application still show variations in the EGR and charge from one engine cycle to the other. This is because a fluctuating

combustion varies the combustion-off phase. Thus, a varying combustion efficiency again affects the gas exchange and the in-cylinder temperatures, causing fluctuations in the EGR and cylinder charge. Nevertheless, the conclusion that external factors have little influence on CCV is not proven to be wrong by the complex interplay described.

5.3.2 Flexibility

For reasons of user flexibility, the CCV model has to be

- able to be switched off and on, and
- simple to use. If needed, an engine-individual CCV model calibration procedure should be simple to perform. The need to calibrate the CCV model is described and discussed in Chapter 6.

After a steady state is reached in the simulation, a definite number of engine cycles has to be calculated with the CCV model switched on, in order to gain a reproducible result for the cyclic combustion variations. The number of engine cycles depends on the level of CCV and on the engine parameters. Figure 5.15 shows the trends in COV_{IMEP} up to $COV_{IMEP,final}$, i.e. after the maximum measured number of 440 cycles, for different engine operating points in the case of the TT1.3 (320). Details of the engine operating points are set out in Table 5.6.

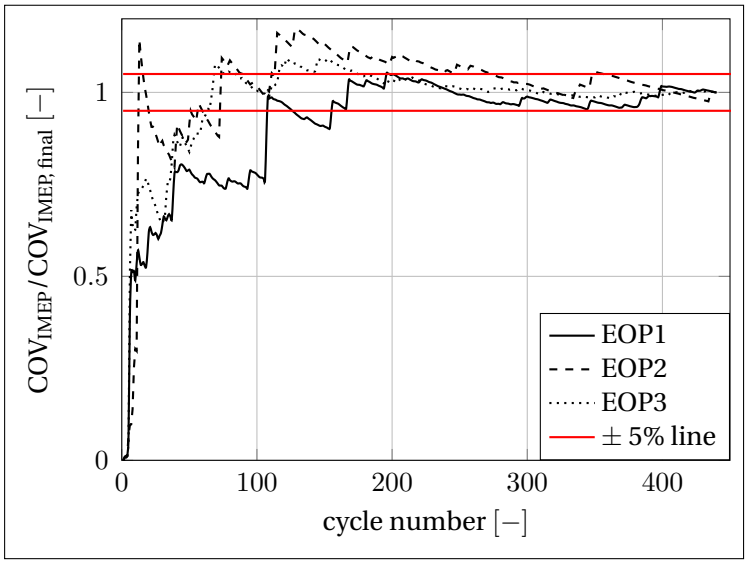

Figure 5.15.: Trend in the relative COV_{IMEP} for different engine operating points.

engine parameter	unit	EOP1	EOP2	EOP3
engine speed	[rpm]	3000	3000	3000
engine load	[-]	WOT	0.1WOT	WOT
MFB50%	[CAD]	8	8	10
λ	[-]	1	1	1.6
EGR	[%]	3.0	9	3
COV_{IMEP}	[%]	0.7	3.1	7.8

Table 5.6.: Reference engine operating points for the sensitivity analysis with the TT1.3 (320).

The objective is to find the number of cycles required to measure a relative deviation in COV_{IMEP} below a certain threshold. From these characteristics, no correlation can be drawn between the absolute COV_{IMEP} and the number of cycles needed for convergence. A sufficient convergence of $\pm 5\,\%$ can be determined to be 250 engine cycles for all three engine operating points.

In the following chapter, the CCV model developed is applied to the SI engines investigated, in order to validate the model by means of measurement results.

Parts of this chapter have previously been published in [76, 77].

This chapter includes the detailed verification and validation of the new CCV model by means of the available combustion processes and varying engine parameters investigated. Furthermore, with the findings in mind, the limits and potentials of the new model approach are indicated at the end of this chapter.

Several SI engines with different underlying combustion processes are investigated, in order to cover a broad experimental basis, cf. Chapter 3. This experimental basis represents one means of validating the new CCV model. The combustion processes include engines with

- high in-cylinder turbulence,
- a fully variable valve train,
- a high compression ratio,
- a long expansion via the crank train,
- and a long expansion via the valve train.

Therefore, it is possible to investigate and integrate factors influencing CCV from various numbers of engine parameters such as

- engine speed,
- engine load,
- ignition timing,
- air-fuel equivalence ratio λ,
- EGR,
- intake valve lift and timing, exhaust valve timing,
- and boost pressure.

The functionality of this CCV model is verified by comparing it to measurement data and another CCV model which is considered the state of the art [127]. This state-of-the-art CCV model has been available in the commercial simulation software GT-Power since V7.5 [46]. However, the number of cycles needed for a sufficiently converged simulation is higher in the commercial software implementation than in the original design by Wenig [127]. For better comparison, the state-of-the-art CCV model will be based upon the same phenomenological turbulence, ignition and combustion model as the CCV model in this work. This is permissible, since the fluctuation parameters in the state-of-the-art CCV model access the same combustion parameters (laminar burning velocity and initial flame kernel growth), described in the combustion model, as in the original design [127]. According to the available parameters and suggestions given in the GT-Power manual [46], the state-of-the-art CCV model is calibrated once for each engine investigated. With the calibration fit parameters, the simulation aims to agree as well as possible with the CCV from experiments within the engine map and with engine parameter variations. In contrast, the newly designed CCV model is only calibrated once, as described in the previous Section 5.2. In the following, the new CCV model is validated regarding the investigated SI engines from Chapter 3 in individual sections.

The variations in the engine operating points of the TT1.3 (320) are defined in Table 6.1. The first four variations are congruent with the variations of the model calibration of Section 5.2, and the last variation is additionally used to verify the model. First, all five variations are illustrated by means of the COV_{IMEP}. Then, for specific engine operating points, the performance of the new CCV model is analyzed in more detail on the basis of p_{max}, *MFB5%*, *MFB50%*, *MFB75%* and *MFB90%* statistics.

engine parameter	unit	VAR1	VAR2	VAR3	VAR4	VAR5
engine speed	[rpm]	3000	3000	3000	variable	3000
engine load	[-]	variable	WOT	WOT	WOT	WOT
MFB50%	[CAD]	8	variable	8	8	variable
λ	[-]	1	1	variable	1	1.4

Table 6.1.: Engine parameter variations used to validate the model with the TT1.3 (320).

The engine parameter variations VAR1 and VAR2 are displayed in Figure 6.1.

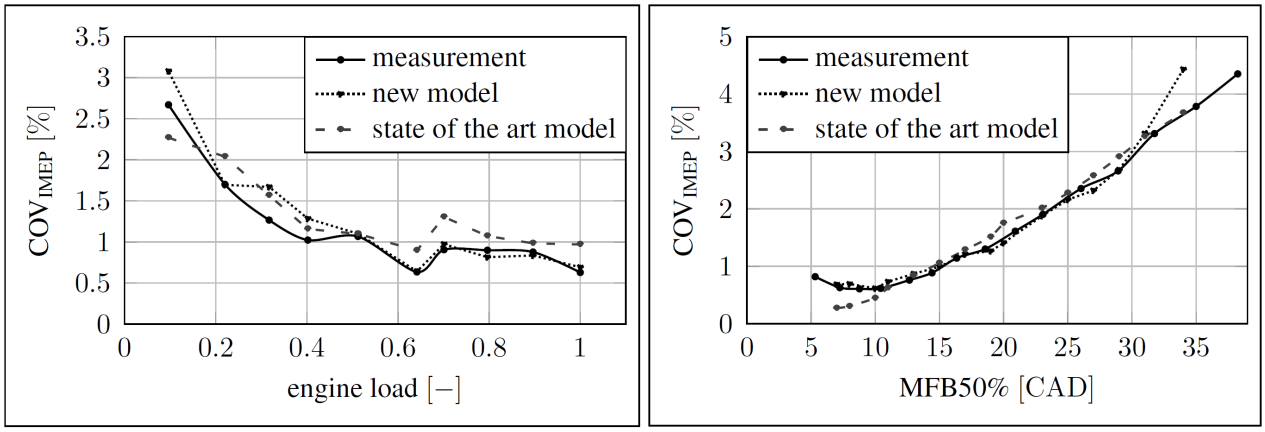

(a) VAR1. (b) VAR2.

Figure 6.1.: Comparison of the TT1.3 (320) engine load and *MFB50%* variations regarding CCV found by measurement, the new CCV model and the state-of-the-art model.

In (a) validation results are shown for the engine load variation. The new CCV model and the state-of-the-art CCV model are able to describe the COV_{IMEP} from the measurement well, with the new model slightly deviating at low loads and the state-of-the-art model for high engine loads. Thus, both models are able to predict CCV qualitatively and quantitatively for this load variation and its influence on the thermodynamic state.

Figure 6.1 (b) shows validation results for the *MFB50%* variation. Deviations in the center of combustion between the measurement data and the CCV models are due to a discrepancy in the predictive combustion calculation in the mean engine cycle. Both CCV models are able to match the increasing COV_{IMEP} with retarded *MFB50%* from the experiment well. The state-of-the-art model deviates with an early *MFB50%*, while the new CCV model deviates with a late center of combustion. Nevertheless, both models are in good agreement with measurements and can be expected to determine cyclic variability from this thermodynamical influence.

Figure 6.2 shows the variations VAR3 and VAR4.

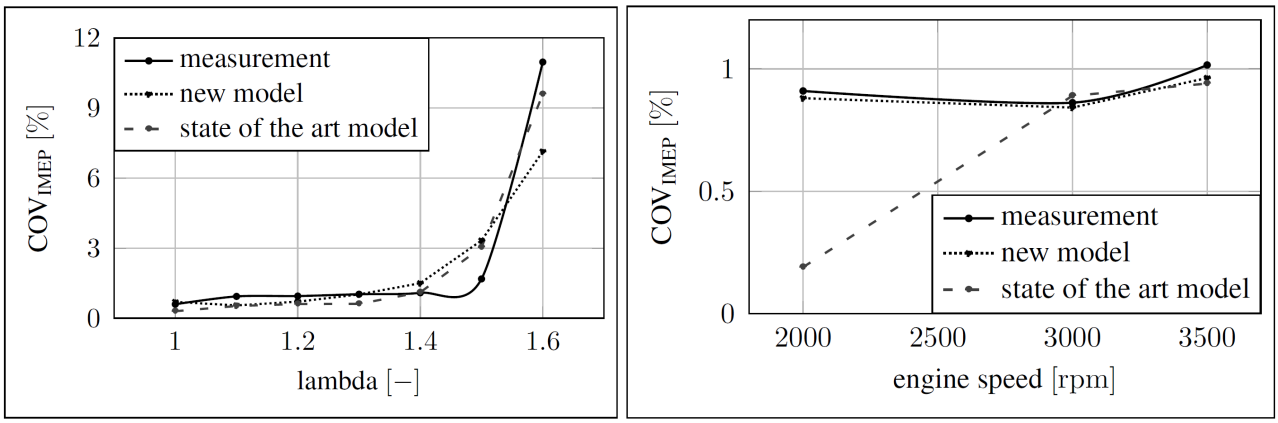

(a) VAR3. (b) VAR4.

Figure 6.2.: Comparison of the TT1.3 (320) λ and engine speed variations regarding CCV found by measurement, the new CCV model and the state-of-the-art model.

For the VAR3 variation in Figure 6.2 (a), it can be seen that the new CCV model is able to describe the COV_{IMEP} gathered from measurement slightly better up to a $\lambda = 1.4$ than the state-of-the-art model. This is the λ range, the combustion model is able to reflect the burn rate from experiments well. For leaner air-fuel mixtures the state-of-the-art CCV model matches the experimental CCV slightly better. At a $\lambda = 1.6$, two cycles misfired in the measurement. Neglecting these cycles, the COV_{IMEP} would be reduced to 6.1 %. However, for the last two engine operating points it has to be stated, that *MFB50%* in the mean engine cycle deviated more than +6 CAD. To conclude, both CCV models show qualitative and quantitative agreement with measurements up to $\lambda = 1.4$, while only qualitative reproduction can be confirmed for higher λ. Here, a better description of the mean cycle may yield improvement.

The engine speed variation in Figure 6.2 (b) is described well by the new CCV model. However, the state-of-the-art model underestimates the COV_{IMEP} at a low engine speed. It is obvious that it is not sufficient to only impose fluctuations on combustion parameters, i.e. laminar burn parameters, as implemented in the state-of-the-art CCV model for simulating cyclic combustion variations. As outlined in Chapter 2, the engine speed has an essential influence on the global and local flow fields. Hence, the design of the new CCV model regarding the implementation of local and global flow fluctuations shows its effectiveness.

The variation VAR5 of the *MFB50%* in combination with $\lambda = 1.4$ is shown in Figure 6.3.

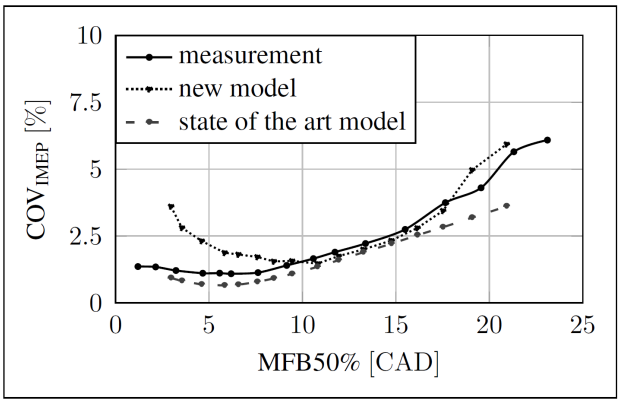

Figure 6.3.: Comparison of the TT1.3 (320) *MFB50%* variation with $\lambda = 1.4$ regarding CCV found by measurement, the new CCV model and the state-of-the-art model.

First, it can be seen that the experimental CCV from this *MFB50%* variation are on a higher level than for VAR2, which is due to the lean air-fuel mixture. The new CCV model overestimates the COV_{IMEP} for a very early center of combustion, but is a good match for the COV_{IMEP} found by measurement for *MFB50%* ≥ 6 CAD. On the

other hand, the state-of-the-art model underestimates the cyclic combustion variations from the experiment, but qualitatively matches the CCV. One reason for the overestimation of the new CCV model may be the increase in CCV seen for very early *MFB50%*, as described in 2.3.3.

The engine load variation VAR1 is investigated in more detail below. Coefficients of variations are shown for the maximum cylinder pressure, *MFB50%*, *MFB0%-MFB5%*, *MFB5%-MFB90%* and *MFB75%-MFB90%*. In Figures 6.4 - 6.6 below, these *COV* are illustrated.

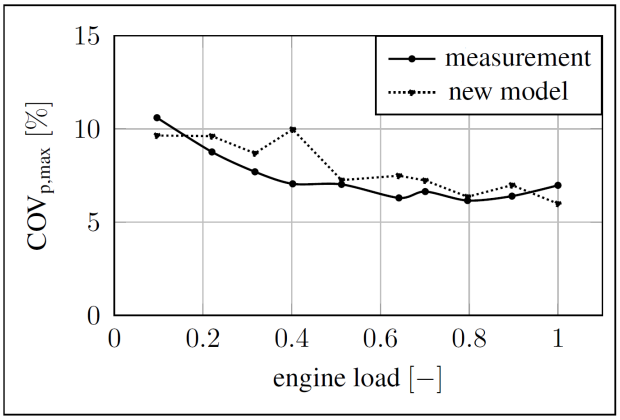

Figure 6.4.: Investigation of the TT1.3 (320) engine load variation regarding COV_{pmax} found by measurement and the new CCV model.

As can be seen, the new CCV model matches the $COV_{p,max}$ found by measurement both in quality and quantity. However, there is one outlier at an engine load of 0.4WOT, which can also be seen in Figure 6.5 (a).

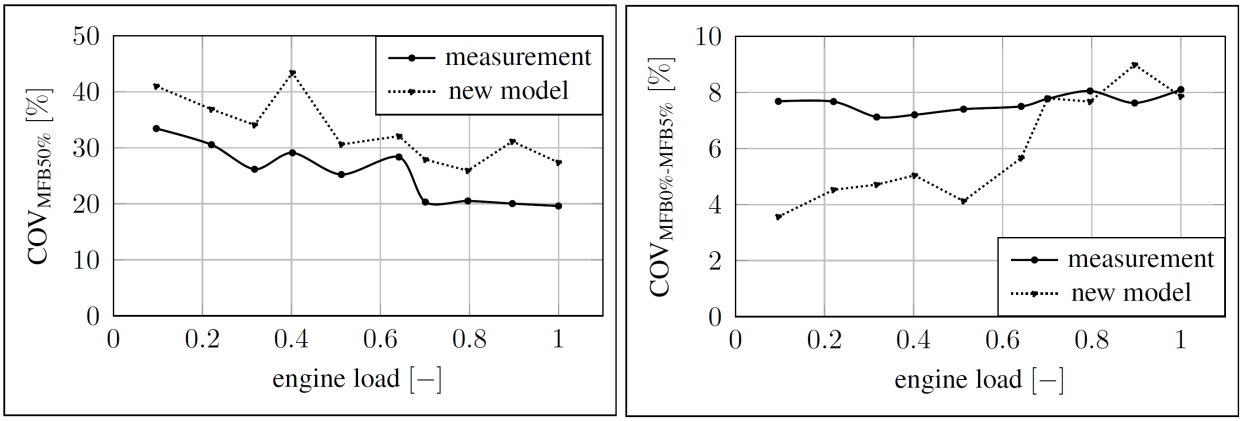

(a) $COV_{MFB50\%}$. (b) $COV_{MFB0\%\text{-}MFB5\%}$.

Figure 6.5.: Investigation of the TT1.3 (320) engine load variation regarding the $COV_{MFB50\%}$ and the $COV_{MFB0\%\text{-}MFB5\%}$ found by measurement and the new CCV model.

From this illustration, it is obvious that the $COV_{MFB50\%}$ qualitatively matches the CCV model overestimating this *COV*. On the right-hand side of Figure 6.5, the *COV* of the ignition delay is illustrated. Here, deviations at a low engine load can be found, whereas at high loads the *COV* is a good match.

The comparison of the $COV_{MFB5\%\text{-}MFB90\%}$ in Figure 6.6 (a) shows the greatest deviations; however, the qualitative trend is still met. Finally, in Figure 6.6 (b), it can be seen that the *COV* from the burn-off phase is matched very well by the CCV model.

Taking a more detailed look at the actual determination of the burn rate, the deviations can be traced back, first to the calculation of the mean cycle and, secondly, to the individual cycles. Here, the evaluation of statistics

comes into play. In the following, this is investigated by means of the engine operating points with engine loads WOT (EOP1) and 0.4WOT (EOP2) in Table 6.2.

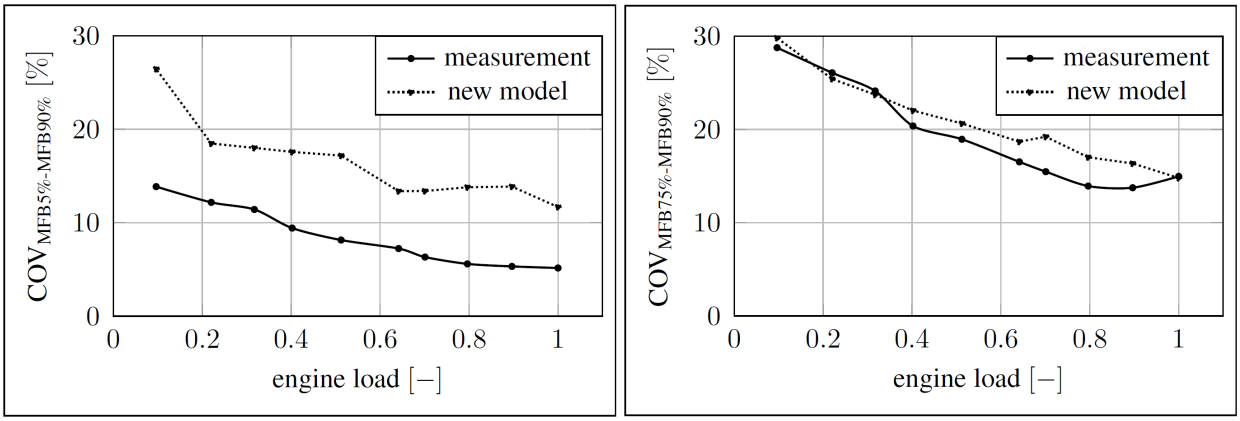

(a) $COV_{MFB5\%\text{-}MFB90\%}$. (b) $COV_{MFB75\%\text{-}MFB90\%}$.

Figure 6.6.: Investigation of the TT1.3 (320) engine load variation regarding the $COV_{MFB5\%\text{-}MFB90\%}$ and the $COV_{MFB75\%\text{-}MFB90\%}$ found by measurement and the new CCV model.

	unit	EOP1 Sim.	EOP1 Meas.	EOP2 Sim.	EOP2 Meas.
MFB5%	[CAD]	-5.8	-5.7.	-8.6	-7.0
MFB50%	[CAD]	8.9	7.5	6.5	6.6
MFB90%	[CAD]	25.6	19.8	23.2	20.4

Table 6.2.: Comparison of mean cycle mass burned fuel points for engine load 0.4WOT and WOT for the variation VAR1 of the TT1.3 (320).

MFB5%, *MFB50%* and *MFB90%* from the mean cycle simulation are compared to the measurement data. From this table, it is obvious that the early combustion, in particular, is very sensitive to the calculation of *COV*. That means that small mean cycle deviations of *MFB5%* have significant effects on the COV of the ignition delay. If the same standard deviation found by simulation were applied to the *MFB5%* found by measurement (EOP2), the $COV_{MFB5\%}$ would be 23 % lower, thus converging to the *COV* from the ignition delay.

Another way to illustrate cyclic combustion variability is using a frequency distribution. In Figures 6.7 - 6.9 three distributions are illustrated for the *MFB5%*, *MFB50%* and *MFB90%* of the engine operating points with engine loads WOT (EOP1) and 0.4WOT (EOP2), see Table 6.2.

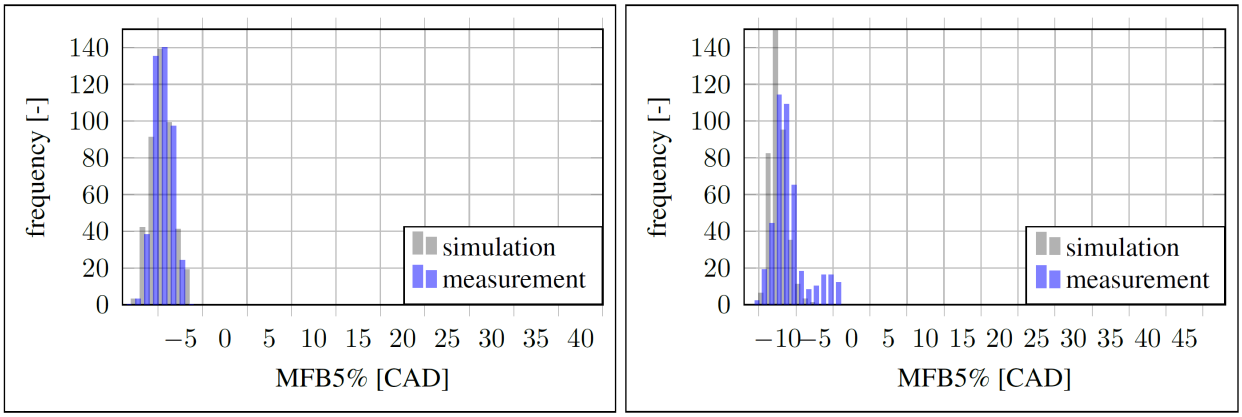

(a) EOP1 (WOT). (b) EOP2 (0.4WOT).

Figure 6.7.: Illustration of the *MFB5%* frequency distributions found by simulation and measurement for the TT1.3 (320) engine operating points EOP1 and EOP2.

The simulated and measured *MFB5%* of the operating point EOP1 in Figure 6.7(a) corresponds very well. First, this can be seen in the accurate match of the *MFB5%* in the mean cycle from Table 6.2. Secondly, this agreement can also be seen in Figure 6.5 (b), in which the $COV_{MFB0\%\text{-}MFB5\%}$ found by measurement is well matched by the simulation. The *MFB5%* of EOP2 is a good match; however, deviations can be seen. For earlier crank angles, the simulation has a higher frequency, whereas the measurement also shows later *MFB5%* which are not reproduced by the simulation. This discrepancy is again visible in the deviation of the mean *MFB5%* in Table 6.2 and for the $COV_{MFB0\%\text{-}MFB5\%}$ in Figure 6.5 (b).

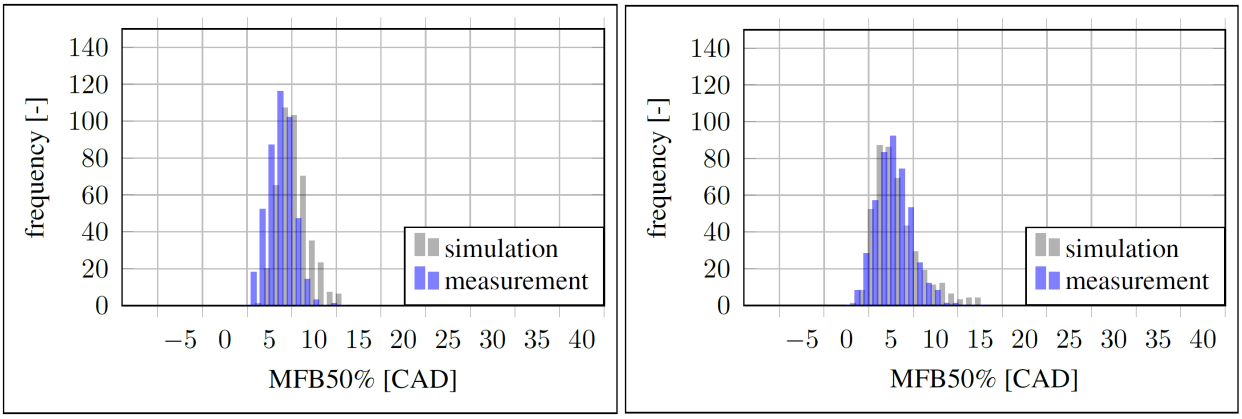

(a) EOP1 (WOT). (b) EOP2 (0.4WOT).

Figure 6.8.: Illustration of the *MFB50%* frequency distributions found by simulation and measurement for the TT1.3 (320) engine operating points EOP1 and EOP2.

In the frequency distribution for the *MFB50%* of operating point EOP1 (Figure 6.8 (a)), a good correspondence can be seen between the measurement and simulation data. The distribution of the simulation is shifted to later centers of combustion. Since the mean *MFB50%* is slightly higher for the simulation, this means that the standard deviation is disproportionally higher; thus the $COV_{MFB50\%}$ found by simulation is 20 % higher than for the measurement. The simulated and measured *MFB50%* distribution for EOP2 in Figure 6.8 (b) corresponds well. The mean *MFB50%* is matched; however, as seen in Figure 6.5 (a) the $COV_{MFB50\%}$ is higher for the simulation. This can be explained by the low frequency in the simulation towards a center of combustion around 10 - 13 CAD.

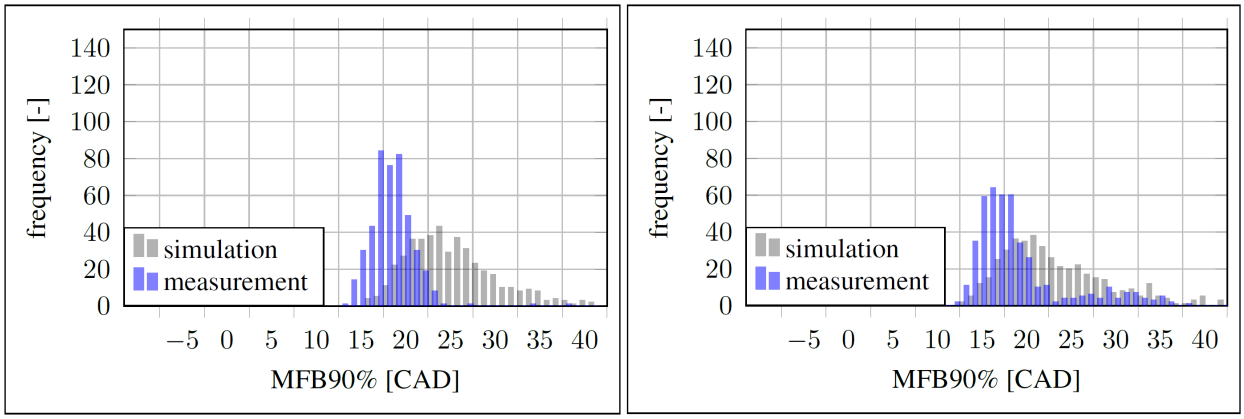

(a) EOP1 (WOT). (b) EOP2 (0.4WOT).

Figure 6.9.: Illustration of the *MFB90%* frequency distributions found by simulation and measurement for the TT1.3 (320) engine operating points EOP1 and EOP2.

The *MFB90%* frequency distributions for both engine operating points show similar behavior. First, it can be seen that the measurement distributions are located earlier in the crank angle degree, which corresponds with the mean engine cycle in Table 6.2. Secondly, the measurement distributions are narrower than the simulation

ones. However, for both engine operating points, the $COV_{MFB75\%\text{-}MFB90\%}$ are matched in Figure 6.6. The reason is that although the mean *MFB90%* is earlier in the measurement, the standard deviation is also smaller.

By means of the new CCV model, the discussed engine TT1.3 (320) shows sufficiently good correspondence regarding simulated and experimental COV_{IMEP}. It is shown that the newly designed CCV model is able to describe CCV from different engine parameter variations regarding engine speed, load, *MFB50%* and λ. Furthermore, it is shown that the underlying combustion is predicted well in the first half regarding the mean cycle as the requirement for CCV simulation. Then, it is demonstrated that the fluctuations produced by the new CCV model indicate a good correspondence with the fluctuating combustion from the experiment.

6.2 Validation on TT1.3 (400)

After the verification of the newly developed CCV model, it is validated on further investigated engines. The first is similar to the design engine, in that it has an expanded Miller intake cam shaft, i.e. the Miller degree is smaller. This engine is investigated regarding variations in the engine speed, engine load and *MFB50%*, analyzing the COV_{IMEP}. Again, the new CCV model is compared to measurement data and simulation results from the CCV model which is considered state of the art [127]. The state-of-the-art CCV model is adjusted once for this engine with its two parameters, available for calibration. Here, for the TT1.3 (400), the flame kernel growth multiplier is adjusted slightly in comparison with the calibration parameters from the TT1.3 (320). In contrast, the CCV model from this study is applied just as designed.

Table 6.3 below gives an overview of the variations, used for the comparison. Note that this engine, due to its smaller Miller intake cam shaft and thus later IVC, achieves a higher cylinder charge. This increases the risk of engine knock at WOT, therefore the engine load and speed variations can not be operated with an optimal center of combustion.

engine parameter	unit	VAR1	VAR2	VAR3	VAR4	VAR5
engine speed	[rpm]	3000	3000	3000	2000	variable
engine load	[-]	variable	variable	WOT	0.5WOT	WOT
MFB50%	[CAD]	15	14	variable	variable	27
λ	[-]	1	1.3	1	1	1

Table 6.3.: Engine parameter variations for the model validation on the TT1.3 (400).

The engine load variations VAR1 and VAR2 are displayed in Figure 6.10.

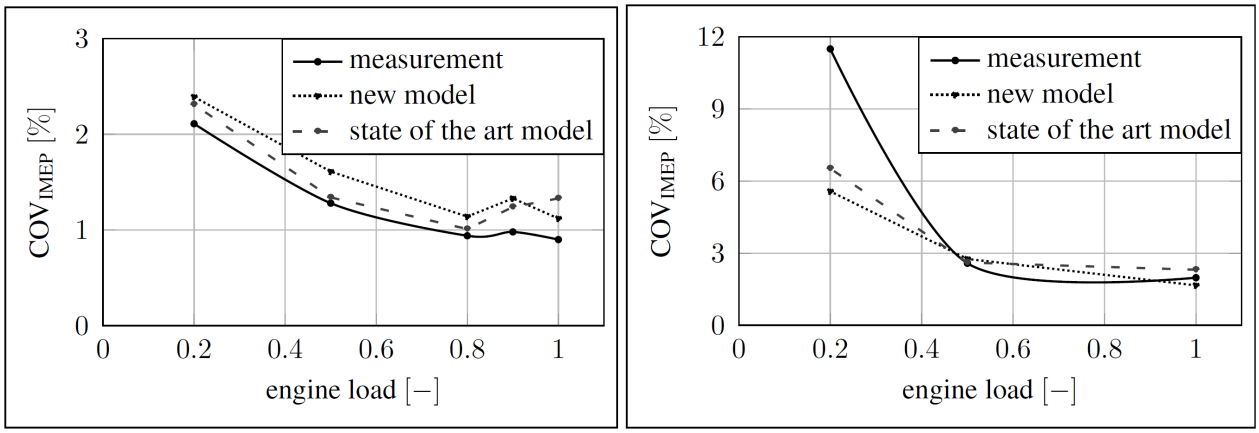

(a) VAR1.

(b) VAR2.

Figure 6.10.: Comparison of the TT1.3 (400) engine load at $\lambda = 1$ and 1.3 regarding COV_{IMEP} found by measurement, the new CCV model and the state-of-the-art model.

The first engine load variation in Figure 6.10 (a) shows an increasing COV_{IMEP} towards a decreasing load. For the 0.5WOT and 0.2WOT load points, the EGR is at 4.0 % and 6.5 %, respectively, whereas the other operating points have an EGR of 3.0 %. It can be seen that the newly designed CCV model is able to follow the qualitative trend of the measurement data. However, an overestimation can be seen of about 20 % for high engine loads and of about 10 % for low engine loads. The state-of-the-art model, including the model adjustment, slightly better describes the experimental COV_{IMEP}.

The validation results for the lean engine load variation in Figure 6.10 (b) indicate that for a $\lambda = 1.3$, the cyclic combustion variations are considerably higher in comparison with the variation from (a). The lean load variation indicates a good agreement between the measurement data and simulation results from both the new as well as the state-of-the-art CCV model for the WOT and 0.5WOT operating points. However, the lowest engine load operating point shows a large deviation regarding the measurement data. This is due to the fact that the 0.2WOT engine operating point has one complete misfired cycle and several cycles with incomplete combustion in the measurement data. If these cycles were not included in the calculation of the COV_{IMEP}, the value would be cut in half, thus the COV_{IMEP} would be matched considerably better.

Both *MFB50%* variations VAR3 and VAR4 are illustrated in Figure 6.11.

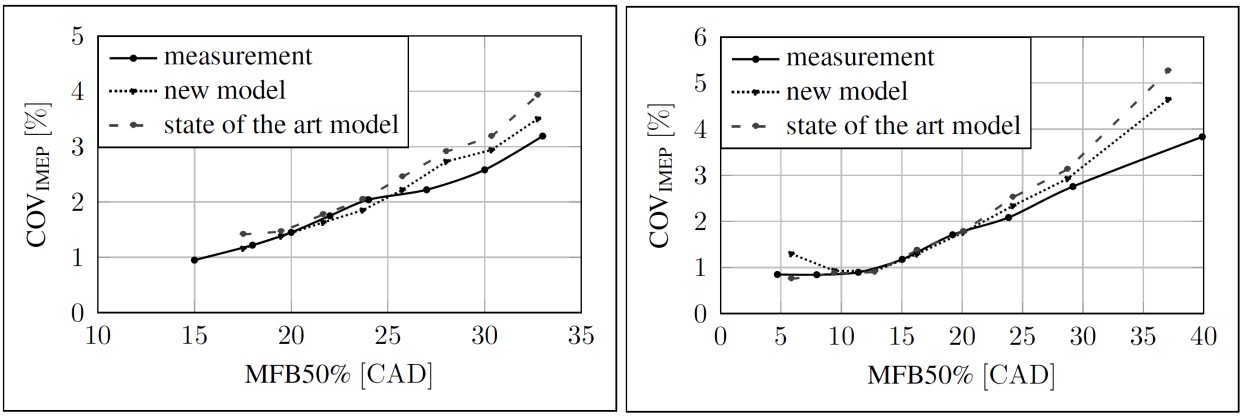

(a) VAR3. (b) VAR4.

Figure 6.11.: Comparison of the TT1.3 (400) *MFB50%* variation at 3000 rpm WOT and 2000 rpm 0.5WOT regarding COV_{IMEP} found by measurement, the new CCV model and the state-of-the-art model.

On the left-hand side of Figure 6.11, the *MFB50%* variation of the stoichiometric 3000 rpm WOT engine operating points is displayed. The difference between the simulated and measured *MFB50%* is due to the deviations in the mean cycle calculations. Nevertheless, it can be seen that the new CCV model matches the COV_{IMEP} gathered from the measurement well, with slight deviations for *MFB50%* > 25 CAD. The state-of-the-art model shows greater deviations, also for *MFB50%* > 25 CAD.

Figure 6.11 (b) presents the stoichiometric 2000 rpm 0.5WOT variation in the center of combustion. Here, it is obvious that the newly designed model has insignificant deviations for early and very late *MFB50%*, whereas the state-of-the-art CCV model shows greater deviations at late centers of combustion.

Note that *MFB50%* > 25 CAD are usually not applied to serial production engines.

The last variation investigated concerning the engine speed is illustrated in Figure 6.12.

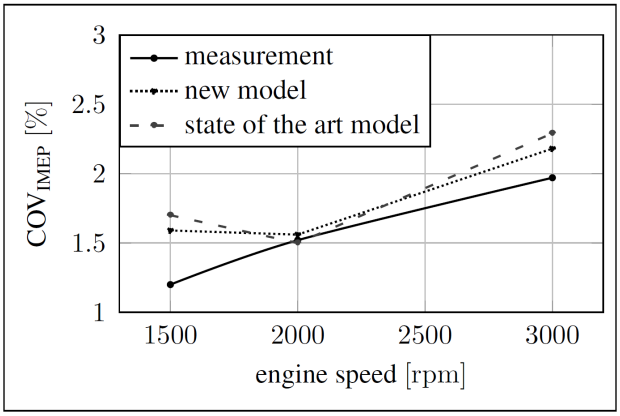

Figure 6.12.: Comparison of the TT1.3 (400) engine speed variation regarding COV_{IMEP} found by measurement, the new CCV model and the state-of-the-art model.

The new CCV model overestimates the 1500 rpm operating point by 33 % and also overestimates the 3000 rpm operating point. Both engine operating points are overestimated more by the state-of-the-art model. However, with the background that the *MFB50%* is at 27 CAD in the mean engine cycle, the deviations can be correlated with the deviations found in the *MFB50%* variations from Figure 6.11.

A more detailed analysis is carried out regarding variation VAR3, in order to investigate the physical functioning of the new CCV model more thoroughly. Therefore, Figure 6.13 shows the coefficient of variation for the *MFB50%* and ignition delay. As can be seen from Figure 6.13 (a), the $COV_{MFB50\%}$ is matched qualitatively. How-

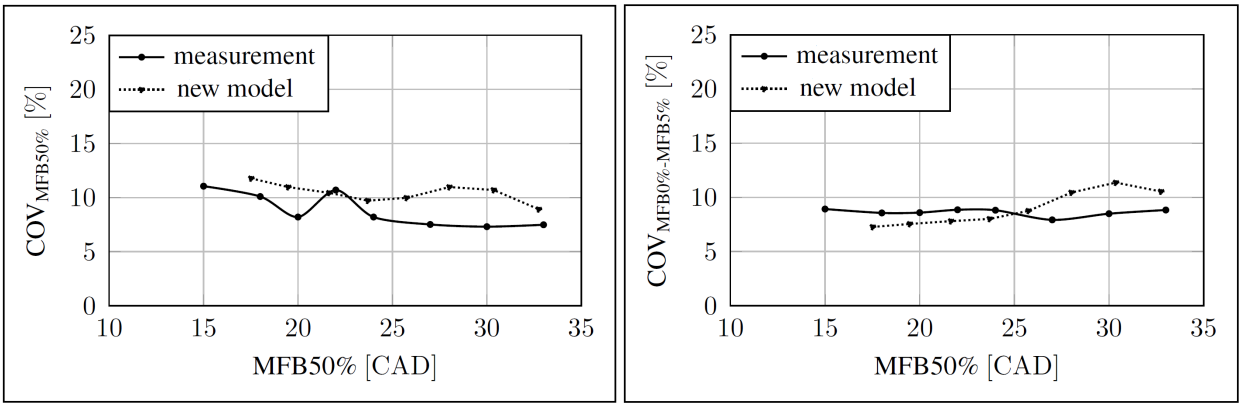

(a) $COV_{MFB50\%}$.

(b) $COV_{MFB0\%\text{-}MFB5\%}$.

Figure 6.13.: Investigation of the TT1.3 (400) *MFB50%* variation regarding $COV_{MFB50\%}$ and $COV_{MFB0\%\text{-}MFB5\%}$ found by measurement and the new CCV model.

ever, there is an overestimation with quantitative deviations of up to 33 %. The *COV* of the ignition delay on the right-hand side also shows deviations, especially for *MFB50%* > 25 CAD. This also correlates with the overestimation of the COV_{IMEP} in this area. Figure 6.14 (a) shows the coefficient of variation of the *MFB5% - MFB90%* combustion duration. The qualitative trend is reproduced well; however, the new model overestimates the *COV* found by measurement. Figure (b) presents the $COV_{MFB75\%\text{-}MFB90\%}$. Here, in contrast, the simulation underestimates the *COV* found by measurement, but the tendency is still correct.

Summing up, it can be said for the validation of the TT1.3 (400) that the new CCV model is able to predictively describe the cyclic combustion variations found by measurement. Against the background that the new CCV model was not adjusted for this engine, the simulation results can be classified as established.

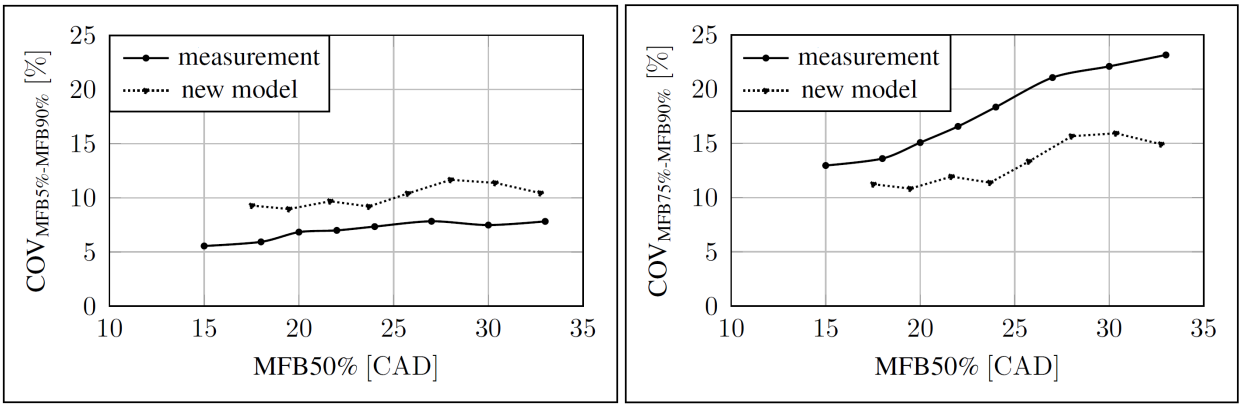

(a) $COV_{MFB5\%\text{-}MFB90\%}$. (b) $COV_{MFB75\%\text{-}MFB90\%}$.

Figure 6.14.: Investigation of the TT1.3 (400) *MFB50%* variation regarding the $COV_{MFB5\%\text{-}MFB90\%}$ and the $COV_{MFB75\%\text{-}MFB90\%}$ found by measurement and the new CCV model.

6.3 Validation on TT1.2

The next engine used for validation is the TT1.2, with a short geometric compression stroke and a long expansion stroke. This engine is investigated concerning variations in the engine speed, engine load and *MFB50%*, analyzing the COV_{IMEP}. Again, the new CCV model is compared to measurement data and the state-of-the-art model. The latter is adjusted once for the TT1.2 with its two calibration parameters. The calibrated parameters are the same as chosen for the TT1.3 (400). In turn, the new CCV model is applied just as designed.

Table 6.4 below gives an overview of the engine parameter variations used for the comparison.

engine parameter	unit	VAR1	VAR2	VAR3
engine speed	[rpm]	3000	variable	3000
engine load	[-]	variable	WOT	WOT
MFB50%	[CAD]	10	17	variable
λ	[-]	1	1	1

Table 6.4.: Engine parameter variations when validating the model on the TT1.2.

In Figure 6.15, the engine load and speed variation are shown. On the left, it can be seen that neither the new

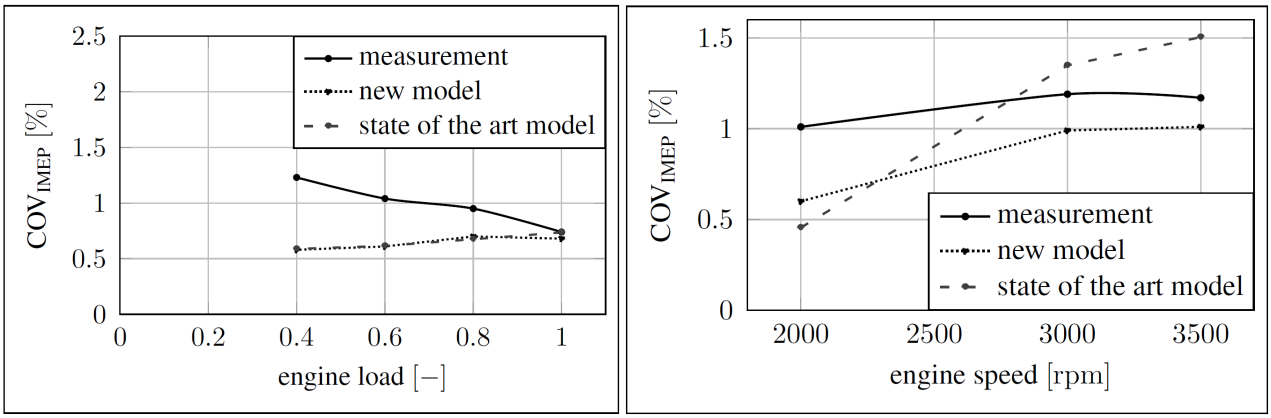

(a) VAR1. (b) VAR2.

Figure 6.15.: Comparison of the TT1.2 engine load and speed variation regarding COV_{IMEP} found by measurement, the new CCV model and the state-of-the-art model.

CCV model nor the state-of-the-art CCV model are able to match the engine load trend from the measurement. However, the WOT operating point is matched for both models. For this variation the *MFB5%*, *MFB50%* and *MFB90%* are accurately simulated for the WOT point in the mean cycle. *MFB5%* and *MFB50%* are also evaluated precisely for the other engine loads; however, the difference of the *MFB90%* increases as the load decreases. The highest deviation of 7 CAD is accounted for by the 0.4WOT point in the mean cycle. This finding is analyzed in detail below in Section 6.4 at a similar case for another engine.

The engine speed variation VAR2 is displayed in Figure 6.15 (b). For this variation, the new CCV model is able to qualitatively follow the COV_{IMEP} found by the measurement, with maximum deviations of 33 % at 2000 rpm. In contrast, the state-of-the-art CCV model overestimates the quality of the COV_{IMEP} trend found by the measurement. Here, an underestimation of CCV is found for a low engine speed, and an overestimation for high engine speeds.

The third variation investigated regarding the center of combustion is displayed in Figure 6.16. The deviations in the measured and simulated results for *MFB50%* are again due to differences in the mean cycle calculations. From this illustration, it can be seen that the new CCV model is able to reproduce the COV_{IMEP} from the mea-

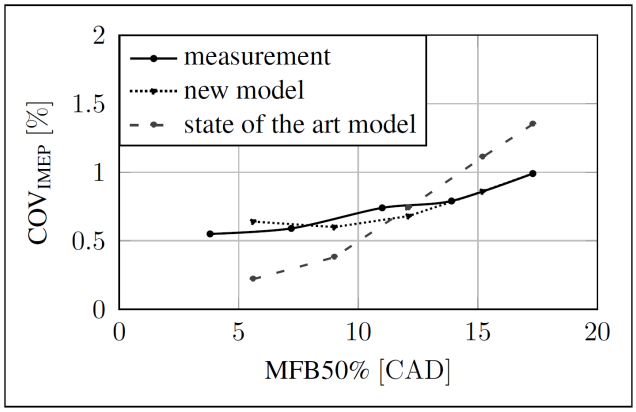

Figure 6.16.: Comparison of the TT1.2 *MFB50%* variation regarding COV_{IMEP} found by measurement, the new CCV model and the state-of-the-art model.

surement in terms of quality and quantity. In contrast, the state-of-the-art model underestimates CCV at early *MFB50%* and overestimates them at a late center of combustion. The underlying combustion variability is investigated in more detail in Figures 6.17 and 6.18. As can be seen from Figure 6.17 (a) the $COV_{MFB50\%}$ is matched

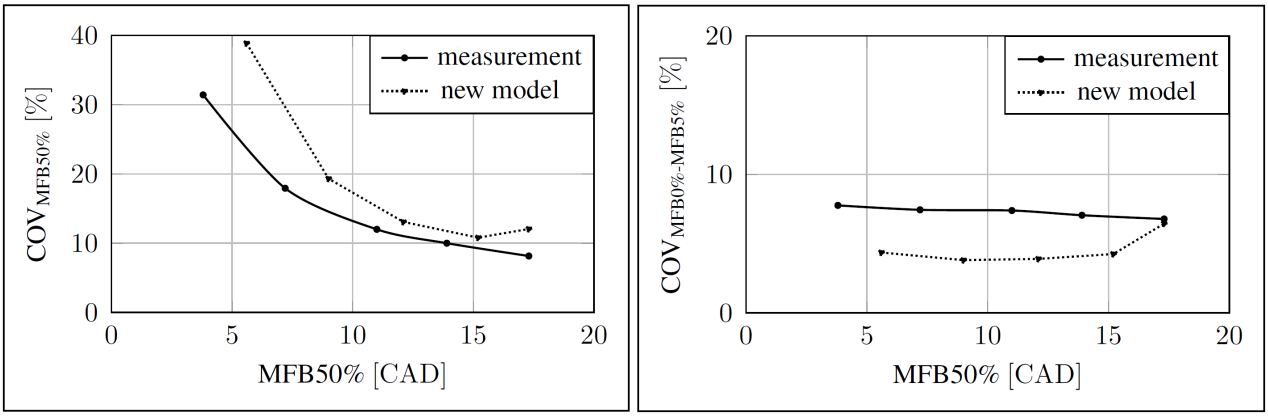

(a) $COV_{MFB50\%}$. (b) $COV_{MFB0\%\text{-}MFB5\%}$.

Figure 6.17.: Investigation of the TT1.2 *MFB50%* variation regarding $COV_{MFB50\%}$ and $COV_{MFB0\%\text{-}MFB5\%}$ found by measurement and the new CCV model.

qualitatively. However, there is an overestimation with quantitative deviations for early *MFB50%*. The *COV* of the ignition delay on the right-hand side also shows quantitative deviations, but the qualitative trend is still

matched.

In Figure 6.18, the *COV* from the burn duration and burn-off phase show qualitative and quantitative disagreement, with an overestimation in the case of the simulation results, in particular, for early *MFB50%*.

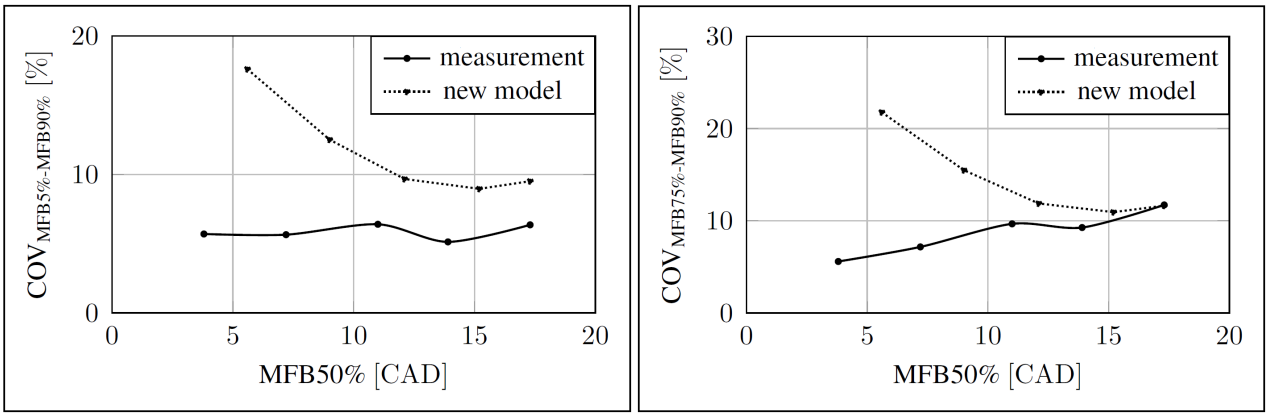

(a) $COV_{MFB5\%\text{-}MFB90\%}$. (b) $COV_{MFB75\%\text{-}MFB90\%}$.

Figure 6.18.: Investigation of the TT1.2 *MFB50%* variation regarding $COV_{MFB5\%\text{-}MFB90\%}$ and $COV_{MFB75\%\text{-}MFB90\%}$ found by measurement and the new CCV model.

Here, it should be noted that deviations regarding the mean cycle *MFB90%* again occur. These deviations are higher, the earlier the *MFB50%* is. Overall, it seems that the underestimation of the *COV* of the ignition delay and the overestimation of the *COV* from the burn duration and burn-off phase are compensated for, and there is still a correct description of COV_{IMEP}. With the assumption that the *MFB90%* is also matched quantitatively, it is supposed that the COV_{IMEP} would then be underestimated in the simulation, as the $COV_{MFB0\%\text{-}MFB5\%}$ indicates.

Summing up for the TT1.2 engine, the validation regarding the engine speed and *MFB50%* variations delivers good results from the new CCV model. However, a weakness is found for the illustration of the engine load variation, in which neither the quality nor the quantity of the COV_{IMEP} matched. Greater deviations can be seen for the state-of-the-art model in all three engine parameter variations; hence, it can be stated, that the new uncalibrated CCV model is still more advanced.

6.4 Validation on B48 with serial pistons

For the B48 engine with serial pistons, the most extensive measurement data basis is available regarding a complete engine map and different engine parameter variations. The new CCV model is applied as designed and the state-of-the-art CCV model calibrated to best match the measurements globally. The fluctuation level on the laminar burning velocity is the same as for the engines from above, while the enforced fluctuations on the initial flame kernel growth multiplier are increased by 20 %.

First, a complete engine map is depicted. This engine map includes engine operating points with a varying intake valve lift and intake and exhaust valve timings. Furthermore, the center of combustion is retarded for high engine loads due to the risk of knock. At high engine speeds and loads the air-fuel mixture is rich, in order to limit the exhaust gas temperatures. At low engine loads, a high valve overlap strategy is implemented, reducing gas exchange losses. Thus, the engine map shows a variety of engine parameter variations. At first, the engine map from the simulation shows results with an uncalibrated turbulence model (this turbulence model is based on the B48 predecessor engine). Then, the simulation results including the calibrated turbulence model are illustrated. This shows the need to calibrate the turbulence model. Figure 6.19 presents the COV_{IMEP} from the measurement data and Figure 6.20 the COV_{IMEP} from the simulation with the new CCV model including the uncalibrated underlying turbulence model.

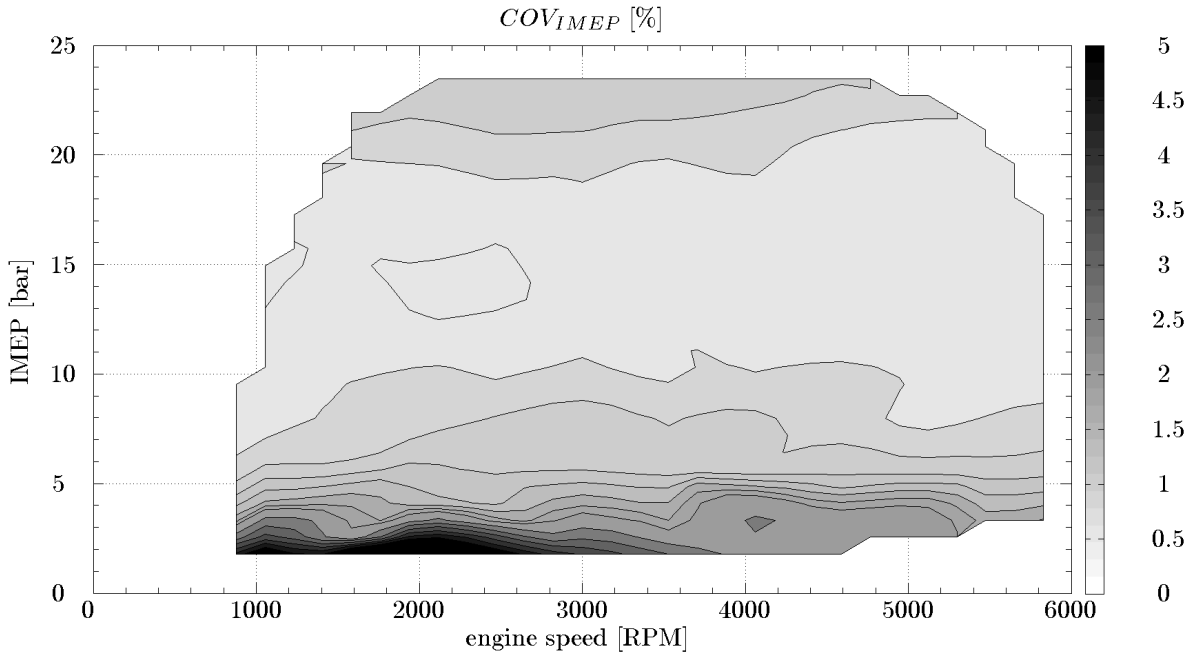

Figure 6.19.: B48 engine map of COV_{IMEP} from the measurement.

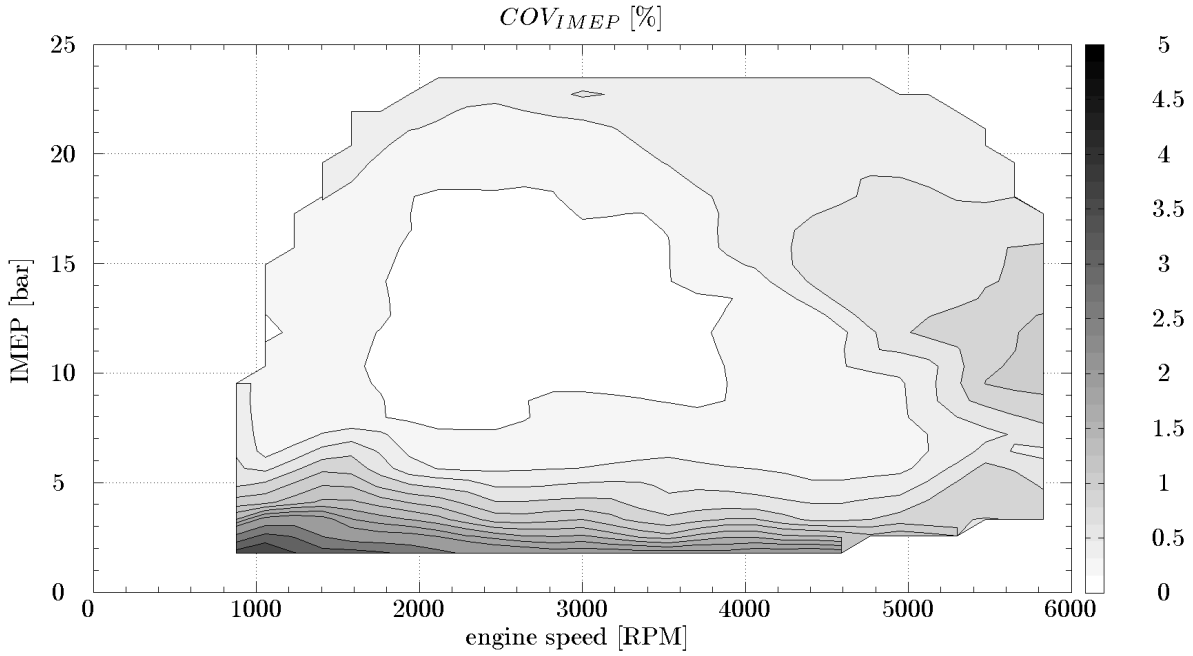

Figure 6.20.: B48 engine map of COV_{IMEP} from the simulation with the new CCV model and the uncalibrated turbulence model.

Comparing the engine maps from Figures 6.19 and 6.20, the qualitative agreement is obvious. However, three areas with quantitative differences can be identified. The first is found when the engine is at full load. Differences in the COV_{IMEP} are as high as 0.5 % absolute, resulting from deviations in the calculation of the mean cycle *MFB50%*. Here, the simulation evaluates slightly earlier centers of combustion. At a high engine speed in the mid-range engine load, the simulation calculates higher cyclic combustion variations. This is also due to differences in the mean cycle *MFB50%*, in which virtual *MFB50%* are later than the experimental data. The third area with deviations is found in the mid-range engine map. Absolutely, the differences are around 0.4 %. However, this virtual underestimation correlates to a factor of up to four. The cause is an overestimation of the

MFB90% when simulating the mean cycle. The difference between the measurement and the simulation can be improved by calibrating the turbulence model and thus better matching the turbulent kinetic energy.

The underestimation of the COV_{IMEP} in the mid-range engine map is investigated in more detail for the engine operating point 3000 rpm, *IMEP* = 14 bar and $\lambda = 1$ in Table 6.5. In this table, the mean cycle mass fuel burned at different crank angles and the specific corresponding *IMEP*, are listed together with the particular *COV*. Measurement data is abbreviated as Meas and the simulation with the new CCV model Sim1. Additionally, the simulative cases Sim2 - Sim4 are displayed, in which the mean cycle combustion is manually retarded to better match the measurement data. Two combustion model calibration factors are used for retarding: c_{Ex}, weighting the expansion factor, and C_{burn}, scaling the characteristic burning time.

output	unit	Meas	Sim1	Sim2	Sim3	Sim4
$IMEP_{MFB5\%}$	[bar]	-3.4	-3.2	-3.2	-3.2	-3.2
$IMEP_{MFB50\%}$	[bar]	-3.1	-3.1	-3.0	-2.9	-2.7
$IMEP_{MFB60\%}$	[bar]	-2.9	-3.0	-2.8	-2.6	-2.3
$IMEP_{MFB70\%}$	[bar]	-2.6	-2.7	-2.4	-2.2	-1.8
$IMEP_{MFB80\%}$	[bar]	-1.1	-2.4	-1.8	-1.5	-1.0
$IMEP_{MFB90\%}$	[bar]	5.6	-1.7	-0.9	-0.5	0.1
IMEP	[bar]	14.0	14.0	14.0	14.0	13.9
MFB5%	[CAD]	-1.9	-2.7	-2.7	-2.0	-1.1
MFB50%	[CAD]	7.5	4.7	6.4	7.9	9.7
MFB60%	[CAD]	9.0	6.6	8.9	10.5	12.4
MFB70%	[CAD]	11.3	8.8	11.7	13.4	15.4
MFB80%	[CAD]	18.2	11.4	15.0	16.8	18.9
MFB90%	[CAD]	51.0	14.7	19.1	21.1	23.4
$COV_{IMEP,\,MFB5\%}$	[%]	0.73	0.72	0.74	0.55	0.4
$COV_{IMEP,\,MFB50\%}$	[%]	6.1	1.0	2.1	2.7	3.7
$COV_{IMEP,\,MFB60\%}$	[%]	8.7	2.1	4.4	5.4	7.1
$COV_{IMEP,\,MFB70\%}$	[%]	15.1	4.0	9.0	11.0	14.5
$COV_{IMEP,\,MFB80\%}$	[%]	119.8	8.1	19.4	25.4	38.0
$COV_{IMEP,\,MFB90\%}$	[%]	12.1	15.5	51.4	94.7	559.7
$\boldsymbol{COV_{IMEP}}$	[%]	**0.59**	**0.15**	**0.33**	**0.44**	**0.50**
$COV_{MFB5\%}$	[%]	68.1	50.5	53.2	72.8	115.8
$COV_{MFB50\%}$	[%]	23.4	11.5	12.1	11.0	8.6
$COV_{MFB60\%}$	[%]	20.8	9.9	11.1	10.4	8.2
$COV_{MFB70\%}$	[%]	19.5	9.5	11.0	10.3	8.2
$COV_{MFB80\%}$	[%]	29.7	9.6	11.2	10.5	8.5
$COV_{MFB90\%}$	[%]	12.9	9.8	11.6	11.0	9.1

Table 6.5.: Detailed investigation of the B48 engine operating point 3000 rpm, $IMEP = 14$ bar and $\lambda = 1$, regarding cyclic combustion variations between measurement and simulation.

From this table, it is obvious that the measured and simulated mean cycle *IMEP* (for the entire cycle), *MFB5%* and *MFB50%* match within the defined limits from Chapter 4. However, the burn-off phase shows significant deviations, thus the *IMEP* at the different *MFB* also deviates. The $IMEP_{MFBxx\%}$ at different *MFBxx%* is calculated by the integration of the pressure-volume diagram starting at -74 CAD up to the specific *MFB*. The COV_{IMEP} found by measurement is strongly underestimated with the new CCV model. If the mean cycle combustion and, in particular, the second half of the burn rate are retarded by adjusting the combustion model calibration parameters, the *COV* of the mass fuel burned and the *IMEP*, both throughout the cycle and at particular crank angles, are explicitly better matched. Therefore, it should be stated that it is important not only to accurately calculate the first half of the burn rate for CCV simulations, but also the burn-off phase. With the general calculation of the *IMEP* in mind, deviations in these specific *MFB* crank angle degrees strongly determine the cylinder pressure. If the combustion has already ended shortly after FTDC, the cylinder volume is still small. For late *MFB90%* the piston has already cleared a greater cylinder volume, thus small cyclic fluctuations in the

MFB90% have stronger effects on the *IMEP* due to the higher cylinder-volume-to-cylinder-pressure correlation.

To explain the need to calibrate the turbulence model, Figure 6.21 shows the engine map for the COV_{IMEP} from the simulation with the new CCV model and the calibrated turbulence model.

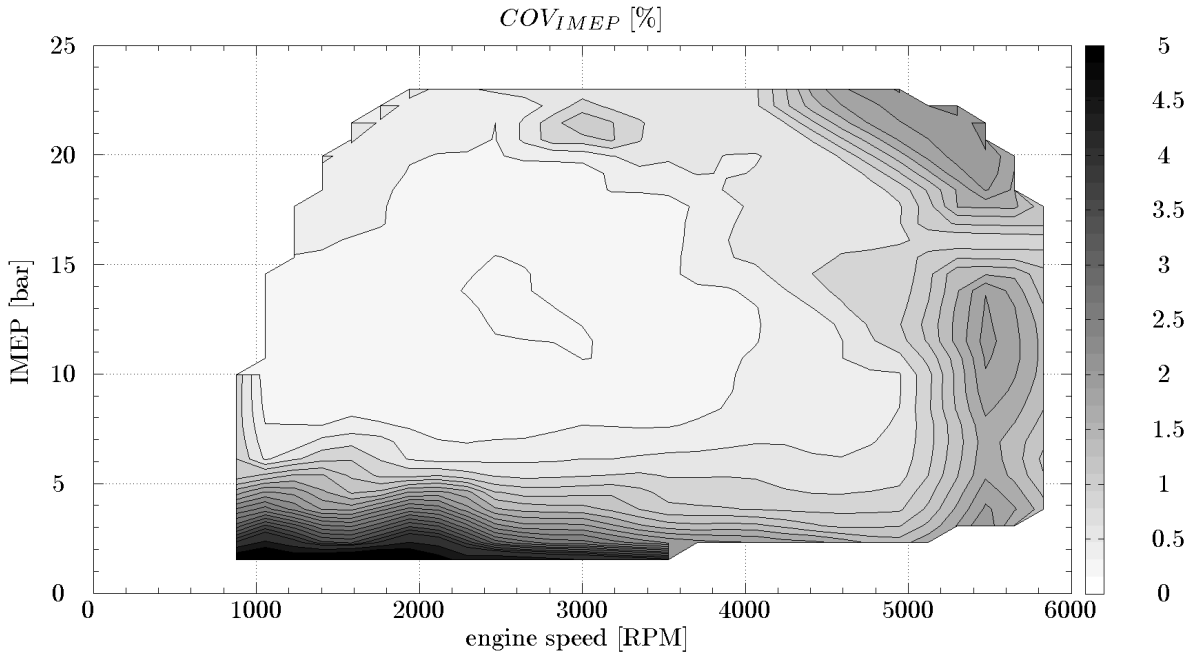

Figure 6.21.: B48 engine map of COV_{IMEP} from the simulation with the new CCV model and the calibrated turbulence model.

As can be seen, the differences in COV_{IMEP} are reduced at high engine loads and in the mid-range speed and load area in comparison with the virtual engine map from Figure 6.20. However, at high engine speeds, the mean cycle virtual *MFB50%* is underestimated more, see also Figure 4.13, thus overestimating the COV_{IMEP} even more. In this map area the TKE might be underestimated in the mean cycle simulation, thus resulting in an excessively slow transition from laminar to turbulent combustion.

The B48 engine map from the simulation with the state-of-the-art CCV model is displayed in Figure 6.22. This map exhibits some different results in comparison to the measurement data. Qualitative and quantitative agreement is only found for the mid-range as well as high speed and load map area. First, the cyclic combustion variations in the map area at low engine speeds and loads are quantitatively underestimated. The mid-range COV_{IMEP} is matched better than it is by the new CCV model. However, at high engine speeds and low loads, the state-of-the-art CCV model strongly overestimates the COV_{IMEP}. This is due to its implementation of engine speed dependence, which intensifies the CCV with increasing speed. The difference between the measurement and the state-of-the-art model at high engine speeds and mid-range engine loads has the same background as for the new CCV model. In this map area, the *MFB50%* is underestimated in the mean cycle. At full load, the state-of-the-art CCV model shows agreement with the measurement, slightly overestimating the COV_{IMEP}. At the full load curve, the engine speed dependence can also be seen again.

For further comparison, engine maps are calculated showing the absolute and relative deviations of COV_{IMEP} in the experiment and simulation for both CCV models, attached in Appendix F.

With the findings from above in mind, the engine parameter variations investigated are shown below, including the results from the state-of-the-art model. These comprise variations in the engine speed, load, *MBF50%*, λ, EGR, fluid mechanics and boost pressure. Table 6.6 provides an overview of the parameter variations, used for the comparison. Note that the calibrated turbulence model is also used for the engine parameter variations.

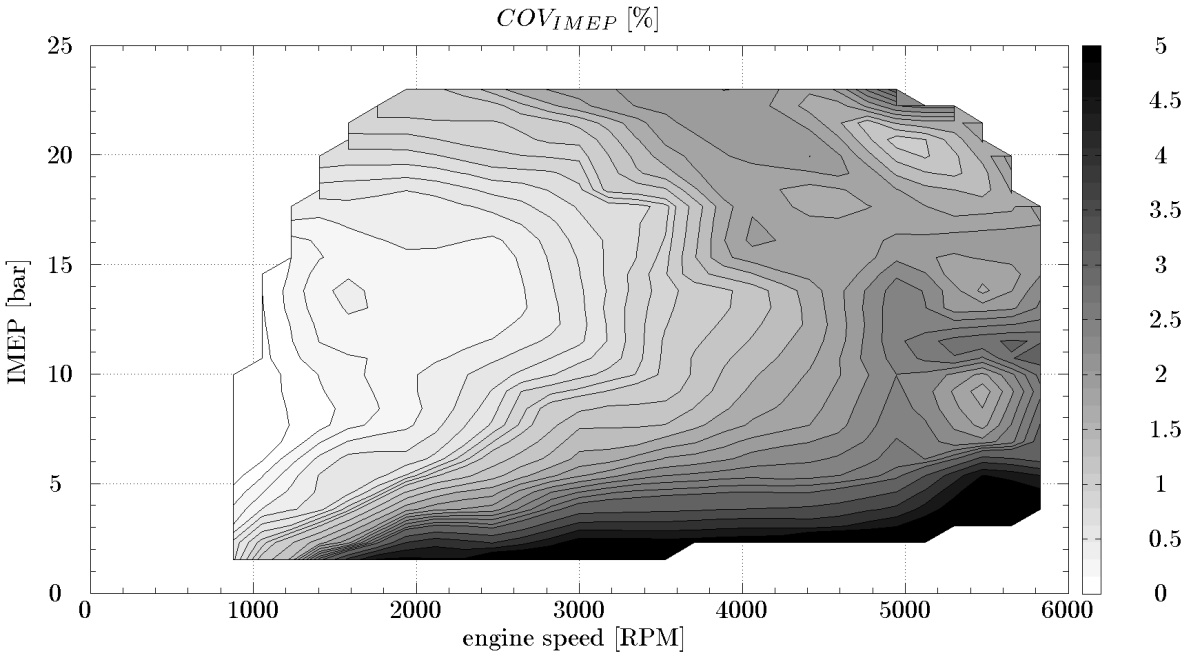

Figure 6.22.: B48 engine map of COV_{IMEP} from the simulation with the state-of-the-art CCV model.

parameter	unit	VAR1	VAR2	VAR3	VAR4	VAR5	VAR6	VAR7
speed	[rpm]	variable	1500	1500	3000	1500	3000	3000
load	[-]	0.2WOT	0.2WOT	0.2WOT	variable	0.5WOT	0.2WOT	0.5WOT
MFB50%	[CAD]	10	8	variable	8	8	8	8
λ	[-]	1	1	1	1	variable	1	1
EVT	[CAD]	80	variable	75	90	100	variable	110
IVT	[CAD]	65	75	55	90	80	variable	110
IVL	[mm]	4.0	3.0	3.3	8.4	1	5.0	variable

[1]EVT: exhaust valve timing, IVT: intake valve timing, IVL: intake valve lift

Table 6.6.: Engine parameter variations for the model validation of the B48 engine with serial pistons.

Figure 6.23 presents the variations in the engine speed and residual gas rate. As shown in Figure 6.23 (a), the

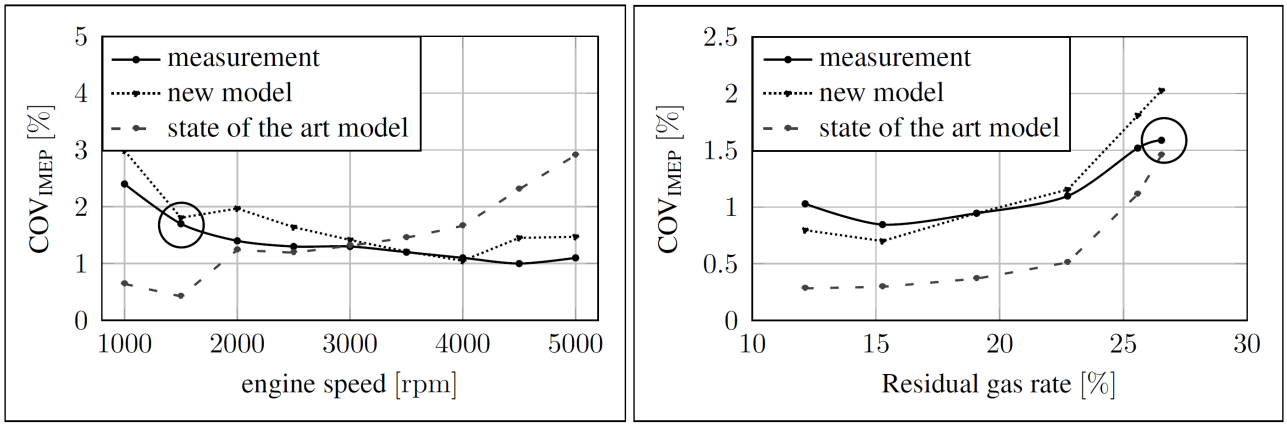

(a) VAR1.

(b) VAR2.

Figure 6.23.: Comparison of the B48 engine speed and residual gas rate variation regarding COV_{IMEP} found by measurement, the new CCV model and the state-of-the-art model with two different 1500 rpm 0.2WOT operating points highlighted by circles.

new CCV model is able to match the COV_{IMEP} found by measurement data qualitatively and mostly quantitatively. However, at some engine speeds, the COV_{IMEP} does not match exactly. These differences can be explained by deviations in the mean cycle combustion simulation. The *MFB50%* and *MFB90%* are determined within the defined limits of ± 3 CAD. However, the *MFB5%* in particular is determined up to 4 CAD too early, resulting in a retarded combustion due to the short ignition delay, which in turn overestimates the COV_{IMEP}. In contrast, the state-of-the-art CCV model is not able to reproduce the CCV found by measurement either qualitatively or quantitatively. At low engine speeds, the cyclic combustion variations are underestimated, and when the engine speed increases to over 3000 rpm, the cyclic combustion variations are overestimated. At this point, for the engine speed variation, it can be said, that the influence of different turbulence fluctuations needs to be covered to improve the results of the state-of-the-art CCV model.

The residual gas rate variation in Figure 6.23 (b) shows a rising COV_{IMEP} as the EGR increases, which is predicted well by the new CCV model, except for the engine operating point with the highest EGR. In contrast, the state-of-the-art model can only reproduce the experimental data qualitatively, not quantitatively, except for the highest EGR, and significantly underestimates the COV_{IMEP}. The last finding indicates, that adjusting the state-of-the-art CCV model's calibration factors might improve this EGR variation, but in turn will worsen the description of the engine speed variation.

In particular, the VAR1 and VAR2 variations show the proof of concept of the new CCV model. This is explained in more detail for the 1500 rpm and 0.2WOT operating point, which is found in both variations and marked with circles in Figure 6.23. For both engine operating points, not only the intake valve lift and the intake valve timing but also the exhaust valve timing and throttle position are different, as shown in Table 6.7.

variation setting	unit	EOP1	EOP2
throttle position	[%]	9.1	10
exhaust valve timing	[CAD]	80	60
intake valve timing	[CAD]	65	75
intake valve lift	[mm]	4	3

Table 6.7.: Explicit investigation of 1500 rpm and 0.2WOT of the B48 for different engine parameter settings.

For the operating point of the engine speed variation, defined as EOP1 in the following, the turbulence intensity level is expected to be higher due to a later intake valve closure and higher intake valve lift; this is also confirmed by the turbulence model results in the mean engine cycle. Engine operating point EOP2 is a reference to the EGR variation. The PTA of both operating points indicates that the EGR of EOP1 is 29.8 % whereas EOP2 exhibits an EGR of 26.5 %. Since the COV_{IMEP} is on the same level in both variations, it can be supposed that higher cyclic combustion variations from an increased EGR are compensated by the higher turbulence intensity level. This phenomenon can be reproduced well by the newly designed CCV model, but not by the state-of-the-art model.

In the following, both engine operating points are investigated regarding frequency distributions of the *MFB5%*, *MFB50%* and *MFB90%*. Table 6.8 shows the mean cycle *MFB5%*, *MFB50%* and *MFB90%* of EOP1 and EOP2 from simulation and measurement. The *MFB5%* and *MFB50%* of EOP1 exceed the defined limits

	unit	EOP1 Sim.	EOP1 Meas.	EOP2 Sim.	EOP2 Meas.
MFB5%	[CAD]	-10.7	-6.7	-9.9	-6.9
MFB50%	[CAD]	5.9	9.1	8.6	9.9
MFB90%	[CAD]	26.0	24.7	33.7	44.0

Table 6.8.: Comparison of virtual and experimental mean cycle mass burned fuel points for EOP1 and EOP2 in the B48.

of Chapter 4. The measured and simulated *MFB90%* of EOP2 also deviates significantly, which is made obvious in the distributions. Figure 6.24 illustrates the distributions for the *MFB5%*.

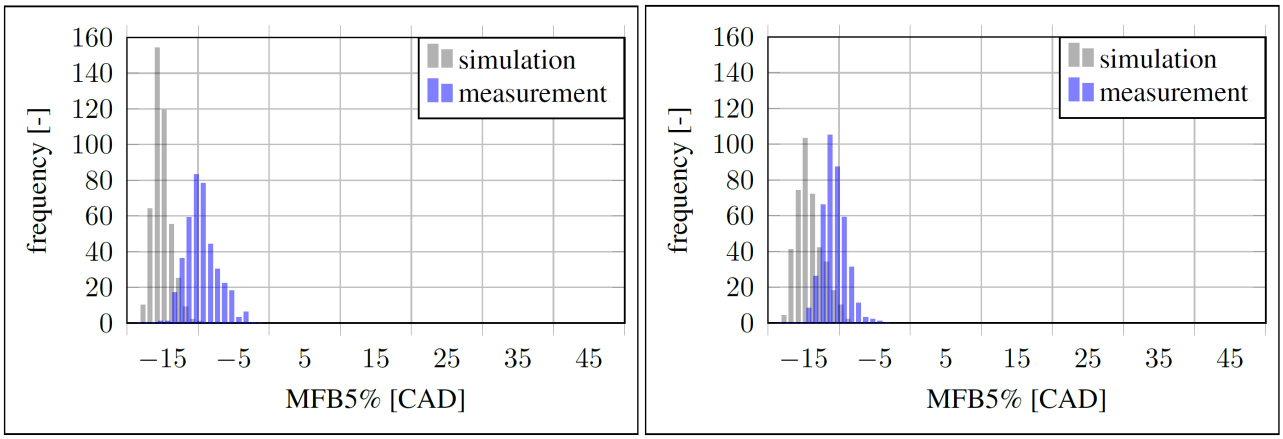

(a) EOP1. (b) EOP2.

Figure 6.24.: Illustration of the *MFB5%* frequency distributions found by simulation and measurement for the B48 engine operating points EOP1 and EOP2.

The measured and simulated *MFB5%* of operating point EOP1 in Figure 6.24 (a) deviate visibly, revealing a difference of 4 CAD in the mean cycle. Since the distribution is wider for the measurement, the standard deviation of the *MFB5%* is higher. The same is seen for EOP2, though the two distributions overlap more and a similar shape can be seen. Thus, the $COV_{MFB0\%\text{-}MFB5\%}$ is also expected to be similar.

In Figure 6.25 distributions are displayed for the *MFB50%*. In the frequency distribution for the *MFB50%* of

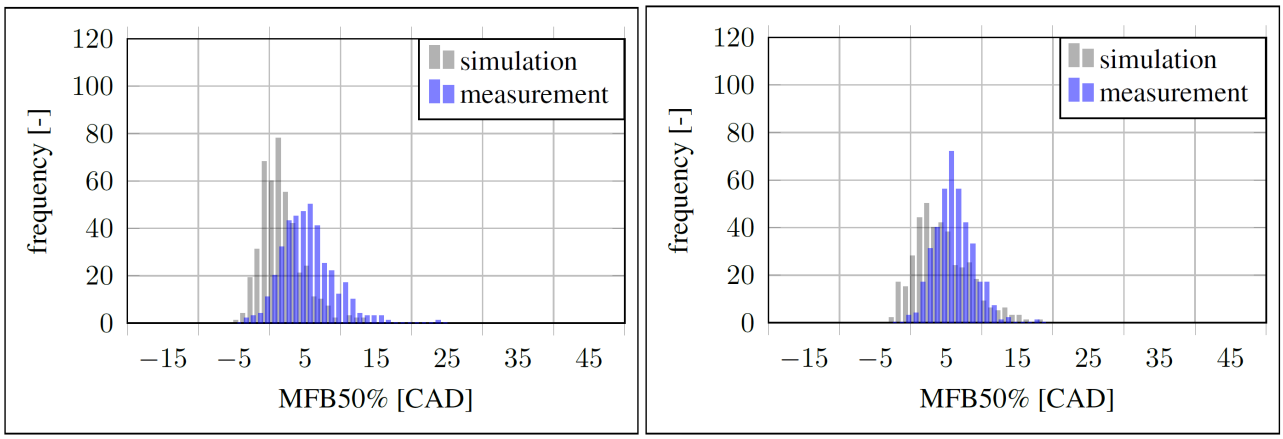

(a) EOP1. (b) EOP2.

Figure 6.25.: Illustration of the *MFB50%* frequency distributions found by simulation and measurement for the B48 engine operating points EOP1 and EOP2.

operating point EOP1 on the left-hand side of Figure 6.25 (a), deviations regarding the shape and CAD of the maximum are obvious. This again corresponds to the differences in the mean cycle center of combustion. Since the shape of the measurement distribution is wider, the *MFB50%* can be expected to exhibit a higher *COV*. In Figure 6.25 (b), both *MFB50%* distributions match better than for EOP1 regarding shape and the mean.

In Figure 6.26 distributions are illustrated for the *MFB90%*. The measured and simulated *MFB90%* frequency distributions for EOP1 corresponds well. However, the opposite is the case for EOP2, where there are substantial deviations concerning the shape and the mean of the distributions. Here, the standard deviation of the *MFB90%* from the simulation is expected to be higher than for the measurement. When comparing the COV_{IMEP} for the two operating points (Figure 6.23), it can be seen at EOP1, the data from the simulation with the new CCV model and the measurement data match considerably better. The detailed analysis of one engine operating point in Table 6.5 indicates that an accurate description of the mean cycle and fluctuations in the burn-off phase is necessary to precisely reproduce the COV_{IMEP}. This can be seen for EOP1, but not for EOP2. Therefore, the over-

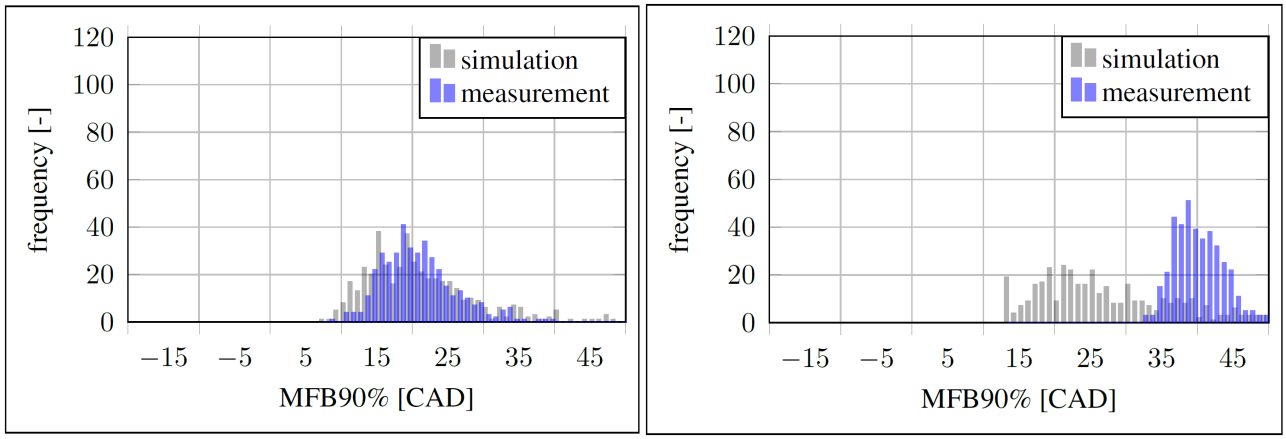

(a) EOP1. (b) EOP2.

Figure 6.26.: Illustration of the *MFB90%* frequency distributions from simulation and measurement for the B48 engine operating point EOP1 and EOP2.

estimation of the COV_{IMEP} may have its origin in the different *MFB90%* distributions found by measurement and simulation.

Two further variations, VAR3 and VAR4, are displayed in Figure 6.27. Note that for the engine load variation, unity is equal to a load of $IMEP = 14$ bar.

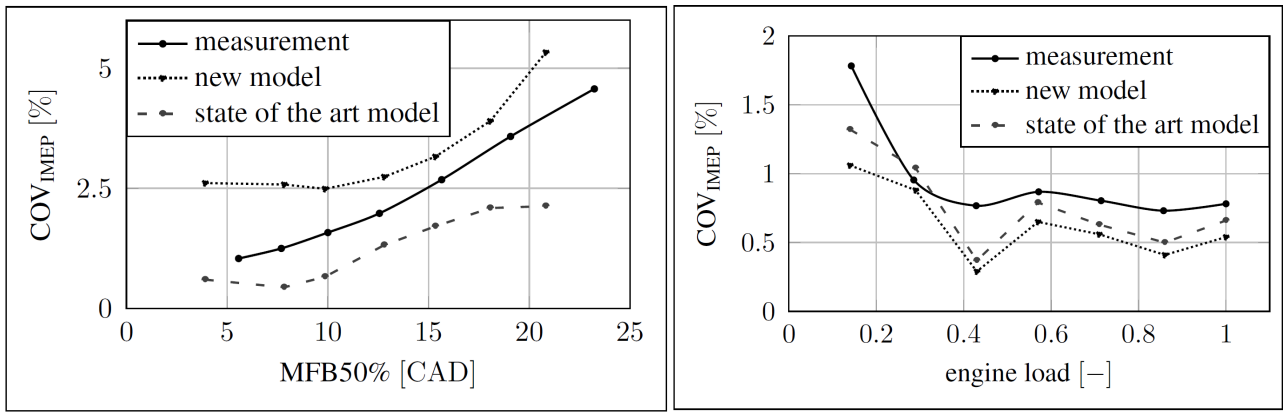

(a) VAR3. (b) VAR4.

Figure 6.27.: Comparison of the B48 *MFB50%* and engine load variation regarding COV_{IMEP} found by measurement, the new CCV model and the state-of-the-art model.

Figure 6.27 (a) exhibits the variation in the *MFB50%*. Differences between the center of combustion found by simulation and measurement are again due to deviations in the calculating of the mean cycle combustion, as already explained above. The new CCV model is able to reproduce the COV_{IMEP} mostly qualitatively, but not quantitatively. For early *MFB50%*, the COV_{IMEP} is overestimated, as also seen for the TT1.3 (400). Within this *MFB50%* variation, the *MFB90%* is calculated up to 10 CAD too late in the mean engine cycle simulation. The state-of-the-art model is also able to express the COV_{IMEP} qualitatively; however, the quantity is underestimated.

Figure 6.27 (b) shows variations in the engine load. Here, both CCV models are mostly able to reproduce the COV_{IMEP} in quality, but cannot reproduce the COV_{IMEP} in absolute values. The new CCV model even underestimates results from the state-of-the-art CCV model. As the mean cycle combustion simulation is within the defined limits, only an increase in the global and local turbulence fluctuation parameters of the new CCV model can result in a more accurate description of the COV_{IMEP} gathered from measurement data.

Figure 6.28 shows variations in the B48 λ and fluid mechanics. The latter is induced by varying the intake valve timing while fixing the intake valve lift. The lower the intake valve timing value, the earlier is the IVC. Since different intake valve timings result in different residual gas rates, the exhaust valve timing is also readjusted to fix the EGR.

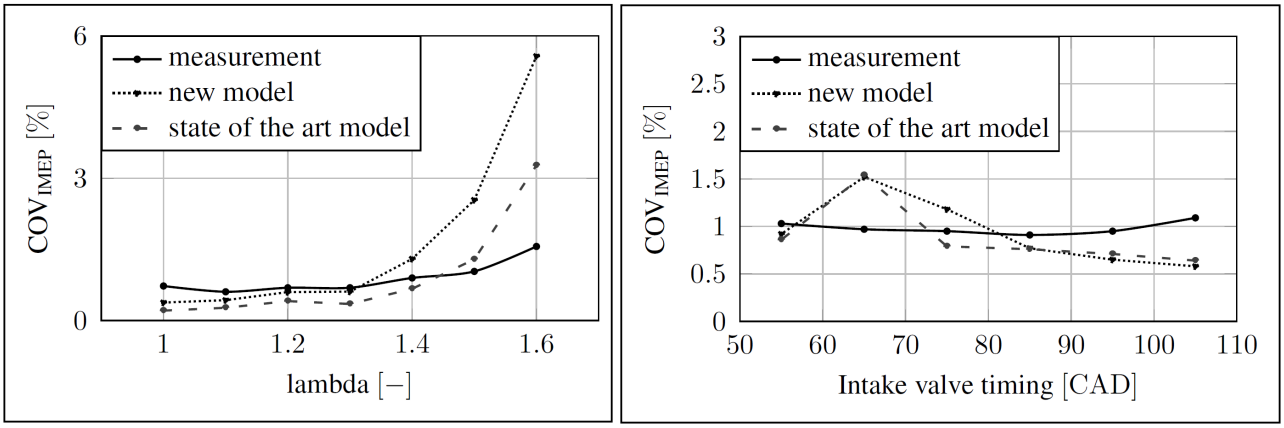

(a) VAR5. (b) VAR6.

Figure 6.28.: Comparison of the B48 λ and fluid mechanics variation regarding COV_{IMEP} found by measurement, the new CCV model and the state-of-the-art model.

The λ variation in Figure 6.28 (a) only shows partial agreement between the simulation with the new CCV model and measurement. At $\lambda = 1$, the COV_{IMEP} is underestimated by the simulation, with improvements towards $\lambda = 1.4$. The underestimation at $\lambda = 1$ may result from a combination of an excessively early mean cycle, *MFB90%* and the underestimation of the turbulent fluctuation factors. For leaner air-fuel mixtures, the new model significantly overestimates the CCV, as also seen for the TT1.3 (320) in Figure 6.2. This is again due to an inaccurate mean cycle combustion calculation with retarded *MFB50%* of more than 6 CAD. The state-of-the-art CCV model first underestimates the COV_{IMEP} up to a λ of 1.4. Then, it matches the measurement data; however, this is only due to the retarded mean cycle burn rate.

Figure 6.28 (b) shows a variation in the fluid mechanics. In the measurement data, marginally higher CCV can be seen for an early IVC; however, the 105 CAD intake valve timing also shows the same CCV level. For this variation, neither the new CCV model nor the state-of-the-art model show qualitative and quantitative agreement with the measurement data. Regarding the new CCV model, this can partly be explained by a retarded virtual mean-cycle *MFB90%* of around 5 CAD for the 55 - 75 CAD intake valve timing operating points. For the latter three operating points, the mean cycle *MFB90%* are matched precisely, as are the *MFB5%* and *MFB50%* for all operating points. The disagreement with the state-of-the-art CCV model cannot only be eliminated by adjusting its calibration parameters.

The last variation investigated regarding the boost pressure is shown in Figure 6.29. The COV_{IMEP} from this variation is mostly underestimated by both CCV models, with the underestimation from the state-of-the-art CCV model being more significant. The mean cycle *MFB5%* and *MFB50%* are reproduced well; however, the *MFB90%* is calculated too early in the simulation, except for the 1150 mbar operating point. Again, the illustration of the state-of-the-art CCV model can be improved by adjusting its calibration parameters.

Summing up, the new CCV model is mostly able to better describe CCV than the state-of-the-art model. However, weaknesses still can be found. One reason may be the deviations found in the calculation of the mean cycle combustion, which in turn leads to an inaccurate reproduction of cyclic combustion variations by the new model. Furthermore, the new model is transferred to the B48 engine, without adjustment, from the design engine TT1.3 (320). Since the B48 enables more engine parameter variations to be measured regarding a more complex gas exchange system, as well as a significant higher in-cylinder turbulence level, adjustments regarding the turbulent fluctuation parameters might improve the description of CCV gathered from measurement data. The limitations of the newly designed model are presented in more detail in Section 6.6.1.

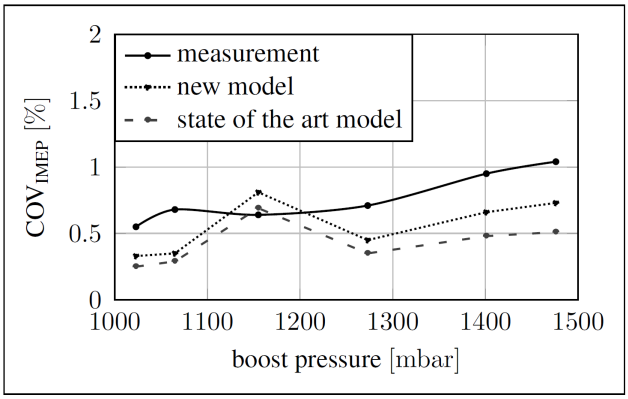

Figure 6.29.: Comparison of the B48 boost pressure variation regarding COV_{IMEP} found by measurement, the new CCV model and the state-of-the-art model.

6.5 Validation on B48 with $\epsilon = 14$ pistons

The validation of the B48 engine with the $\epsilon = 14$ piston is performed by means of three variations, listed in Table 6.9.

parameter	unit	VAR1	VAR2	VAR3
speed	[rpm]	variable	1500	1500
load	[-]	0.2WOT	variable	0.2WOT
MFB50%	[CAD]	8	result	8
λ	[-]	1	1	1
EGR	[%]	result	result	variable

Table 6.9.: Engine parameter variations to validate the model on the B48 engine with $\epsilon = 14$ pistons.

The state-of-the-art CCV model calibration factors are again adjusted to best match measurement data regarding the COV_{IMEP}. The calibration procedure reveals that the state-of-the-art model has the same parameters as found for the B48 engine with serial pistons. The engine load variation investigated includes a retarding of the *MFB50%* at higher engine loads due to the risk of knock. Furthermore, since the intake valve lift, intake valve timing and exhaust valve timing vary in terms of the engine speed and load variations, the EGR is a result of the respective setting.

Figure 6.30 shows the engine speed and load variations. For the latter, the engine load at unity corresponds to an *IMEP* of 14 bar.

The new CCV model only shows partial agreement with the measurement data on the engine speed variation (Figure 6.30 (a)), for different reasons all related to the mean engine cycle. In the simulation at 1000 rpm, the *MFB90%* is delayed by 8 CAD, while at 1500 rpm and 2000 rpm the EGR is determined too high by 5 %. Therefore, at these operating points the cyclic combustion variations are overestimated. For the highest engine speeds, the deviations from the experiment are minor. By contrast, the state-of-the-art model overestimates CCV for engine speeds higher than 1500 rpm. First, this is due to the higher weighting of CCV as the engine speed increases. At engine operating points up to 2000 rpm, in which weaknesses in the mean engine cycle are found, the better COV_{IMEP} reproduction of the state-of-the-art CCV model is only due to the non-physical adjustment of the calibration factors, not due to its physical description.

Figure 6.30 (b) demonstrates that the engine load variation is reproduced qualitatively and to some extent quantitatively by both CCV models. In the measurement data, the lowest engine load operating point indicates one complete misfire and several incomplete combustion rates, thus leading to this high COV_{IMEP}, which is also reproduced by both models. For the second and third engine operating points, the burn rate is slightly underestimated and the EGR overestimated in the mean cycle, leading to a higher virtual COV_{IMEP} found by the new

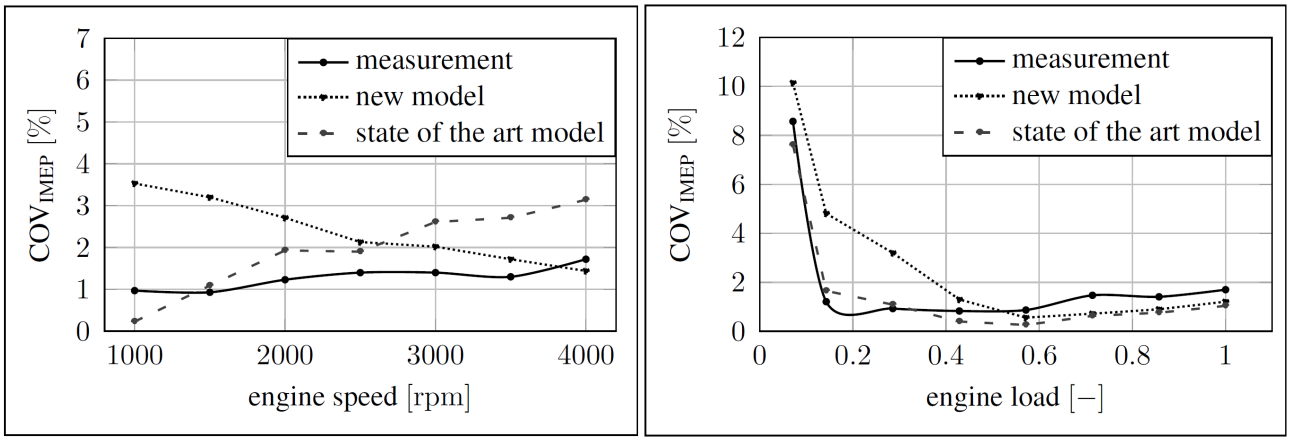

(a) VAR1. (b) VAR2.

Figure 6.30.: Comparison of the engine speed and load variations of the B48 with $\epsilon = 14$ piston regarding COV_{IMEP} found by measurement, the new CCV model and the state-of-the-art model.

CCV model. The mean cycle combustion for the other engine operating points are predicted well, which is also seen in the better reproduction of the COV_{IMEP} from the new model. The state-of-the-art model indicates a good match with measurement data.

The variation of residual gas is illustrated in Figure 6.31. For this variation, the experimental mean cycle

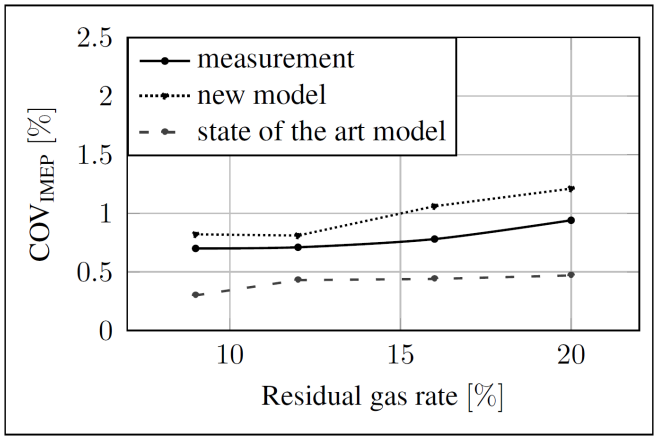

Figure 6.31.: Comparison of the residual gas rate variation of the B48 with $\epsilon = 14$ piston regarding COV_{IMEP} found by measurement, the new CCV model and the state-of-the-art model.

residual gas rate and the combustion rate are matched well by the simulation. Hence, good agreement is found between the measurement data and the new CCV model throughout the EGR range, though with an overestimation at higher EGR. The state-of-the-art CCV model reproduces experimental cyclic combustion variations qualitatively, but underestimates them quantitatively. An adjustment of the calibration factors can lead to improvements, but worsen the description of the engine load and speed variation.

Summing up, the uncalibrated, new CCV model is only able to reproduce the cyclic combustion variations better to a limited extent for the B48 with $\epsilon = 14$ pistons than the calibrated state-of-the-art model. For a more precise description of the mean cyclic gas exchange and combustion process, a better match is expected to be possible.

6.6 Limits and potentials of the new model approach

Summing up the conclusions from this chapter, the limits and potentials of the newly designed CCV model are described in the following. The findings from the new and the state-of-the-art CCV models are outlined along with the investigations of the different SI combustion engines.

6.6.1 Limits

The development of a new CCV model depends on input data. In this study the input is delivered from experimental data on different SI engines, as well as from the literature. From this experimental data, statistical information is used regarding the *IMEP*, different crank angles of the mass fuel burned and the cylinder pressure. Inaccuracies in the indicated measurement of the cylinder pressure or in the evaluation are directly implemented in the model development. Thus, a new CCV model can only be as accurate as the underlying measurement and evaluation data. Weaknesses in the measurement systems are outlined in Chapter 3; in particular, the error chain of the indication system has a significant effect.

A further limitation is the experimental combustion engine itself. Some engines exhibit varying cyclic combustion variations for individual cylinders at engine operating points with high CCV. For instance, this is the case for very lean air-fuel mixtures of the TT1.3 (320), which can even lead to misfires. These misfires are only seen from time to time, i.e. misfires are recorded in some measurement data for a certain engine operating point but not in other data. Furthermore, small differences in the engine periphery and combustion chamber setup can have an effect on CCV. As described in Chapter 2, small differences in the machined edges at the intake port can have a significant effect on the cyclic turbulent intake flow structure. Additionally, the spark plug in individual cylinders is orientated differently. Thus, the initial flame kernel is affected differently by the local flow for different cylinders, which leads to slight deviations in the combustion process. A quasi-dimensional CCV model can only take the engine's average properties into account.

Within the quasi-dimensional simulation environment, the development of a new CCV model depends significantly on the accurate description of the gas exchange and combustion process in the mean cycle. This includes the precise determination of the in-cylinder air charge and residual gas rate. Furthermore, in the case of in-cylinder predictive models at intake valve open, the accurate calculation of the intake mass flow and intake velocity is essential for a correct description of in-cylinder turbulence. Limitations regarding the turbulence model are outlined in detail in [49]. The combustion calculation is heavily dependent on an accurate formulation of the laminar burning velocity. Although sophisticated formulations exist, there are known to be remaining weaknesses in the case of very lean air-fuel mixtures, cf. Chapter 4 and [29]. As indicated in the model validation for several investigated engines, there are deviations regarding the mean cycle combustion. These lead to uncertainties regarding the determination of the virtual cyclic combustion variations, as shown for the B48 with serial pistons. Here, it is shown that the burn-off phase has to be determined accurately to correctly reproduce CCV. This finding is in contrast to mean cycle simulations, in which the burn-off phase only marginally influences the determination of the *IMEP*.

Local effects on cyclic combustion variations such as mixture in-homogenization and local flow structure fluctuations cannot be taken into account in a quasi-dimensional simulation environment. Thus, there are weaknesses regarding the simulation environment and the underlying models, as outlined in the following.

Some limitations of the new CCV model may originate in the development process itself. Although the most significant physical causes described in the literature are introduced in the new model, further adjustment is needed. The fluctuations of the physical causes alone can describe the CCV from the design engine operating point of the TT1.3 (320) well. However, for different engine parameter variations, the physical fluctuation parameters are weighted in the form of a calibration, in order to also quantitatively describe CCV. One major target of the calibration is to enable the CCV model, to accurately describe cyclic combustion variations globally, i.e. for very different engine operating points. The final CCV model developed in this study shows good results for the TT1.3 (400) and TT1.2, as long as the underlying predictive models work correctly. Nevertheless, for the B48 engine with serial pistons, there are engine operating points, in which the underlying mean cycle combustion matches the measurement data, but the new CCV model underestimates cyclic combustion variations from

experiments. One reason may be the inaccurate description of the fluctuating turbulence factors within the CCV model, which were initially determined according to 3D CFD LES from the literature for a similar engine regarding the TT1.3 (320). The CCV model development mostly works well for the B48 engine operating points up to load points, in which turbocharging is included. Therefore, increasing the turbulent fluctuation factors for charged operating points could improve the B48 CCV description, but would also worsen those at other operating points or of the other engines investigated.

All these limitations compromise the development and application of the new CCV model. The limitations in the development process, in particular, coincide with other CCV model developments found in the literature [106, 127]. Even for a physical development, weaknesses are found in terms of the description of CCV for a certain engine if the engine speed and load are different from the design engine operating point [106].

6.6.2 Potentials

The newly designed CCV model in this study is set up on the basis of highly sophisticated turbulence, ignition and combustion models. The model includes the most significant physical causes of cyclic combustion variations and the factors influencing them, extracted from extensive research into the literature. An integrated stochastic model imposes fluctuations on these physical causes, thus CCV is not only described by empirical tuning, but also physically. The new CCV model is applied to different SI combustion engines with different engine parameter variations, in order to investigate and analyze its functioning. It is shown that, for different SI combustion processes such as the TT1.3 (320), TT1.3 (400) and TT1.2, the reproduction of CCV can be considered advanced within the quasi-dimensional simulation environment. In particular, the COV_{IMEP} and the underlying cyclic combustion are predicted well regarding variations in the engine speed, load and *MFB50%*. Furthermore, the B48 engines with serial and $\epsilon = 14$ pistons are predicted in good accordance with the measurement data without adjusting the CCV model. For the serial B48 especially, this can be seen as an improvement, since the model is able to reproduce a complete engine map and different engine parameter variations qualitatively and mostly quantitatively. Using regression plots for all the engines investigated, describing the newly designed CCV model and the state-of-the-art model, the potential is outlined in Figure 6.32.

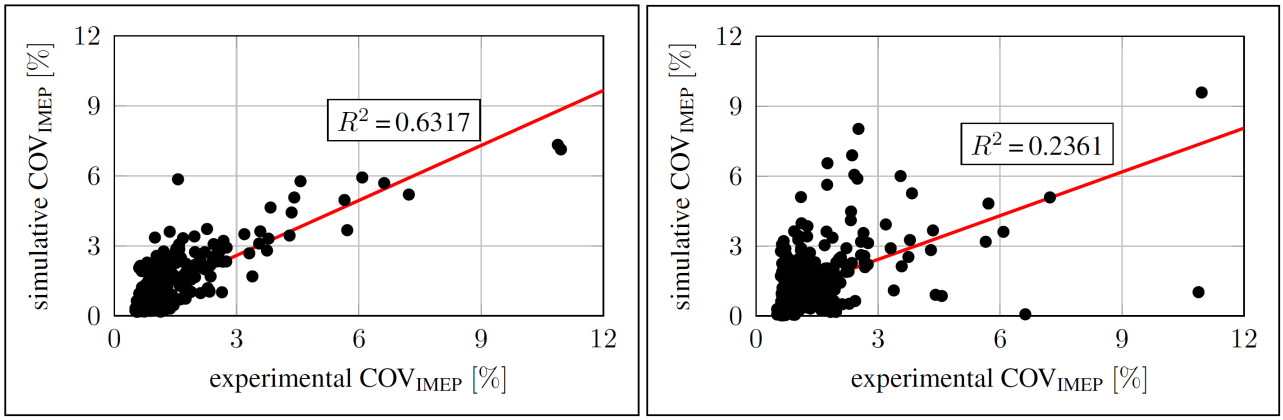

(a) New CCV model. (b) State-of-the-art CCV model.

Figure 6.32.: Comparison of the experimental and virtual COV_{IMEP} in regression plots regarding the newly designed and the state-of-the-art CCV models.

This illustration presents the COV_{IMEP} from experiments and the respective simulation results of the CCV models. Visually, and from the regression coefficient of determination R^2, it can be clearly seen that the new, uncalibrated CCV model can better describe cyclic combustion variations than the calibrated state-of-the-art CCV model.

With this finding in mind, the new CCV model can be used in virtual engine calibration procedures, e.g. to set up different engine parameters such as the intake valve timing and valve lift. Thus, the new model can be used as an additional engine design criterion. Due to its predictive capability it can even be used when no actual test engine is yet available. When the CCV model is applied in engine process simulations, especially in areas with

severe limitations on engine smoothness, it leads to more reliable results within short computing times. This makes the quasi-dimensional simulation environment even more attractive in addition to engine test bench operations and fully resolved 3D CFD simulations.

In this thesis, a new quasi-dimensional model to physically describe cyclic combustion variations is developed. The motivations driving this work are listed in the following.

- Existing CCV models do not yet include all physical CCV causes and factors influencing them. Furthermore, most models are largely empirical, matching the CCV found by experiment to the virtual CCV by a tuning procedure.
- For most of the existing CCV models, only one or very few different SI engines were used to develop and validate the model. Therefore, no general conclusions can be drawn regarding the correct functioning of the individual CCV model, covering different SI combustion processes.
- In addition, when developing and validating previous CCV models only very few engine parameter variations were considered. Therefore, again, no universal statements can be made regarding the accurate functioning of the unique CCV models in the case of engine parameter variations which have not been implemented or investigated.
- When simulating the mean cycle, previous CCV model developers did not have access to highly sophisticated turbulence, ignition and combustion models. Thus, their CCV model development process was limited, since not all physical CCV causes could be implemented.
- The above mentioned items indicate that there is some need to develop and calibrate CCV models, in order to reproduce virtual cyclic combustion variations.

In contrast, the model development process from this work can access an extensive experimental data basis, established for this work. The simulation basis of the new CCV model consists of previously developed, sophisticated turbulence, ignition and combustion models which are as yet only able to describe the mean engine cycle. The simulation environment is determined by a commercial 0D/1D gas exchange and combustion tool and the turbulence, ignition and combustion models included by user FORTRAN routines. Within those routines, first, a stochastic model is included in the new CCV model. Then, the most significant physical causes of CCV, extracted from research into the literature, are implemented alongside the factors influencing CCV. Finally, a comprehensive model validation is successfully undertaken.

The experimental data basis consists of conventional and unconventional SI engines. Three unconventional SI engines are investigated; one engine is distinguished by a long expansion in the working stroke via the crank train and the other two engines by a long expansion stroke via the valve train. Furthermore, two combustion engines with a conventional crank train and two different pistons, one from serial production and the other with a high compression ratio, are examined. The causes and influences of cyclic combustion variations resulting from the fluid mechanics, the chemical gas composition and the thermodynamical state are analyzed and quantified. These investigations imply that there are engine parameter variations regarding the engine speed, load, ignition timing, air-fuel equivalence ratio, intake and exhaust valve timings, intake valve lift and boost pressure.

Within the 0D/1D simulation environment, first, the gas exchange and combustion components are verified and, if necessary, adjusted, to provide a precise basis for simulating CCV. Among other things, these adjustments included the adaptation of the valves discharge coefficients and the Woschni heat transfer model for each engine investigated. Furthermore, the previously developed quasi-dimensional turbulence, ignition and combustion models are individually adjusted to the specific SI engines according to the models' authors. The turbulence model is calibrated with detailed 3D CFD data and the ignition and combustion models with measurement data individually for each engine investigated. Additionally, for a better description of very lean air-fuel mixtures, alternative formulations for the laminar burning velocity are examined, though with no appreciable success. With the help of the three models, it is possible to describe the in-cylinder phenomena in all four engine strokes. Furthermore, the physical parameters, on which fluctuations are imposed in the CCV model, are available.

After the simulation basis is set up, the CCV model is designed. First, a stochastic model is developed, describing a probability density function (PDF), focusing on reproducing the variance of physical causes found in the literature. Here, a standard deviation of 2σ is chosen, to account for the major part under the PDF while leaving enough emphasis on the border areas. By means of the stochastic model, fluctuations are imposed on the most significant physical causes of CCV, extracted from extensive research into the literature. These parameters are global and local flow structure fluctuations, i.e. the production of the turbulent kinetic energy, the integral length scale, the initial flame kernel size, the eccentricity of the flame kernel and the flame-wall quenching distance. The factors influencing cyclic combustion variations are integrated by a physical parameterization of the engine speed, load, center of combustion and air-fuel equivalence ratio. The CCV model is to react predictively to other changes in the engine parameters due to the underlying physical models.

The newly designed CCV model is first verified in detail for the engine with a long expansion stroke via the valve train, used to develop the model. The simulation results show very good agreement with the measurement data regarding the COV_{IMEP} for the variation of the engine speed, load and center of combustion. The variation of the air-fuel equivalence ratio shows deviations for very lean mixtures. Here, the burn rate is retarded considerably in the mean engine cycle, thus, the cyclic combustion variations are overestimated. This finding is the result of a detailed analysis of retarding the mean cycle combustion and its resulting cyclic combustion variations. Furthermore, it is shown that the underlying fluctuating combustion concerning the ignition, the main combustion phase and the burn-off phase matches reasonably well. Further validation is undertaken for the other four engines investigated without adjusting the developed CCV model, revealing that the new CCV model has been applied successfully both qualitatively and, to a large extent, quantitatively. It is demonstrated that CCV for engine operating points with the same engine speed, load and center of combustion, but different levels of fluid mechanics and chemical gas composition can be reproduced well by the new model, but not as well by the state-of-the-art model. Quantitative limitations are again found for lean air-fuel mixtures and in addition for engine operating points, in which the burn-off phase is overestimated in the mean cycle simulation. It is pointed out that small deviations in the mean cycle burn-off have only marginal effects on the determination of the *IMEP*, but major effects on the description of the CCV. A third deviation can be found in the conventional SI engine, in the case of charged operating points, in which the mean cycle simulation reproduces the gas exchange and combustion correctly, but cyclic combustion variations are still underestimated. The end result is an underestimation of the turbulent fluctuation parameters.

Hence, to summarize, the newly designed CCV model is able to reproduce cyclic combustion variations for a large variety of engine parameter changes and different SI combustion processes without calibration. Therefore, it closes the gap between very time-consuming and accurate 3D CFD LES and low-dimensional empirical CCV models. Due to its predictive capability, the CCV model can be used for virtual engine calibration concerning the setup of different engine parameters, including calibrations, where no actual test engine is yet available. Therefore, the CCV model can be used as a further engine design criterion and makes the results of engine process simulations more reliable, especially in areas with severe limitations on engine smoothness. However, its limitations also have to be kept in mind, first concerning the experimental analysis. The new model can only be as good as it is possible within the tolerances of measurement and analysis of experimental data. Furthermore, it is essential to correctly describe the gas exchange and combustion process simulation in the mean engine cycle. In particular, it is shown that the burn-off phase must be accurate. Limitations on the CCV model development process itself can be diminished with 3D CFD Large Eddy Simulations, especially for conventional engines in charged engine operating points, in order to also gain detailed insights into cyclic combustion variations in these engine characteristics.

The newly designed CCV model can also be used in transient simulations, e.g. in driving cycles. This is expected to reduce previous inaccuracies regarding the determination of the fuel consumption and pollutant emissions, since the variance of combustion and its deviations in terms of cyclic exhaust energy and emissions, efficiency as well as power are considered. Another possible application is the virtual investigation of engine knock. It is known that engine knock is a significantly cyclic phenomenon. So far, knock simulations have only been performed for the mean engine cycle with limited success. However, with the accurate description of the underlying cyclic combustion, further improvement should be possible.

[1] Abdi Aghdam, E., Burluka, A. A. and Hattrell, T. (2007): *Study of Cyclic Variation in a SI Engine Using Quasi-Dimensional Combustion Model*. SAE paper, (2007-01-0939).

[2] Adomeit, P., Lang, O., Pischinger, S., Aymanns, R., Graf, M. and Stapf, G. (2007): *Analysis of Cyclic Fluctuations of Charge Motion and Mixture Formation in a DISI Engine in Stratified Operation*. SAE paper, (2007-01-1412).

[3] Aleiferis, P., Taylor, A., Whitelaw, J., Ishii, K. and Urata, Y. (2000): *Cyclic Variations of Initial Flame Kernel Growth in a Honda VTEC-E Lean-Burn Spark-Ignition Engine*. SAE paper, (2000-01-1207).

[4] Angelberger, C. (2013): *Using Large-Eddy & System Simulation to Address Non-cyclic Engine Combustion*. ERC Symposium 05.06.2013.

[5] Ayala, F. and Heywood, J. (2007): *Lean SI Engines: The role of combustion variability in defining lean limits*. SAE paper, 2007-24-0030.

[6] Aydin, K. (2011): *Effect of Engine Parameter on Cyclic Variations in Spark Ignition Engines*. 6th International Advanced Technologies Symposium.

[7] Ball, J. K. (1998): *Cycle-by-cycle variation in spark ignition internal combustion engines*. Ph.d. thesis, University of Oxford, Oxford.

[8] Bargende, M. (1995): *Schwerpunkt-Kriterium und automatische Klingelerkennung*. MTZ Motortechnische Zeitschrift, vol. 56(10), pp. 632–638.

[9] Bates, S. (1989): *Flame Imaging Studies of Cycle-by-cycle Combustion Variation in a SI Four-Stroke Engine*. SAE paper, (892086).

[10] Baumann, P., Schröder, M., Kurz, H., Maier, T., Thiel, W. and Strehl, U. (2015): *Investigation of the Influencing Parameters Using Optimized Exhaust Emissions Measurement Systems with Different Modern Plug-in Hybrid Electrical Vehicles*. SAE paper, (2015-01-1069).

[11] Blizard, Norman C. and Keck, James C. (1974): *Experimental and Theoretical Investigation of Turbulent Burning Model for Internal Combustion Engines*. SAE paper, (740191).

[12] Bode, J., Schorr, J., Krüger, C., Dreizler, A. and Böhm, B. (2016): *Influence of three-dimensional in-cylinder flows on cycle-to-cycle variations in a fired stratified DISI engine measured by time-resolved dual-plane PIV*. Proceedings of the Combustion Institute, vol. 36(3), pp. 3477–3485.

[13] Böhm, B., Di Mare, D. and Dreizler, A. (2010): *Characterisation of cyclic variability in an optically accessible IC Engine by means of phase-independent POD*. Les Rencontres Scientifiques de IFP - LES for Internal Combustion Engine Flows (18-19. November 2010).

[14] Boree, J., Maurel, S. and Bazile, R. (2002): *Disruption of a compressed vortex*. Physics of Fluids, vol. 14(7), pp. 2543–2550.

[15] Brunt, M. and Emtage, A. (1997): *Evaluation of Burn Rate Routines and Analysis Errors*. SAE Paper, 970037.

[16] Brunt, M. and Pond, C. (1997): *Evaluation of Techniques for Absolute Cylinder Pressure Correction*. SAE Paper, 970036.

[17] Bueno, A. V., Velasquez, J.A. and Milanez, L. F. (2012): *Internal Combustion Engine Indicating Measurements*. INTECH.

[18] Buhl, S., Gleiss, F., Köhler, M., Hartmann, F., Messig, D.and Brücker, C. and Hasse, C. (2016): *A combined numerical and experimental study of the 3D tumble structure and piston boundary layer development during the intake stroke of a gasoline engine*. Flow, Turbulence and Combustion, vol. 98(2), pp. 579–600.

[19] Buhl, S., Hartmann, F. and Hasse, C. (2015): *Identification of Large-Scale Structure Fluctuations in IC Engines using POD-Based Conditional Averaging*. Oil & Gas Science and Technology, vol. 71(1), pp. 1–16.

[20] Buschbeck, M. (2013): *Laseroptische Analyse der zyklischen Schwankungen in einem Transparentmotor*. Ph.D. thesis, TU Darmstadt.

[21] Buschbeck, M., Bittner, N., Halfmann, T. and Arndt, S. (2012): *Dependence of combustion dynamics in a gasoline engine upon the in-cylinder flow field, determined by high-speed PIV*. Experiments in Fluids, vol. 53(6), pp. 1701–1712.

[22] Cantera (2017): *Chemical Kinetics,Thermodynamics and Transport Processes*, http://cantera.github.io/docs/sphinx/html/index.html.

[23] Ceviz, M. A., Öner, I. V., Kaya, F. and Karacali, T. (2010): *Analysis of the thermal efficiency and cyclic variations in a SI engine under lean combustion conditions*. Journal of Thermal Science and Technology, vol. 31(1), pp. 121–127.

[24] Clerk, D. (1882): *The Theory of the Gas Engine*. D. Van Nostrand Magazine, ISBN 978-0-548-77536-3.

[25] Czarnigowski, J. (2011): *Analysis of cycle-to-cycle variation and non-uniformity of energy production: Tests on individual cylinders of a radial piston engine*. Applied Thermal Engineering, vol. 31(10), pp. 1816–1824.

[26] Dai, W., Trigui, N. and Lu, Y. (2000): *Modeling of Cyclic Variations in Spark-Ignition Engines*. SAE paper, (2000-01-2036).

[27] Daily, J. (1987): *Cycle-To-Cycle Variations: A Chaotic Proces*. SAE paper, (870165).

[28] Daily, J. W. (1988): *Cycle-to-Cycle Variations: A Chaotic Process?*. Combustion Science and Technology, vol. 57(4-6), pp. 149–162.

[29] Daleiden, P. (2010): *Kennfeldweite Modellierung des Brennverzugs in einem turboaufgeladenem Benzindirekteinspritzer-Motor mit vvariable Ventiltrieb mittels Simulation und Versuch*. Master's thesis, TU Kaiserslautern.

[30] Daw, C., Finney, C., Green, J., Kennel, M., Thomas, J. and Connolly, F. (1996): *A Simple Model for Cyclic Variations in a Spark-Ignition Engine*. SAE paper, (962086).

[31] Daw, C., Finney, C., Kennel, M. and Connolly, F. (1997): *Cycle-by-cycle combustion variations in spark-ignited engines*. Fourth Experimental Chaos Conference, Boca Raton, Florida, USA.

[32] Dorsch, M., Neumann, J. and Hasse, C. (2016): *Application of a Phenomenological Model for the Engine-Out Emissions of Unburned Hydrocarbons in Driving Cycles*. Journal of Energy Resources Technology, vol. 138(2), pp. 022201–10.

[33] Dulbecco, A., Richard, S. and Angelberger, C. (2015): *Investigation on the Potential of Quantitatively Predicting CCV in DI-SI Engines by Using a One-Dimensional CFD Physical Modeling Approach: Focus on Charge Dilution and In-Cylinder Aerodynamics Intensity*. SAE paper, (2015-24-2401).

[34] Dumböck, O. (2016): *Thermodynamische Untersuchung von Ottomotoren mit verlängerter Expansion und anderen unkonventionellen Konzepten zur Wirkungsgradsteigerung*. Ph.D. thesis, Technische Universität Graz.

[35] Eichlseder, H., Klueting, M. and Piock, W. (2008): *Grundlagen und Technologien des Ottomotors: Der Fahrzeugantrieb*. Springer, Wien.

[36] Enaux, B., Granet, V., Vermorel, O., Lacour, C., Pera, C., Angelberger, C. and Poinsot, T. (2010): *LES study of cycle-to-cycle variations in a spark ignition engine*. Proceedings of the Combustion Institute, vol. 33(2), pp. 3115–3122.

[37] Enaux, B., Granet, V., Vermorel, O., Lacour, C., Pera, C., Angelberger, C. and Poinsot, T. (2012): *LES and experimental study of cycle-to-cycle variations in a spark ignition engine*. 33rd International Symposium on Combustion.

[38] Enaux, B., Granet, V., Vermorel, O., Lacour, C., Thobois, L., Dugue, V. and Poinsot, T. (2011): *Large Eddy Simulation of a motored single-cylinder piston engine: numerical strategies and validation*. Flow turbulence and combustion, vol. 86(2), pp. 153–177.

[39] Etheridge, J., Mosbach, S., Kraft, M., Wu, H. and Collings, N. (2008): *Investigating Cycle to Cycle Variations in an SI EngineThrough Experiments and a New Computational Model*, Technical Report 62, c4e-Preprint Series, Cambridge.

[40] Etheridge, J., Mosbach, S., Kraft, M., Wu, H. and Collings, N. (2010): *Modelling cycle to cycle variations in an SI engine with detailed chemical kinetics*. Combustion and Flame, vol. 158(1), pp. 179–188.

[41] Ewald, J. (2006): *A Level-Set Based Flamelet Model for the Prediction of Combustion in Homogeneous Charge and Direct Injection Spark Ignition Engines*. Ph.d. thesis, Rheinisch-Westfälischen Technischen Hochschule Aachen, Aachen.

[42] Fischer, J. and Spicher, U. (2004): *"Experimentelle Untersuchung zyklischer Schwankungen der Verbrennung im Hinblick auf Reduzierung der Motor-Rohemissionen bei Ottomotoren mit Benzin-Direkteinspritzung"*. Tech. rep., Institut für Kolbenmaschinen, Universität Karlsruhe, Karlsruhe.

[43] Fischer, J., Velji, A. and Spicher, U. (2004): *Investigation of Cycle-to-Cycle Variations of In-Cylinder Processes in Gasoline Direct Injection Engines Operating With Variable Tumble Systems*. SAE paper, (2004-01-0044).

[44] Gamma, Technologies (2015): *Flow Theory Manual*, Gamma Technologies Inc.

[45] Gamma, Technologies (2015): *GT-SUITE Engine Performance Application Manual Version 7.5*, Gamma Technologies Inc.

[46] GammaTechnologies (2015): *GT EngCylinderCCV template help*, Gamma Technologies.

[47] Goryntsev, D., Sadik, A., Klein, M. and Janicka, J. (2008): *Large eddy simulation based analysis of the effects of cycle-to-cycle variations on air/fuel mixing in realistic DISI IC-engines*. Proceedings of the Combustion Institute, vol. 32(2), pp. 2759–2766.

[48] Granet, V., Vermorel, O., Lacour, C., Enaux, B., Dugue, V. and Poinsot, T. (2012): *Large-Eddy Simulation and experimental study of cycle-to-cycle variations of stable and unstable operating points in a spark-ignition engine*. Combustion and Flame, vol. 159(4), pp. 1562–1575.

[49] Grasreiner, S. (2012): *Combustion modeling for virtual SI engine calibration with the help of 0D/3D methods*. Ph.d. thesis, TU Bergakademie Freiberg, Freiberg.

[50] Grasreiner, S., Neumann, J., Luttermann, C., Wensing, M. and Hasse, C. (2014): *A quasi-dimensional model of turbulence and global charge motion for spark ignition engines with fully variable valvetrains*. International Journal of Engine Research, vol. 15(15), pp. 805–816.

[51] Grasreiner, S., Neumann, J., Wensing, M. and Hasse, C. (2015): *A Quasi-Dimensional Model of the Ignition Delay for Combustion Modeling in Spark-Ignition Engines*. Journal of Engineering for Gas Turbines and Power, vol. 137(7), pp. 1–7.

[52] Green, J.B., Daw, C.S. and Armfield, J.S. (1998): *Time Irreversibility and Comparison of Cyclic-Variability Models*. SAE paper, (1999-01-0221).

[53] Green, J.B., Daw, C.S., Armfield, J.S., Finney, C.E.A. and Durbetaki, P. (1998): *Time Irreversibility of Cycle-by-Cycle Engine Combustion Variations*. Proceedings of the 1998 Technical Meeting of the Central States Section of the Combustion Institute.

[54] Grill, M. (2006): *Objektorientierte Prozessrechnung von Verbrennungsmotoren*. Ph.d. thesis, Universität Stuttgart, Stuttgart.

[55] Gross, V., Kubach, H., Spicher, U., Schiessl, R. and Maas, U. (2010): *Laserzündung und Verbrennung im Ottomotor mit Direkteinspritzung*. MTZ Motortechnische Zeitung, vol. 71(7), pp. 532–539.

[56] Group, Kistler (2015): *Watercooled PiezoStar Pressure Sensor*, data manual.

[57] Hall, M. and Bracco, F. (1986): *Cycle-Resolved Velocity and Turbulence Measurements Near the Cylinder Wall of a Firing S.I. Engine*. SAE paper, (861530).

[58] Han, S. B. and Hwang, S. Il. (2013): *Cycle-to-Cycle Fluctuations in a Spark Ignition Engineat Low Speed and Load*. Journal of Energy Engineering, vol. 22(2), pp. 205–210.

[59] Hasse, C. (2016): *Scale-resolving simulations in engine combustion process design based on a systematic approach for model development*. International Journal of Engine Research, vol. 17(1), pp. 44–62.

[60] Hasse, C., Sohm, V. and Durst, B. (2008): *Detached eddy simulation of cyclic large scale fluctuations in a simplified engine setup*. International Journal of Heat and Fluid Flow, vol. 30(1), pp. 32–43.

[61] Hasse, C., Sohm, V. and Durst, B. (2009): *Numerical investigation of cyclic variations in gasoline engines using a hybrid URANS/LES modeling approach*. Computer & Fluids, vol. 39(1), pp. 25–48.

[62] Haworth, D. (1999): *Large-Eddy Simulation of In-Cylinder Flows*. Oil & Gas Science and Technology, vol. 54(2), pp. 175–185.

[63] Herden, W. (2001): *Zündung und Entflammung bei Benzindirekteinspritzung*. Benzin- und Dieseldirekteinspritzung, pp. 223–237, expert Verlag.

[64] Heywood, J. B. (1988): *Internal Combustion Engine Fundamentals*. McGraw-Hill, Inc.

[65] Hinze, P. C. (1997): *Cycle-to-cycle combustion Variations in a spark-ignition engine operating at idle*. Ph.d. thesis, Massachusetts Institute of Technology, Cambridge.

[66] Hoard, J. and Rehagen, L. (1997): *Relating Subjective Idle Quality to Engine Combustion*. SAE paper, (970035).

[67] Incorporated, Gamma Technologies (2017): *www.gtisoft.com*.

[68] Jerzembeck, S. (2010): *Experimentelle und numerische Untersuchung instationärer lalaminar Flammen bei hohem Druck*. Ph.d. thesis, Rheinisch-Westfälischen Technischen Hochschule Aachen, Aachen.

[69] Johansson, B. (1995): *On Cycle-to-Cycle Variations in Spark Ignition Engines*. Ph.d. thesis, Lund Institute of Technology, Lund.

[70] Johansson, B. (1996): *Cycle-to-Cycle Variations in S.I. Engines - The Effects of Fluid Flow and Gas Composition in the Vicinity of the Spark Plug on Early Combustion*. SAE paper, (962084).

[71] Joos, F. (2006): *Technische Verbrennung: Verbrennungstechnik, Verbrennungsmodellierung, Emissionen*. Springer, Berlin, ISBN 978-3-540-34334-9.

[72] Karim, G. A. (1967): *An Examination of the Nature of the Random Cyclic Pressure Variations in a Spark-Ignition Engine*. Journal of the Institute of Petroleum, vol. 53(519), pp. 112–120.

[73] Karvountzis-Kontakiotis, A., Ntziachristos, L., Samaras, Z. and Dimaratos, A. (2015): *Experimental Investigation of Cyclic Variability on Combustion and Emissions of a High-Speed SI Engine*. SAE paper, (2015-01-0742).

[74] Klenk, M., Moser, W., Mueller, W. and Wimmer, W. (1993): *Misfire Detection by Evaluating Crankshaft Speed-A Means to Comply with OBDII*. SAE paper, (930399).

[75] Kohn, W. (2004): *Datenanalyse und Wahrscheinlichkeitsrechnung*. Springer, Berlin, ISBN 978-3-540-21677-3.

[76] Krost, P., Hübner, W. and Hasse, C. (2017): *A physical-based approach for modeling cycle-to-cycle variations within a 0D/1D simulation environment*. International Journal of Engine Research, (Special Issue Article).

[77] Krost, P., Hübner, W. and Hasse, C. (2017): *A Physical-Based Approach for Modeling Cycle-to-Cycle Variations within a 0D/1D Simulation Environment*. Internationale Konferenz der Motorischen Verbrennung am Haus der Technik.

[78] Larimore, J., Hellstroem, E., Jade, S., Stefanopoulou, AG and Jiang, L. (2014): *Real-time internal residual mass estimation for combustion with high cyclic variability*. International Journal of Engine Research, vol. 16(3), pp. 474–484.

[79] Lauer, T. and Geringer, B. (2008): *Bewertung der Restgastoleranz bei homogenen Brennverfahren für hohe Abgasrückführraten*. MTZ Motortechnische Zeitung, vol. 69(2), pp. 154–161.

[80] Lee, K. H. and Foster, D. E. (1995): *Cycle-by-Cycle Variations in Combustion and Mixture Concentration in the Vicinity of Spark Plug Gap*. SAE paper, (950814).

[81] Letellier, C., Meunier-Guttin-Cluzel, S., Gouesbet, G., Neveu, F., Duverger, T. and Cousyn, B. (1997): *Use of the Nonlinear Dynamical System Theory to Study Cycle-to-Cycle Variations from Spark Ignition Engine Pressure Data*. SAE paper, (971640).

[82] Lyon, D. (1986): *Knock and cyclic dispersion in a spark ignition engine*. IMECHE - Conference Journal, vol. 1986/11(C307/86), pp. 105–15.

[83] Martin, J., Plee, S. and Remboski, D. (1988): *Burn Modes and Prior-Cycle Effects on Cyclic Variations in Lean-Burn Spark-Ignition Engine Combustion*. SAE paper, (880201).

[84] Matekunas, F. A. (1983): *Modes and Measures of Cyclic Combustion Variability*. SAE paper, (830337).

[85] Merker, G. and Schwarz, C. (2009): *Grundlagen Verbrennungsmotoren: Simulation der Gemischbildung, Verbrennung, Schadstoffbildung und Aufladung.*. ATZ/MTZ-Fachbuch. Vieweg and Teubner, Wiesbaden, ISBN 978-3-834-89344-4.

[86] Merker, G., Schwarz, C., Stiesch, G. and Otto, F. (2006): *Grundlagen Verbrennungsmotoren: Simulation der Verbrennung und Schwadstoffbildung.*. Vieweg and Teubner, Wiesbaden, ISBN 978-3-8351-9069-6.

[87] Metghalchi, M. and Keck, J. C. (1982): *Burning Velocities of Mixture of Air with Methanol, Isooctane, and Indolene at High Pressure and Temperature*. Combustion and Flame, vol. 48, pp. 191–210.

[88] Mickelsen, W. R. and Ernstein, N. E. (1953): *Growth rates of turbulent free flames*. Fourth international Symposium on Combustion, pp. 325–333, Williams & Wilkins, Baltimore.

[89] Millo, F., Rolando, L., Pautasso, E. and Servetto, E. (2014): *A Methodology to Mimic Cycle to Cycle Variations and to Predict Knock Occurrence through Numerical Simulation*. SAE paper, (2014-01-1070).

[90] Nefischer, A. (2009): *Quasidimensionale Modellierung turbulenzgetriebener Phänomene in Ottomotoren*. Ph.D. thesis, TU Graz.

[91] Nefischer, A., Hallmannsegger, M., Wimmer, A. and Pirker, G. (2009): *Application of a Flow Field Based Heat Transfer Model to Hydrogen Internal Combustion Engines*. SAE paper, (2009-01-1423).

[92] Nefischer, A., Neumann, J. and Stanciu, A. (2014): *Quasi-dimensional modelling of turbulence-driven phenomena in SI engines*. Int. J. Vehicle Design, vol. 66(3), pp. 297–316.

[93] Omura, T., Nakata, K., Yoshihara, Y. and Takahashi, D. (2016): *Research on the Measures for Improving Cycle-to-Cycle Variations under High Tumble Combustion*. SAE paper, (2016-01-0694).

[94] Omura, T., Takahashi, D., Yoshihara, Y. and Nakata, K. (2016): *Development of the Measures to Improve Cycle-to-Cycle Variations in SI High Tumble Combustion*. JSAE Annual Congress (25-27 May 2016).

[95] Ozdor, N., Dulger, M. and Sher, E. (1994): *Cyclic Variability in Spark Ignition Engines - A Literature Survey*. SAE paper, (940987).

[96] Ozdor, N., Dulger, M. and Sher, E. (1996): *An Experimental Study of the Cyclic Variability in Spark Ignition Engines*. SAE paper, (960611).

[97] Patterson, D. J. (1966): *Pressure Variation, A Fundamental Combustion Problem.* SAE paper, (660129).

[98] Pera, C., Knop, V. and Reveillon, J. (2014): *Influence of flow and ignition fluctuations on cycle-to-cycle variations in early flame kernel growth.* Elsevier, vol. 35(3), pp. 2897–2905.

[99] Peters, B. D. and Borman, G.L. (1970): *Cyclic Variations and Average Burning Rate in a S. I. Engine.* SAE paper, (700064).

[100] Peters, N. (2004): *Turbulent Combustion.* Cambridge University Press, Cambridge, ISBN 0-521-66082-3.

[101] Pischinger, R., Kell, M. and Sams, T. (2009): *Thermodynamik der Verbrennungskraftmaschine: Der Fahrzeugantrieb.* Springer, Wien, ISBN 978-3-211-99277-7.

[102] Pischinger, S. and Heywood, J. B. (1990): *How Heat Losses to the Spark Plug Electrodes Affect Flame Kernel Development in a SI-Engine.* SAE paper, (900021).

[103] Poetsch, C., Schuemie, H., Ofner, H. and Tatschl, R. (2013): *A Computional Study on the Impact of Cycle-to-Cycle Fluctuations on Fuel Consumption and Knock in Steady-State and Drivecycle Operation.* SAE paper, (2013-24-0030).

[104] Pundir, B., Zvonow, V. A. and Gupta, C. P. (1981): *Effect of Charge Non-Homogeneity on Cycle-by-Cycle Variations in Combustion in SI Engines.* SAE paper, (810774).

[105] Qin, W., Xu, M. and Yin, P. (2015): *Analysis of the Cycle-to-Cycle Variations of the In-Cylinder Vortex Structure and Vorticity using Phase-Invariant Proper Orthogonal Decomposition.* SAE paper, (2015-01-1904).

[106] Richard, S., Dulbecco, A., Angelberger, C. and Truffin, K. (2015): *Development of a one-dimensional computational fluid dynamics modeling approach to predict cycle to-cycle variability in spark-ignition engines based on physical understanding acquired from large eddy simulation.* International Journal of Engine Research, vol. 16(3), pp. 379–402.

[107] Roithmeier, C. (2011): *Virtuelle Applikation von Motorsteuerungsfunktionen am Beispiel der Lasterfassung und der Fahrdynamikfunktionen.* Ph.D. thesis, Karlsruher Institute für Technologie.

[108] Scarcelli, R., Richards, K., Pomraning, E., Senecal, P. K., Wallner, T. and Sevik, J. (2016): *Cycle-to-Cycle Variations in Multi-Cycle Engine RANS Simulations.* SAE paper, (2016-01-0593).

[109] Schäfer, L., Miklautschitsch, M., Kleemann, A. and Hausner, O. (2013): *Experimental investigation of spark ignition in turbo-charged direct-injection SI engines.* Internationale Konferenz der motorischen Verbrennung am Haus der Technik.

[110] Schiffmann, P., Paltrinieri, S., Shekhawat, Y., Reuss, D.L., Sick, V., Fontanesi, S. and Haworth, D.C. (2014): *An Integrated Experimental and Simulation Study of Cycle-to-Cycle Variations in a Homogeneous-Charge Spark-Ignition Engine.* International Multidimensional Engine Modeling Users Group Meeting.

[111] Schück, C., Tagel, S., Towae, OO., Samenfink, W., Schünemann, E. and Koch, T. (2017): *Analyse der Partikelentstehung bei dynamischen Lastwechsel mit Saugrohreinspritzung an einem endoskopisch zugänglichen 4-Zylinder-Ottomotor mit Turboaufladung.* Internationaler Kongress der motorischen Verbrennung am Haus der Technik.

[112] Shen, H., Hinze, P. C. and Heywood, J. B. (1996): *A Study of Cycle-to-Cycle Variations in SI Engines Using a Modified Quasi-Dimensional Model.* SAE paper, (961187).

[113] Sjeric, M., Kozarac, D. and Taritas, I. (2014): *Experimentally Supported Modeling of Cycle-to-Cycle Variations of SI Engine Using Cycle-Simulation Model.* SAE paper, (2014-01-1069).

[114] Sjeric, M., Kozarac, D. and Tatschl, R. (2015): *Modelling of early flame kernel growth towards a better undertanding of cyclic combustion variability in SI engines.* Elsevier, vol. 103, pp. 895–909.

[115] Smooke, M. D. and Giovangigli, V. (1991): *Formulation of the premixed and nonpremixed test problems*, vol. 138. Mechanical Engineering, Berlin, ISBN 978-3-540-47496-8.

[116] Soltau, J. P. (1960): *Cylinder Pressure Variations in Petrol Engines*. Proceedings of the Institution of Mechanical Engineers, vol. 14(1), pp. 99–117.

[117] Steurs, K., Blomberg, C. K. and Boulouchos, K. (2014): *Knock in an Ethanol Fueled Spark Ignition Engine: Detection Methods with Cycle-Statistical Analysis and Predictions Using Different Auto-Ignition Models*. SAE paper, (2014-01-1215).

[118] Stone, C. R., Brown, A. G. and Beckwith, P. (1996): *Cycle-by-Cycle Variations in Spark Ignition Engine Combustion - Part II: Modelling of Flame Kernel Displacements as a Cause of Cycle-by-Cycle Variations*. SAE paper, (960613).

[119] Suckart, D., Linse, D., Schutting, E. and Eichlseder, H. (2016): *Experimental and simulative investigation of flame-wall interactions and quenching in spark-ignition engines*. Automotive and Engine Technology.

[120] Sztenderowicz, M. and Heywood, J. B. (1990): *Mixture Nonuniformity Effects on S.I. Engine Combustion Variability*. SAE paper, (902142).

[121] Tuner, M. (2008): *Stochastic Reactor Models for Engine Simulations*. Ph.d. thesis, University Lund, Lund.

[122] v. Basshuysen, R. and Schäfer, F. (2015): *Handbuch Verbrennungsmotor - Grundlagen, Komponenten, Systeme, Perspektiven*. Springer, Wiesbaden, ISBN 978-3-658-10901-1.

[123] Vermorel, O., Richard, S., Colin, O., Angelberger, C., Benkenida, A. and Veyante, D. (2008): *Understanding cyclic variability in a spark ignited engine using multi-cycle LES*. Combustion and Flame, vol. 156(8), pp. 1525–1541.

[124] Vitek, O. and Macek, J. (2013): *Modeling Cycle-to-Cycle Variations in 0-D/1-D Simulation by Means of Combustion Model Parameter Perturbations based on Statistics of Cycle-Resolved Data*. SAE paper, (2013-01-1314).

[125] Vitek, O., Macek, J., Z, Pavlovic and Tatschl, R. (2016): *Statistical Analysis of Detailed 3-D CFD LES Simulations with Regard to CCV Modeling*. Journal of Middle European Construction and Design of Cars, vol. 14(1), pp. 1–16, ISSN 1804-9338.

[126] Wagner, R. M., Drallmeier, J.A. and Daw, C.S. (1998): *Origins of cyclic Dispersion patterns in Spark Ignition Engines*. Proceedings of the Central States Section of the Combustion Institute (31. May - 2.June 1998).

[127] Wenig, M. (2013): *Simulation der ottomotorischen Zyklenschwankungen*. Ph.d. thesis, Universität Stuttgart, Stuttgart.

[128] Wenig, M. (2013): *Zyklenschankungen - Simulation der ottomotorischen Zyklenschankungen*. FVV.

[129] Wenig, M., Grill, M. and Bargende, M. (2013): *A New Approach for Modeling Cycle-to-Cycle Variations within the Framework of a Real Working-Process Simulation*. SAE paper, (2013-01-1315).

[130] Witt, A. (1999): *Analyse der thermodynamischen Verluste eines Ottomotors unter den Randbedingungen variabler Steuerzeiten*. Ph.d. thesis, Technical University Graz, Graz.

[131] Wu, H. (2013): *Study of spark ignition engine combustion model for the analysis of cyclic variation and combustion stability at lean operating conditions*. Master thesis, Michigan Technological University.

[132] Young, M. (1980): *Cyclic Dispersion - Some Quantitative Cause-and-Effect Relationships*. SAE paper, (800459).

[133] Young, M. B. (1981): *Cyclic Dispersion in the Homogeneous-Charge Spark-Ignition Engine - A Literature Survey*. SAE paper, (810020).

[134] Zervas, E. (2004): *Correlations between cycle-to-cycle variations and combustion parameters of a spark ignition engine*. Applied Thermal-Engineering, vol. 24(14-15), pp. 2073–2081.

A Visualisation possibilities of CCV

The following figure shows 100 consecutive engine cycles of an example engine operating point at 1500 rpm with a mean *IMEP* of 4 bar. It gives a good overview of the *IMEP* output of individual cycles in subfigure (a) which can directly be correlated to the combustion rate when explicitly compared to mass fraction burn points such as *MFB5%*, *MFB50%* and *MFB90%* in subfigure (b).

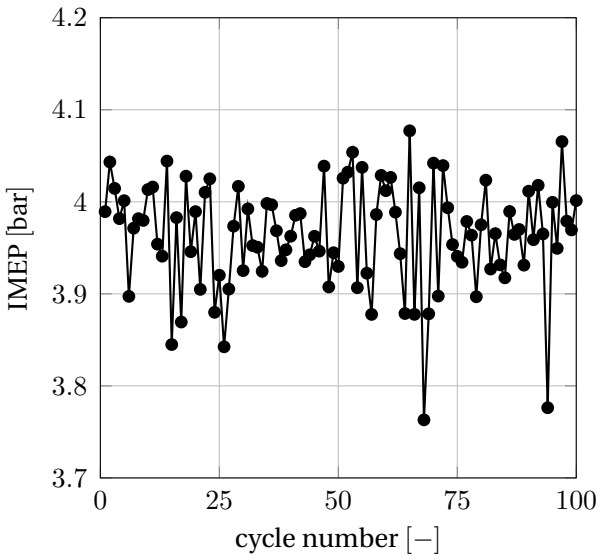

(a) 100 consecutive cycles at a mean *IMEP* of 4 bar.

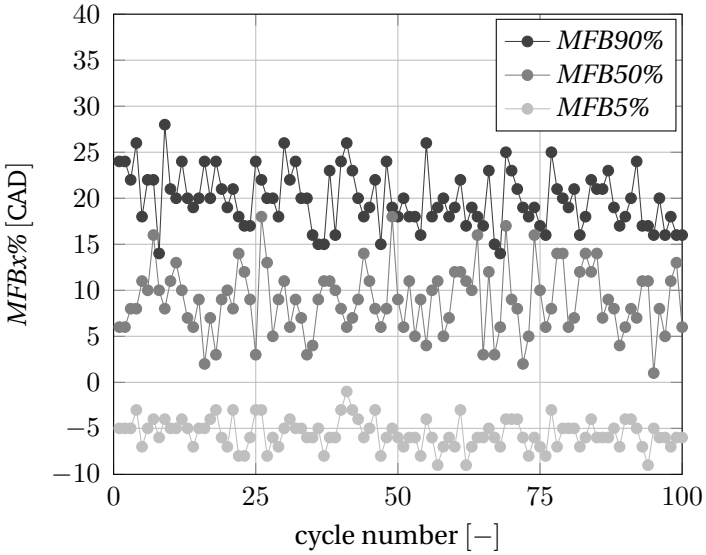

(b) *MFB5%*, *MFB50%* and *MFB90%* at the 100 consecutive cycles corresponding to the IMEP from (a).

Figure A.1.: Different ways of illustrating cycle-to-cycle variations.

B 3D CFD simulation properties

The properties of the 3D CFD RANS simulations from the TU Freiberg and from BMW are as shown in the following table.

creator	software	spatial resolution	combustion chamber
TU Freiberg	Ansys CFX	$1.4 \cdot 10^7$ cells @ FTDC	half model
BMW	Ansys CFX	$1.4 \cdot 10^7$ cells @ FTDC	full model

Table B.1.: 3D RANS simulation properties from the TU Freiberg and BMW.

creator	turbulence model	combustion model
TU Freiberg	k-ω SST	G-equation with flamelet-tables
BMW	k-ω SST	G-equation with flamelet-tables

Table B.2.: 3D RANS simulation properties from the TU Freiberg and BMW.

C Calibration factors of the 0D turbulence model

The calibration factors of the turbulence model for the SI engines investigated are shown in the following table in relation to the design engine N20 [49]. That means, that each factor is set to unity for the N20 first and then, calculated in relation for the factors of the other engines.

calibration factor	N20	B48 serial pistons	B48 $\epsilon = 14$ pistons	TT1.2	TT1.3 (320)	TT1.3 (400)
lt_{exp}	1	1.03	1.06	1	1	1
$TKE_{prod,xy,intake}$	1	1	1	0.5	0.42	0.41
$TKE_{prod,z,intake}$	1	1	1	0.5	0.37	0.36
$TKE_{prod,xy,compress}$	1	0.66	0.66	0.5	0.42	0.41
$TKE_{prod,z,compress}$	1	1	1	0.5	0.42	0.41
$TKE_{prod,intake}$	1	3	3	0.5	0.4	0.39

Table C.1.: Calibration factors of the turbulence model for the SI engines investigated.

lt_{exp} is a calibration factor regarding the integral length scale l_t. Here, an increase in the factor decreases the length scale and thus, increases dissipation, see Equations 4.20 and 4.21. Only minor adaptations are needed for the B48 engine with serial pistons and $\epsilon = 14$ pistons. The four calibration factors $TKE_{prod,xy,intake}$, $TKE_{prod,z,intake}$, $TKE_{prod,xy,compress}$ and $TKE_{prod,z,compress}$ are used for the adjustment of the tumble and swirl motion build up during the intake and compression stroke, see Equations 4.34 and 4.35. Here, relevant changes can be seen for the TT1.2, TT1.3 (320 and 400). The intake ports of these naturally aspirated SI engines are optimized for maximum power output, thus, no tumble ports are implemented, in comparison to the N20 and B48 engine. The calibration factor $TKE_{prod,intake}$ is used, in order to adapt the turbulent kinetic energy, produced by instant shearing turbulence, cf. Equation 4.38. Again, for the TT1.2 and TT1.3 (320 and 400) the factor is reduced, whereas for the B48 engine with serial pistons and $\epsilon = 14$ pistons the factor is increased. Note that a factor of three in comparison to the N20 engine increases the TKE at ITDC around 1-2 %.

D Summary table of state-of-the-art CCV models

The following two tables give an overview of the year of publication, model type, model design, model calibration as well as special features and findings of state-of-the-art CCV models.

author(s)	year	model typ	model design
Poetsch et al. [103]	2013	empirical	random perturbations on Vibe parameters
Vitek et al. [124]	2013	empirical	perturbations on the turbulent length scale, ignition delay parameter and flame-wall interaction parameter
Sjeric et al. [113]	2014	empirical	perturbations on turbulence production parameters during the intake stroke (also effect ignition and combustion model)
Wenig [127]	2013	empirical	perturbations on two constants within the laminar burning velocity formulation and on the flame kernel growth
Dulbecco et al. [33]	2015	physical	perturbations on tumble ratio and integral length scale
Richard et al. [106]	2015	physical	perturbations on tumble ratio, integral length scale and flow convection in the spark plug vicinity

Table D.1.: Literature overview of 0D state-of-the-art CCV model approaches.

author(s)	model calibration	special features/findings
Poetsch et al. [103]	mean values and standard deviations of the Vibe parameters are adjusted to match experimental CCV data	applied to transient simulations
Vitek et al. [124]	PDF and cross-correlations of the three parameter are adjusted to match cyclic burn rates from experiment	for predictability reasons 3D CFD LES would be a good measure for an accurate calibration
Sjeric et al. [113]	standard deviations of the PDF are determined by matching COV_{IMEP} found by simulation to experiment	turbulence parameter perturbations have higehst effect on CCV
Wenig [127]	cross-correlations are implemented in dependence of speed, ignition delay, burn duration and unburned temperature	four different conventional SI combustion processes are used for the CCV model design
Dulbecco et al. [33]	standard deviations of the PDFs are determined by comparing of COV of $IMEP, p_{max}$ and $CA_{p,max}$ found by simulation to experiment	physical causes are identified by means of 3D CFD LES
Richard et al. [106]	standard deviations of the PDFs are determined by comparing COV_{IMEP} from simulation to experiment	physical causes are identified by means of 3D CFD LES

Table D.2.: Literature overview of 0D state-of-the-art CCV model approaches.

E Influencing factor matrix of the calibration procedure

The following two tables display the resulting matrix of the calibration procedure. Hereby, the M_d is defined as the actual engine load in the specific engine operating point, whereas the $M_{d,max}$ is determined to be the maximum load, the engine can output at the specific engine speed. In order to get the actual physical limit, finally, the influencing factor term of each physical cause has to be multiplied with the fixed value, defined in table 5.3.

physical cause	engine speed n_{engine}	engine load M_d	λ
dk_{prod}	$\frac{-0.14 \cdot \ln n_{engine} + 1.4}{0.32}$	$\frac{0.55 \cdot \exp \frac{-0.39 \cdot M_d \cdot \lambda}{M_{d,max}}}{0.38}$	1
l_t	$\frac{-0.14 \cdot \ln n_{engine} + 1.4}{0.32}$	$\frac{0.55 \cdot \exp \frac{-0.39 \cdot M_d \cdot \lambda}{M_{d,max}}}{0.38}$	1
$r_{k,init}$	1	1	$\frac{-0.50 \cdot \lambda^2 + 1.74 \cdot \lambda - 1.05}{0.2}$
r_{ecc}	1	1	$\frac{-0.50 \cdot \lambda^2 + 1.74 \cdot \lambda - 0.95}{0.3}$
s_{quench}	1	1	$\frac{-0.50 \cdot \lambda^2 + 1.74 \cdot \lambda - 0.95}{0.3}$

Table E.1.: Parameterization matrix of engine speed and load for the five physical causes.

physical cause	*MFB50%*
dk_{prod}	$\frac{0.12 \cdot 10^{-5} \mathit{MFB50\%}^4 - 0.13 \cdot 10^{-3} \mathit{MFB50\%}^3 + 0.50 \cdot 10^{-2} \cdot \mathit{MFB50\%}^2 - 0.82 \cdot 10^{-1} \cdot \mathit{MFB50\%} + 0.75}{0.38}$
l_t	$\frac{0.12 \cdot 10^{-5} \mathit{MFB50\%}^4 - 0.13 \cdot 10^{-3} \mathit{MFB50\%}^3 + 0.50 \cdot 10^{-2} \cdot \mathit{MFB50\%}^2 - 0.82 \cdot 10^{-1} \cdot \mathit{MFB50\%} + 0.75}{0.38}$
$r_{k,init}$	$\frac{0.40 \cdot 10^{-3} \cdot \mathit{MFB50\%}^2 - 0.52 \cdot 10^{-2} \cdot \mathit{MFB50\%} + 0.21}{0.2}$
r_{ecc}	$\frac{0.50 \cdot 10^{-6} \mathit{MFB50\%}^4 - 0.55 \cdot 10^{-4} \mathit{MFB50\%}^3 + 0.22 \cdot 10^{-2} \cdot \mathit{MFB50\%}^2 - 0.38 \cdot 10^{-1} \cdot \mathit{MFB50\%} + 0.45}{0.3}$
s_{quench}	$\frac{0.10 \cdot 10^{-5} \mathit{MFB50\%}^4 - 0.10 \cdot 10^{-3} \mathit{MFB50\%}^3 + 0.38 \cdot 10^{-2} \cdot \mathit{MFB50\%}^2 - 0.58 \cdot 10^{-1} \cdot \mathit{MFB50\%} + 0.52}{0.3}$

Table E.2.: Parameterization matrix of *MFB50%* and λ for the five physical causes.

F Comparison of B48 engine map with new and state-of-the-art CCV models

In this appendix, engine maps of the B48 with serial pistons are shown regarding the relative and absolute deviation of COV_{IMEP} between experiment and simulation, calculated with the following Equations F.1 and F.2, respectively.

$$COV_{dev,rel} = COV_{IMEP,\,exp} - COV_{IMEP,\,sim} \tag{F.1}$$

$$COV_{dev,abs} = \frac{COV_{IMEP,\,exp}}{COV_{IMEP,\,sim}} \tag{F.2}$$

The following illustrations show the relative and the absolute deviations for the state-of-the-art CCV model [46] and the new CCV model. As it can be seen from the illustrations only the results from both equations together should be compared. For example, at a given engine operating point of 3000 rpm and an $IMEP = 10$ bar the new CCV model relatively deviates from experiment by a $COV_{IMEP,\,dev,\,rel}$ of around 0.4 %. This does not seem to be a lot of difference, since there are engine map areas of COV_{IMEP} around 5 %. However, at the given engine operating point, the experimental COV_{IMEP} is at 0.6 %. This means that there is an absolute deviation of $COV_{IMEP,\,dev,\,abs}$ of a factor 3, which on the other hand seems to be high. Therefore, it can be said that the engine map areas in which the new CCV model underestimates the experimental COV_{IMEP} by a $COV_{IMEP,\,dev,\,abs}$ of 2 to 3 are areas with low relative deviations and overall COV_{IMEP}.

The state-of-the-art CCV model on the other hand underestimates the experimental COV_{IMEP} at low engine speeds and loads both relatively and quantitatively, as it can be seen at first sight from the illustrations. At high engine speeds and low loads the state-of-the-art CCV model overestimates COV_{IMEP} relatively and absolutely high.

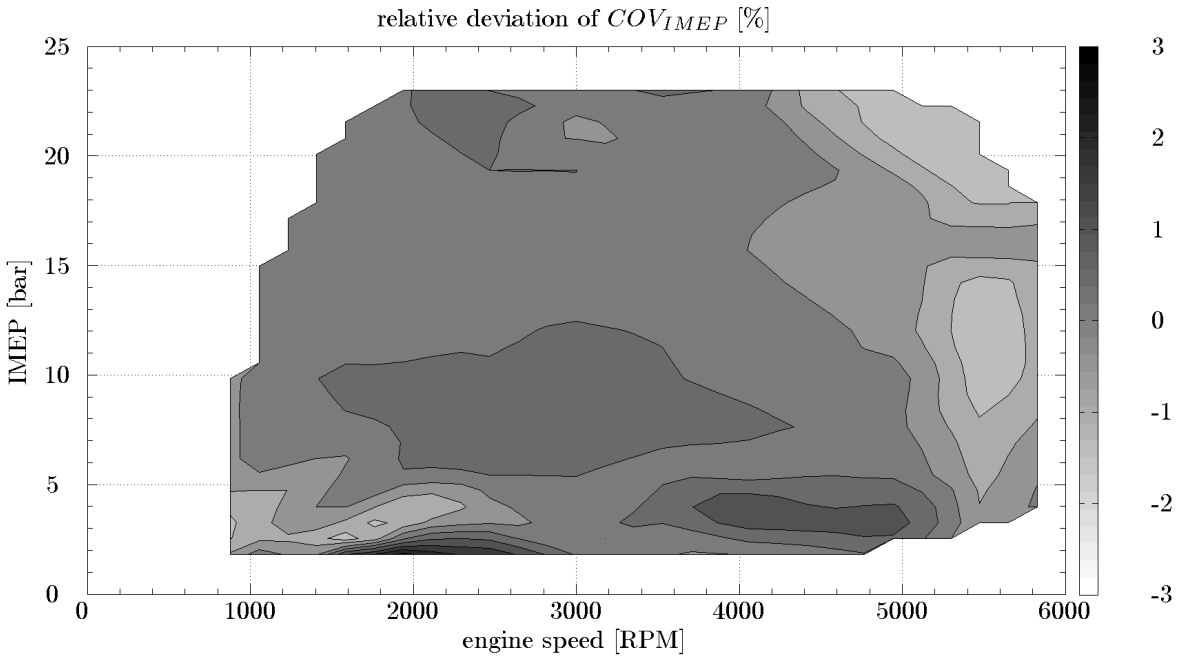

Figure F.1.: Relative deviations of COV_{IMEP} from the new CCV model.

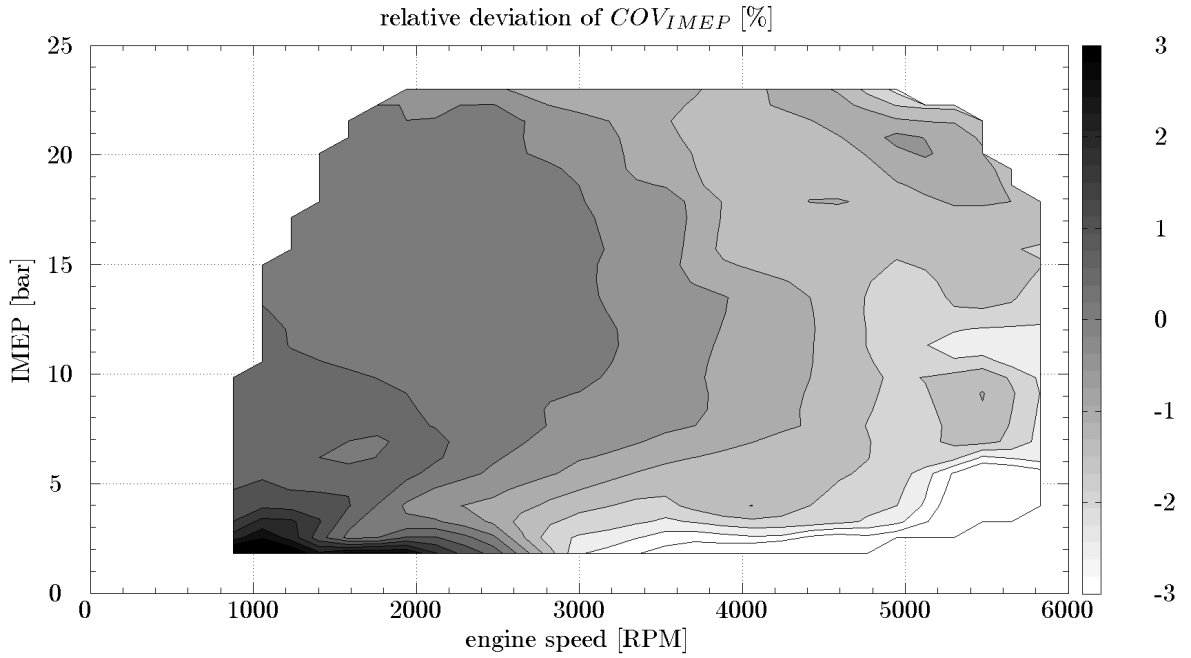

Figure F.2.: Relative deviations of COV_{IMEP} from the state-of-the-art CCV model.

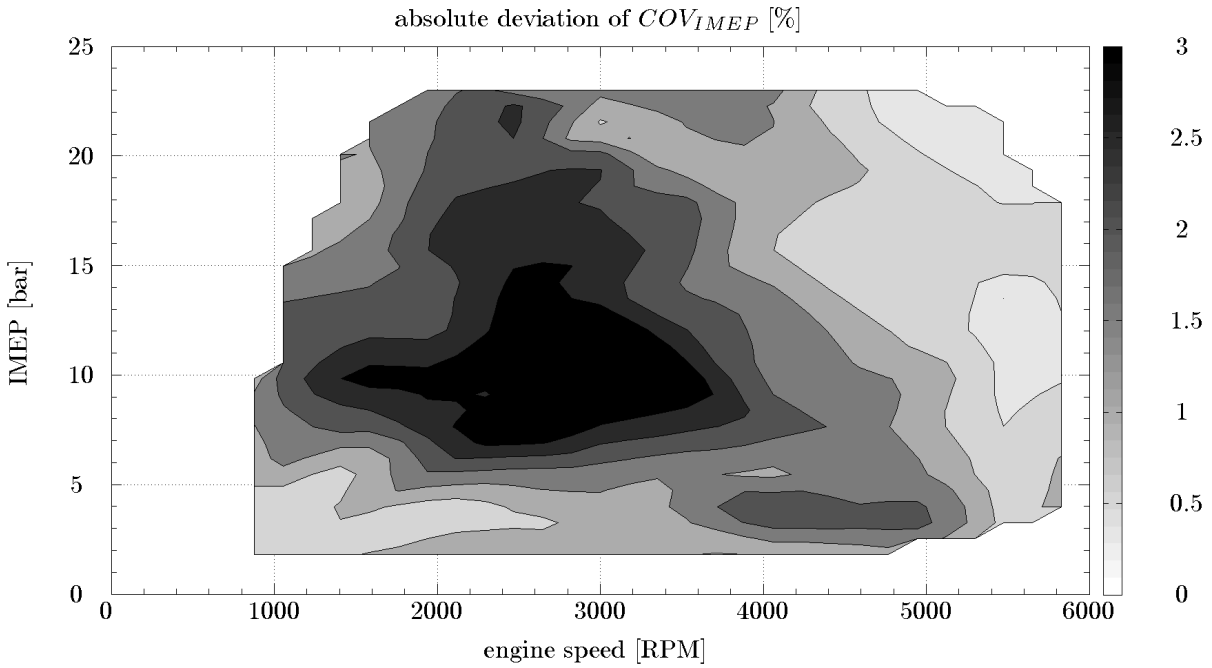

Figure F.3.: Absolute deviations of COV_{IMEP} from the new CCV model.

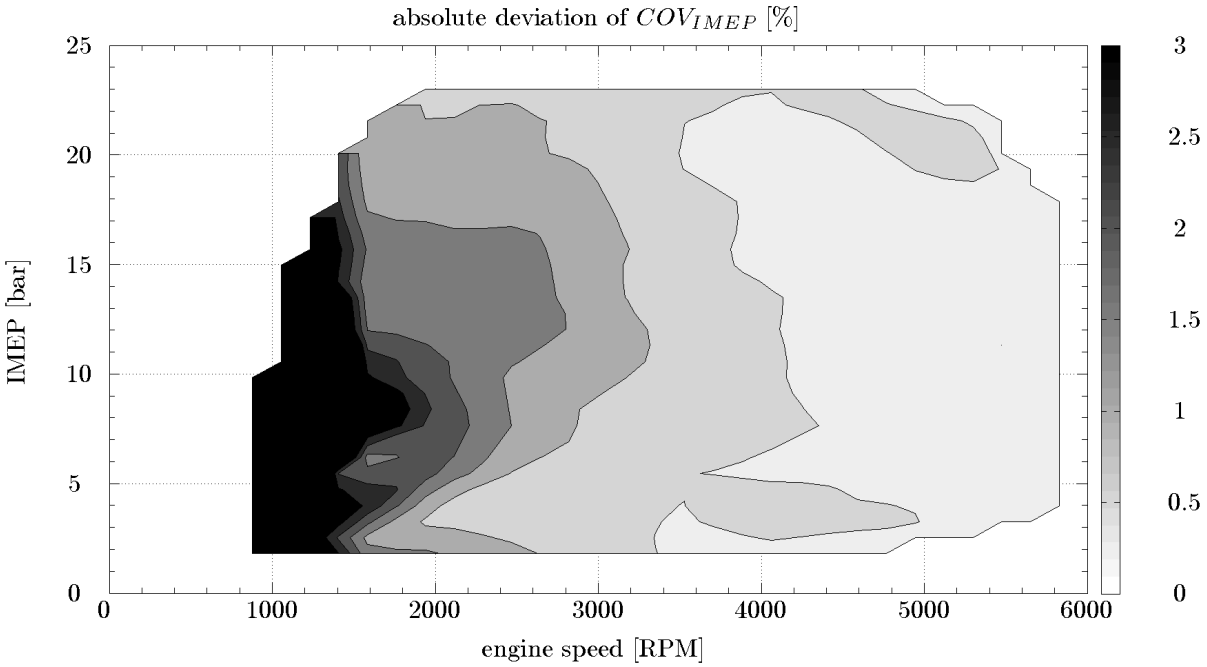

Figure F.4.: Absolute deviations of COV_{IMEP} from the state-of-the-art CCV model.